Spring 5-2021

Design and Modeling of Bioinspired Polyelectrolytes with Controlled Architectures for Gene Delivery Applications

Kelli Stockmal

DESIGN AND MODELING OF BIOINSPIRED POLYELECTROLYTES WITH CONTROLLED ARCHITECTURES FOR GENE DELIVERY APPLICATIONS

by

Kelli Anne Stockmal

A Dissertation
Submitted to the Graduate School,
the College of Arts and Sciences
and the School of Polymer Science and Engineering
at The University of Southern Mississippi
in Partial Fulfillment of the Requirements
for the Degree of Doctor of Philosophy

Approved by:

Dr. Sarah E. Morgan, Committee Chair
Dr. Xiaodan Gu
Dr. Robert L. Lochhead
Dr. Sergei I. Nazarenko
Dr. Charles W. Scales

May 2021

Published by the Graduate School

ABSTRACT

This dissertation focuses on the development of a range of bioinspired polyelectrolytes with controlled architectures for gene and drug delivery applications. Glycans are ubiquitous in biological systems, and understanding the role of saccharide stereochemistry, as well as cationic charge, on polymer behavior in aqueous solution and the interactions with nucleic acids can provide insight into how synthetic polyelectrolytes can be used for non-viral gene delivery and other biological applications.

The first chapter provides an introductory overview on how cationic polyelectrolytes can be used to aid the delivery of RNA for controlling gene expression in a variety of cell types, how molecular dynamics can be used to simulate the interactions between the cationic polyelectrolytes and RNA, and finally how pH-responsive hydrogels can be used to facilitate drug delivery for a range of biomedical applications. In the second chapter, the synthesis of cationic glycopolyelectrolytes for RNA interference in tick cells is presented, where the polymers are functionalized with either glucose or galactose pendant groups as well as tertiary amine pendant groups. The saccharide stereochemistry is shown to influence the intermolecular interactions between the glycopolyelectrolytes and double-stranded RNA (dsRNA), which ultimately causes differences in the relative expression of SelenoK transcripts within the tick cells. In the third chapter, molecular dynamics simulations are conducted to further understand the role of saccharide structure on the dynamics of glycomonomers and cationic oligomers in aqueous solution. Glucose- and galactose-functionalized monomers and oligomers are observed to have different intermolecular hydrogen bonding behavior in solution, which influence glycopolymer interchain interactions and their interactions with dsRNA. In the

fourth chapter, characterization of anionic multilayer hydrogels by atomic force microscopy nanoindentation is discussed. The surface morphology and modulus of pH-responsive multilayer hydrogel networks prepared by layer-by-layer assembly are shown to be highly influenced by fabrication conditions, which includes polymer deposition method (dip-coating or spin-coating) and sacrificial layer polymer molecular weight.

ACKNOWLEDGEMENTS

I am truly grateful to have received the education that I have at USM and I have many people to thank for their years of encouragement. First and foremost, I would like to thank my research advisor, Dr. Sarah Morgan, for her continued guidance and support. Dr. Morgan has held to the highest standards as a graduate student and has provided me countless opportunities to develop myself into a better scientist, communicator, and person throughout these last five years. Thank you for accepting me into your research group. I would also like to thank the Morgan Research Group lab manager, Dr. Lisa Kemp, for helping me develop my writing and speaking skills throughout the last few years, and has helped me extensively with planning my experiments more efficiently. I would like to thank my committee members Dr. Robert Lochhead, Dr. Sergei Nazarenko, Dr. Charles Scales, and Dr. Xiaodan Gu for their continued support. I would be remiss if I did not thank the past and present graduate students of the Morgan Research Group, including Dr. Ashleigh Bristol, Dr. April Fogel, Dr. Pradipta Das, Dr. Levi Moore, Dr. Katrina Knauer, Mitch Woellner, Rahul Shankar, Anthony Benasco, Kyle Mehringer, Garrett Abrahamsen, Hannah George, Molly Jones, Toby Edwards, and Kevin Green. Thank you to my undergraduate students Bishal Upadhyay, Ashley Davis, and Valeria Coello for helping me become a better teacher and mentor. I wish you all the best.

I'd like to also thank my numerous collaborators, including members of the Karim and Rangachari Research Groups at the University of Southern Mississippi and the Kharlampieva Research Group at the University of Alabama at Birmingham. It has been a pleasure working with each of you, and I greatly value the skills of effective

communication and collaboration across different disciplines that I have been able to learn.

I'd also like to thank all my colleagues and staff who have helped me complete my research over the years, including Dr. Charles McCormick, Dr. Bill Jarrett, Dr. Brian Olson, Dr. Keith Parsons, Dr. Brooks Abel, Dr. Jonathan Lindner, Dr. Bret Calhoun, Kim Wingo, Dana Froelich, Toni Altom, Anna Patterson, Ryan Dufrene, Chuck Collen, and Jeff Hollingsworth. I would also like to thank my funding sources for making this research possible, including the NSF-NRT Award 1449999, NIH GM-008098, and EPSCoR DGE-1632825, NSF MRI Grant ACI-1626217, and the MS INBRE facility (NIH IDeA Award P20GM103476).

Finally, I am grateful to all my family and friends who have provided me with memories that have made graduate school much more meaningful and enjoyable. I can't express how much I appreciate your love, friendship, and encouragement.

DEDICATION

This dissertation is dedicated to my parents, Joseph and Catherine Stockmal. I love you both and I have the sincerest gratitude for everything you have done for me. I wouldn't have been able to receive the excellent education that I have without your help.

TABLE OF CONTENTS

LIST OF TABLES

LIST OF ILLUSTRATIONS

LIST OF ABBREVIATIONS

AcGalEAm	2’-acrylamidoethyl-2,3,4,6-tetra-O-acetyl-β-D-galactopyranoside
AcGlcEAm	2’-acrylamidoethyl-2,3,4,6-tetra-O-acetyl-β-D-glucopyranoside
AFM	atomic force microscopy
ASEC-MALLS	aqueous size exclusion chromatography with multi-angle laser light scattering
CEP	4-cyano-4-(ethylsulfanylthiocarbonylsulfanyl) pentanoic acid
CTA	chain transfer agent
Đ	polymer dispersity
D_2O	deuterated water
DMAPAm	N-(3-(dimethylamino)propyl)acrylamide
DMT	Derjaguin-Mueller-Toporov (modulus)
DMSO	dimethylsulfoxide
DNA	*deoxyribonucleic acid*
dn/dc	refractive index increment
DLS	dynamic light scattering
DP	degree of polymerization
dsRNA	double-stranded ribonucleic acid
EMSA	electrophoretic mobility shift assay
FF	force field

GalEAm	2’-acrylamidoethyl-β-D-galactopyranoside
GlcEAm	2’-acrylamidoethyl-β-D-glucopyranoside
HB	hydrogen bond
HEAm	hydroxyethyl acrylamide
interHB	intermolecular hydrogen bond
intraHB	intramolecular hydrogen bond
LbL	layer-by-layer (assembly)
LDH	lactate dehydrogenase
MD	molecular dynamics
MeOH	methanol
M_n	number average molecular weight
M_w	weight average molecular weight
mRNA	messenger RNA
MWCO	molecular weight cutoff
NMR	nuclear magnetic resonance
N:P	nitrogen to phosphate ratio
PAPAm	poly(*N*-3-aminopropylacrylamide)
PCR	polymerase chain reaction
PDMAPAm	poly(*N*-(3-(dimethylamino)propyl)acrylamide)
PDMS	polydimethylsiloxane
PGal	poly(2’-acrylamidoethyl-β-D-galactopyranoside)
PGlc	poly(2’-acrylamidoethyl-β-D-glucopyranoside)
PBS	phosphate buffer saline

pDNA	plasmid DNA
PEG	polyethylene glycol
PEI	polyethyleneimine
PMAA	poly(methacrylic acid)
PS	polystyrene
PVPON	poly(N-vinyl pyrrolidone)
QNM	quantitative nanomechanical mapping
qRT-PCR	quantitative reverse-transcriptase PCR
RAFT	reversible addition-fragmentation chain-transfer
RI	refractive index
RISC	RNA-induced silencing complex
RMSD	root mean square deviation
RMSF	root mean square fluctuation
RNA	ribonucleic acid
RNAi	RNA interference
R_q	roughness
SA	spin-assisted
siRNA	small interfering RNA
TAE	Tris-acetate-ethylenediaminetetraacetic acid
V-501	4,4’-azobis(4-cyanovaleric aci

CHAPTER I – INTRODUCTION

The unifying theme of this work is to understand the role of noncovalent intermolecular interactions within bioinspired polyelectrolyte-based systems for better design of gene and/or drug delivery platforms. The research outlined in this dissertation is a compilation of three main concepts: 1) determining the effects of saccharide stereochemistry and charge on cytotoxicity, dsRNA binding, and RNA transfection in tick cells, 2) understanding the role of glycopolymer saccharide stereochemistry on intermolecular interactions related to polymer/dsRNA binding using computational tools, and 3) evaluating the role of layer-by-layer assembly conditions on pH-responsive modulus changes within anionic hydrogels with controlled internal architectures. This introductory chapter provides a review of pertinent literature regarding RNA interference and the use of glycopolyelectrolytes as non-viral polynucleotide transfection agents, molecular dynamics, and use of pH-responsive layer-by-layer derived hydrogels for controlled delivery. Finally, the objectives of the research outlined in this dissertation are presented.

1.1 RNA interference

1.1.1 RNAi mechanism

RNA interference (RNAi), also referred to as post-transcriptional gene silencing (PTGS), is a process in which the introduction of double-stranded RNAs (dsRNAs) triggers the destruction of targeted complementary messenger RNA (mRNA) transcripts to knock down expression of a particular protein and cause a change in cellular/organismal phenotype. Since its discovery by Fire and coworkers in *C. elegans*,

RNAi has proven to be a powerful reverse genetics tool to manipulate gene expression in not only cells but whole organisms.[1]

The underlying mechanism of RNAi is highly conserved among different organisms.[2] Upon introduction of exogenous dsRNA into cells, the RNase III Dicer (DCR) enzyme cleaves the dsRNA into smaller fragments of ~19-25 nucleotides (nt), which is referred to as small interfering RNA (siRNA). These siRNA fragments have a 2-nt 3' overhang that is recognized by RNAi machinery and are loaded into the multi-protein RNA-induced silencing complex (RISC), where the double-stranded siRNA is unwound by helicases and the antisense passenger strand is cleaved and removed by RISC protein Ago2. The activated RISC with the remaining siRNA sense strand binds with the target complimentary antisense mRNA strand, which is then degraded by Ago2. Thus, protein translation/expression is prevented and a loss in phenotype is observed (gene silencing).

1.1.2 RNAi pathways in non-mammalian cells

Although RNAi in mammalian cells for cancer therapeutics has been explored extensively, its popularity has become overshadowed as genomic editing technologies such as CRISPR-Cas9 become more advanced.[3] Nonetheless, RNAi is a useful tool for regulating gene expression in insects, particularly for crop protection.[4] Although the underlying mechanism of RNAi is highly conserved among different organisms, several key differences between mammalian and insect/arthropod RNAi pathways exist. In mammalian cells, exogenous dsRNA must be limited in terms of length to elicit specific gene silencing; use of dsRNA longer than 30 nt sequences activates the interferon signaling pathway and results in non-specific sequence effects and/or cellular apoptosis.[5]

Many non-mammalian eukaryotic organisms (including arthropods) lack this interferon response and longer dsRNAs (200-500 nts) can be used to result in higher RNAi efficiency, presumably due to the production of many siRNAs against the targeted mRNA transcript.[6-8] Furthermore, RNAi in insects enables a non-cell-autonomous response, unlike mammalian cells that only undergo cell-autonomous RNAi responses. This eliminates the need for targeted dsRNA delivery to enable systemic gene knockdown in non-mammalian organisms.[9] Transgenerational effects have also been observed, although it is likely that effects would be highly species-dependent.[10-11]

1.1.3 Barriers to successful RNAi

Regardless of cell or species type, successful RNAi requires overcoming intracellular/extracellular barriers including cellular uptake, protection against degradation, diffusion through the extracellular matrix, and endosomal escape/payload release.[12] Upon introduction of exogenous RNA to cells/organisms, non-specific RNAses attack and degrade the delivered RNA. RNA is also unstable and inherently susceptible to self-hydrolysis; nucleophilic 2'-OH groups on the ribose sugars can readily react with adjacent phosphodiester bonds on the sugar-phosphate RNA backbone to result in cleavage of RNA strands. Cell internalization of naked polynucleotides is typically hindered due to excessive anionic charges, which makes it difficult for them to traverse hydrophobic cell membranes through passive uptake pathways.[13] Alternatively, dsRNA may be internalized through receptor-mediated endocytosis, where endosomal escape is critical to release the dsRNA cargo into the cytoplasm for processing with DCR and RISC protein complexes for successful RNAi.

1.2 Cationic polyelectrolytes for nucleic acid transfection

1.2.1 Interactions of dsRNA with cationic biopolymers

Noncovalent interactions such as intermolecular hydrogen bonds (interHBs), intramolecular hydrogen bonds (intraHBs), and electrostatic interactions are critical in regulating folding, association, and ligand interactions in RNA systems. Until recently, it was thought that RNA-protein binding was reliant on well-defined RNA binding domains (RBDs) such as RNA recognition motifs (RRMs), zinc fingers, human heterogeneous nuclear ribonucleoprotein (hnRNP) K homology (KH) domains, or dsRNA binding domains (RBDs). However, RNA interactome capture has recently shown that many RNA binding proteins do not necessarily require well-defined binding domains and instead can harbor intrinsically disordered regions that allow for more flexible and dynamic RNA binding.[14-15] Examples of these regions include short linear motifs (SLiMs), RG[G] repeats, RS/RG-rich regions, K/R patches, and low-complexity (LC) sequences.[16]

1.2.2 Cationic polyelectrolyte transfection agents

Cationic polyelectrolytes interact with nucleic acids in a similar manner to amphiphilic biopolymers, which makes them promising materials to facilitate condensation of RNA into smaller particles for cell uptake. These are known as interpolyelectrolyte complexes, or polyplexes.[17] Polyplex formation is driven by entropic release of counterions, which occurs upon mixing aqueous solutions of oppositely charged polyelectrolytes (polycations and negatively charged polynucleotides) (Figure 1.1).

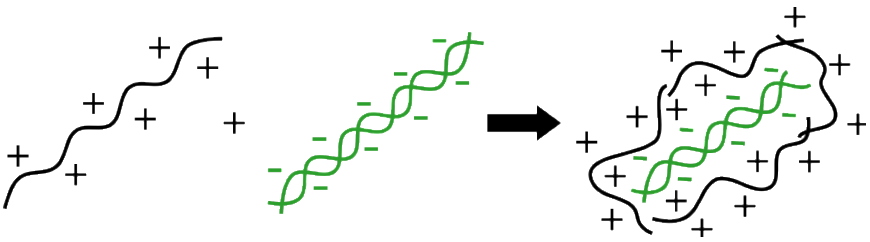

Figure 1.1 *Polyplex formation is achieved by mixing aqueous solutions of oppositely charged polyelectrolytes.*

Cationic charges on polycation transfection agents are most commonly charged amines, where polyethyleneimine (PEI, Lipofectamine) is widely regarded to be the "gold standard" for polymer-based transfection agents.[18-19] Other amine-functionalized polymers include chitosan,[20-21] poly(L-lysines),[22-23] poly(amidoamines),[24] poly(amino esters),[25] as well as a variety of cationic poly(meth)acrylates and poly(meth)acrylamides. Polynucleotide complexation and transfection efficiency will be affected by a number of properties including polymer molecular weight,[26] hydrophilicity,[27-28] self-assembling behavior,[29] degree of crosslinking,[30] and degree of branching.[31] McCormick and coworkers have shown that charge density and covalent attachment of RNA to polymers can also have considerable effects on gene delivery efficiency.[32-35]

Polyplex formation is primarily affected by polymer structure and the ratio of cationic amine charges on the polymer to anionic charges on the nucleic acids (herein referred to as N:P ratio), as well as ionic environment.[36] Although full encapsulation of the nucleic acids is typically desired for nucleic acid delivery in human cells, it is often not necessary for transfection into insect cells. For example, Avila and coworkers demonstrated that a mixture of cationic peptide-based capsules with lethal dsRNAs was still able to facilitate efficient cellular uptake and subsequent knockdown in both *T. castaneum* and *A. pisum* organisms upon oral delivery.[37]

Although popular candidates for non-viral gene delivery, polycations generally suffer in terms of their biocompatibility. Generally, cationic polyelectrolytes are highly cytotoxic, hence their frequent use in antibacterial/antimicrobial applications.[38-41] Polycation cytotoxicity can be dependent on cationic charge structure,[42-44] cationic charge density, molecular weight, concentration, and incubation/exposure time.[45-48] Given this challenge, significant effort has been put forth towards designing materials with increased biocompatibility through incorporation of neutral hydrophilic comonomers or grafted hydrophilic polymer chains.[49-58]

1.2.3 Glycopolyelectrolytes

Polysaccharides are the most abundant polymers on earth, and approximately half of all proteins (including RNA binding proteins) are glycosylated as a result of post-translational modifications.[59] Given the prevalence of saccharides in biological systems, synthetic cationic copolymers containing saccharide pendant groups (i.e. cationic glycopolyelectrolytes) have become interesting materials to explore as non-viral vectors for nucleic acid transfection, as well as for a variety of other biomaterials applications, due to their structural similarity to naturally occurring biomacromolecules like polysaccharides and glycoproteins.[60] Common saccharide pendant groups within synthetic glycopolymers include glucose,[61-65] galactose,[62, 66-73] mannose,[41, 72-76] *N*-acetyl glucosamine,[72, 77-78] N-acetyl galactosamine,[77] fructose,[79-81] maltose,[82] lactose,[83-84] trehalose,[83, 85-86] cyclodextrin,[87] among several others (Figure 1.2).[88-91]

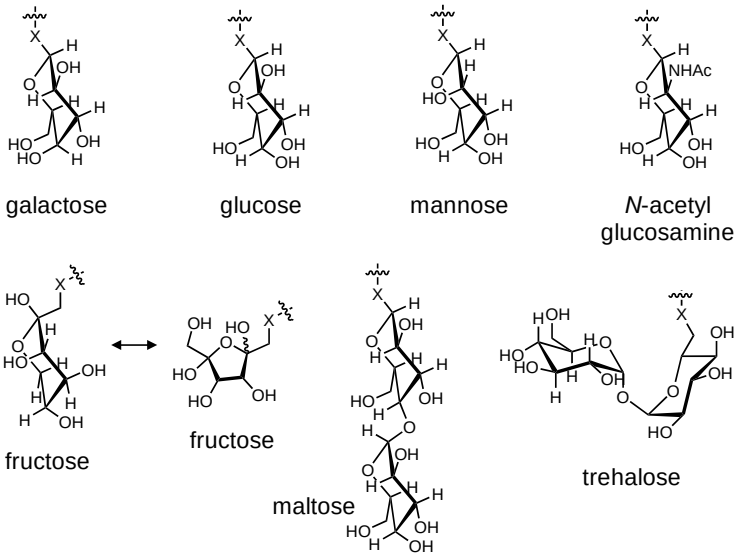

Figure 1.2 *Examples of commonly used saccharides in glycopolymers for gene delivery, drug delivery, and other biomaterials applications. Saccharides are frequently linked to the polymer backbone through heteroatoms (X = O, N, S).*

Glycopolymers are typically poly(meth)acrylamides and/or poly(meth)acrylates because of their easy preparation through reversible addition-fragmentation chain transfer (RAFT) polymerization. However, glycopolymers have also been prepared through other polymerization methods including atom-transfer radical polymerization (ATRP),[77] ring-opening metathesis polymerization (ROMP),[92] nitroxide-mediated polymerization (NMP),[66] and through a variety of post-polymerization modification techniques.[78, 92-96] In addition to varying the saccharide structure, other aspects of the glycopolymer structures have been varied to modulate biological interactions including sequence control/polymer architecture[97-102] and covalent attachment to other biological molecules.[71, 103-105]

1.3 Modeling of nucleic acid/polyelectrolyte interactions

Polyelectrolytes have experimentally been shown to have interesting solution properties, and molecular dynamics (MD) simulations have become a useful tool for gaining further insight into the behavior of both solvated polyelectrolytes by themselves as well as polyelectrolyte mixtures.[106-108] Considerable work has also been done to further

understand synthetic polymer and biopolymer behavior in solution, particularly for simulations involving nucleic acids.[76, 109-114]

MD simulations have also been especially useful for describing the intermolecular interactions between nucleic acids and a variety of cationic polymers, particularly for non-viral gene delivery applications.[115-124] As mentioned previously, many of these polyplex interactions are a result of electrostatic, hydrogen bonding, and hydrophobic interactions. However, because MD is a computational technique, great care must be taken in experimental setup as the results of the experiments are highly dependent on the simulation parameters.[125-126] For example, both MD force field (FF) and water model can have an effect on the resulting properties,[112] yet the presence of salts does not appear to have much of an effect.[127-128] Other limitations for nucleic acid simulations include poor force field approximations and limited time scales.[114, 129] Analysis of full-sized polymers is also often not possible using all-atomistic approaches due to limitations in computational power, and information about subtle pendant group stereochemical differences may be lost when using coarse-grained approaches. Nevertheless, much information can be learned about simulation biopolymer and bioinspired polymer systems using SPC/E and TIP3P water models.

1.3.1 Hydrogen bonding in saccharide-based systems

Experimentally, the extent of hydrogen bonding within a system may be estimated through density,[130] acoustic,[131] calorimetry,[132] or viscosity experiments.[133] However, hydration is a dynamic process, and hydrogen bonding behavior of monosaccharides and disaccharides can vary greatly despite having the same number of hydroxyl groups.[134-136] Saccharide aggregation is particularly common in aqueous systems due to the

glycocluster effect,[137] and can be observed in similar systems containing aqueous monosaccharides,[138] disaccharides,[139] and saccharide-functionalized polymers.[65, 71, 140-141] In synthetic saccharide-functionalized monomer or polymer systems, an extensive number of interHBs between these compounds and surrounding water and/or nucleic acids would be expected. For example, in acrylamide-based polymers with pendant glucose and/or galactose saccharides, a total of 8 heteroatoms are present in each monomer that are arranged in various functional groups (-C=O, -NH, -O-, -OH), all of which are capable of participating in multiple hydrogen bonds. In several cases, excessive hydrogen bonding has led to polyplex aggregation, particularly in glycopolymer-based systems.[65, 83, 142] Analysis of monomer/oligomer/polymer root mean square fluctuations (RMSF)[143] and hydrogen bonds (both intermolecular and intramolecular intraHBs)[144] from simulation trajectories can provide information on how the polymers and nucleic acids interact.

1.4 Hydrogels for biomedical applications

Hydrogels are hydrophilic three-dimensional crosslinked networks that are capable of absorbing large quantities of water. Since the first synthetic hydrogels were studied for tissue applications sixty years ago,[145] their ease of fabrication and property tunability has enabled expansion of their utility for biomedical applications including contact lenses/ophthalmology, biosensors, drug delivery vehicles, tissue scaffolds, and mucosa-mimetic materials.[146-147] However, two of the major limitations of hydrogel materials include poor control over mechanical properties and heterogeneous structures/architectures. Because of the difficulty required to obtain hierarchical and complex network structures, many synthetic models reported to date have not been able

to provide the required versatility to mimic behavior of natural systems, and there has been considerable effort in developing new hydrogels that can mimic biological structures at different length scales.[148]

1.4.1 Multilayered hydrogels

Layer-by-layer (LbL) assembly has enabled the development of ultrathin multilayered hydrogels, which has expanded the range of hydrogels for biomedical applications because parameters such as internal architecture and response to environmental stimuli (pH and temperature) can be precisely controlled through fabrication conditions.[149] For example, Kozlovskaya and coworkers demonstrated that partially crosslinked single-component films with structural complexity normal to the substrate (z-direction) have allowed for LbL hydrogels with enhanced swelling in partially crosslinked poly(methacrylic acid) films and capsules.[150] Although the pH-responsive swelling can be easily tuned, there is little known about the changes in hydrogel modulus and their mechanical properties in physiological conditions.

1.5 Motivation and objectives of research

Regardless of cell line, polymer/dsRNA complexation and polyplex cell uptake is critical for gene knockdown. Although the use of saccharide-functionalized cationic polymers has not been explored in ticks or other arthropods, cationic glycopolymer/dsRNA complexation for gene delivery in ticks is especially interesting because many tick salivary gland proteins have been shown to be glycosylated through post-translational modifications, and the diverse glycobiology in ticks has increasingly been shown to play a role in vector-host-pathogen interactions. Previous work in our research group has shown that saccharide stereochemistry plays a crucial role in

modulating glycopolymer/peptide intermolecular interactions, and can even influence peptide aggregation pathways. It has been proposed that this is due to differences in hydrogen bonding patterns between the glycopolymers and the peptides. The structure-property relationships of cationic glycopolymer/nucleic acid binding have yet to be resolved through either experimental or computational methods, yet it is expected that cationic glycopolymer structure will govern dsRNA complexation and gene knockdown.

The use of hydrogel networks for gene delivery is an emerging yet promising application, but their application has largely been hindered by the lack of controlled release mechanisms resulting from the inherent structural network heterogeneity that is characteristic of conventional hydrogels. With the development of novel stimuli-responsive multilayer hydrogel networks using simple layer-by-layer deposition techniques, hydrogel internal architecture can be precisely controlled, resulting in highly tunable swelling responses. However, there is a significant lack of understanding in terms of the relationship between layer-by-layer deposition conditions and the resulting network morphology, and how this affects mechanical properties in hydrated systems. These critical parameters must be thoroughly studied prior to attempting to use these materials for gene delivery applications, as hydrogel modulus affects surface interactions with biological materials.

The specific objectives of this research are the following:

1. Determine the influence of glycopolymer stereochemistry and charge on polyplex formation with tick dsRNA, RNA transfection efficiency, and cytotoxicity within tick cell lines.

a. Synthesize and characterize neutral and cationic glycopolymers with stereospecific β,D-glucose and β,D-galactose pendant groups.
b. Assess polymer cytotoxicity within a tick-specific cell line.
c. Evaluate in vitro structure/binding relationships of the cationic glycopolymers with tick dsRNA.
d. Complete RNAi/gene knockdown experiments in tick cells.

2. Define the effects of glycomonomer structure on intermolecular interactions with dsRNA through molecular dynamics simulations.
    a. Assess the role of glycomonomer structure on monomer conformation and solvation in aqueous solution.
    b. Compare intermolecular and intramolecular hydrogen bonding patterns in stereospecific neutral and cationic oligomer systems.
    c. Determine how oligomer saccharide structure affects intermolecular interactions with a model dsRNA.
3. Establish the role of assembly conditions on pH-responsive swelling and modulus in layer-by-layer hydrogel networks through atomic force microscopy nanoindentation techniques.
    a. Determine the influence of sacrificial layer molecular weight on the morphology and modulus of pre- and post-crosslinked spin-assisted multilayer films.
    b. Evaluate how LbL deposition technique (spin-assisted or dipped) and sacrificial layer molecular weight affect properties of LbL-derived hydrogels surfaces under ambient (dry) and hydrated (fluid) conditions.

1.6 References

1. Fire, A.; Xu, S.; Montgomery, M. K.; Kostas, S. A.; Driver, S. E.; Mello, C. C., Potent and specific genetic interference by double-stranded RNA in Caenorhabditis elegans. *Nature* **1998,** *391* (6669), 806-811.

2. Agrawal, N.; Dasaradhi, P. V. N.; Mohmmed, A.; Malhotra, P.; Bhatnagar, R. K.; Mukherjee, S. K., RNA Interference: Biology, Mechanism, and Applications. *Microbiology and Molecular Biology Reviews* **2003,** *67* (4), 657.

3. Unniyampurath, U.; Pilankatta, R.; Krishnan, M. N., RNA interference in the age of CRISPR: will CRISPR interfere with RNAi? *International Journal of Molecular Sciences* **2016,** *17* (3), 291/1-291/15.

4. Bramlett, M.; Plaetinck, G.; Maienfisch, P., RNA-Based Biocontrol - A New Paradigm in Crop Protection. *Engineering* **2020,** *6* (5), 522-527.

5. Wang, Q.; Carmichael, G. G., Effects of length and location on the cellular response to double-stranded RNA. *Microbiology and Molecular Biology Reviews* **2004,** *68* (3), 432-452.

6. Huvenne, H.; Smagghe, G., Mechanisms of dsRNA uptake in insects and potential of RNAi for pest control: A review. *Journal of Insect Physiology* **2010,** *56* (3), 227-235.

7. Wang, K.; Peng, Y.; Fu, W.; Shen, Z.; Han, Z., Key factors determining variations in RNA interference efficacy mediated by different double-stranded RNA lengths inTribolium castaneum. *Insect Molecular Biology* **2019,** *28* (2), 235-245.

8. Scott, J. G.; Michel, K.; Bartholomay, L. C.; Siegfried, B. D.; Hunter, W. B.; Smagghe, G.; Zhu, K. Y.; Douglas, A. E., Towards the elements of successful insect RNAi. *Journal of Insect Physiology* **2013,** *59* (12), 1212-1221.

9. Joga, M. R.; Zotti, M. J.; Smagghe, G.; Christiaens, O., RNAi Efficiency, Systemic Properties, and Novel Delivery Methods for Pest Insect Control: What We Know So Far. *Frontiers in Physiology* **2016,** *7*, 553.

10. Brown, K. C.; Montgomery, T. A., Transgenerational Inheritance: Perpetuating RNAi. *Current Biology* **2017,** *27* (10), R383-R385.

11. Grishok, A.; Tabara, H.; Mello, C. C., Genetic Requirements for Inheritance of RNAi in C. elegans. *Science* **2000,** *287* (5462), 2494.

12. Uz, M.; Alsoy Altinkaya, S.; Mallapragada, S. K., Stimuli responsive polymer-based strategies for polynucleotide delivery. *Journal of Materials Research* **2017,** *32* (15), 2930-2953.

13. Yu, N.; Christiaens, O.; Liu, J.; Niu, J.; Cappelle, K.; Caccia, S.; Huvenne, H.; Smagghe, G., Delivery of dsRNA for RNAi in insects: an overview and future directions. *Insect Science* **2013,** *20* (1), 4-14.

14. Perez-Perri, J. I.; Rogell, B.; Schwarzl, T.; Stein, F.; Zhou, Y.; Rettel, M.; Brosig, A.; Hentze, M. W., Discovery of RNA-binding proteins and characterization of their dynamic responses by enhanced RNA interactome capture. *Nature Communications* **2018,** *9* (1), 4408.

15. Hentze, M. W.; Castello, A.; Schwarzl, T.; Preiss, T., A brave new world of RNA-binding proteins. *Nature Reviews Molecular Cell Biology* **2018,** *19* (5), 327-341.

16. Balcerak, A.; Trebinska-Stryjewska, A.; Konopinski, R.; Wakula, M.; Grzybowska, E. A., RNA-protein interactions: disorder, moonlighting and junk contribute to eukaryotic complexity. *Open Biology* **2019,** *9* (6), 190096.

17. Nie, X.; Zhang, Z.; Wang, C.-H.; Fan, Y.-S.; Meng, Q.-Y.; You, Y.-Z., Interactions in DNA Condensation: An Important Factor for Improving the Efficacy of Gene Transfection. *Bioconjugate Chemistry* **2019,** *30* (2), 284-292.

18. Jaeger, M.; Schubert, S.; Ochrimenko, S.; Fischer, D.; Schubert, U. S., Branched and linear poly(ethylene imine)-based conjugates: synthetic modification, characterization, and application. *Chemical Society Reviews* **2012,** *41* (13), 4755-4767.

19. Whyard, S.; Singh, A. D.; Wong, S., Ingested double-stranded RNAs can act as species-specific insecticides. *Insect Biochemistry and Molecular Biology* **2009,** *39* (11), 824-832.

20. Cohen, J. L.; Schubert, S.; Wich, P. R.; Cui, L.; Cohen, J. A.; Mynar, J. L.; Frechet, J. M. J., Acid-Degradable Cationic Dextran Particles for the Delivery of siRNA Therapeutics. *Bioconjugate Chemistry* **2011,** *22* (6), 1056-1065.

21. Lichtenberg, S. S.; Tsyusko, O. V.; Palli, S. R.; Unrine, J. M., Uptake and Bioactivity of Chitosan/Double-Stranded RNA Polyplex Nanoparticles in Caenorhabditis elegans. *Environmental Science & Technology* **2019,** *53* (7), 3832-3840.

22. Kwoh, D. Y.; Coffin, C. C.; Lollo, C. P.; Jovenal, J.; Banaszczyk, M. G.; Mullen, P.; Phillips, A.; Amini, A.; Fabrycki, J.; Bartholomew, R. M.; Brostoff, S. W.; Carlo, D. J., Stabilization of poly-l-lysine/DNA polyplexes for in vivo gene delivery to the liver. *Biochimica et Biophysica Acta* **1999,** *1444* (2), 171-190.

23. Hartono, S. B.; Phuoc, N. T.; Yu, M.; Jia, Z.; Monteiro, M. J.; Qiao, S.; Yu, C., Functionalized large pore mesoporous silica nanoparticles for gene delivery featuring controlled release and co-delivery. *Journal of Materials Chemistry B* **2014,** *2* (6), 718-726.

24. Esfand, R.; Tomalia, D. A., Poly(amidoamine) (PAMAM) dendrimers: from biomimicry to drug delivery and biomedical applications. *Drug Discovery Today* **2001,** *6* (8), 427-436.

25. Lim, Y.-b.; Kim, S.-M.; Lee, Y.; Lee, W.-k.; Yang, T.-g.; Lee, M.-j.; Suh, H.; Park, J.-s., Cationic Hyperbranched Poly(amino ester): A Novel Class of DNA Condensing Molecule with Cationic Surface, Biodegradable Three-Dimensional Structure, and Tertiary Amine Groups in the Interior. *Journal of the American Chemical Society* **2001,** *123* (10), 2460-2461.

26. Seymour, L. W.; Duncan, R.; Strohalm, J.; Kope?ek, J., Effect of molecular weight of N-(2-hydroxypropyl)methacrylamide copolymers on body distribution and rate of excretion after subcutaneous, intraperitoneal, and intravenous administration to rats. *Journal of Biomedical Materials Research* **1987,** *21* (11), 1341-1358.

27. Yi, X.; Batrakova, E.; Banks, W. A.; Vinogradov, S.; Kabanov, A. V., Protein Conjugation with Amphiphilic Block Copolymers for Enhanced Cellular Delivery. *Bioconjugate Chemistry* **2008,** *19* (5), 1071-1077.

28. Han, S.; Wan, H.; Lin, D.; Guo, S.; Dong, H.; Zhang, J.; Deng, L.; Liu, R.; Tang, H.; Dong, A., Contribution of hydrophobic/hydrophilic modification on cationic chains of poly(caprolactone)-graft-poly(dimethylaminoethylmethacrylate) amphiphilic co-polymer in gene delivery. *Acta Biomateriala* **2014,** *10* (2), 670-679.

29. Guo, S.; Huang, Y.; Wei, T.; Zhang, W.; Wang, W.; Lin, D.; Zhang, X.; Kumar, A.; Du, Q.; Xing, J.; Deng, L.; Liang, Z.; Wang, P. C.; Dong, A.; Liang, X.-J., Amphiphilic and biodegradable methoxy polyethylene glycol-block-(polycaprolactone-graft-poly(2-(dimethylamino)ethyl methacrylate)) as an effective gene carrier. *Biomaterials* **2010,** *32* (3), 879-889.

30. Kim, Y.; Pourgholami, M. H.; Morris, D. L.; Stenzel, M. H., Effect of Cross-Linking on the Performance of Micelles As Drug Delivery Carriers: A Cell Uptake Study. *Biomacromolecules* **2012,** *13* (3), 814-825.

31. Chen, Q.-R.; Zhang, L.; Luther, P. W.; Mixson, A. J., Optimal transfection with the HK polymer depends on its degree of branching and the pH of endocytic vesicles. *Nucleic Acids Research* **2002,** *30* (6), 1338-1345.

32. Holley, A. C.; Parsons, K. H.; Wan, W.; Lyons, D. F.; Bishop, G. R.; Correia, J. J.; Huang, F.; McCormick, C. L., Block ionomer complexes consisting of siRNA and aRAFT-synthesized hydrophilic-block-cationic copolymers: the influence of cationic block length on gene suppression. *Polymer Chemistry* **2014,** *5* (24), 6967-6976.

33. Parsons, K. H.; Holley, A. C.; Munn, G. A.; Flynt, A. S.; McCormick, C. L., Block ionomer complexes consisting of siRNA and aRAFT-synthesized hydrophilic-block-cationic copolymers II: the influence of cationic block charge density on gene suppression. *Polymer Chemistry* **2016,** *7* (39), 6044-6054.

34. York, A. W.; Huang, F.; McCormick, C. L., Rational Design of Targeted Cancer Therapeutics through the Multiconjugation of Folate and Cleavable siRNA to RAFT-Synthesized (HPMA-s-APMA) Copolymers. *Biomacromolecules* **2010,** *11* (2), 505-514.

35. Smith, D.; Holley, A. C.; McCormick, C. L., RAFT-synthesized copolymers and conjugates designed for therapeutic delivery of siRNA. *Polymer Chemistry* **2011,** *2* (7), 1428-1441.

36. Malloggi, C.; Pezzoli, D.; Magagnin, L.; De Nardo, L.; Mantovani, D.; Tallarita, E.; Candiani, G., Comparative evaluation and optimization of off-the-shelf cationic polymers for gene delivery purposes. *Polymer Chemistry* **2015,** *6* (35), 6325-6339.

37. Avila, L. A.; Chandrasekar, R.; Wilkinson, K. E.; Balthazor, J.; Heerman, M.; Bechard, J.; Brown, S.; Park, Y.; Dhar, S.; Reeck, G. R.; Tomich, J. M., Delivery of lethal dsRNAs in insect diets by branched amphiphilic peptide capsules. *Journal of Controlled Release* **2018,** *273*, 139-146.

38. Kuroki, A.; Sangwan, P.; Qu, Y.; Peltier, R.; Sanchez-Cano, C.; Moat, J.; Dowson, C. G.; Williams, E. G. L.; Locock, K. E. S.; Hartlieb, M.; Perrier, S., Sequence Control as a Powerful Tool for Improving the Selectivity of Antimicrobial Polymers. *ACS Applied Materials & Interfaces* **2017,** *9* (46), 40117-40126.

39. Paslay, L. C.; Abel, B. A.; Brown, T. D.; Koul, V.; Choudhary, V.; McCormick, C. L.; Morgan, S. E., Antimicrobial Poly(methacrylamide) Derivatives Prepared via Aqueous RAFT Polymerization Exhibit Biocidal Efficiency Dependent upon Cation Structure. *Biomacromolecules* **2012,** *13* (8), 2472-2482.

40. Exley, S. E.; Paslay, L. C.; Sahukhal, G. S.; Abel, B. A.; Brown, T. D.; McCormick, C. L.; Heinhorst, S.; Koul, V.; Choudhary, V.; Elasri, M. O.; Morgan, S. E., Antimicrobial Peptide Mimicking Primary Amine and Guanidine Containing Methacrylamide Copolymers Prepared by Raft Polymerization. *Biomacromolecules* **2015,** *16* (12), 3845-3852.

41. Miao, Z.; Li, D.; Zheng, Z.; Zhang, Q., Synthesis of chitosan-mimicking cationic glycopolymers by Cu(0)-LRP for efficient capture and killing of bacteria. *Polymer Chemistry* **2019,** *10* (29), 4059-4066.

42. Qin, Z.; Liu, W.; Guo, L.; Li, X., Studies on guanidinated N-3-aminopropyl methacrylamide-N-2-hydroxypropyl methacrylamide co-polymers as gene delivery carrier. *Journal of Biomaterials Science, Polymer Edition* **2012,** *23* (1-4), 133-152.

43. Zhu, C.; Jung, S.; Si, G.; Cheng, R.; Meng, F.; Zhu, X.; Park, T. G.; Zhong, Z., Cationic methacrylate copolymers containing primary and tertiary amino side groups: controlled synthesis via RAFT polymerization, DNA condensation, and in vitro gene transfection. *Journal of Polymer Science Part A: Polymer Chemistry* **2010,** *48* (13), 2869-2877.

44. Wu, Y.; Wang, M.; Sprouse, D.; Smith, A. E.; Reineke, T. M., Glucose-Containing Diblock Polycations Exhibit Molecular Weight, Charge, and Cell-Type Dependence for pDNA Delivery. *Biomacromolecules* **2014,** *15* (5), 1716-1726.

45. Cai, J.; Yue, Y.; Rui, D.; Zhang, Y.; Liu, S.; Wu, C., Effect of Chain Length on Cytotoxicity and Endocytosis of Cationic Polymers. *Macromolecules* **2011,** *44* (7), 2050-2057.

46. Synatschke, C. V.; Schallon, A.; Jerome, V.; Freitag, R.; Mueller, A. H. E., Influence of Polymer Architecture and Molecular Weight of Poly(2-(dimethylamino)ethyl methacrylate) Polycations on Transfection Efficiency and Cell Viability in Gene Delivery. *Biomacromolecules* **2011,** *12* (12), 4247-4255.

47. Fischer, D.; Li, Y.; Ahlemeyer, B.; Krieglstein, J.; Kissel, T., In vitro cytotoxicity testing of polycations: influence of polymer structure on cell viability and hemolysis. *Biomaterials* **2003,** *24* (7), 1121-1131.

48. Trützschler, A.-K.; Bus, T.; Reifarth, M.; Brendel, J. C.; Hoeppener, S.; Traeger, A.; Schubert, U. S., Beyond Gene Transfection with Methacrylate-Based Polyplexes—The Influence of the Amino Substitution Pattern. *Bioconjugate Chemistry* **2018,** *29* (7), 2181-2194.

49. Mishra, S.; Webster, P.; Davis, M. E., PEGylation significantly affects cellular uptake and intracellular trafficking of non-viral gene delivery particles. *European Journal of Cell Biology* **2004,** *83* (3), 97-111.

50. Ogris, M.; Brunner, S.; Schuller, S.; Kircheis, R.; Wagner, E., PEGylated DNA/transferrin-PEI complexes: reduced interaction with blood components, extended circulation in blood and potential for systemic gene delivery. *Gene Therapy* **1999,** *6* (4), 595-605.

51. Dash, P. R.; Read, M. L.; Fisher, K. D.; Howard, K. A.; Wolfert, M.; Oupicky, D.; Subr, V.; Strohalm, J.; Ulbrich, K.; Seymour, L. W., Decreased binding to proteins and cells of polymeric gene delivery vectors surface modified with a multivalent hydrophilic polymer and retargeting through attachment of transferrin. *Journal of Biological Chemistry* **2000,** *275* (6), 3793-3802.

52. Ballarin-Gonzalez, B.; Howard, K. A., Polycation-based nanoparticle delivery of RNAi therapeutics: Adverse effects and solutions. *Advanced Drug Delivery Reviews* **2012,** *64* (15), 1717-1729.

53. Wang, T.; Upponi, J. R.; Torchilin, V. P., Design of multifunctional non-viral gene vectors to overcome physiological barriers: Dilemmas and strategies. *International Journal of Pharmaceutics* **2012,** *427* (1), 3-20.

54. Rinkenauer, A. C.; Schubert, S.; Traeger, A.; Schubert, U. S., The influence of polymer architecture on in vitro pDNA transfection. *Journal of Materials Chemistry B* **2015,** *3* (38), 7477-7493.

55. Yue, Y.; Wu, C., Progress and perspectives in developing polymeric vectors for in vitro gene delivery. *Biomaterials Science* **2013,** *1* (2), 152-170.

56. Samal, S. K.; Dash, M.; Van Vlierberghe, S.; Kaplan, D. L.; Chiellini, E.; van Blitterswijk, C.; Moroni, L.; Dubruel, P., Cationic polymers and their therapeutic potential. *Chemical Society Reviews* **2012,** *41* (21), 7147-7194.

57. Scales, C. W.; Huang, F.; Li, N.; Vasilieva, Y. A.; Ray, J.; Convertine, A. J.; McCormick, C. L., Corona-Stabilized Interpolyelectrolyte Complexes of SiRNA with Nonimmunogenic, Hydrophilic/Cationic Block Copolymers Prepared by Aqueous RAFT Polymerization. *Macromolecules* **2006,** *39* (20), 6871-6881.

58. Moraes, J.; Peltier, R.; Gody, G.; Blum, M.; Recalcati, S.; Klok, H.-A.; Perrier, S., Influence of Block versus Random Monomer Distribution on the Cellular Uptake of Hydrophilic Copolymers. *ACS Macro Letters* **2016,** *5* (12), 1416-1420.

59. Apweiler, R.; Hermakob, H.; Sharon, N., On the frequency of protein glycosylation, as deduced from analysis of the SWISS-PROT database. *Biochimica et Biophysica Acta* **1999,** *1473* (1), 4-8.

60. Babiuch, K.; Stenzel, M. H., Synthesis and Application of Glycopolymers. *Encyclopedia of Polymer Science and Technology* **2014**, 1-58.

61. Lowe, A. B.; Sumerlin, B. S.; McCormick, C. L., The direct polymerization of 2-methacryloxyethyl glucoside via aqueous reversible addition-fragmentation chain transfer (RAFT) polymerization. *Polymer* **2003,** *44* (22), 6761-6765.

62. Ambrosi, M.; Batsanov, A. S.; Cameron, N. R.; Davis, B. G.; Howard, J. A. K.; Hunter, R., Influence of preparation procedure on polymer composition: synthesis and characterization of polymethacrylates bearing β-D-glucopyranoside and β-D-galactopyranoside residues. *Journal of the Chemical Society, Perkin Transactions 1* **2002,** (1), 45-52.

63. Wang, X.; Geng, X.; Ye, L.; Zhang, A.-y.; Feng, Z.-g., Synthesis and characterization of novel glucose- and lactose-containing methacrylate-based radiopaque glycopolymers. *Reactive and Functional Polymers* **2009,** *69* (12), 857-863.

64. Xiao, Y.; Sun, H.; Du, J., Sugar-Breathing Glycopolymersomes for Regulating Glucose Level. *Journal of the American Chemical Society* **2017,** *139* (22), 7640-7647.

65. Dan, K.; Ghosh, S., pH-Responsive Aggregation of Amphiphilic Glyco-Homopolymer. *Macromolecular Rapid Communications* **2012,** *33* (2), 127-132.

66. Ting, S. R. S.; Min, E.-H.; Escale, P.; Save, M.; Billon, L.; Stenzel, M. H., Lectin Recognizable Biomaterials Synthesized via Nitroxide-Mediated Polymerization of a Methacryloyl Galactose Monomer. *Macromolecules* **2009,** *42* (24), 9422-9434.

67. Spain, S. G.; Albertin, L.; Cameron, N. R., Facile in situ preparation of biologically active multivalent glyconanoparticles. *Chemical Communications* **2006,** (40), 4198-4200.

68. Hoffmann, M.; Gau, E.; Braun, S.; Pich, A.; Elling, L., Enzymatic Synthesis of 2-(B-Galactosyl)-ethyl Methacrylate by B-Galactosidase from Pyrococcus woesei and Application for Glycopolymer Synthesis and Lectin Studies. *Biomacromolecules* **2020,** *21* (2), 974-987.

69. Liu, L.; Zhou, F.; Hu, J.; Cheng, X.; Zhang, W.; Zhang, Z.; Chen, G.; Zhou, N.; Zhu, X., Topological Glycopolymers as Agglutinator and Inhibitor: Cyclic versus Linear. *Macromolecular Rapid Communications* **2019,** *40* (16), 1900223.

70. Ladmiral, V.; Semsarilar, M.; Canton, I.; Armes, S. P., Polymerization-Induced Self-Assembly of Galactose-Functionalized Biocompatible Diblock Copolymers for Intracellular Delivery. *Journal of the American Chemical Society* **2013,** *135* (36), 13574-13581.

71. Wang, Z.; Luo, T.; Cao, A.; Sun, J.; Jia, L.; Sheng, R., Morphology-Variable Aggregates Prepared from Cholesterol-Containing Amphiphilic Glycopolymers: Their Protein Recognition/Adsorption and Drug Delivery Applications. *Nanomaterials* **2018,** *8* (3), 136.

72. Song, E.-H.; Manganiello, M. J.; Chow, Y.-H.; Ghosn, B.; Convertine, A. J.; Stayton, P. S.; Schnapp, L. M.; Ratner, D. M., In vivo targeting of alveolar macrophages via RAFT-based glycopolymers. *Biomaterials* **2012,** *33* (28), 6889-6897.

73. Ladmiral, V.; Mantovani, G.; Clarkson, G. J.; Cauet, S.; Irwin, J. L.; Haddleton, D. M., Synthesis of Neoglycopolymers by a Combination of "Click Chemistry" and Living Radical Polymerization. *Journal of the American Chemical Society* **2006,** *128* (14), 4823-4830.

74. Obata, M.; Shimizu, M.; Ohta, T.; Matsushige, A.; Iwai, K.; Hirohara, S.; Tanihara, M., Synthesis, characterization and cellular internalization of poly(2-hydroxyethyl methacrylate) bearing α-D-mannopyranose. *Polymer Chemistry* **2011,** *2* (3), 651-658.

75. Obata, M.; Kobori, T.; Hirohara, S.; Tanihara, M., Aqueous RAFT synthesis of block and statistical copolymers of 2-(α-D-mannopyranosyloxy)ethyl methacrylate with 2-(N,N-dimethylamino)ethyl methacrylate and their application for nonviral gene delivery. *Polymer Chemistry* **2015,** *6* (10), 1793-1804.

76. Madeira do O, J.; Foralosso, R.; Yilmaz, G.; Mastrotto, F.; King, P. J. S.; Xerri, R. M.; He, Y.; van der Walle, C. F.; Fernandez-Trillo, F.; Laughton, C. A.; Styliari, I.; Stolnik, S.; Mantovani, G., Poly(triazolyl methacrylate) glycopolymers as potential targeted unimolecular nanocarriers. *Nanoscale* **2019,** *11* (44), 21155-21166.

77. Vazquez-Dorbatt, V.; Maynard, H. D., Biotinylated Glycopolymers Synthesized by Atom Transfer Radical Polymerization. *Biomacromolecules* **2006,** *7* (8), 2297-2302.

78. Muñoz-Bonilla, A.; León, O.; Cerrada, M. L.; Rodríguez-Hernández, J.; Sánchez-Chaves, M.; Fernández-García, M., Chemical modification of block copolymers based on 2-hydroxyethyl acrylate to obtain amphiphilic glycopolymers. *European Polymer Journal* **2015,** *62*, 167-178.

79. von der Ehe, C.; Rinkenauer, A.; Weber, C.; Szamosvari, D.; Gottschaldt, M.; Schubert, U. S., Selective Uptake of a Fructose Glycopolymer Prepared by RAFT Polymerization into Human Breast Cancer Cells. *Macromolecular Bioscience* **2016,** *16* (4), 508-521.

80. Cao, C.; Zhao, J.; Chen, F.; Lu, M.; Khine, Y. Y.; Macmillan, A.; Garvey, C. J.; Stenzel, M. H., Drug-Induced Morphology Transition of Self-Assembled Glycopolymers: Insight into the Drug–Polymer Interaction. *Chemistry of Materials* **2018,** *30* (15), 5227-5236.

81. Lu, M.; Khine, Y. Y.; Chen, F.; Cao, C.; Garvey, C. J.; Lu, H.; Stenzel, M. H., Sugar Concentration and Arrangement on the Surface of Glycopolymer Micelles Affect the Interaction with Cancer Cells. *Biomacromolecules* **2019,** *20* (1), 273-284.

82. Motoyanagi, J.; Nguyen, M. T.; Tanaka, T.; Minoda, M., Protecting group-free synthesis of glycopolymer-type amphiphilic macromonomers and their use for the preparation of carbohydrate-decorated polymer particles. *Biomolecules* **2019,** *9* (2), 72.

83. Madeira do O, J.; Mastrotto, F.; Francini, N.; Allen, S.; van der Walle, C. F.; Stolnik, S.; Mantovani, G., Synthetic glycopolymers as modulators of protein aggregation: influences of chemical composition, topology and concentration. *Journal of Materials Chemistry B* **2018,** *6* (7), 1044-1054.

84. Singhsa, P.; Diaz-Dussan, D.; Manuspiya, H.; Narain, R., Well-Defined Cationic N-[3-(Dimethylamino)propyl]methacrylamide Hydrochloride-Based (Co)polymers for siRNA Delivery. *Biomacromolecules* **2018,** *19* (1), 209-221.

85. Sizovs, A.; Xue, L.; Tolstyka, Z. P.; Ingle, N. P.; Wu, Y.; Cortez, M.; Reineke, T. M., Poly(trehalose): Sugar-Coated Nanocomplexes Promote Stabilization and Effective Polyplex-Mediated siRNA Delivery. *Journal of the American Chemical Society* **2013,** *135* (41), 15417-15424.

86. Tolstyka, Z. P.; Phillips, H.; Cortez, M.; Wu, Y.; Ingle, N.; Bell, J. B.; Hackett, P. B.; Reineke, T. M., Trehalose-Based Block Copolycations Promote Polyplex

Stabilization for Lyophilization and in Vivo pDNA Delivery. *ACS Biomaterials Science & Engineering* **2016,** *2* (1), 43-55.

87. Yilmaz, G.; Uzunova, V.; Napier, R.; Becer, C. R., Single-Chain Glycopolymer Folding via Host–Guest Interactions and Its Unprecedented Effect on DC-SIGN Binding. *Biomacromolecules* **2018,** *19* (7), 3040-3047.

88. Chen, Y.; Diaz-Dussan, D.; Peng, Y.-Y.; Narain, R., Hydroxyl-Rich PGMA-Based Cationic Glycopolymers for Intracellular siRNA Delivery: Biocompatibility and Effect of Sugar Decoration Degree. *Biomacromolecules* **2019,** *20* (5), 2068-2074.

89. Besenius, P.; Slavin, S.; Vilela, F.; Sherrington, D. C., Synthesis and characterization of water-soluble densely branched glycopolymers. *Reactive and Functional Polymers* **2008,** *68* (11), 1524-1533.

90. Semsarilar, M.; Ladmiral, V.; Perrier, S., Highly Branched and Hyperbranched Glycopolymers via Reversible Addition-Fragmentation Chain Transfer Polymerization and Click Chemistry. *Macromolecules* **2010,** *43* (3), 1438-1443.

91. Bordege, V.; Munoz-Bonilla, A.; Leon, O.; Cuervo-Rodriguez, R.; Sanchez-Chaves, M.; Fernandez-Garcia, M., Statistical Glycopolymers Based on 2-Hydroxyethyl Methacrylate: Copolymerization, Thermal Properties, and Lectin Interaction Studies. *Macromolecular Chemistry and Physics* **2011,** *212* (12), 1294-1304.

92. Graham, B.; Fayter, A. E. R.; Houston, J. E.; Evans, R. C.; Gibson, M. I., Facially Amphipathic Glycopolymers Inhibit Ice Recrystallization. *Journal of the American Chemical Society* **2018,** *140* (17), 5682-5685.

93. Otsubo, T.; Tanaka, T.; Motoyanagi, J.; Minoda, M., An Alternating Glycopolymer Composed of Carbohydrate-carrying Maleimide and OH-functionalized

Vinyl Ether- A New Synthetic Strategy for Glycosaminoglycan Mimics. *Chemical Letters* **2019,** *48* (5), 465-467.

94. Fukuda, T.; Tsuji, S.; Miura, Y., Glycopolymer preparation via post-polymerization modification using N-succinimidyl monomers. *Polymer Journal* **2019,** *51* (6), 617-625.

95. Slavin, S.; Burns, J.; Haddleton, D. M.; Becer, C. R., Synthesis of glycopolymers via click reactions. *European Polymer Journal* **2011,** *47* (4), 435-446.

96. Martin, L.; Gurnani, P.; Zhang, J.; Hartlieb, M.; Cameron, N. R.; Eissa, A. M.; Perrier, S., Polydimethylsiloxane-Based Giant Glycosylated Polymersomes with Tunable Bacterial Affinity. *Biomacromolecules* **2019,** *20* (3), 1297-1307.

97. Sprouse, D.; Reineke, T. M., Investigating the Effects of Block versus Statistical Glycopolycations Containing Primary and Tertiary Amines for Plasmid DNA Delivery. *Biomacromolecules* **2014,** *15* (7), 2616-2628.

98. Wang, Y.; Hong, C.-Y.; Pan, C.-Y., Galactose-Based Amphiphilic Block Copolymers: Synthesis, Micellization, and Bioapplication. *Biomacromolecules* **2013,** *14* (5), 1444-1451.

99. Ahmed, M.; Narain, R., The effect of molecular weight, compositions and lectin type on the properties of hyperbranched glycopolymers as non-viral gene delivery systems. *Biomaterials* **2012,** *33* (15), 3990-4001.

100. Smith, A. E.; Sizovs, A.; Grandinetti, G.; Xue, L.; Reineke, T. M., Diblock Glycopolymers Promote Colloidal Stability of Polyplexes and Effective pDNA and siRNA Delivery under Physiological Salt and Serum Conditions. *Biomacromolecules* **2011,** *12* (8), 3015-3022.

101. Abdouni, Y.; Yilmaz, G.; Becer, C. R., Sequence and Architectural Control in Glycopolymer Synthesis. *Macromolecular Rapid Communications* **2017,** *38* (24), 1700212.

102. Williams, E. G. L.; Hutt, O. E.; Hinton, T. M.; Larnaudie, S. C.; Le, T.; MacDonald, J. M.; Gunatillake, P.; Thang, S. H.; Duggan, P. J., Glycosylated Reversible Addition–Fragmentation Chain Transfer Polymers with Varying Polyethylene Glycol Linkers Produce Different Short Interfering RNA Uptake, Gene Silencing, and Toxicity Profiles. *Biomacromolecules* **2017,** *18* (12), 4099-4112.

103. Xia, X.; Zhou, Z.; DeSantis, C.; Rossi, J. J.; Bong, D., Triplex Hybridization of siRNA with Bifacial Glycopolymer Nucleic Acid Enables Hepatocyte-Targeted Silencing. *ACS Chemical Biology* **2019,** *14* (6), 1310-1318.

104. Vazquez-Dorbatt, V.; Tolstyka, Z. P.; Chang, C.-W.; Maynard, H. D., Synthesis of a Pyridyl Disulfide End-Functionalized Glycopolymer for Conjugation to Biomolecules and Patterning on Gold Surfaces. *Biomacromolecules* **2009,** *10* (8), 2207-2212.

105. Fingernagel, J.; Boye, S.; Kietz, A.; Höbel, S.; Wozniak, K.; Moreno, S.; Janke, A.; Lederer, A.; Aigner, A.; Temme, A.; Voit, B.; Appelhans, D., Mono- and Polyassociation Processes of Pentavalent Biotinylated PEI Glycopolymers for the Fabrication of Biohybrid Structures with Targeting Properties. *Biomacromolecules* **2019,** *20* (9), 3408-3424.

106. Mintis, D. G.; Dompé, M.; Kamperman, M.; Mavrantzas, V. G., Effect of Polymer Concentration on the Structure and Dynamics of Short Poly(N,N-dimethylaminoethyl methacrylate) in Aqueous Solution: A Combined Experimental and

Molecular Dynamics Study. *The Journal of Physical Chemistry B* **2020,** *124* (1), 240-252.

107. Shakya, A.; Girard, M.; King, J. T.; Olvera de la Cruz, M., Role of Chain Flexibility in Asymmetric Polyelectrolyte Complexation in Salt Solutions. *Macromolecules* **2020,** *53* (4), 1258-1269.

108. Ivanov, I.; Vemparala, S.; Pophristic, V.; Kuroda, K.; DeGrado, W. F.; McCammon, J. A.; Klein, M. L., Characterization of Nonbiological Antimicrobial Polymers in Aqueous Solution and at Water–Lipid Interfaces From All-Atom Molecular Dynamics. *Journal of the American Chemical Society* **2006,** *128*, 1778.

109. Garcia, E. J.; Hasse, H., Studying equilibria of polymers in solution by direct molecular dynamics simulations: poly(N-isopropylacrylamide) in water as a test case. *European Physics Journal Special Topics* **2019,** *227* (14), 1547-1558.

110. Alexiou, T. S.; Alatas, P. V.; Tsalikis, D. G.; Mavrantzas, V. G., Conformational and Dynamic Properties of Short DNA Minicircles in Aqueous Solution from Atomistic Molecular Dynamics Simulations. *Macromolecules* **2020,** *53* (14), 5903-5918.

111. Batys, P.; Kivistö, S.; Lalwani, S. M.; Lutkenhaus, J. L.; Sammalkorpi, M., Comparing water-mediated hydrogen-bonding in different polyelectrolyte complexes. *Soft Matter* **2019,** *15* (39), 7823-7831.

112. Rukmani, S. J.; Kupgan, G.; Anstine, D. M.; Colina, C. M., A molecular dynamics study of water-soluble polymers: analysis of force fields from atomistic simulations. *Molecular Simulation* **2019,** *45* (4-5), 310-321.

113. Sponer, J.; Krepl, M.; Banas, P.; Kuhrova, P.; Zgarbova, M.; Jurecka, P.; Havrila, M.; Otyepka, M., How to understand atomistic molecular dynamics simulations of RNA and protein-RNA complexes? *Wiley Interdisciplinary Reviews: RNA* **2017,** *8* (3), e1405.

114. Sponer, J.; Bussi, G.; Krepl, M.; Banas, P.; Bottaro, S.; Cunha, R. A.; Gil-Ley, A.; Pinamonti, G.; Poblete, S.; Jurecka, P.; Walter, N. G.; Otyepka, M., RNA Structural Dynamics As Captured by Molecular Simulations: A Comprehensive Overview. *Chemical Reviews* **2018,** *118* (8), 4177.

115. García-Sosa, A. T.; Tulp, I. A.-O.; Langel, K. A.-O.; Langel, Ü., Peptide-ligand binding modeling of siRNA with cell-penetrating peptides. *BioMed Research International* **2014,** *2014*.

116. Heller, P.; Zhou, J.; Weber, B.; Hobernik, D.; Bros, M.; Schmid, F.; Barz, M., The Influence of Block Ionomer Microstructure on Polyplex Properties: Can Simulations Help to Understand Differences in Transfection Efficiency? *Small* **2017,** *13* (17), n/a.

117. Kondinskaia, D. A.; Kostritskii, A. Y.; Nesterenko, A. M.; Antipina, A. Y.; Gurtovenko, A. A., Atomic-Scale Molecular Dynamics Simulations of DNA–Polycation Complexes: Two Distinct Binding Patterns. *The Journal of Physical Chemistry B* **2016,** *120* (27), 6546-6554.

118. Shen, Z.-l.; Xia, Y.-q.; Yang, Q.-s.; Tian, W.-d.; Chen, K.; Ma, Y.-q., Polymer-Nucleic Acid Interactions. *Topics in Current Chemistry* **2017,** *375* (2), 1-24.

119. Vasiliu, T.; Cojocaru, C.; Rotaru, A.; Pricope, G.; Pinteala, M.; Clima, L., Optimization of polyplex formation between DNA oligonucleotide and poly(L-Lysine): Experimental study and modeling approach. *International Journal of Molecular Sciences* **2017,** *18* (6), 1291/1-1291/15.

120. Semenyuk, P. I.; Zhiryakova, M. V.; Izumrudov, V. A., Supercharged Polyplexes: Full-Atom Molecular Dynamics Simulations and Experimental Study. *Macromolecules* **2018,** *51* (14), 5450-5459.

121. Clima, L.; Ursu, E. L.; Cojocaru, C.; Rotaru, A.; Barboiu, M.; Pinteala, M., Experimental design, modeling and optimization of polyplex formation between DNA oligonucleotides and branched polyethylenimine. *Organic and Biomolecular Chemistry* **2015,** *13* (36), 9445-9456.

122. Farcas, A.; Beu, T. A., Complexation of DNA with cationic polymers. *Stud. Univ. Babes-Bolyai, Chem.* **2018,** *63* (2), 165-172.

123. Tabujew, I.; Heidari, M.; Freidel, C.; Helm, M.; Tebbe, L.; Wolfrum, U.; Nagel-Wolfrum, K.; Koynov, K.; Biehl, P.; Schacher, F. H.; Potestio, R.; Peneva, K., Tackling the Limitations of Copolymeric Small Interfering RNA Delivery Agents by a Combined Experimental–Computational Approach. *Biomacromolecules* **2019,** *20* (12), 4389-4406.

124. Gallops, C. E.; Ziebarth, J. D.; Wang, Y., Coarse-Grained Simulations of the Impact of Chain Length and Stiffness on the Formation and Aggregation of Polyelectrolyte Complexes. *Macromolecular Theory and Simulations* **2020**, Ahead of Print.

125. Frenkel, D., Simulations: The dark side. *The European Physical Journal Plus* **2013,** *128* (1), 10.

126. Gartner, T. E.; Jayaraman, A., Modeling and Simulations of Polymers: A Roadmap. *Macromolecules* **2019,** *52* (3), 755-786.

127. Besseova, I.; Banas, P.; Kuhrova, P.; Kosinova, P.; Otyepka, M.; Sponer, J., Simulations of A-RNA Duplexes. The Effect of Sequence, Solute Force Field, Water Model, and Salt Concentration. *Journal of Physical Chemistry B* **2012,** *116* (33), 9899.

128. Sklenovsky, P.; Florova, P.; Banas, P.; Reblova, K.; Lankas, F.; Otyepka, M.; Sponer, J., Understanding RNA Flexibility Using Explicit Solvent Simulations: The Ribosomal and Group I Intron Reverse Kink-Turn Motifs. *Journal of Chemical Theory and Computation* **2011,** *7*, 2963.

129. Šponer, J.; Banáš, P.; Jurečka, P.; Zgarbová, M.; Kührová, P.; Havrila, M.; Krepl, M.; Stadlbauer, P.; Otyepka, M., Molecular Dynamics Simulations of Nucleic Acids. From Tetranucleotides to the Ribosome. *The Journal of Physical Chemistry Letters* **2014,** *5* (10), 1771-1782.

130. Gharsallaoui, A.; Roge, B.; Genotelle, J.; Mathlouthi, M., Relationships between hydration number, water activity and density of aqueous sugar solutions. *Food Chemistry* **2007,** *106* (4), 1443-1453.

131. Galema, S. A.; Hoeiland, H., Stereochemical aspects of hydration of carbohydrates in aqueous solutions. 3. Density and ultrasound measurements. *The Journal of Physical Chemistry* **1991,** *95* (13), 5321-5326.

132. Furuki, T., Effect of molecular structure on thermodynamic properties of carbohydrates. A calorimetric study of aqueous di- and oligosaccharides at subzero temperatures. *Carbohydrate Research* **2002,** *337* (5), 441-450.

133. Branca, C.; Magazu, S.; Maisano, G.; Migliardo, F.; Migliardo, P.; Romeo, G., α, α-Trehalose/Water Solutions. 5. Hydration and Viscosity in Dilute and Semidilute Disaccharide Solutions. *Journal of Physical Chemistry B* **2001,** *105* (41), 10140-10145.

134. Dashnau, J. L.; Sharp, K. A.; Vanderkooi, J. M., Carbohydrate Intramolecular Hydrogen Bonding Cooperativity and Its Effect on Water Structure. *The Journal of Physical Chemistry B* **2005,** *109* (50), 24152-24159.

135. Shiraga, K.; Suzuki, T.; Kondo, N.; De Baerdemaeker, J.; Ogawa, Y., Quantitative characterization of hydration state and destructuring effect of monosaccharides and disaccharides on water hydrogen bond network. *Carbohydrate Research* **2015,** *406*, 46-54.

136. Uedaira, H.; Uedaira, H., Sugar-water interaction from diffusion measurements. *Journal of Solution Chemistry* **1985,** *14* (1), 27-34.

137. Delbianco, M.; Bharate, P.; Varela-Aramburu, S.; Seeberger, P. H., Carbohydrates in Supramolecular Chemistry. *Chemical Reviews* **2016,** *116* (4), 1693-1752.

138. Sonoda, M. T.; Skaf, M. S., Carbohydrate Clustering in Aqueous Solutions and the Dynamics of Confined Water. *Journal of Physical Chemistry B* **2007,** *111* (41), 11948-11956.

139. Kumar, A.; Cincotti, A.; Aparicio, S., A Theoretical Study on Trehalose + Water Mixtures for Dry Preservation Purposes. *Molecules* **2020,** *25* (6).

140. Zidar, J.; Lim, G. S.; Cheong, D. W.; Klähn, M., Protein-Like Dynamics of Polycarbonate Polymers in Water. *The Journal of Physical Chemistry B* **2015,** *119* (1), 316-329.

141. Zhang, Q.; Wilson, P.; Anastasaki, A.; McHale, R.; Haddleton, D. M., Synthesis and Aggregation of Double Hydrophilic Diblock Glycopolymers via Aqueous SET-LRP. *ACS Macro Letters* **2014,** *3* (5), 491-495.

142. Ahmed, M.; Narain, R., The effect of polymer architecture, composition, and molecular weight on the properties of glycopolymer-based non-viral gene delivery systems. *Biomaterials* **2011,** *32* (22), 5279-5290.

143. Blessy, J. J.; Sharmila, D. J. S., Molecular simulation of N-acetylneuraminic acid analogs and molecular dynamics studies of cholera toxin-Neu5Gc complex. *Journal of Biomolecular Structure and Dynamics* **2015,** *33* (5), 1126-1139.

144. Jefferies, J. L.; Abdul Samad, F.; Suliman, B. A.; Basha, S. H.; Manivasagam, T.; Essa, M. M., A Comprehensive In Silico Analysis on the Structural and Functional Impact of SNPs in the Congenital Heart Defects Associated with NKX2-5 Gene—A Molecular Dynamic Simulation Approach. *PLoS ONE* **2016,** *11* (5), e0153999.

145. Wichterle, O.; LÍM, D., Hydrophilic Gels for Biological Use. *Nature* **1960,** *185* (4706), 117-118.

146. Gyles, D. A.; Castro, L. D.; Silva, J. O. C.; Ribeiro-Costa, R. M., A review of the designs and prominent biomedical advances of natural and synthetic hydrogel formulations. *European Polymer Journal* **2017,** *88*, 373-392.

147. Ahmed, E. M., Hydrogel: Preparation, characterization, and applications: A review. *Journal of Advanced Research* **2015,** *6* (2), 105-121.

148. Fan, H.; Gong, J. P., Fabrication of Bioinspired Hydrogels: Challenges and Opportunities. *Macromolecules* **2020,** *53* (8), 2769-2782.

149. Liu, G.; Ding, Z.; Yuan, Q.; Xie, H.; Gu, Z., Multi-Layered Hydrogels for Biomedical Applications. *Frontiers in Chemistry* **2018,** *6*, 439.

150. Kozlovskaya, V.; Kharlampieva, E.; Mansfield, M. L.; Sukhishvili, S. A., Poly(methacrylic acid) Hydrogel Films and Capsules: Response to pH and Ionic strength, and Encapsulation of Macromolecules. *Chem. Mater.* **2006,** *18*, 328.

CHAPTER II – CATIONIC GLYCOPOLYELECTROLYTES FOR RNA INTERFERENCE IN TICK CELLS

2.1 Introduction

Blacklegged ticks (*I. scapularis*) are vectors for a number of pathogenic bacteria, parasites, and viruses that affect both humans and livestock. The most common tick-borne disease, Lyme disease (LD), is transmitted by the spirochetes *B. burgdorferi* and is estimated to infect between 296,000 and 376,000 people annually in the United States alone.[1] Unfortunately, there is currently no way to prevent tick attachment and/or pathogen transmission and affected individuals are plagued by a lack of treatment options other than aggressive treatment with antibiotics.

Vector-borne pathogen transmission occurs during blood-feeding stages after prolonged host attachment, where the risk of LD infection increases to 50% after 60-70 hours of tick attachment.[2-3] After tick attachment, one of the host's first defenses is generation of reactive oxygen species (ROS). The tick can overcome this response by upregulating the production of a range of Se-containing proteins (selenoproteins), which are critical for not only mitigation of oxidative stress but also successful pathogen colonization.[4-5] Recently, Kumar and coworkers demonstrated that downregulation of Selenoprotein K gene transcripts through RNA interference (RNAi) drastically impairs the survival of *B. burgdorferi* colonies in *I. scapularis*, thereby reducing the probability of host infection.[6] RNAi has proven to be an especially useful technique for understanding the pathogen-vector interface in ticks.[7-11]

Delivery of dsRNA for modulation of salivary gland proteins in tick organisms is most commonly achieved by microinjection directly into the organism, which is effective

but can lead to increased stress response and high mortality rates.[12-16] Alternatively, soaking the whole organism, or even isolated salivary glands, in solutions of dsRNA can elicit RNAi responses, although this can be experimentally difficult and is often accompanied by irreproducibility.[17] Regardless, effective cellular uptake of the dsRNA is critical for gene knockdown and is challenging without protecting the naked dsRNA.[8, 18] The use of cationic polyelectrolytes as non-viral transfection agents has become a promising approach for aiding the delivery of nucleic acids within a range of arthropod and insect species, although cationic polymers with high cationic charge densities such as Lipofectamine tend to be highly cytotoxic.[19-23] To circumvent this challenge within mammalian cells, incorporation of saccharide functionalities has been shown to reduce the cytotoxic response because of the structural similarity to naturally occurring polysaccharides and glycoproteins.[24-26] Although the use of saccharide-functionalized transfection agents have not been explored in ticks or other arthropods, this is especially interesting because many tick salivary gland proteins have been shown to be glycosylated through post-translational modifications, and the diverse glycobiology in ticks has increasingly been shown to play a role in vector-host-pathogen interactions.[27-28]

Although there are many examples of synthetic cationic glycopolyelectrolytes for nucleic acid transfection in literature, the nature of saccharide stereochemistry and how it affects factors relevant for dsRNA transfection, in ticks or other organisms, has yet to be reported. Previous work in our research group has shown that incubation of amyloid beta peptides with polyacrylamide-based glycopolymers functionalized with either β,D-glucose or β,D-galactose pendant groups results in different peptide aggregation pathways due to the distinct peptide/polymer hydrogen bonding patterns.[29-30] In this

work, acrylamide-based cationic glycopolyelectrolytes with stereospecific β,D-glucose or β,D-galactose pendant groups were synthesized via RAFT polymerization to understand how saccharide structure and cationic charge ultimately affects knockdown of SelenoK transcripts in tick cells. Glycopolyelectrolyte cytotoxicity was examined and polymer/dsRNA binding mechanisms were assessed to understand how the copolymer structure affects dsRNA delivery and RNAi efficiency. Defining the effects of glycopolyelectrolyte structure on dsRNA binding will provide a greater understanding of biologically relevant parameters for the design of gene delivery vehicles.

2.2 Experimental

2.2.1 Materials

N-hydroxyethyl acrylamide (97%), silver trifluoromethanesulfonate (AgOTf, ≥99%), acetobromo-α-D-glucose (AcBrGlc, ≥95%), acetobromo-α-D-galactose (AcBrGal, ≥93%), sodium bicarbonate (≥99.5%), sodium methoxide solution (25 wt% in methanol), 4 Å molecular sieves (powdered), anhydrous sodium sulfate (≥99%), 4'-azobis(4-cyanovaleric acid) (V-501), trimesic acid (95%), anhydrous dimethyl sulfoxide (≥99.9%), 1,3,5-trioxane (≥99%), and deuterium oxide (D, 99.9%) were purchased from Sigma Aldrich. Sodium chloride (≥99%), concentrated hydrochloric acid, pH reference buffers (pH 4.00, 7.00, 10.00), and ethidium bromide solution (EtBr, 10 mg/mL) were purchased from Fisher Scientific. Dimethylaminopropylacrylamide (DMAPAm, >98%) was purchased from TCI Chemicals and distilled before use. Dimethyl sulfoxide-d6 (D, 99.9%) and chloroform-d (D, 99.8%) were purchased from Cambridge Isotope Laboratories, Inc. Gel loading dye (6X) was purchased from New England BioLabs. Tris-EDTA buffer (TAE, 100X) was purchased from G Biosciences and diluted before use.

The chain transfer agent 4-cyano-4-(ethylsulfanylthiocarbonyl) sulfanylpentanoic acid (CEP) and glycomonomers were synthesized as described previously.[31-33] Synthetic procedures for CEP, AcGlcEAm, and AcGalEAm are provided in A.1 and A.2 and corresponding NMR spectra in $CDCl_3$ are provided in Figure A.1-Figure A.10. All solvents were purchased from Fisher Scientific unless otherwise stated.

2.2.2 Cationic glycopolymer synthesis

Glucose- and galactose-functionalized homopolymers were synthesized from acetylated glycomonomers as previously described (A.2).[30] The fully cationic polymer PDMAPAm was prepared similarly, where the DMAPAm monomer was polymerized as the hydrochloride salt (A.3).[34] Cationic glycopolymers with pendant tertiary amines were synthesized by copolymerizing the acetylated glycomonomer with either 10 mol% or 30 mol% of the cationic monomer DMAPAm, followed by post-polymerization deprotection of the hydroxyl groups (Figure 2.1). In an example copolymerization for a copolymer with 30% DMAPAm comonomer, DMAPAm (0.18 g, 1.11 mmol) and concentrated HCl (93.0 μL) were dissolved in 3.0 mL DMSO in a graduated cylinder to prepare the hydrochloride salt. Then, AcGalEAm (1.17 g, 2.63 mmol), CEP (13.83 mg, 0.053 mmol), and trimesic acid (39.40 mg, 0.188 mmol) were dissolved in this same solution. A 1 mg/mL stock solution of V-501 was prepared in DMSO and 2.94 mL (0.0105 mmol) was added to the polymerization mixture in the graduated cylinder. The polymerization mixture was then diluted to a total volume of 7.50 mL, transferred to a round-bottomed flask, and degassed with ultrapure N_2 for 45 minutes. The polymerization was conducted at 70 °C and was quenched in liquid N_2 at approximately $p = 0.7$. The polymerization solution was diluted with 15.0 mL of anhydrous MeOH and the acetyl groups were

removed through addition of NaOMe/MeOH (0.5 eq. per monomer unit) while stirring at room temperature, where the deprotected copolymer precipitated from solution. After two hours, the crude polymer was isolated by centrifuging and then rinsing with additional MeOH. The crude P(Gal-*s*-DMAPAm) was further purified by dialyzing for 2 days using 1 kDa MWC RC dialysis tubing (SpectraPor) under acidic conditions (pH 3-4) with frequent water exchanges. The copolymer was isolated by freeze-drying for 2 days.

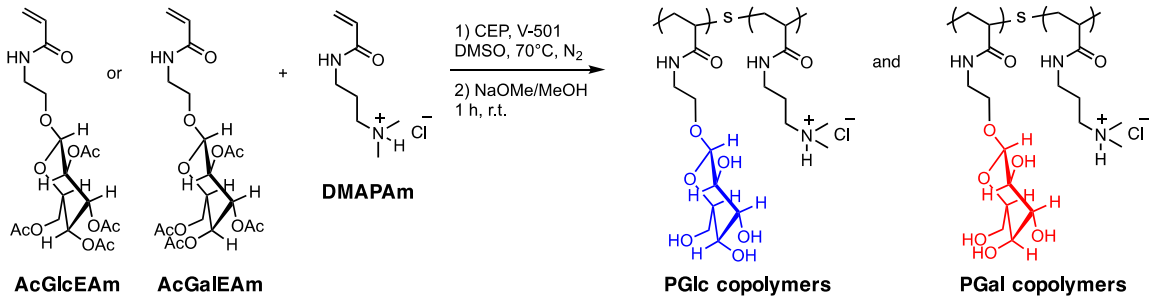

Figure 2.1 *Synthesis of glucose- and galactose-functionalized cationic glycopolymers via RAFT polymerization and base-catalyzed post-polymerization deprotection.*

2.2.3 NMR spectroscopy

^{1}H and ^{13}C NMR spectroscopy were performed using a 600 MHz Bruker Advance III (TopSpin 3.1p17) spectrometer. Monomer and polymer spectra were acquired utilizing a delay time of 5 sec and 2 sec, respectively. Monomer conversion was monitored by comparing the integrations of the vinyl peaks (5.0-7.0 ppm) to that of the unique proton peak of the trimesic acid (8.60 ppm) internal standard. Copolymer composition was determined by comparing integrations of the relative intensities on the saccharide anomeric proton on C1 (4.49 ppm) to that of the six protons on the DMAPAm methyl groups (2.98 ppm). All NMR spectra were processed and analyzed using MNova software.

2.2.4 Aqueous size exclusion chromatography with multi-angle laser light scattering (ASEC-MALLS)

Polymers were characterized using aqueous size exclusion chromatography (SEC) with multi-angle laser light scattering on an Agilent 1260 Infinity II LC system with a Wyatt DAWN HELEOS-II light scattering detector (λ = 633 nm) and an Optilab T-rEX refractometer. An aqueous eluent of 0.1 M Na_2SO_4 in 0.1 v/v% acetic acid at a flow rate of 0.25 mL/min at 25 °C was used with Eprogen Inc. CATSEC columns (1000, 300, and 100 Å). Values for polymer refractive index increment (dn/dc) were calculated as the weight-fraction averages of each monomer component (w_A and w_B) based on the respective homopolymer dn/dc values determined using an offline refractometer at 25 °C in the ASEC eluent and copolymer compositions measured by NMR spectroscopy (Equation 2.1). Wyatt ASTRA SEC/LS software (version 7.1.4.8) was used to determine number-average molecular weight (M_n), weight-average molecular weight (M_w) and polymer dispersity (Đ). All measurements were performed in triplicate.

$$dn/dc = w_A(dn/dc)_A + w_B(dn/dc)_B \qquad \text{Equation 2.1}$$

2.2.5 Cell viability

Cytotoxicity was assessed using a lactate dehydrogenase (LDH) release assay (Sigma Aldrich) following the manufacturer's instructions. Briefly, ISE6 cells were seeded in a 24-well plate at a density of 4 x 10^5 cells/well and incubated for 48 hours. Complete media was replaced with OptiMEM™ reduced serum media (Fisher Scientific) and polymer solution resulting in 5 and 20 µg/mL concentrations. Media samples from each well (100 µL) were assayed after 0.5, 1, 2, 4, 12, and 24 hours of polymer exposure. 1X PBS buffer (137 mM NaCl, 2.7 mM KCl, 10 mM Na_2HPO_4, 1.8 mM KH_2PO_4,

pH=7.4) was used as a negative control and 3% Triton X-100 was used as a positive control of 100% cytotoxicity (LDH release). Lipofectamine-3000™ and PEG were used as references for polymer toxicity. The absorbance was measured at 490 nm with a reference wavelength of 690 nm. The relative cytotoxicity was assessed using the ratio of LDH released in the test sample to that released by the positive control (Equation 2.2).

$$Cytotoxicity\ (\%) = \frac{OD_{490nm,sample} - OD_{490nm,neg\ control}}{OD_{490nm,pos\ control} - OD_{490,neg\ control}} \times\ 100 \qquad \text{Equation 2.2}$$

2.2.6 Synthesis of dsRNA

Preparation of SelenoK dsRNA (dsSelK) was performed as described previously.[6, 35] Briefly, a DNA template with T7 promoter sequences added to the 5' and 3' ends of the gene specific product was generated using PCR. The SelenoK gene was amplified using gene-specific primers. The product was purified and used as the template for a PCR reaction with SelenoK primers containing the T7 flanking. Primer sequences are provided in Table S.1. The resulting product was purified with the QIAquick PCR Purification Kit (Qiagen) and then transcribed into dsRNA using the HiScribe™ T7 Quick High Yield RNA Synthesis Kit (New England BioLabs, Ipswich, MA). The dsSelK was isolated by precipitation in ethanol and the concentration and purity was determined using NanoDrop analysis at 260/280 nm and 260/230 nm ratio absorbances. The dsSelK was labeled with a Cy3 fluorescent probe (*Silencer*™ siRNA labeling kit, Invitrogen™) following the manufacturer's protocol.

2.2.7 Gel electrophoresis

Polymer/dsRNA polyplex formulations were prepared at several nitrogen-to-phosphorus (N:P) ratios of 0, 0.25, 0.5, 1, 5, 10, 25, 50, and 75 by mixing 1 µL of 1 µg/µL dsRNA with the proper volume of either a 1 µg/µL or 10 µg/µL polymer solution

(in 1X PBS buffer) in a centrifuge tube. N:P ratios were calculated based on the total amount of amines on the copolymers assuming full amine protonation. Polymer/dsRNA mixtures were vortexed for 15 seconds and left to equilibrate for 30 minutes at 25 °C before being loaded into a 1% agarose gel stained with EtBr. Diluted 6X loading dye was loaded into a separate well to monitor dsRNA mobility. Gel electrophoresis was performed in 1X TAE buffer with an adjusted pH of 8.0 to facilitate copolymer/dsRNA complexation based on the pK_a of the tertiary amines. Gels were run for 25 minutes at a run voltage of 80 V. Gels were imaged using a Bio-Rad ChemiDoc MP Imaging System.

2.2.8 Zeta potential and dynamic light scattering

Dynamic light scattering (DLS) was performed on a Malvern Instruments Zetasizer Nano ZS (633 nm incident wavelength, 173° scattering angle) operating at 25 °C. DLS measurements were carried out at a complex concentration of 1 mg/mL in either 1X PBS solution or OptiMEM® reduced serum transfection medium. Samples were vortexed for 15 seconds and equilibrated for 30 minutes prior to measurements. Zeta potential samples were prepared similarly and experiments were performed in a DTS1070 folded capillary cell (Malvern). Zeta potential values were determined from electrophoretic mobility using the Smoluchowski approximation for polar media. All measurements were performed in triplicate.

2.2.9 RNA transfection and qRT-PCR

ISE6 cells were seeded in a 24-well plate at a cell density of 4×10^5 cells/well and incubated at 34 °C for 48 hours. For transfection, the media was removed and replaced with transfection reaction media (OptiMEM Reduced Serum Medium, Glutamax supplement (Invitrogen) and polymer/dsRNA polyplexes). Cells were incubated with

1000 ng dsRNA for 60 hours and RNA was harvested using TRIzol reagent (Invitrogen). Complimentary DNA (cDNA) synthesis and qRT-PCR were conducted using the gene-specific primer sequences designed to amplify specific cDNA fragments from ISE6 cells.[6] Transcriptional gene expression of the *I. scapularis* selenoprotein K (SelK) genes in ISE6 cells was normalized against the highly expressed tick ribosomal protein S4 (Rps4) gene expression as an internal reference gene.[36] The synthesized cDNA was used to quantify mRNA levels by qRT-PCR using the CFX96 Real Time System (Bio-Rad Inc., Hercules, CA) as described previously.[37]

2.2.10 Confocal microscopy

Delivery of dsRNA-Cy3 was monitored in ISE6 cells using a Leica TCS SP8 confocal microscope. Briefly, the cells were grown to confluency on 35 mm optical bottom petri dishes (Fisher Scientific) and incubated with dsRNA-Cy3 polyplexes in a temperature controlled chamber (Zeiss, Heidelberg, Germany). Images were captured every 5 minutes for 2 hours and compiled into a motion picture using the LSM 510 META confocal microscope running ZEN 2009 software (Zeiss, Heidelberg, Germany) using the 40× objective.

2.3 Results and discussion

2.3.1 Synthesis of cationic glycopolyelectrolytes

Prior to conducting copolymerizations, saccharide-functionalized homopolymers were prepared to determine the appropriate copolymerization conditions, following a previously published method.[30] After an initial induction period, pseudo first-order polymerization kinetics are observed for both types of glycomonomers via ^{1}H NMR spectroscopy, where target monomer conversions ($p = 0.7$) are achieved for PAcGlcEAm

and PAcGalEAm after 160 minutes and 315 minutes, respectively (Figure A.11). Here, loss in control of the polymerization was evident at higher monomer conversions. Base-catalyzed deprotection of acetyl groups was evidenced by ^{1}H NMR with no evidence of ring-opened saccharides (Figure A.12 and Figure A.13). Deprotection was accompanied by a loss in yellow color due to trithiocarbonate cleavage. This is further evidenced by comparing the UV-Vis spectra of the protected and deprotected polymers in DMSO, where a decrease in absorption at 308 nm is observed (Figure A.14). For the polymerization of PDMAPAm, pseudo-first order kinetics are observed, where the target monomer conversion ($p = 0.7$) was achieved at 105 minutes (Figure A.15).

A total of four cationic glycopolymers were synthesized via RAFT copolymerization with varying glycomonomer type (AcGlcEAm or AcGalEAm) and monomer feed ratios (Figure 2.1). Similar to the homopolymers, each copolymer was synthesized by copolymerizing the glycomonomers in their protected forms in DMSO with the hydrochloride salt of DMAPAm. Kinetics were analyzed by ^{1}H NMR spectroscopy, where the integrations of both monomer vinyl peaks were shown to decrease with increasing polymerization time, indicating a random monomer distribution within the copolymer chains. Acetyl groups were removed through base-catalyzed hydroxyl group deprotection, where the copolymers precipitated from the deprotection solution as white pellets and were further purified by dialysis. Removal of saccharide protecting groups and copolymer composition were determined through ^{1}H NMR spectroscopy in D_2O (Figure 2.2).

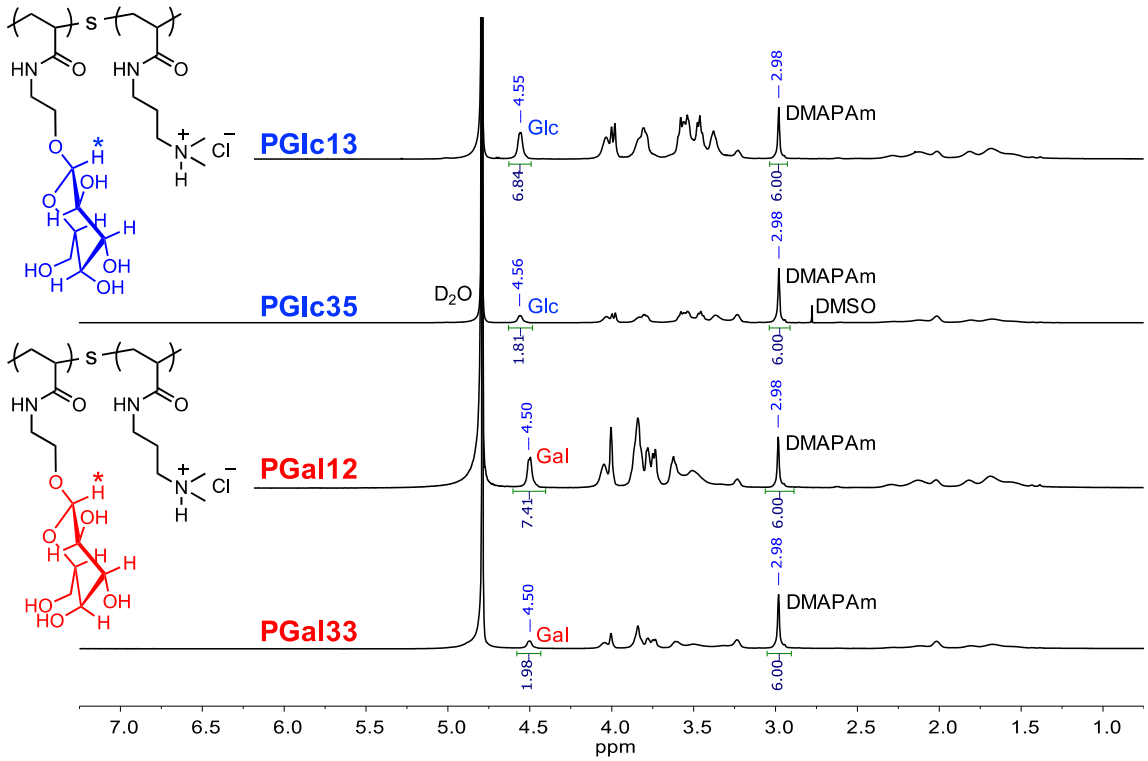

Figure 2.2 *^{1}H NMR spectra of cationic glycopolymers. Copolymer composition was determined by comparing the integrations of saccharide anomeric proton peaks (4.50-4.56 ppm) to the methyl proton peaks on DMAPAm (2.98 ppm). Peak shifts are referenced to D_2O (4.79 ppm).*

Acetyl group removal is evidenced by the disappearance of the sharp singlet peaks at 2.20 and 2.26 ppm (D_2O) in ^{1}H NMR spectra corresponding to the acetyl methyl protons and a downfield shift in each of the anomeric (C1) proton peaks from 4.34 ppm to 4.50-4.56 ppm. By comparing the integrations of the singlet peak corresponding to the six methyl protons on DMAPAm at 2.98 ppm to the singlet peak corresponding to the anomeric proton on the saccharides (glucose, 4.55 ppm; galactose, 4.50 ppm), copolymer compositions were determined.

Figure 2.3 shows ASEC-MALLS traces for the homopolymers and copolymers and Table 2.1 provides a summary of the molecular weights and compositions. For simplicity, each copolymer is named based on the structure of the saccharide, followed

by the mol % of incorporated DMAPAm comonomer (i.e. PGlc13 is a copolymer with glucose pendant groups and 13 mol % incorporation of DMAPAm). The copolymers display narrow and symmetric chromatograms, indicating controlled polymerizations, where molecular weights range between 17 kDa and 22 kDa with low molecular weight distributions (Đ < 1.1). In the final copolymers, incorporation of DMAPAm comonomer is slightly higher than the feed ratio.

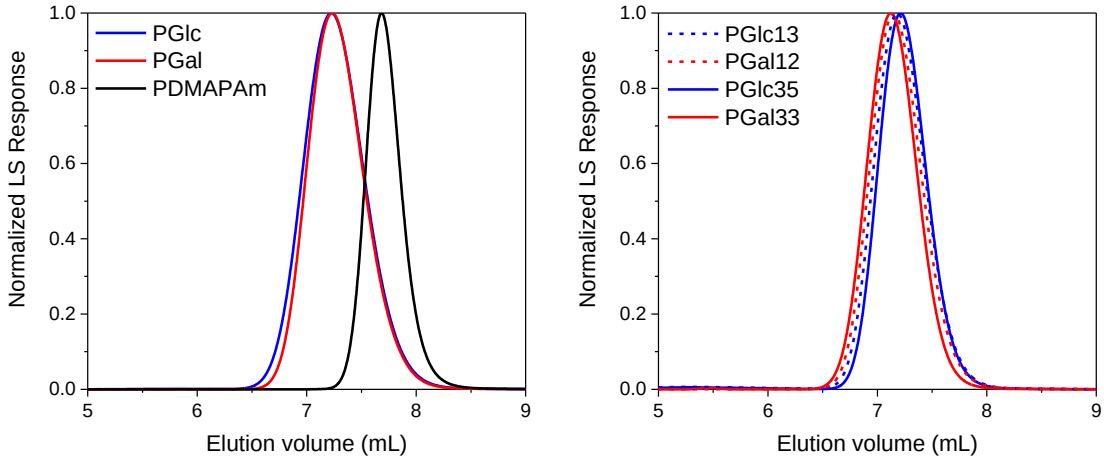

Figure 2.3 *ASEC-MALLS chromatograms of (left) homopolymers and (right) cationic glycopolymers determined in 0.1 M Na_2SO_4 and 0.1 v/v% acetic acid (pH = 3) with CATSEC columns (1000, 300, and 100 Å; Eprogen, Inc).*

Although a DP of 50 was targeted, each of the polymers displays a higher DP than intended (1.2-1.5x higher). Similar deviations in theoretical vs. experimental molecular weight have been observed by McCormick and coworkers in polyacrylamides polymerized under similar conditions, where it was suggested that this was due to decreased CTA efficiency from early termination events in the RAFT polymerization process.[38]

Table 2.1 *Composition, conversion (p), molecular weights (M_n), dispersity (Đ), and dn/dc values of homopolymers and cationic glycopolymers.*

Polymer	Cat. mol% (th)	Cat. mol% (exp)[a]	p[b]	$M_{n,\,exp}$ (kDa)[c]	Đ[c]	Glyco DP	Cationic DP	d*n*/d*c*[d]
PGlc	--	--	0.76	21.2	1.01	75	--	0.1563
PGal	--	--	0.74	20.6	1.04	73	--	0.1505
PDMAPAm	100	100	0.80	13.2	1.01	--	67	0.1689
PGlc13	10	13	0.75	21.3	1.07	69	10	0.1575
PGal12	10	12	0.68	20.9	1.04	68	9	0.1521
PGlc35	30	35	0.78	17.0	1.02	44	24	0.1598
PGal33	30	33	0.84	21.1	1.02	56	28	0.1553

[a]Copolymer composition determined by comparing integrations of anomeric protons on either GlcEAm or GalEAm to protons on DMAPAm (6H, 2.98 ppm) in D_2O using 600 MHz ^{1}H NMR spectroscopy, relaxation delay = 2 sec.

[b]Conversion determined by 600 MHz ^{1}H NMR spectroscopy in DMSO, relaxation delay = 5 sec.

[c]Determined using ASEC-MALLS in 0.1 M Na_2SO_4 and 0.1 v/v% acetic acid (pH = 3) with Eprogen CATSEC columns (1000, 300, and 100 Å).

[d]Homopolymer (PGlc, PGal, and PDMAPAm) d*n*/d*c* values determined using an off-line refractometer at 25°C. Copolymer d*n*/d*c* values calculated based on the monomer weight fractions in the copolymer and homopolymer d*n*/d*c* values.

2.3.2 Polymer cytotoxicity

One important consideration in designing cationic polyelectrolytes for non-viral gene transfection is polymer cytotoxicity. Inclusion of saccharide functionalities into cationic polymers has been shown to reduce the cytotoxic effects from cations, but the influence of saccharide structure on cytotoxicity is not clear. To the best of our knowledge, these effects have not been assessed in non-mammalian eukaryotic cells. Thus, polymer cytotoxicity was evaluated in ISE6 cells (*I. scapularis*) over different time periods to understand the effect of saccharide structure and cationic monomer loading on

cytotoxicity. Figure 2.4 shows cytotoxicity for 20 µg/mL polymer solutions incubated for 12 hours with ISE6 cells.

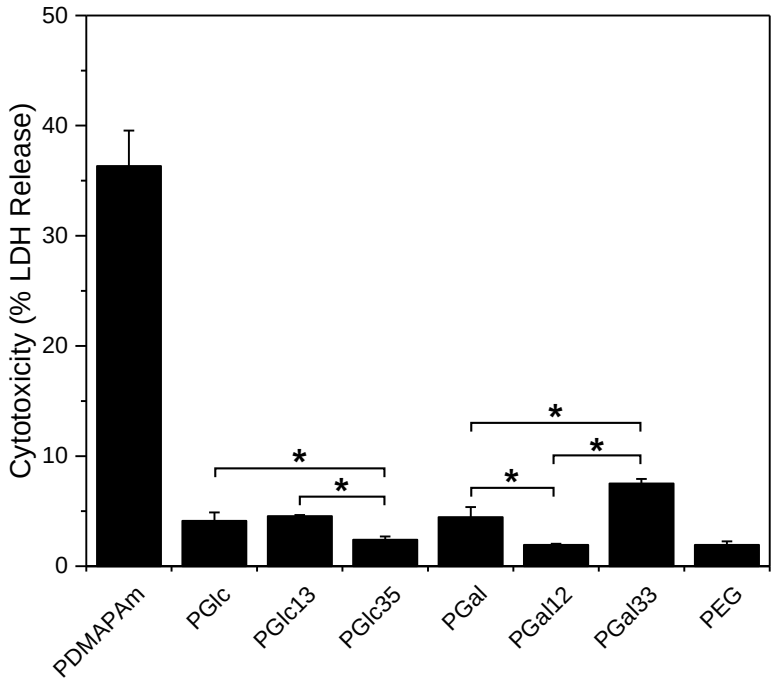

Figure 2.4 *Polymer cytotoxicity after 12 hours of exposure in ISE6 cells determined using an LDH assay (positive control = Triton-X 100, negative control = 1X PBS buffer, polymer concentration of 20 µg/mL). PDMAPAm is significantly more toxic than the saccharide containing polymers. Asterisks above bars represent statistically significant data ($p < 0.05$). The cytotoxicity of PEG is lower than all polymers apart from PGlc35 and PGal12 ($p < 0.05$, not indicated in graph).*

The glycopolymers show levels of cytotoxicity similar to that of PEG, which is commonly used in biomaterials applications. The PDMAPAm cationic homopolymer, on the other hand, displays dramatically higher cytotoxicity, attributed to its high cationic charge density. Statistically significant differences are observed among the glycopolymers, with PGal33 showing the highest toxicity and PGlc35 showing the

lowest. However, all glycopolymers except for PGal33 display cytotoxicity of less than 5%. These results indicate that incorporation of glycomonomer reduces toxicity in cationic copolymers, and glucose functionalized polymers appear to be less toxic than galactose copolymers. The differences in cytotoxicity may be the result of differences in glucose and galactose pendant group interactions with the cell membrane, particularly in terms of cell uptake.[39]

Time-dependent cytotoxicity for all polymers is observed (Figure A.18), and similar trends are observed for lower polymer concentrations of 5 ng/μL (Figure A.19). Cytotoxicity of PDMAPAm also increases as a function of degree of polymerization, where DP 36 polymers are less toxic than DP 67 polymers (Figure A.20). The glycopolymers, cationic copolymers, and the PDMAPAm homopolymer all yield lower toxicity than the commercially available transfection agent Lipofectamine. To compare the effect of charge structure, cationic homopolymers with pendant primary amines (PAPAm) were prepared (synthesis and characterization outlined in A.5, Figure A.21-Figure A.24). Cytotoxicity measurements showed these polymers exhibit significantly higher cytotoxicity than those with pendant tertiary amines, thus we chose not to pursue cationic primary-amine functionalized glycopolymers for further studies.

2.3.3 In vitro copolymer/dsRNA interactions

It is challenging for polynucleotides to enter cells and enable an RNAi response because of the plethora of negative charges on the surfaces of cell membranes. Complexation of RNA with cationic transfection agents helps facilitate cell uptake by providing positive surface charges, where the primary driving force for complexation is through electrostatic interactions and hydrogen bonding. Unlike siRNAs that are

typically used for RNAi in mammalian cells (19-25 nts), ticks require longer dsRNAs to elicit substantial RNAi responses.[18] The dsRNA selective for Selenoprotein K was used (herein referred to as dsSelK), which is approximately 300 nts in length.

To confirm whether the cationic glycopolymers were able to complex with the dsSelK, electrophoretic mobility shift assays (EMSA) were conducted on polyplexes prepared at a range of N:P ratios.[21] Here, N:P ratio is defined as the ratio of the positively charged nitrogens on the copolymers to the negatively charged phosphates on the RNA backbone. In the EMSA gel, the wells can be placed in the middle of the gel, and complexation behavior of dsRNA with other macromolecules is assessed based on how the copolymers retard the mobility of dsRNA based on size and charge.[40] EMSA gels for polyplexes prepared with the four cationic glycopolymers are shown in Figure 2.5, where naked dsSelK is included as a control. The negatively charged species migrate towards the positively charged cathode (bottom) and positively charged species migrate in the opposite direction towards the negatively charged anode (top). No fluorescence is observed from uncomplexed cationic glycopolymers (Figure A.25).

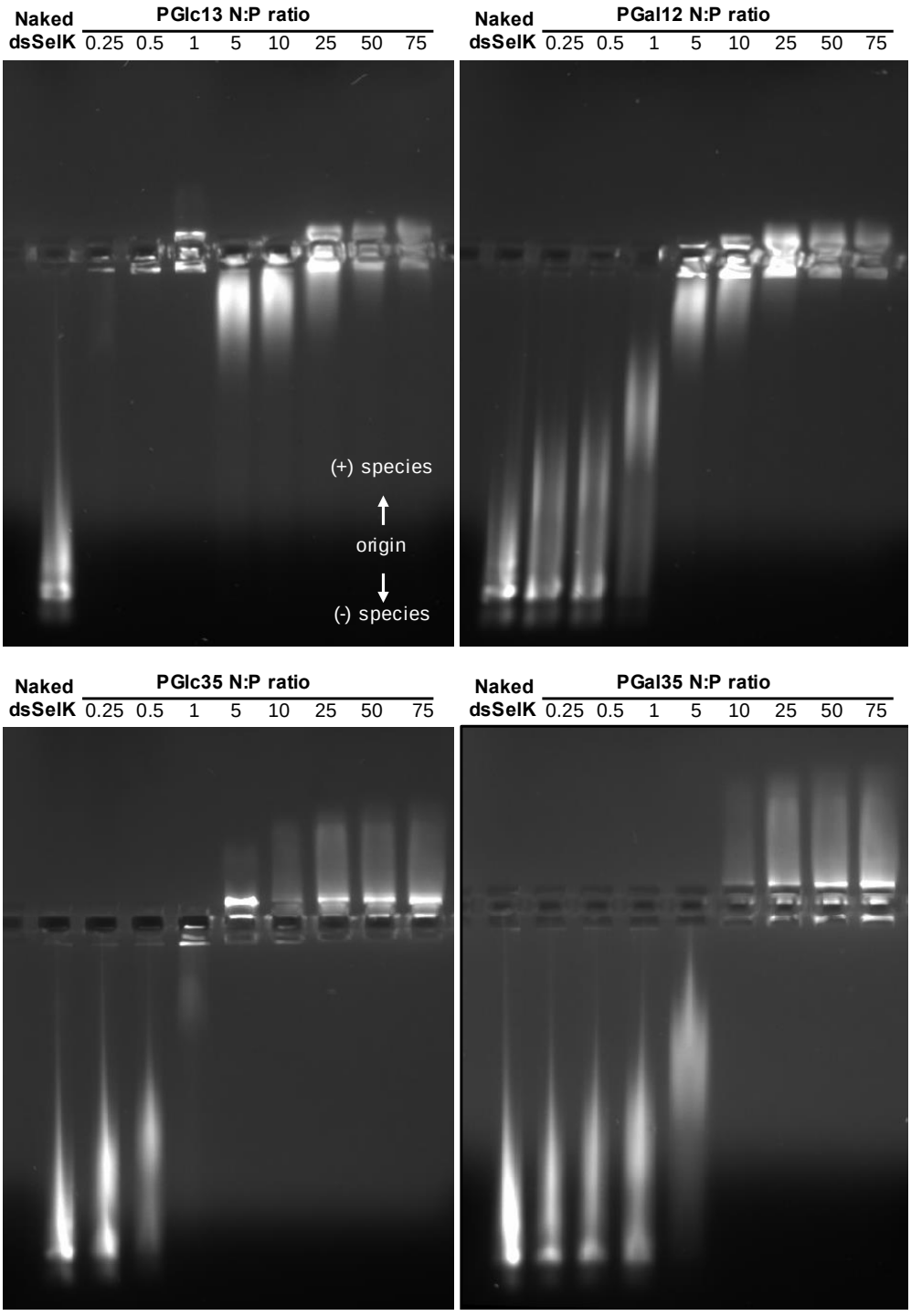

Figure 2.5 *Agarose gel electrophoresis of cationic glycopolymer/dsSelK polyplexes in TAE buffer (pH = 8.0) at N:P ratios ranging from 0.25 to 75. Naked dsSelK is included as a control. Visualization of dsRNA and/or copolymer/dsSelK polyplexes is achieved with fluorescent EtBr staining.*

In each of the EMSA gels, naked dsSelK travels the furthest down the agarose gel due to the highly negatively charged polyphosphate backbone. In general, complexation of the copolymers with dsSelK results in reduced dsSelK mobility. For both PGlc13 and PGal12, high N:P ratios (of approximately 50) are required for dsSelK charge neutralization. Here, no polyplex migration is observed towards the anode, which would indicate formation of positively charged polyplexes. Instead, the PGlc13/dsRNA and PGal12/dsRNA polyplexes remain in the origin wells. This shows complexation occurs between the two species, but does not necessarily indicate formation of cationic polyplexes. However, this may also indicate the formation of large particles that are unable to penetrate the gel pores. Interestingly, EMSA gels of PDMAPAm/dsSelK polyplexes show similar results, where complexation is achieved (albeit at lower N:P ratios), but no dsSelK mobility is observed out of the origin wells at higher N:P ratios (Figure A.26). Charge neutralization of dsSelK with both PGlc35 and PGal33 is achieved using considerably lower N:P ratios of 5 and 10, respectively, and incorporation of more copolymer into the polyplex formulations results in positively charged particles that are able to migrate towards the anode. Overall, these results indicate that copolymers with more DMAPAm content yield higher dsRNA complexation, although it is difficult to deconvolute complexation effects related to particle size.

To further probe the interactions between dsSelK and the copolymers in terms of charge, the ζ-potentials of several polyplexes were measured in both PBS and OptiMEM transfection media at a complex concentration (dsSelK + copolymer) of 1 mg/mL (Figure 2.6). PBS is commonly used for cell culture and cytotoxicity experiments, while OptiMEM is used for nucleic acid transfection experiments. Here, it is important to note

that these two solvents have slightly lower pHs (pH 7.4 for PBS and pH 7.3 for OptiMEM) that are more comparable to physiological conditions for transfection than the TAE buffer used in the gel experiments (pH 8.0). N:P ratios of 10 and 50 were chosen, as these represent the ratios observed in EMSA gels to retard mobility of dsSelK in copolymers with high and low DMAPAm loadings, respectively. Neat polymer solutions exhibit positive zeta potentials in both PBS and OptiMEM (Table A.2).

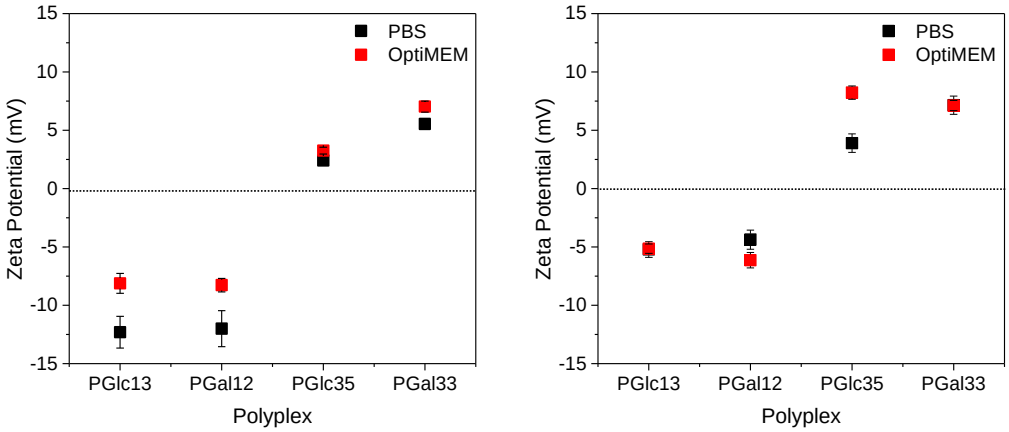

Figure 2.6 *Zeta potential measurements of cationic glycopolymer/dsSelK polyplexes (1 mg/mL) in PBS (pH = 7.4) and OptiMEM (pH = 7.3) transfection medium. This data is summarized in table form in Table S.3.*

At N:P ratios of 10, neither PGlc13 nor PGal12 is able to efficiently complex with dsSelK to provide positive surface charges. This is consistent with the EMSA gel data. On the other hand, PGlc35 and PGal33 both complex with dsRNA to afford positively charged polyplexes, with the galactose copolymer displaying higher ζ-potential in both buffers. In PBS, the ζ-potentials of PGal33 and PGlc35 polyplexes are 5.54 ± 0.36 mV and 2.42 ± 0.41 mV ($p = 0.0006$), respectively. In OptiMEM, the ζ-potentials of PGal33 and PGlc35 polyplexes are 7.03 ± 0.47 mV and 3.26 ± 0.29 mV ($p = 0.0003$), respectively. This suggests that the pendant saccharide structure affects the intermolecular interactions with the dsRNA, presumably due to differences in hydrogen

bonding patterns and/or hydrophobicity. The higher ζ-potentials in OptiMEM may be attributed to differences in solution pH.

At N:P ratios of 50, higher ζ-potentials are observed for all polyplex formulations, due to the overall increased concentration of cationic charges. However, PGlc13 and PGal12 complexation of the dsSelK is still poor, where both solutions exhibit negative ζ-potentials. These results highlight the importance of copolymer cationic charge density in dsSelK binding. Additional experiments were conducted using a commercially available scrambled siRNA of shorter length (*Silencer*™ Negative Control No. 1 siRNA, Invitrogen, 21 nts) to determine the effects of RNA size on complexation. In this system polyplexes with positive ζ-potentials are obtained for all copolymers and the same trends are observed, with the copolymers with higher cationic comonomer content and the galactose pendant group displaying the highest ζ-potential (Table A.4). Together, these findings indicate that copolymer/RNA binding is dependent not only on cationic charge and saccharide structure, but also on RNA length.

Based on the EMSA gels, it is suspected that the polyplexes exhibit large particle sizes, particularly for the PGlc13 and PGal12 polyplexes. Previously, we reported self-associative behavior of PGlc and PGal homopolymers of higher molecular weights (65 kDa and 72 kDa, respectively) in aqueous solution.[30] To examine the potential aggregation behavior of cationic glycopolymers under our experimental conditions, dynamic light scattering (DLS) experiments were performed on 1 mg/mL polymer solutions prepared in PBS (Figure 7) and OptiMEM (Figure S27). Regardless of copolymer composition or solvent, multiple particle size distributions with hydrodynamic diameters (D_H) are observed, indicating copolymer self-associative behavior. Particles in

these size ranges have been observed in similar cationic glycopolymer systems with glucose and maltose saccharides, where it has been proposed that the smaller particles represent single glycopolymer micelles while larger particles represent aggregates of multiple chains. For both particle sizes, formation is due to a combination of intermolecular and intramolecular hydrogen bonding between the highly hydrophilic pendant groups and hydrophobic interactions involving the polyacrylamide backbones.

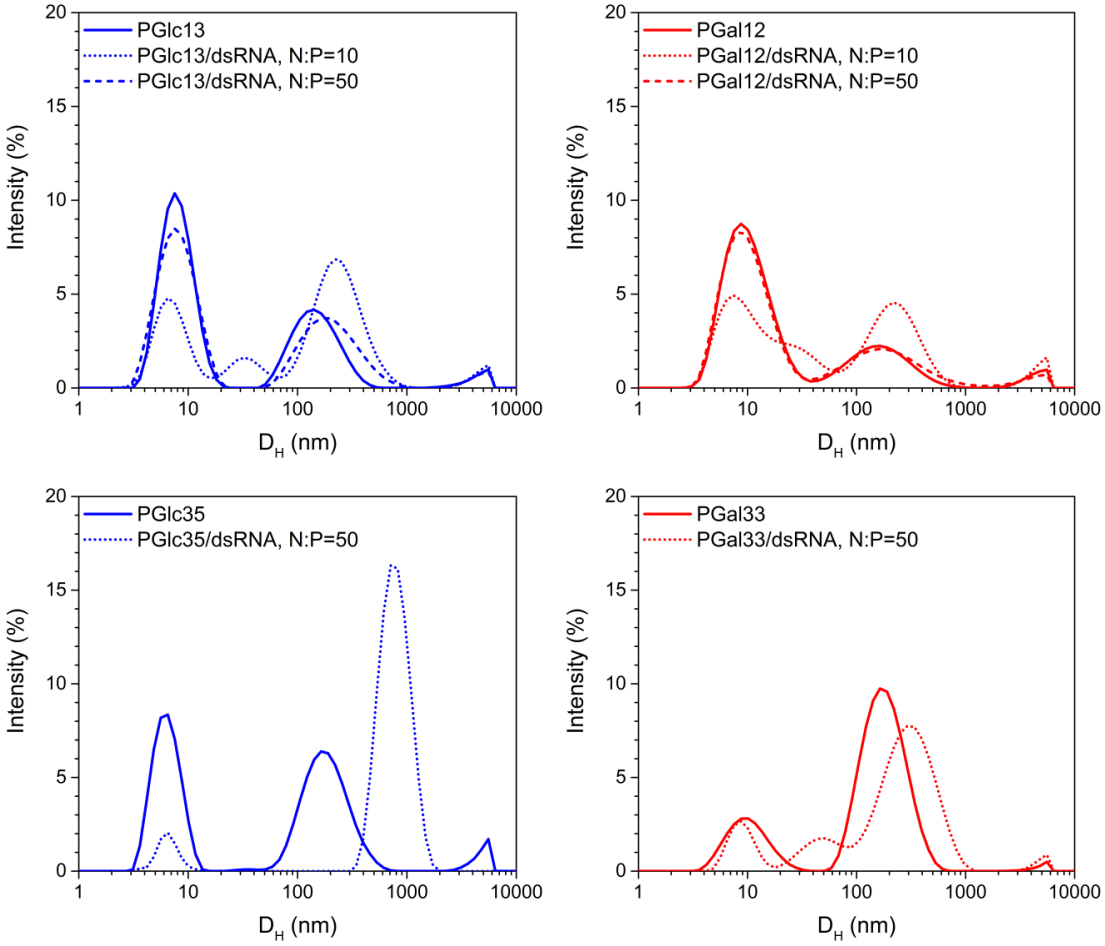

Figure 2.7 *Hydrodynamic diameter (D_H) of filtered cationic glycopolymer and dsRNA/copolymer polyplex solutions in PBS (1 mg/mL). Multiple particle size distributions are observed in all solutions.*

Particles in these size ranges have been observed in similar cationic glycopolymer systems with glucose and maltose saccharides, where it has been proposed that the smaller particles represent single glycopolymer micelles while larger particles represent aggregates of multiple chains.[41] For both particle sizes, polyplex formation is due to a combination of intermolecular and intramolecular hydrogen bonding between the highly hydrophilic pendant groups and hydrophobic interactions involving the polyacrylamide backbones.[42-43]

Polyplex cell uptake for RNA transfection can be affected by both polyplex size and charge, and from the DLS and the EMSA gel data, it is evident that the cationic glycopolymers interact not only with the dsSelK, but also with themselves. Copolymer/dsRNA polyplexes prepared for DLS (polyplex concentration of 1 mg/mL) at an N:P ratio of 10 resulted in turbid solutions that were not conducive to light scattering measurements, indicating the presence of large particles in solution. As mentioned previously, large particles could explain the EMSA gel results, where limited mobility of PGlc13 and PGal12 polyplexes was observed outside of the origin wells even at high N:P ratios. As the neat copolymer solutions were transparent, this finding indicates that aggregates and polyplexes formed in the presence of dsSelK are substantially larger than glycopolyelectrolyte aggregates (> 400 nm). Polyplex solutions prepared at N:P ratios of 50 were clear, and multiple size distributions are observed by DLS (Figure 2.7). As observed for the neat glycopolymer solutions, one distribution at 10 nm is attributed to the unaggregated glycopolymer, and perhaps uncomplexed dsRNA, and larger distributions of hundreds of nanometers that represent polyplexes and aggregates. In contrast to the neat glycopolymer solutions, an additional intermediate aggregate in the

range of 50-60 nm is observed for the PGal33/dsRNA solutions, and micron size aggregates are observed for the PGlc35/dsRNA solutions. Similar results were obtained for polyplexes prepared in OptiMEM (Figure A.27).

Interestingly, Lichtenberg and coworkers recently observed similar trends in chitosan/dsRNA (200 nts) polyplexes, where the size and morphology of the polyplexes were shown to be highly heterogeneous through a combination of transmission electron microscopy, fluorescence correlation spectroscopy, and dynamic light scattering experiments, and in some cases also observed particles large enough to be seen with the naked eye.[44] While it is not possible to clearly differentiate our polyplexes from glycopolymer aggregates, the polyplex sizes appear to be more affected by N:P ratio than saccharide structure or cationic monomer loading.

2.3.4 Cationic glycopolymer/dsSelK transfection and RNA interference in ISE6 cells

Zeta potential experiments indicate that saccharide structure and N:P ratio influence polyplex surface charge. Thus, polyplexes were prepared in PBS at N:P ratios of 10 and 50, and then **i**ncubated with the ISE6 cells 60 hours, and relative expression of SelK transcripts was determined by qRT-PCR following literature procedure (Figure 2.8).[45] Naked dsSelK and dsRNA (dsLacZ) are included as negative controls and Lipofectamine is included as a comparison to a commercial cationic polyelectrolyte transfection agent.

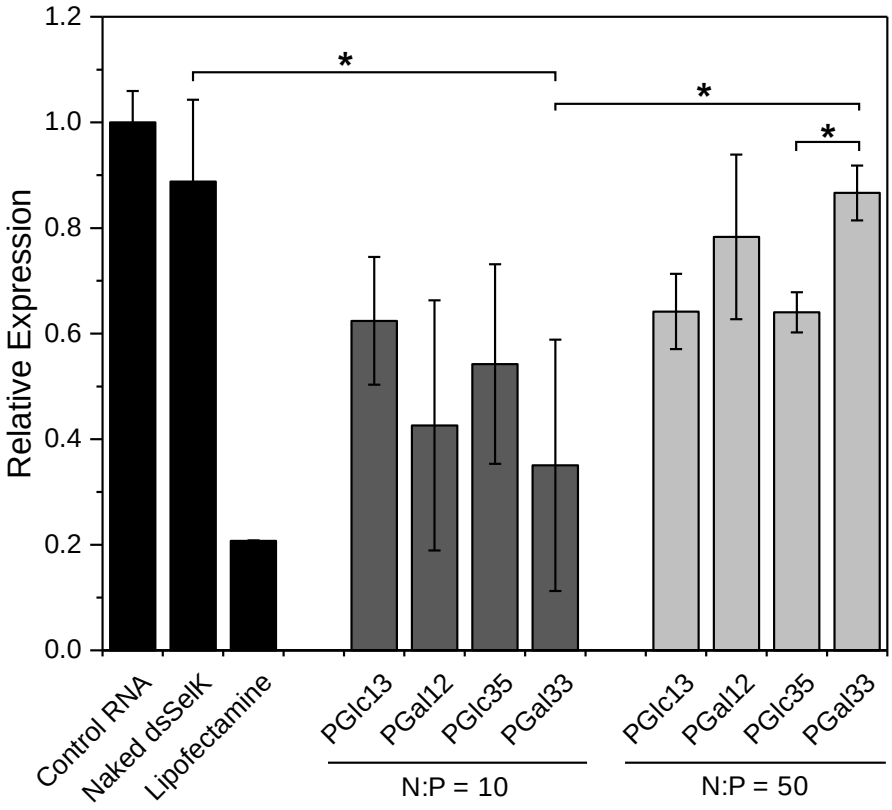

Figure 2.8 *Relative expression of SelK/Rps4 gene transcripts in ISE6 cells determined by qRT-PCR after incubating with cationic glycopolymer/dsSelK polyplexes at N:P ratios of 10 and 50 for 60 hours. Expression of SelK/Rps4 (mean ± standard deviation) is normalized relative to the expression of an irrelevant dsRNA control (dsLacZ). Asterisks above bars represent statistically significant data in comparison to expression of naked dsSelK ($p < 0.05$).*

As expected, no effect on knockdown of the SelK transcripts is observed with the non-targeting control dsRNA. Transfection of the naked dsSelK is also ineffective and is likely due to poor cell uptake. Interestingly, dsSelK complexation specifically with the galactose-functionalized cationic glycopolymers at N:P ratios of 10 are the only conditions where gene knockdown of SelK transcripts is observed. Efficient gene knockdown is unexpected with PGal12, since the PGal12/dsSelK polyplexes have overall

negative surface charges which could hinder polyplex cell uptake. This suggests that cationic glycopolymer saccharide structure does affect gene knockdown, although positive surface charges may not necessarily be required for achieving reduced gene expression.

Another interesting observation is that even though the polyplexes with N:P ratios of 50 have overall more positive surface charges, complexation of the dsSelK with more cationic copolymer also does not result in better knockdown. This poor transfection efficiency could result from a variety of factors, including reduced polyplex cell uptake due to polyplex size, or perhaps poor dsSelK release from the polyplexes. Lipofectamine, which is the most efficient transfection agent in reducing SelK transcripts, has the greatest density of cationic charges and the highest cytotoxicity compared to any of the copolymers considered this study. Thus, the poor transfection efficiency with the polyplexes formed at N:P ratios of 50 is unlikely to be related to differences in post-transfection cell mortality.

At N:P ratios of 10, the best knockdown was achieved using the PGal33/dsSelK polyplex. The cytotoxicity of PGal33 is also the highest of the four cationic glycopolymers. A possible reason for the observed transfection efficiency with this copolymer, as well as the higher cytotoxicity, is better cell uptake of the galactose-functionalized polymer itself. To evaluate whether there were differences between the copolymers in terms of cell uptake, dsSelK was labeled with a fluorescent probe (Cy3) and polyplexes were prepared with each copolymer at N:P ratios of 10. Polyplex cell uptake was visualized using confocal fluorescence microscopy, where dsSelK-Cy3 is indicated by the magenta color of the Cy3 fluorescent probe (Figure 2.9). Here, cell

uptake of each copolymer/dsSelK-Cy3 polyplex is compared to that of naked dsSelK-Cy3 and Lipofectamine/dsSelK-Cy3 polyplexes over the course of two hours.

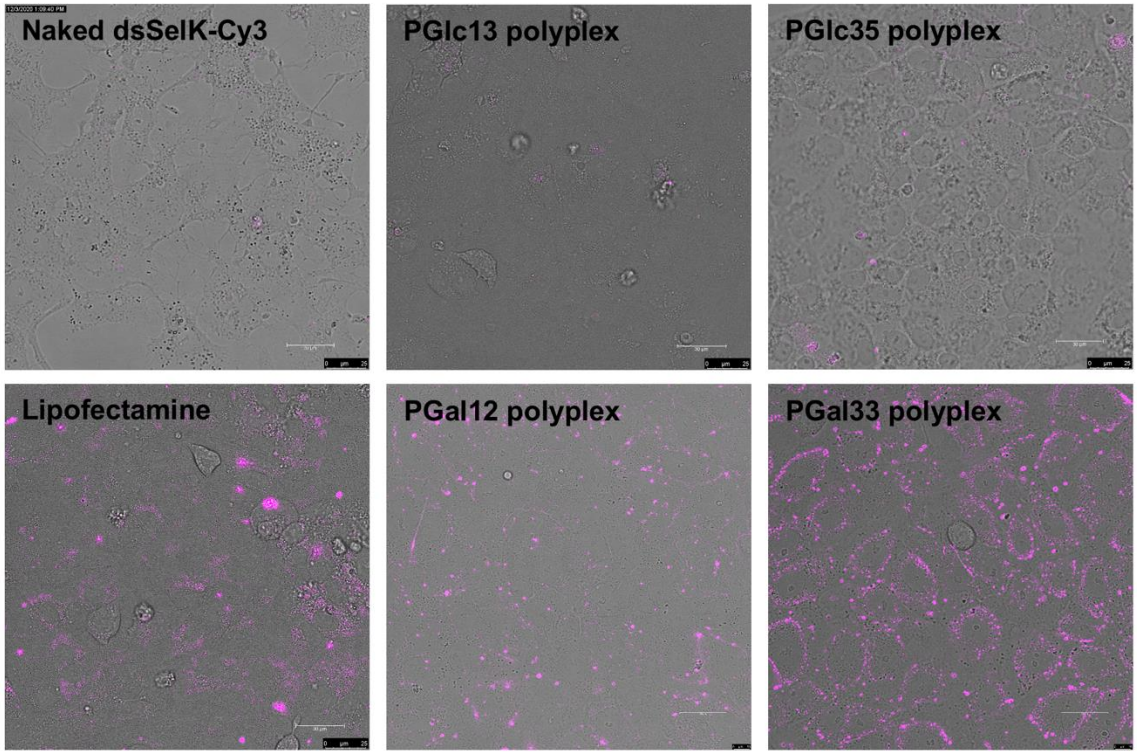

Figure 2.9 *Merged brightfield and Cy3 fluorescence confocal microscopy images of naked dsSelK-Cy3, Lipofectamine polyplexes, and copolymer polyplexes prepared at N:P ratios of 10. Images represent cell uptake (ISE6 cells) after two hours of polyplex exposure at 40X magnification. Cy3 excitation = 555 nm, Cy3 emission = 569 nm. Scale bar = 30 µm.*

Introduction of dsSelK-Cy3 resulted in very little fluorescence, indicating little cell uptake of the RNA even after two hours of polyplex exposure. Complexation of the dsSelK-Cy3 with the commercial standard Lipofectamine resulted in enhanced cell uptake compared to naked dsRNA, which is indicated by the magenta color. As can be seen in Figure 10, delivery of dsSelK-Cy3 with each of the copolymers is more efficient

in comparison to naked dsSelK-Cy3. In both copolymer series, the copolymers with higher cationic content exhibit higher fluorescent signals, which suggests that increasing the amount of cationic charges on the copolymers results in better RNA delivery.

The PGal copolymer series exhibits higher fluorescence than the PGlc copolymer series, demonstrating that the galactose-functionalized polymers have higher cell uptake than those functionalized with glucose. This enhanced cell uptake of PGal33 is likely why this copolymer exhibits the highest cytotoxicity, yet also the best knockdown in SelK transcripts.

2.4 Conclusions

Cationic glycopolyelectrolytes functionalized with either β,D-glucose or β,D-galactose pendant groups were prepared by RAFT polymerization and the effects of saccharide structure and cationic comonomer incorporation on cytotoxicity, dsSelK binding, and RNAi efficiency in tick cells were evaluated. Each of the cationic glycopolymers exhibited low cytotoxicity in comparison to a commercially-available transfection agent regardless of cationic monomer incorporation. Binding studies with the cationic glycopolymers showed that sufficient cationic charges on the copolymer chains (~ 30 mol%) were necessary for dsSelK complexation in vitro, and that the galactose-functionalized copolymers resulted in more polyplex positive surface charges in comparison to those functionalized with glucose. Glycopolymer and/or polyplex aggregation was evident, resulting in heterogeneous polyplex size distributions. However, regardless of charge or size, only the dsSelK polyplexes formed using galactose-functionalized copolymers were able to elicit an RNAi response at N:P ratios of 10. Copolymer/dsRNA complexation at higher N:P ratios of 50 were not efficient for

reducing the expression of SelK transcripts, indicating that in addition to saccharide stereochemistry and cationic charge, N:P ratio is also important for gene transfection. The galactose functionalities were shown to enhance the cell uptake of the dsRNA, demonstrating that saccharide structure in cationic glycopolymers is an important consideration when designing glycopolymer-based nucleic acid transfection agents as saccharide structure can affect resulting transfection efficiencies.

2.5 References

1. Nelson, C.; Saha, S.; Kugeler, K.; Delorey, M.; Shankar, M.; Hinckley, A.; Mead, P., Incidence of Clinician-Diagnosed Lyme Disease, United States, 2005–2010. *Emerging Infectious Disease Journal* **2015,** *21* (9), 1625.

2. Hojgaard, A.; Eisen, R.; Piesman, J., Transmission dynamics of Borrelia burgdorferi s.s. during the key third day of feeding by nymphal Ixodes scapularis (Acari: Ixodidae). *Journal of Medical Entomology* **2008,** *45* (4), 732-736.

3. des Vignes, F.; Piesman, J.; Heffernan, R.; Schulze, T. L.; Stafford Iii, K. C.; Fish, D., Effect of Tick Removal on Transmission of Borrelia burgdorferi and Ehrlichia phagocytophila by Ixodes scapularis Nymphs. *Journal of Infectious Diseases* **2001,** *183* (5), 773-778.

4. Budachetri, K.; Crispell, G.; Karim, S., Amblyomma maculatum SECIS binding protein 2 and putative selenoprotein P are indispensable for pathogen replication and tick fecundity. *Insect Biochemistry and Molecular Biology* **2017,** *88*, 37-47.

5. Budachetri, K.; Kumar, D.; Crispell, G.; Beck, C.; Dasch, G.; Karim, S. A.-O., The tick endosymbiont Candidatus Midichloria mitochondrii and selenoproteins are essential for the growth of Rickettsia parkeri in the Gulf Coast tick vector. *Microbiome* **2018,** *6* (2049-2618 (Electronic)).

6. Kumar, D.; Karim, S.; Embers, M.; Mather, T. N., Is selenoprotein K required for Borrelia burgdorferi infection within the tick vector Ixodes scapularis? *Parasites & Vectors* **2019,** *12* (1), 289.

7. Barnard, A.-C.; Nijhof, A. M.; Fick, W.; Stutzer, C.; Maritz-Olivier, C., RNAi in Arthropods: Insight into the Machinery and Applications for Understanding the Pathogen-Vector Interface. *Genes* **2012,** *3* (4), 702-741.

8. Vélez, A. M.; Fishilevich, E., The mysteries of insect RNAi: A focus on dsRNA uptake and transport. *Pesticide Biochemistry and Physiology* **2018,** *151*, 25-31.

9. Galay, R. L.; Umemiya-Shirafuji, R.; Mochizuki, M.; Fujisaki, K.; Tanaka, T., *RNA interference - a powerful functional analysis tool for studying tick biology and its control*. InTech: 2016; p 411-445.

10. Ramakrishnan, V. G.; Aljamali, M. N.; Sauer, J. R.; Essenberg, R. C., Application of RNA interference in tick salivary gland research. *Journal of Biomolecular Techniques* **2005,** *16* (4), 297-305.

11. Kocan, K. M.; Blouin, E.; de, l. F. J., RNA interference in ticks. *Journal of Visualized Experiments* **2011,** (47).

12. Karim, S.; Kenny, B.; Troiano, E.; Mather, T. N., RNAi-mediated gene silencing in tick synganglia: a proof of concept study. *BMC Biotechnology* **2008,** *8*, 30-30.

13. Munderloh, Ulrike G.; Adamson, S. W.; Browning, R. E.; Budachetri, K.; Ribeiro, J. M. C.; Karim, S., Knockdown of Selenocysteine-Specific Elongation Factor in Amblyomma maculatum Alters the Pathogen Burden of Rickettsia parkeri with Epigenetic Control by the Sin3 Histone Deacetylase Corepressor Complex. *PLoS ONE* **2013,** *8* (11), e82012.

14. Browning, R.; Karim, S., RNA interference-mediated depletion of N-ethylmaleimide Sensitive Fusion Protein and Synaptosomal Associated Protein of 25 kDa

results in the inhibition of blood feeding of the Gulf Coast tick, Amblyomma maculatum. *Insect Molecular Biology* **2013,** *22* (3), 245-257.

15. Villarreal, A. M.; Adamson, S. W.; Browning, R. E.; Budachetri, K.; Sajid, M. S.; Karim, S., Molecular characterization and functional significance of the Vti family of SNARE proteins in tick salivary glands. *Insect Biochemistry and Molecular Biology* **2013,** *43* (5), 483-493.

16. Chalaire, K. C.; Kim, T. K.; Garcia-Rodriguez, H.; Mulenga, A., Amblyomma americanum (L.) (Acari: Ixodidae) tick salivary gland serine protease inhibitor (serpin) 6 is secreted into tick saliva during tick feeding. *Journal of Experimental Biology* **2011,** *214* (4), 665-673.

17. Yu, N.; Christiaens, O.; Liu, J.; Niu, J.; Cappelle, K.; Caccia, S.; Huvenne, H.; Smagghe, G., Delivery of dsRNA for RNAi in insects: an overview and future directions. *Insect Science* **2013,** *20* (1), 4-14.

18. Barry, G.; Alberdi, P.; Schnettler, E.; Weisheit, S.; Kohl, A.; Fazakerley, J. K.; Bell-Sakyi, L., Gene silencing in tick cell lines using small interfering or long double-stranded RNA. *Experimental and Applied Acarology* **2013,** *59* (3), 319-338.

19. Taning, C. N. T.; Christiaens, O.; Berkvens, N.; Casteels, H.; Maes, M.; Smagghe, G., Oral RNAi to control Drosophila suzukii: laboratory testing against larval and adult stages. *Journal of Pest Science* **2016,** *89* (3), 803-814.

20. Avila, L. A.; Chandrasekar, R.; Wilkinson, K. E.; Balthazor, J.; Heerman, M.; Bechard, J.; Brown, S.; Park, Y.; Dhar, S.; Reeck, G. R.; Tomich, J. M., Delivery of lethal dsRNAs in insect diets by branched amphiphilic peptide capsules. *Journal of Controlled Release* **2018,** *273*, 139-146.

21. Parsons, K. H.; Mondal, M. H.; McCormick, C. L.; Flynt, A. S., Guanidinium-Functionalized Interpolyelectrolyte Complexes Enabling RNAi in Resistant Insect Pests. *Biomacromolecules* **2018,** *19* (4), 1111-1117.

22. Zhang, Y.; Cui, J.; Zhou, Y.; Cao, J.; Gong, H.; Zhang, H.; Zhou, J., Liposome mediated double-stranded RNA delivery to silence ribosomal protein P0 in the tick Rhipicephalus haemaphysaloides. *Ticks and Tick-borne Diseases* **2018,** *9* (3), 638-644.

23. Rahman, M. K.; Kim, B.; You, M., Molecular cloning, expression and impact of ribosomal protein S-27 silencing in Haemaphysalis longicornis (Acari: Ixodidae). *Experimental Parasitology* **2020,** *209*, 107829.

24. Van Bruggen, C.; Hexum, J. K.; Tan, Z.; Dalal, R. J.; Reineke, T. M., Nonviral Gene Delivery with Cationic Glycopolymers. *Accounts of Chemical Research* **2019,** *52* (5), 1347-1358.

25. Ahmed, M.; Narain, R., The effect of polymer architecture, composition, and molecular weight on the properties of glycopolymer-based non-viral gene delivery systems. *Biomaterials* **2011,** *32* (22), 5279-5290.

26. Deng, Z.; Ahmed, M.; Narain, R., Novel well-defined glycopolymers synthesized via the reversible addition fragmentation chain transfer process in aqueous media. *Journal of Polymer Science Part A: Polymer Chemistry* **2009,** *47* (2), 614-627.

27. UhlÍR, J.; Grubhoffer, L.; BorskÝ, I.; DusbÁBek, F., Antigens and glycoproteins of larvae, nymphs and adults of the tick Ixodes ricinus. *Medical and Veterinary Entomology* **1994,** *8* (2), 141-150.

28. Vechtova, P.; Sterbova, J.; Sterba, J.; Vancova, M.; Rego, R. O. M.; Selinger, M.; Strnad, M.; Golovchenko, M.; Rudenko, N.; Grubhoffer, L., A bite so sweet: the

glycobiology interface of tick-host-pathogen interactions. *Parasites & Vectors* **2018,** *11* (1), 594-594.

29. Das, P. K.; Dean, D. N.; Fogel, A. L.; Liu, F.; Abel, B. A.; McCormick, C. L.; Kharlampieva, E.; Rangachari, V.; Morgan, S. E., Aqueous RAFT Synthesis of Glycopolymers for Determination of Saccharide Structure and Concentration Effects on Amyloid β Aggregation. *Biomacromolecules* **2017,** *18* (10), 3359-3366.

30. Bristol, A. N.; Saha, J.; George, H. E.; Das, P. K.; Kemp, L. K.; Jarrett, W. L.; Rangachari, V.; Morgan, S. E., Effects of Stereochemistry and Hydrogen Bonding on Glycopolymer – Amyloid-β Interactions. *Biomacromolecules* **2020**.

31. Convertine, A. J.; Benoit, D. S. W.; Duvall, C. L.; Hoffman, A. S.; Stayton, P. S., Development of a novel endosomolytic diblock copolymer for siRNA delivery. *Journal of Controlled Release* **2009,** *133* (3), 221-229.

32. Das, B. P.; Tsianou, M., From Polyelectrolyte Complexes to Polyelectrolyte Multilayers: Electrostatic Assembly, Nanostructure, Dynamics, and Functional Properties. *Adv. Colloid Interface Sci.* **2017,** *244*, 71.

33. Judzewitsch, P. R.; Zhao, L.; Wong, E. H. H.; Boyer, C., High-Throughput Synthesis of Antimicrobial Copolymers and Rapid Evaluation of Their Bioactivity. *Macromolecules* **2019,** *52* (11), 3975-3986.

34. Singhsa, P.; Diaz-Dussan, D.; Manuspiya, H.; Narain, R., Well-Defined Cationic N-[3-(Dimethylamino)propyl]methacrylamide Hydrochloride-Based (Co)polymers for siRNA Delivery. *Biomacromolecules* **2018,** *19* (1), 209-221.

35. Bullard, R. L.; Williams, J.; Karim, S., Temporal gene expression analysis and RNA silencing of single and multiple members of gene family in the lone star tick Amblyomma americanum. *PLoS ONE* **2016,** *11* (2), e0147966/1-e0147966/24.

36. Koči, J.; Šimo, L.; Park, Y., Validation of Internal Reference Genes for Real-Time Quantitative Polymerase Chain Reaction Studies in the Tick, Ixodes scapularis (Acari: Ixodidae). *Journal of Medical Entomology* **2013,** *50* (1), 79-84.

37. Budachetri, K.; Karim, S., An insight into the functional role of thioredoxin reductase, a selenoprotein, in maintaining normal native microbiota in the Gulf Coast tick (Amblyomma maculatum). *Insect Molecular Biology* **2015,** *24* (5), 570-581.

38. Thomas, D. B.; Convertine, A. J.; Myrick, L. J.; Scales, C. W.; Smith, A. E.; Lowe, A. B.; Vasilieva, Y. A.; Ayres, N.; McCormick, C. L., Kinetics and Molecular Weight Control of the Polymerization of Acrylamide via RAFT. *Macromolecules* **2004,** *37* (24), 8941-8950.

39. von der Ehe, C.; Rinkenauer, A.; Weber, C.; Szamosvari, D.; Gottschaldt, M.; Schubert, U. S., Selective Uptake of a Fructose Glycopolymer Prepared by RAFT Polymerization into Human Breast Cancer Cells. *Macromolecular Bioscience* **2016,** *16* (4), 508-521.

40. Hellman, L. M.; Fried, M. G., Electrophoretic mobility shift assay (EMSA) for detecting protein–nucleic acid interactions. *Nature Protocols* **2007,** *2* (8), 1849-1861.

41. Mees, M. A.; Effenberg, C.; Appelhans, D.; Hoogenboom, R., Sweet Polymers: Poly(2-ethyl-2-oxazoline) Glycopolymers by Reductive Amination. *Biomacromolecules* **2016,** *17* (12), 4027-4036.

42. Bordegé, V.; Muñoz-Bonilla, A.; León, O.; Sánchez-Chaves, M.; Cuervo-Rodríguez, R.; Fernández-García, M., Glycopolymers with glucosamine pendant groups: Copolymerization, physico-chemical and interaction properties. *Reactive and Functional Polymers* **2011,** *71* (1), 1-10.

43. Liang, Y.-Z.; Li, Z.-C.; Li, F.-M., Self-Association of Poly[2-(β-D-glucosyloxy)ethyl Acrylate] in Water. *Journal of Colloid and Interface Science* **2000,** *224* (1), 84-90.

44. Lichtenberg, S. S.; Nuti, K.; DeRouchey, J.; Tsyusko, O. V.; Unrine, J. M., Efficacy of chitosan/double-stranded RNA polyplex nanoparticles for gene silencing under variable environmental conditions. *Environmental Science: Nano* **2020,** *7* (5), 1582-1592.

45. Grabowski, J. M.; Gulia-Nuss, M.; Kuhn, R. J.; Hill, C. A., RNAi reveals proteins for metabolism and protein processing associated with Langat virus infection in Ixodes scapularis (black-legged tick) ISE6 cells. *Parasites & Vectors* **2017,** *10* (1), 24.

CHAPTER III – CHARACTERIZATION OF NONCOVALENT INTERACTIONS BETWEEN GLYCOPOLYMERS AND DSRNA BY ALL-ATOMISTIC MOLECULAR DYNAMICS SIMULATIONS

3.1 Introduction

The structural differences between hexopyranose monosaccharides are subtle, and because of this, it can be difficult to design experiments exploring structure-property relationships related to saccharide stereochemistry. With the ongoing development of advanced computational techniques, molecular dynamics (MD) simulations have become an invaluable tool for further understanding how differences in monosaccharide structure affects solute hydration and water structuring in aqueous solution. Studies by Dashnau, Deshmukh, and Suzuki have shown that the OH4 orientation in hexopyranose stereoisomers plays a pivotal role in saccharide hydrogen bonding patterns.[1-3] Unsurprisingly, there have been limited MD studies on acrylamide-based saccharide-functionalized polymers for the purpose of understanding how polymer behavior in aqueous solution is affected by saccharide stereochemistry.[4]

RNA is chaperoned by glycosylated proteins essentially from synthesis to degradation, but there is little known about the effects of saccharide structure on RNA interactions..[5-6] The range of glycopolymer structures for siRNA transfection within mammalian cells is wide, and understanding how RNA duplexes interact with glycopolymers would provide valuable insight towards designing better gene delivery vehicles.

Binding and dsRNA transfection experiments have shown that complexation of dsRNA (300+ nt) with either glucose- or galactose-functionalized cationic copolymers results in different polyplex morphologies and can affect gene knockdown, demonstrating that saccharide stereochemistry can play a critical role in the design of delivery vehicles for RNAi (CHAPTER II). In this study, the lowest energy conformations and electrostatic potentials of glucose- and galactose-functionalized monomers were characterized to first understand the effect of saccharide stereochemistry on glycomonomer conformation and electrostatic properties in aqueous solution. Monomer-water, monomer-monomer, oligomer-water and oligomer-oligomer hydrogen bonding patterns were then assessed in both neutral and cationic oligomer systems. Finally, the intermolecular interactions between individual monomers and cationic oligomers with a model dsRNA duplex were investigated.

3.2 Experimental

3.2.1 MD simulations

Acrylamide-based monomers functionalized with either glucose (GlcEAm) or galactose (GalEAm) pendant groups were built explicitly with rings in the $^4C_1$ ring conformation. Glycomonomers were solvated with water using either the extended simple point charge (SPC/E)[7] or 3-point transferable intermolecular potential (TIP3P)[8] rigid water models. Atactic oligomers with a degree of polymerization of 10 and experimental end groups derived from RAFT polymerization were constructed. Statistical cationic glyco-oligomers were constructed with the general sequence Initiator-AABAABAABA-Terminator. The conformational energies of all chemical structures were minimized in water using the generalized optimized potential for liquid simulations

force field (OPLS3e FF) prior to solvation. A Watson-Crick 16mer dsRNA helix (5'-AGAGAAGAUCUUCUCU-3', PDB ID: 3ND4) was used to model intermolecular interactions with monomers and oligomers. The imported PDB structure was prepared for simulations by removing associated water molecules and ions (Na^+, K^+, and Mg^{2+}), adding stoichiometric amounts of Na^+ ions for charge balance, and filling in missing hydrogen atoms. All simulation box sizes were determined on the basis of providing a 10 Å buffer between the material and the box boundaries. All simulation box parameters are provided in the Appendix (B.1).

Each solvated box was first relaxed into a local energy minimum by simulating Brownian motion for 100.00 ps and using a built-in compressive relaxation protocol. Solvated systems were initialized using randomized velocities and a time step of 10.0 ps. Monomer systems were modeled for a minimum of 10.0 ns. Oligomer and dsRNA boxes were modeled for longer times of 20.0 and 40.0 ns, respectively. All final trajectory files consisted of 1000 frames. The reversible reference system propagator algorithms (RESPA) parameters for bonded, near, and far time steps were 2.0 fs, 2.0 fs, and 6.0 fs, respectively. The isothermal-isobaric (NTP) ensemble was used at 300.0 K and 1.01325 bar, using the Nose-Hoover chain thermostat method (1.0 ps relaxation time) and Martyna-Tobias-Klein barostat method (2.0 ps relaxation time), respectively. Short-range Coulombic interactions were defined with a cutoff radius of 9.0 Å. All molecular dynamics simulations were performed with the OPLS3e FF in Desmond using the Schrödinger Materials Science platform.

3.2.2 MD trajectory analysis.

MD trajectories were analyzed using the Schrödinger tools MD Trajectory Analysis, Simulation Event Analysis, and Simulation Interactions Diagram. Only the last 20% of simulation data was analyzed (data from 200 frames), unless otherwise specified, to ensure the solvated systems were properly equilibrated. All simulations were performed in triplicate.

Root mean square fluctuation (RMSF) of each atom in the monomers was calculated to characterize change in atom positions using Equation 3.1, where *T* is the trajectory time, t_0 is the time zero (frame 1), r_i' is the initial position of atom *i* at t_0, and r_i the position of atom *i* at time *t*.

$$RMSF_i = \sqrt{\frac{1}{T}\sum_{T=1}^{T}[r_i(t) - r_i'(t_0)]^2} \qquad \text{Equation 3.1}$$

Radius of gyration was calculated using Equation 3.2, where *M* is the molecular weight, r_{CoM} is the center of mass of the molecule, and m_n and r_n are the mass and position of atom *n*, respectively.

$$R_g = \sqrt{\frac{1}{M}\sum_n m_n(r_n - r_{CoM})^2} \qquad \text{Equation 3.2}$$

3.3 Results and discussion.

3.3.1 Characterization of monomers

3.3.1.1 Monomer conformation

Stereospecific acrylamide monomers with either β,D-glucose (GlcEAm) or β,D-galactose (GalEAm) pendant groups were constructed in the Schrödinger Materials Science suite to model the differences between the two glycomonomers in their lowest energy conformations in water (Figure 3.1). Glycomonomers were built with the

saccharide rings explicitly in the $^4C_1$ conformation, which is the lowest energy conformation for many D-sugars.[9] In GlcEAm, the stereochemistry of OH4 in the β,D-Glc pendant group is equatorial (*e*-OH4), while OH4 is axial in the β,D-Gal pendant group in GalEAm (*a*-OH4).

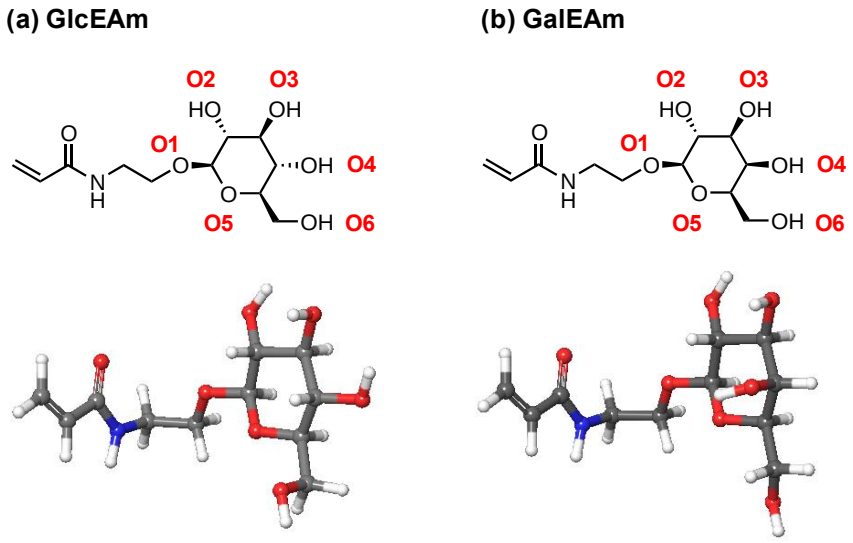

Figure 3.1 *(a) GlcEAm and (b) GalEAm labeled chemical structures and their lowest energy conformations in water.*

Although the only difference between the chemical structures of GlcEAm and GalEAm is the stereochemistry of OH4, the position of OH6 (-CH_2-OH) was shown to differ by 120° due to rotation around the C5-C6 bond to mitigate steric overlap of the OH4/OH6 hydroxyl groups. This demonstrates that a simple change in saccharide OH4 stereochemistry also influences the OH6 hydroxyl group orientation.

3.3.1.2 Electrostatic potential maps

In β,D-Glc, the α and β faces have approximate symmetry because of the all-equatorial positions of the OH groups (*e*-OH2, *e*-OH3, and *e*-OH4). However, the α and β faces of β,D-Gal are asymmetric because of *a*-OH4. As a result, the α face of the β,D-Gal has a "nonpolar patch" that is not only relatively hydrophobic, but also electropositive,

which allows for weak C-H···O dipole interactions to occur.[10-13] Similar to the monosaccharides, electrostatic potential maps of each monomer display minor electrostatic differences between GlcEAm and GalEAm (Figure 3.2), where red represents electronegative regions and blue represents electropositive regions.

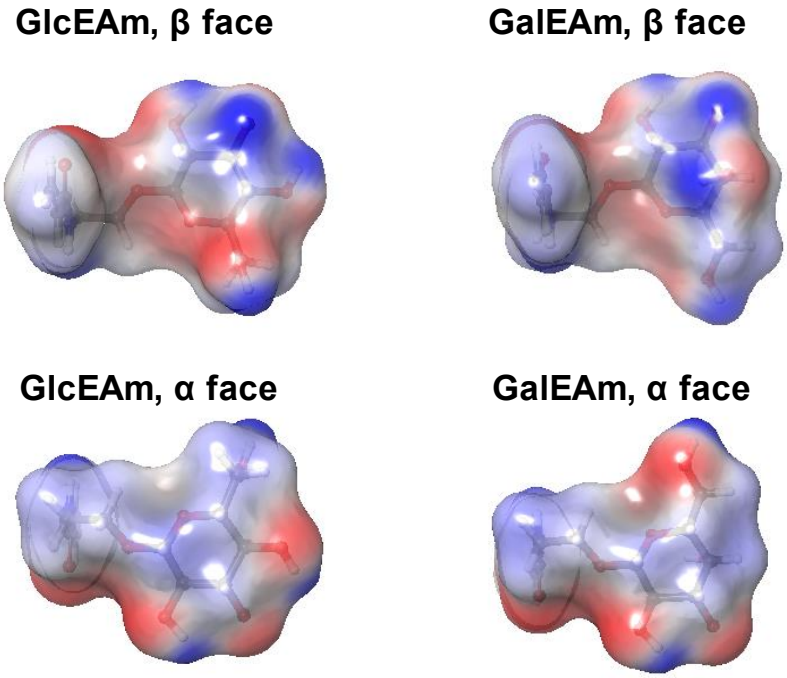

Figure 3.2 *Electrostatic potential maps of monomers in their lowest energy conformations in water.*

In both GlcEAm and GalEAm, the *β* face exhibits both electronegative (red) and electropositive (blue) regions due to differences in electron density around the hydroxyl groups. In the *β* faces, GlcEAm exhibits more electronegativity than GalEAm. This is primarily due to the position of OH6 in GlcEAm, which is very electronegative. However, GalEAm is more electronegative on the *β* face specifically at OH4. On the *α* faces of the two monomers, the center of the saccharide is electropositive, and GalEAm is more electropositive at OH4 than GlcEAm. Due to the position of OH6 on GalEAm,

there is some electronegativity at OH6, although this bond freely rotates in solution. These results are in agreement with previous literature, where the galactose exhibits more electropositivity than glucose on the α face of OH4.[14] Other C-H···π interactions can also occur between the β,D-Gal α face and electronegative aromatic amino acid residues (such as tryptophan, histidine, and tyrosine).[15] It is possible that similar interactions may be observed for the α face of galactose monomer with the aromatic groups on the RNA/nucleotide bases.

3.3.1.3 Root mean square fluctuations

Root mean square fluctuation (RMSF) analysis of the monomers was conducted using the trajectory data from 10.0 ns simulations of single monomers solvated in both SPC/E and TIP3P water to understand how OH4 stereochemistry affects the overall glycomonomer flexibility in solution (Figure 3.3).

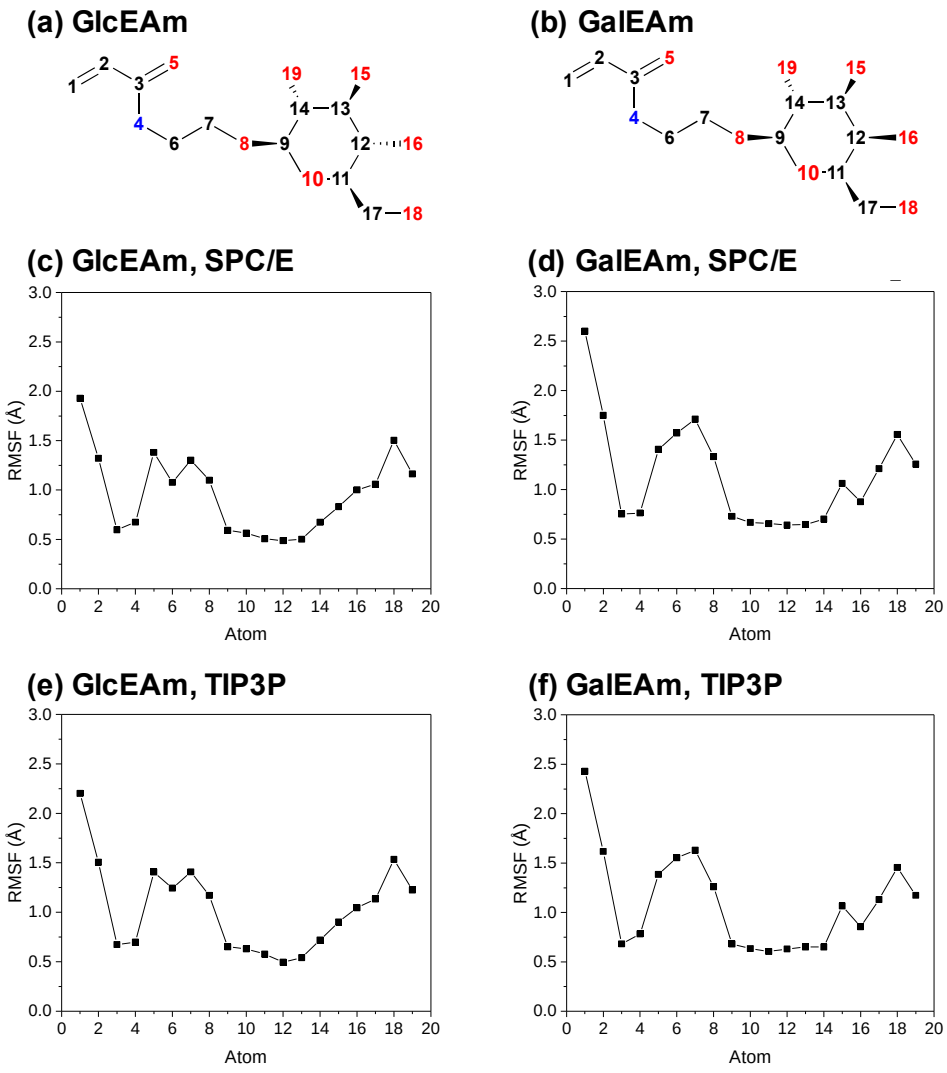

Figure 3.3 *RMSF of GlcEAm and GalEAm carbon (black), oxygen (red), and nitrogen (blue) atoms using SPC/E and TIP3P water models.*

Little difference is observed in RMSF plots produced by the two water models. In both glycomonomers, the vinyl groups (atoms 1 and 2), the flexible alkyl spacers (atoms 4-8), and the secondary hydroxyl groups on the rings at C6 (atoms 17 and 18) have higher RMSF values in comparison to the atoms in the closed saccharide rings (atoms 9-14). The saccharide atoms exhibit little fluctuation in position due to torsional restrictions. Atoms 6, 7, and 15 display higher RMSF values in GalEAm than in

GlcEAm. Atoms 6 and 7, which correspond to the ethylene spacer between the acrylamide and the saccharide, have higher flexibility in GalEAm because of the position of OH6. Atom 15 (O3) in GalEAm (equatorial) is less sterically restrained because of the axial position of O4.

3.3.1.4 Intermolecular hydrogen bonding between glycomonomers and water

The number of intermolecular hydrogen bonds between the saccharide monomer and surrounding water molecules was monitored over the course of 10.0 ns simulations (1000 frames total) in SPC and TIP3P water. Plots in Figure 3.4 show the number of hydrogen bonding events as a function over time for three replicate simulations under each condition.[16]

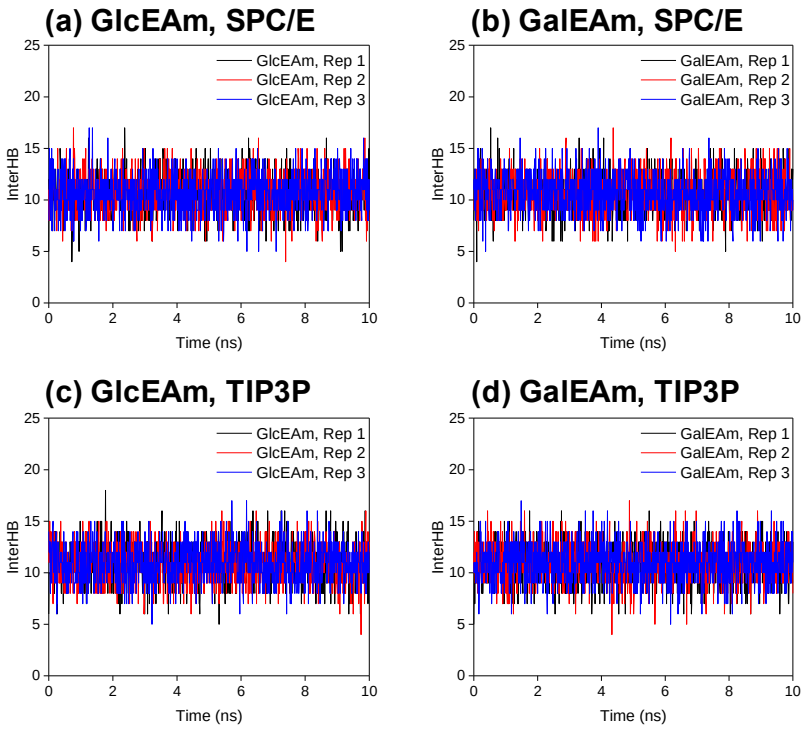

Figure 3.4 *Number of intermolecular hydrogen bonding events between glycomonomers and water over a 10.0 ns simulation.*

GlcEAm and GalEAm are both shown to participate in a wide range of interHBs with solvent molecules, as hydrogen bonding is a dynamic process where the bonds can be broken and reformed. The range, mean, and standard deviation of interHBs for the two glycomonomers are shown in Table 3.1. Given the chemical structure and conformation similarities in aqueous solution, it is unsurprising that the two monomers showed similar hydrogen bonding behavior with water, where it is shown that the glycomonomers and water have an average of approximately 11 interHBs.

Table 3.1 *Intermolecular hydrogen bonding events between glycomonomer and water*

Monomer	Water Model	Minimum interHBs observed	Maximum interHBs observed	Mean interHBs ± St. Dev.
GlcEAm	SPC/E	5	16	10.8 ± 1.8
GalEAm	SPC/E	6	15	10.7 ± 1.9
GlcEAm	TIP3P	4	16	10.9 ± 1.9
GalEAm	TIP3P	6	16	10.9 ± 1.8

The number of hydrogen bonds quantified here is consistent with previous studies describing hydration patterns of monosaccharides through ab initio and MD simulations, where an average of 10 interHBs was calculated.[3, 17-18] No difference is observed between the two glycomonomers or water models.

3.3.1.5 Glycomonomer radial distribution functions

To understand more about the intermolecular interactions between the glycomonomers and surrounding water molecules, interatomic distances between the oxygens on the saccharide ring (O1-O6) and the oxygens on the surrounding water molecules were monitored through the course of a 10.0 ns simulation. Radial distribution functions (g(r)), also referred to as pair distribution functions or pair correlation

functions, were plotted to describe the density probability of finding a water oxygen at a given distance *r* from a saccharide oxygen reference point ($g(r)_{O\text{-}O}$) (Figure 3.5).

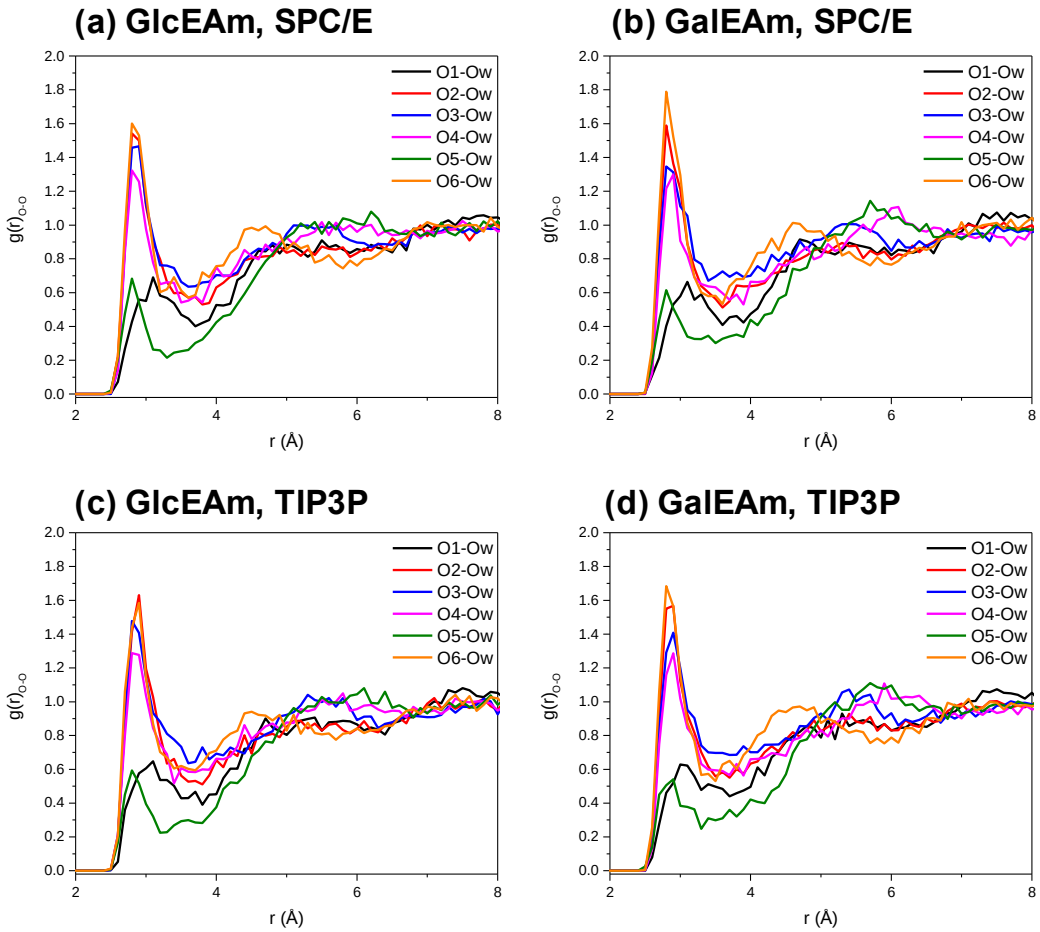

Figure 3.5 *Radial distribution functions of GlcEAm and GalEAm in (a,b) SPC/E and (c,d) TIP3P water.*

In these RDF plots, O1-Ow refers to the interatomic distance between O1 on the saccharide ring and oxygens on surrounding water molecules within 8 Å. In general, shorter ($g(r)_{O\text{-}O}$) distances indicate stronger charge transfer, which is related to hydrogen bond strength.[3] Analyses of RDFs between saccharide hydroxyl groups and water oxygens ($g(r)_{O\text{-}O}$) in monosaccharide and disaccharide solutions have shown that hydroxyl group stereochemistry can induce polarity changes in solution and affect solute

intermolecular interactions and hydration.[1, 19-20] In these RDFs for GlcEAm and GalEAm, hydrogen bonding in the first hydration shell is indicated by a sharp peaks at 2.8 – 3.1 Å, while the second and third hydration shells are broad and poorly defined at larger distances. The RDFs for GlcEAm and GalEAm in SPC/E water are similar. For both molecules, O1 exhibits a weak peak at 3.1 Å, attributed to the steric bulkiness of the surrounding saccharides that constrains the proximity of this oxygen to water molecules. The peaks corresponding to the ether linkages in the rings at O5 are also weak, but these have diminished propensity to hydrogen bond in comparison to O2, O3, O4, and O6, which all have strong peaks at 2.8 Å. Although these hydroxyl groups display similar peaks in the first hydration shell, there are some differences that correspond to the second hydration shells of O4. In GlcEAm, the second hydration shell is poorly defined, whereas GalEAm shows a well-defined maximum at 6.1 Å. Similar O4 second hydration shell behavior is observed in RDFs of the TIP3P water model, along with a more pronounced second hydration shell peak for O6 in GalEAm (4.7 Å). The data indicate that GalEAm undergoes stronger hydrogen bonding with water at O4 and O6 in comparison to GlcEAm, attributed to the differences in stereochemistry at O4. It is likely that intermolecular associations with other molecules will also be affected by the differences in stereochemistry.

3.3.1.6 Intramolecular hydrogen bonding in glycomonomers

The nature of intraHBs in saccharides is complex and substantial effort has been put forth to understand hydrogen bonding patterns in β,D-Glc and β,D-Gal systems.[1, 21-22] Similar to the previous experiments monitoring interHBs between glycomonomers and water, intramolecular hydrogen bonds (intraHBs) in the glycomonomers were monitored

using the same set of 10.0 ns trajectories for the glycomonomers in both SPC/E and TIP3P water (Figure 3.6).

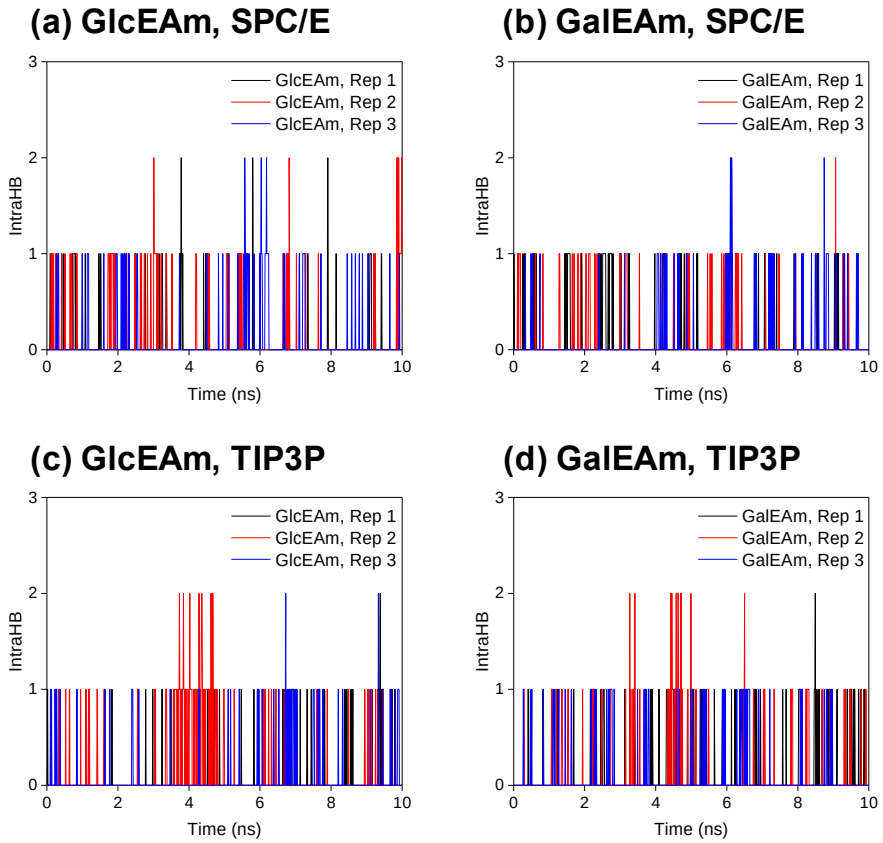

Figure 3.6 *Intramolecular hydrogen bonds in (a) GlcEAm and (b) GalEAm in SPC/E H_2O over the course of 10.0 ns.*

In these graphs, each point represents the number of intraHBs present within the glycomonomer structure at any given time throughout the simulations and does not account for any intermolecular hydrogen bonds. Here, up to two intraHBs are observed in each of the solvated glycomonomer systems, although analysis of the frequency of intraHBs in the monomeric systems shows that for most the simulation time, the glycomonomers do not undergo any intramolecular hydrogen bonding (graphically depicted as zero intraHBs) (Table 3.2).

Table 3.2 *Glycomonomer intramolecular hydrogen bond frequency*

Monomer	Water model	Range	Freq. of 0 IntraHBs	Freq. of 1 IntraHB	Freq. of 2 IntraHBs
GlcEAm	SPC/E	0-2	0.944	0.050	0.007
GalEAm	SPC/E	0-2	0.929	0.068	0.003
GlcEAm	TIP3P	0-2	0.929	0.068	0.003
GalEAm	TIP3P	0-2	0.907	0.091	0.002

These values were calculated by averaging the last 20 % of the trajectory data (frames 800-1000) from 3 replicate simulations starting from the same simulation box. For both water models, GalEAm is shown to undergo more frequent intramolecular hydrogen bonding interactions in comparison to GlcEAm. This demonstrates that although the number of intraHBs may be the same between the two monomers, the frequency at which the monomers experience intraHBs in aqueous solution are different because of OH4 stereochemistry. It could not be distinguished which water model better described glycomonomer dynamics and behavior in aqueous solution, so the subsequent experiments were conducted using a single water model (TIP3P).

3.3.2 Oligomer interactions in solution

3.3.2.1 Neutral and cationic oligomer structures and simulations

To understand whether pendant group stereochemistry affects intermolecular and intramolecular interactions of oligomers in solution, interHB and intraHB patterns of glucose- and galactose-functionalized oligomers ($PGlc_{10}$ and $PGal_{10}$) were investigated using the same methods used for the monomers. Hydrogen bonding patterns of a fully cationic tertiary amine functionalized oligomer poly(*N*-(3-(dimethylamino)propyl)acrylamide) ($PDMAPAm_{10}$) were also characterized as this was the structure chosen to provide cationic tertiary amines within synthetic cationic

glycopolymers. Two cationic oligomers with 30% cationic tertiary amine-functionalized comonomers were also constructed to represent the experimental cationic glycopolymers with 30% cationic monomers. These five oligomer structures are shown in Figure 3.7.

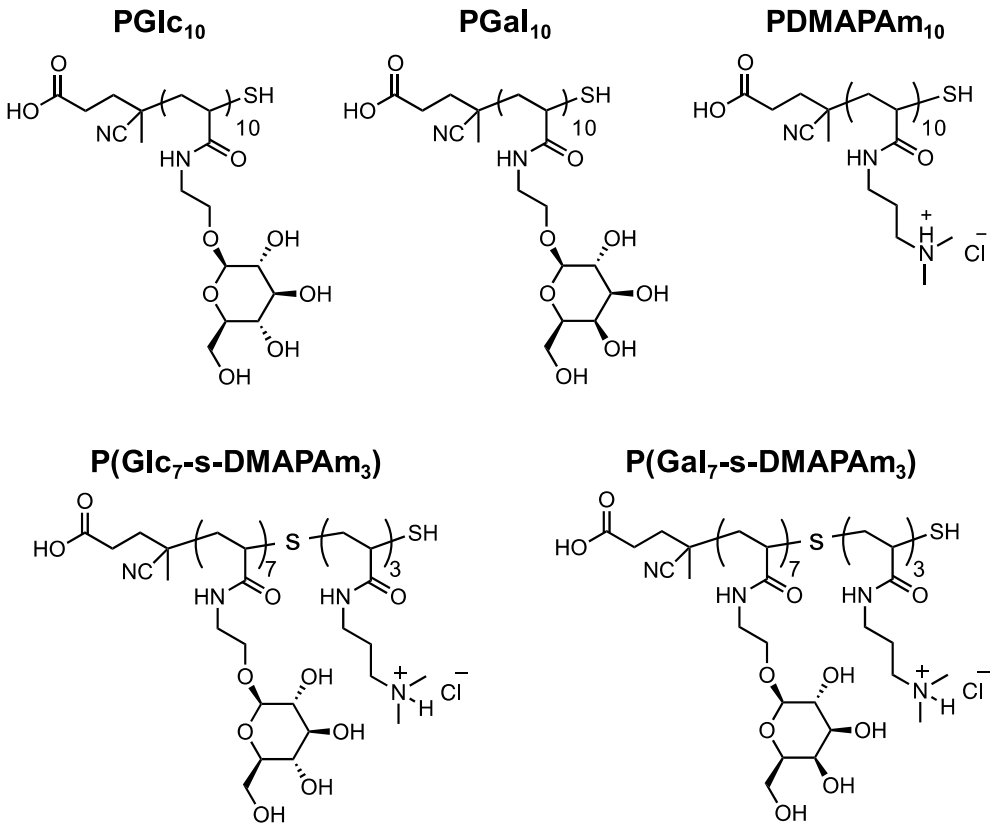

Figure 3.7 *Structures of neutral and cationic DP=10 oligomers with end groups derived from CEP.*

For each of these oligomers, a degree of polymerization of 10 was chosen to allow for hydrogen bonding behavior without the need to deconvolute effects related to chain entanglements. Initiator and terminator groups were chosen based on experimentally-derived polymer structures synthesized by RAFT polymerization utilizing 4-cyano-4-(ethylsulfanylthiocarbonyl)sulfanylpentanoic acid (CEP) as the chain transfer agent (CHAPTER II).

Oligomer simulations were run for longer time periods (20.0 ns) to account for additional time for the molecules to rearrange and reach the proper equilibrium states (i.e. convergence). Analysis of the root mean square deviation (RMSD) of oligomer coordinates (Figure 3.8) and radius of gyration (R_g) (Figure 3.9) of the oligomers as a function of time for three replicate trajectories indicates that the oligomer simulation boxes converge within 10.0 ns.[23-24]

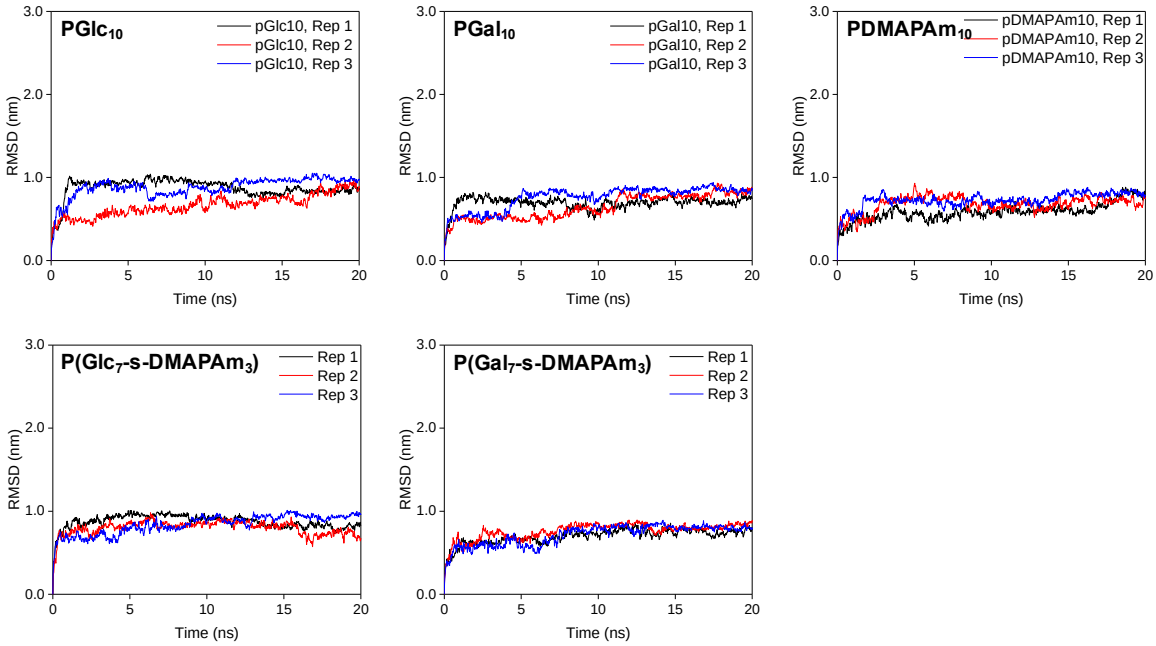

Figure 3.8 *Root mean square deviation (RMSD) of oligomers in TIP3P H_2O.*

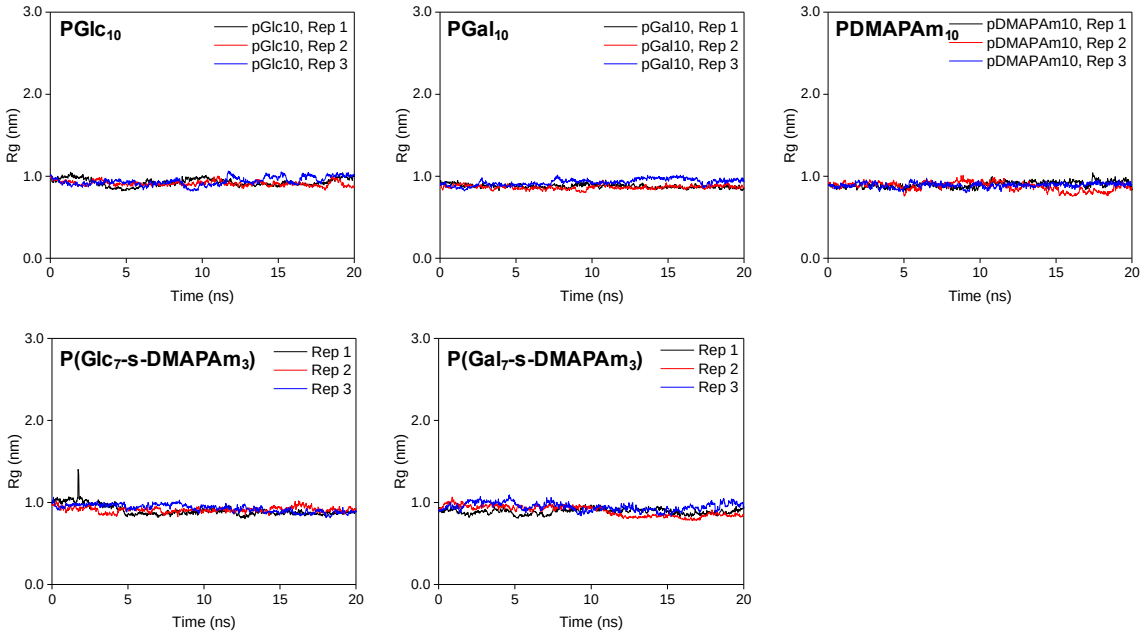

Figure 3.9 *Radius of gyration (R_g) of oligomers in TIP3P H_2O.*

3.3.2.2 Oligomer-water intermolecular hydrogen bonds

Average interHBs and intraHBs for the oligomers are displayed in Figure 3.10. $PGal_{10}$ has a higher average number of interHBs with surrounding water molecules in comparison to $PGlc_{10}$ (87.4 ± 6.4 for $PGal_{10}$ and 84.5 ± 5.9 for $PGlc_{10}$, $p < 0.0001$ based on 600 data points). Interestingly, $PGal_{10}$ shows a minimum and maximum of 65 and 109 intermolecular hydrogen bonding events with water, respectively. This range of $PGal_{10}$ interHBs (65-109) is wider than that of the $PGlc_{10}$ oligomer (69-102), demonstrating that the $PGal_{10}$ oligomer can undergo more intermolecular hydrogen bonding events with surrounding water molecules. This is likely a result of stronger hydrogen bond formation inferred from the GalEAm monomer RDFs in TIP3P water.

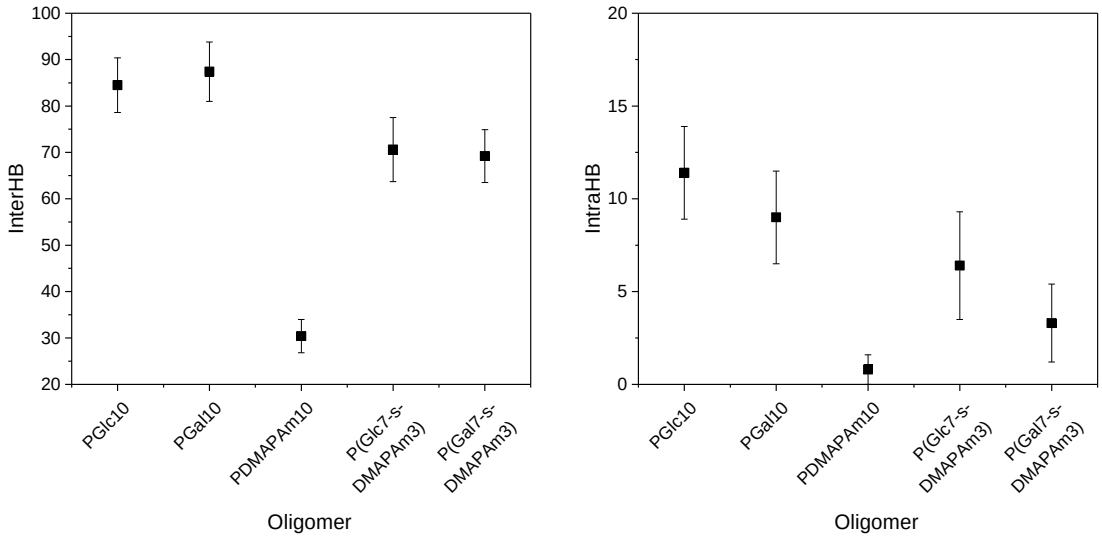

Figure 3.10 *Average number of (left) intermolecular and (right) intramolecular hydrogen bonds for neutral and cationic oligomers in TIP3P water. Error bars represent standard deviation.*

Fewer interHBs are observed in the cationic oligomer systems. The average number of interHBs calculated for $PDMAPAm_{10}$ (30.4 ± 3.6 interHBs) is less than half that of the neutral saccharide-functionalized oligomers, attributed to the lower number of heteroatoms capable of hydrogen bonding. The fully cationic oligomer also shows a reduced range of interHBs with water (19-41). The cationic glycooligomers display intermediate behavior, with $P(Glc_7\text{-s-}DMAPAm_3)$ showing slightly more interHBs than $P(Gal_7\text{-s-}DMAPAm_3)$ (70.6 ± 6.9 interHBs for $P(Glc_7\text{-s-}DMAPAm_3)$ and 69.2 ± 5.7 for $P(Gal_7\text{-s-}DMAPAm_3)$, $p < 0.0001$). Figure B.1 and Figure B.2 show the intermolecular and intramolecular hydrogen bonds over the course of each simulation and summarized data are presented in Table B.5.

It is important to note that for the cationic oligomers, hydrogen bonds are determined based on the distance between the oligomer heteroatoms and water

molecules, as well as the angle of interactions. Because of these criteria in defining a hydrogen bond, purely hydrogen bonding interactions and electrostatic interactions originating from the cationic charge on the pendant amines could not be differentiated, thus the interHBs calculated is recognized to be a combined number consisting of both electrostatic and hydrogen bonding intermolecular interactions.

3.3.2.3 Oligomer intramolecular hydrogen bonds

The number of intraHBs in the solvated oligomer systems was also monitored throughout the MD simulations (Figure 3.10), where $PGlc_{10}$ shows a higher average number of intraHBs than $PGal_{10}$ (11.4 ± 2.5 vs. 9.0 ± 2.5, $p < 0.0001$). This is consistent with the monomer simulation results, where GlcEAm shows more intramolecular hydrogen bonding behavior in comparison to GalEAm. Likewise, cationic saccharide-functionalized oligomers follow a similar trend. P(Glc_7-s-$DMAPAm_3$) displays more intraHBs than P(Gal_7-s-$DMAPAm_3$) (6.4 ± 2.9 for P(Glc_7-s-$DMAPAm_3$) and 3.3 ± 2.1 for P(Gal_7-s-$DMAPAm_3$), $p < 0.0001$). The number of intraHBs is substantially higher than that calculated for $PDMAPAm_{10}$, which on average has less than one intraHB. Summarized data are presented in Table B.5.

Many different types of intramolecular hydrogen bonding interactions are observed in the saccharide-functionalized neutral and cationic oligomers. Specifically, carbonyl acrylamide groups undergo hydrogen-bonding interactions with functional groups on surrounding pendant groups, including charged tertiary amine protons, saccharide hydroxyl groups, and the amines of acrylamide groups. Amine acrylamide groups also interact with hydroxyl groups on the pendant saccharides. In the four oligomers with saccharide pendant groups, intramolecular hydrogen bonds are observed

not only between hydroxyl groups on the same saccharide (akin to the interactions observed in the monomers), but also between hydroxyl groups of different saccharide pendant groups. The proton on the thiol chain ends can hydrogen bond with saccharide hydroxyl groups as well as the carbonyl on the terminal monomer unit. The oligomer $PDMAPAm_{10}$ has fewer intramolecular hydrogen bonds resulting from the electrostatic repulsions from charges on the pendant groups, although acrylamide NH groups on the polymer backbone can hydrogen bond with other acrylamide C=O groups within the chain (but not between adjacent monomer units). The carboxylic acid present in the initiator structure (the structure derived from V-501) could also hydrogen bond with acrylamides on the polymer backbone.

3.3.2.4 Oligomer-oligomer interchain interactions

To gain insight into how the oligomers interact with one another, three pre-equilibrated oligomer chains were placed in a simulation box with TIP3P water and MD simulations were run for 40.0 ns (Figure 3.11). In these simulations, all the oligomer chains interact with one another through intermolecular hydrogen bonds between pendant saccharides, with the exception of $PDMAPAm_{10}$.

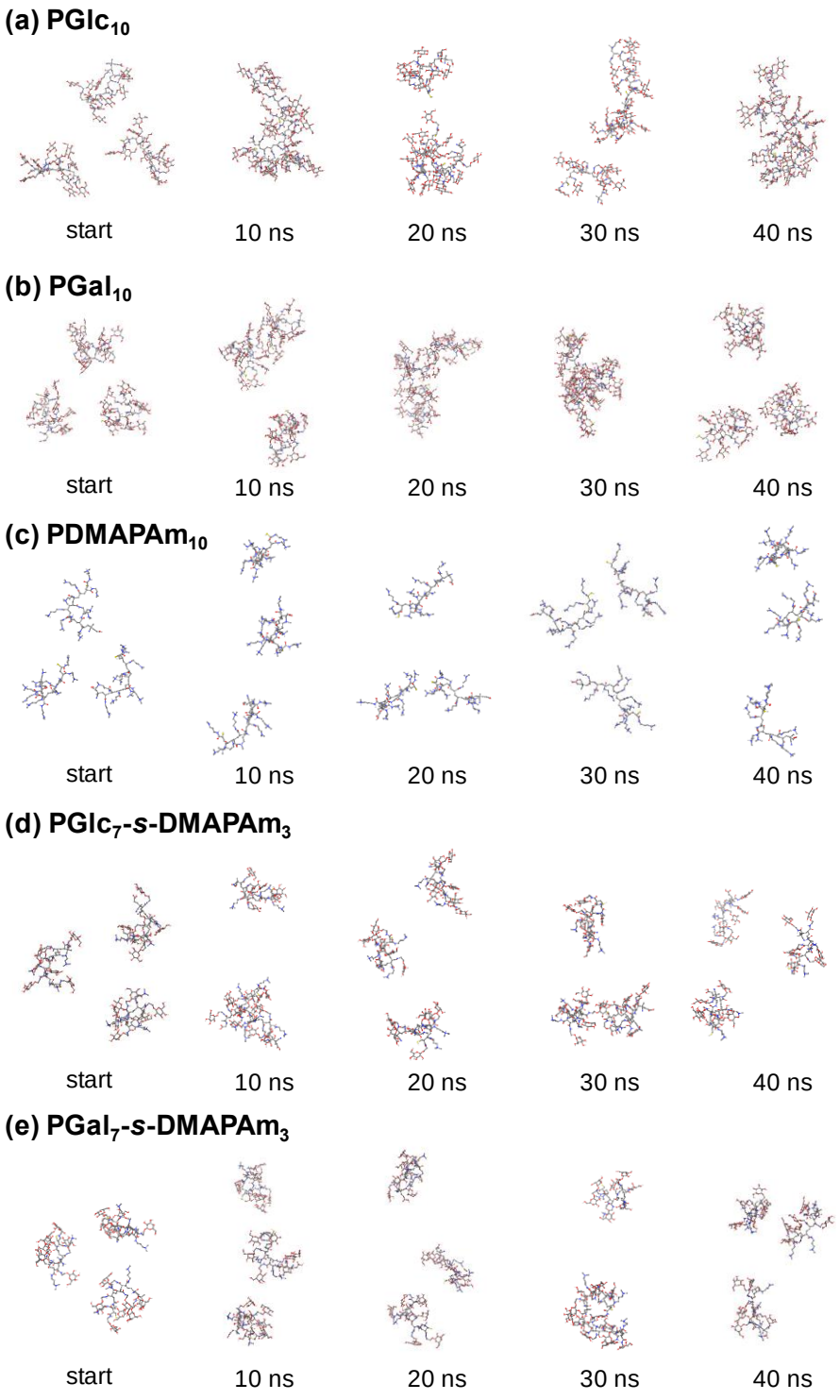

Figure 3.11 *Snapshots of MD trajectories of (a) $PGlc_{10}$, (b) $PGal_{10}$, (c) $PDMAPAm_{10}$, (d) $P(Glc_7$-s-$DMAPAm_3)$, and (e) $P(Gal_7$-s-$DMAPAm_3)$ oligomers at the starting frame (0 ns), 10 ns, 20 ns, 30 ns, and 40 ns in TIP3P H_2O. Water molecules, ions, and nonpolar hydrogens are omitted from the image for clarity.*

In these simulations, interchain interactions between oligomers are transient and no permanent associations are observed. This supports previous data suggesting glycopolymer aggregation results from extensive interchain interHBs between the highly hydrophilic pendant group saccharides.[25] Due to short oligomer lengths, chain entanglements were not considered to contribute towards any oligomer interchain interactions in these simulations. For each of the simulated co-oligomers, transient interchain saccharide interactions are observed despite electrostatic repulsion from the charged DMAPAm pendant groups, which extend towards the solvent to maximize favorable DMAPAm/water interactions.

The observed interchain interactions between cationic polymers was not unexpected; interchain interactions have also been observed in similar systems of hydrophobic/cationic methacrylate-based oligomers (DP = 10) in TIP3P water.[26] These results highlight the strength of the intermolecular interactions involving the hydrophilic saccharide pendant groups, which are able to associate even in the presence of electrostatic repulsions from cationic charge incorporation. InterHB and intraHB data are summarized in Table B.6. In the case of the fully cationic $PDMAPAm_{10}$ oligomers, each of the chains is fully extended and no interchain interactions are observed due to electrostatic repulsions from the charged amines. Mintis and coworkers investigated the conformational properties of fully ionized poly(dimethylaminoethylmethacrylate) oligomers (DP = 20) at various concentrations in salt-free solutions and observed similar results, where no interchain interactions were observed in TIP4P water (a 4-point water model similar to TIP3P).[27]

3.3.3 Simulations with dsRNA

To understand noncovalent interactions between oligomers and dsRNA, simulations of dsRNA were first conducted, followed by dsRNA/oligomer systems. First, simulations with only dsRNA in TIP3P water were conducted, where the duplex structure was relaxed and equilibrated. Here, the number of intermolecular hydrogen bonds between the separate dsRNA strands was monitored (Figure 3.12) to make sure the strands were properly duplexed. Assuming all bases were paired through hydrogen bonding, approximately 40 intraHBs between the two chains could be expected. In the simulations, an average of 37 interHBs is observed with a range of 32 to 39. Average interHBs between the duplex and water are 325.4 ± 8.3, with a range of 294 – 352 interHBs.

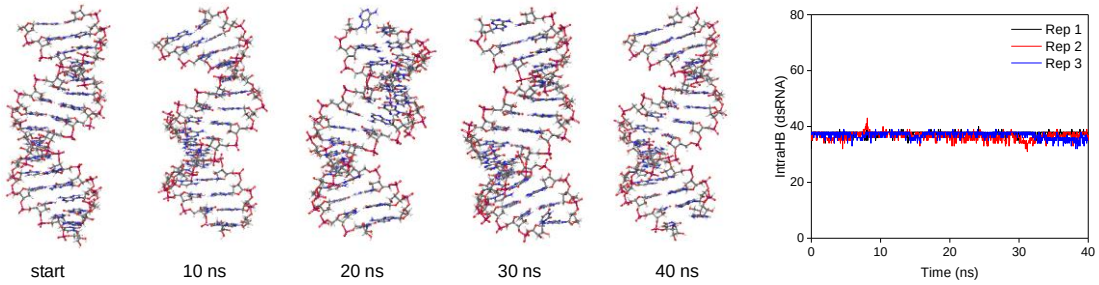

Figure 3.12 *Snapshots of MD trajectories of dsRNA (left) and the average number of interHBs between dsRNA strands from three replicate simulations (right).*

Visual inspection of the dsRNA strands in the trajectories shows that hydrogen bonds between the A=U terminal base pairs can break and allow the terminal nucleotides to extend into the surrounding solution. An example of this is shown in in Figure 3.12 at t = 40 ns. In subsequent frames, terminal bases in some cases display reformation of the hydrogen bonds, and in other cases rearrange to form a stacked motif resulting from π-

interactions (not shown). Base pair fraying between terminal nucleic acid base pairs is not unusual, and it has been observed in both experimental and computational experiments.[28]

3.3.4 Monomer/dsRNA interactions

To understand how each monomer interacted with dsRNA, simulations were conducted involving the monomers and dsRNA. To increase the likelihood of interactions between dsRNA and the monomers, three monomer molecules were placed in the simulation boxes instead of only one, and five replicate simulations were conducted instead of three for each type of monomer. Simulations of dsRNA with monomers did not adversely affect the number of hydrogen bonds between the dsRNA strands in TIP3P water (Figure B.3).

GlcEAm interacts with dsRNA through multiple hydrogen bonds, most frequently through saccharide hydroxyl groups (OH2, OH3, OH4, OH6), the acrylamide NH bond, and the saccharide ether (O5). These functional groups primarily hydrogen bond with the -P=O, -P-O^-, and ribose 2'-OH functionalities on the dsRNA sugar-phosphate backbone. Several examples of dsRNA/GlcEAm interactions are shown in Figure 3.13. Here, grey atoms are carbons, red atoms are oxygens, and blue atoms are nitrogens.

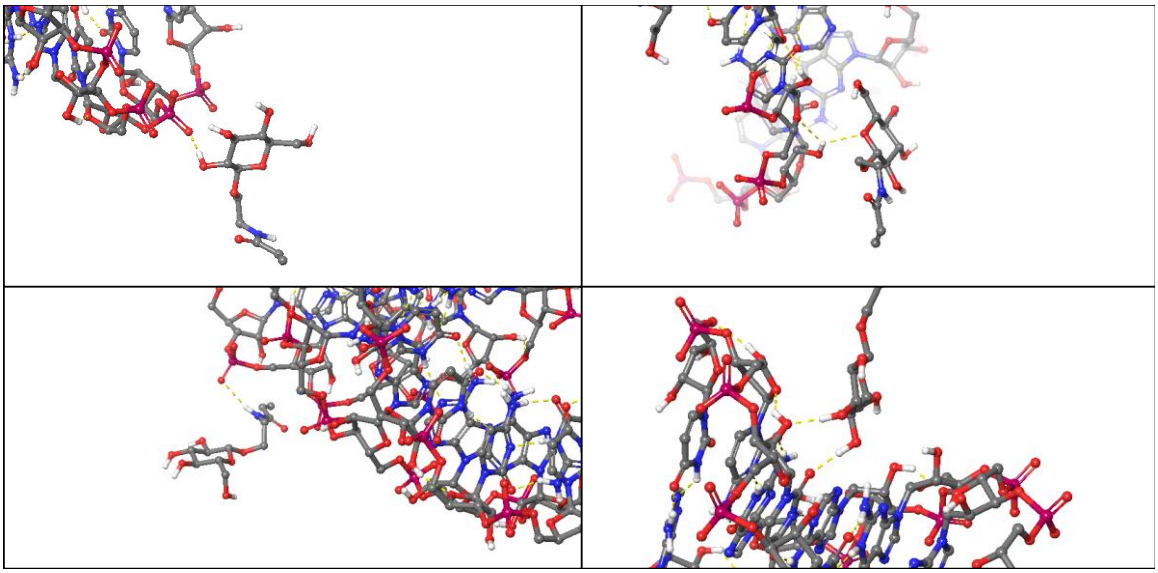

Figure 3.13 *Examples of hydrogen bonding interactions (yellow dashed line) between GlcEAm monomers and dsRNA. Water molecules, ions, and nonpolar hydrogens are omitted from the image for clarity.*

Additional noncovalent interactions also include H-bonding between the glycomonomers and the NH_2 functional groups on C, G, and A nucleotide bases, and at the dsRNA chain ends, where both conventional H-bonds and aromatic H-bonds are observed. Similar interactions are observed in GalEAm/dsRNA simulations (Figure 3.14). Monitoring of hydrogen bonding interactions between dsRNA and three cationic DMAPAm oligomers demonstrates a constant number of interHBs through the simulations. In addition to hydrogen bonding, salt bridges with the negatively charged dsRNA sugar-phosphate backbone are also observed (Figure 3.15).

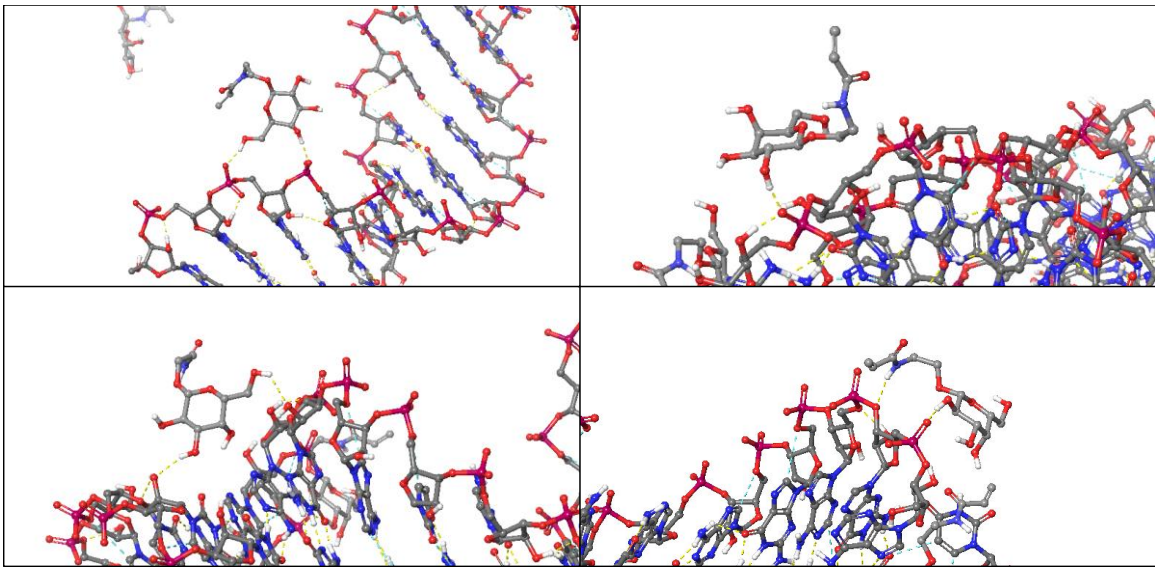

Figure 3.14 *Examples of hydrogen bonding interactions (yellow dashed line) between GlcEAm monomers and dsRNA. Water molecules, ions, and nonpolar hydrogens are omitted from the image for clarity.*

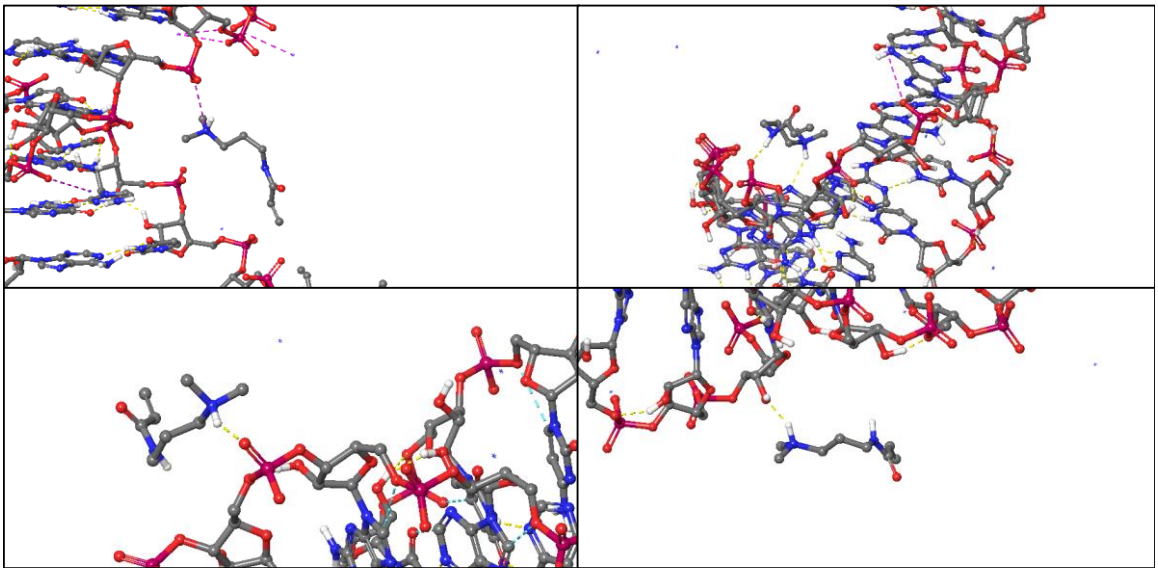

Figure 3.15 *Examples of hydrogen bonding (yellow) and electrostatic salt bridging (purple) interactions between DMAPAm monomers and dsRNA. Water molecules and nonpolar hydrogens are omitted from the image for clarity.*

The number of interHBs between the monomers and the dsRNA were also monitored for each simulation (Figure B.4), although because the number of interHBs between the glycomonomers and the dsRNA are not constant throughout the simulations, and it is difficult to characterize the individual interactions of each glycomonomer with dsRNA because monomer-water and monomer-monomer interactions are also prevalent. Thus, no difference in the average number of interHBs between GlcEAm and GalEAm are observed. Here, the three GlcEAm monomers exhibit the highest total number of interHBs with the dsRNA duplex (up to 10 interHBs), while the three GalEAm monomers and the three DMAPAm monomers both display up to 7 interHBs with dsRNA. Data are summarized in Table B.7.

3.3.5 Oligomer/dsRNA interactions.

Oligomers were simulated in the presence of a model dsRNA to determine interactions. Previously, many interchain interactions were observed in the simulations involving three saccharide-functionalized oligomers per simulation box, whether they were neutral or cationic, so simulations of oligomers with dsRNA were conducted with only one individual oligomer chain and dsRNA per box for simplicity. The total number of interHBs was monitored between the two species across five replicate experiments (Figure 3.16). Similar to the monomer/dsRNA simulations, the oligomers do not appear to influence the total number of hydrogen bonds between the dsRNA strands, which would have been indicative of a poor-quality simulation where hydrogen bonds between the strands would break (Figure B.5).

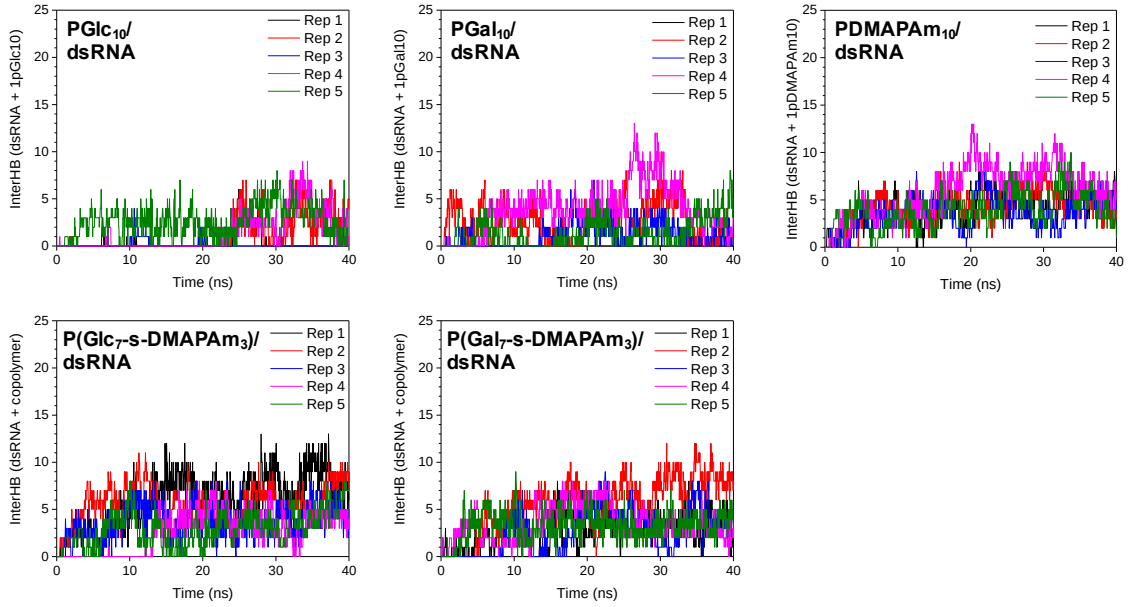

Figure 3.16 *Intermolecular hydrogen bonds in solvated dsRNA/oligomer simulations over the course of 40.0 ns in TIP3P water.*

The interactions between the oligomers and the dsRNA are dynamic, and there are several instances in which no interactions were observed at all due to reversible formation and breaking of hydrogen bonds and/or electrostatic interactions. Because of this, it is difficult to quantitatively discern differences in how the saccharides affect the interactions with dsRNA. In these simulations, $PGlc_{10}$ appears to interact more with dsRNA specifically during the last 20% of the simulations. However, because the interactions between the oligomers and the dsRNA are transient, measuring the average amount of interHBs between these two species is inherently unreliable. Alternatively, instead of calculating the number of interHBs between the oligomer and the dsRNA, the interHBs between dsRNA and water are quantified, where complexation of the oligomers with the dsRNA would result in fewer interHBs between dsRNA and water due to displacement. Here, the number of interHBs between dsRNA and water in the presence

of $PGlc_{10}$ (320.8 ± 8.1 interHBs) is less than that in the presence of $PGal_{10}$ (322.1 ± 8.7 interHBs) ($p = 0.0262$), which again suggests that the dsRNA undergoes more hydrogen bonding with $PGlc_{10}$ than with $PGal_{10}$. It is important again to note that this may not be representative of the entire simulation.

Unsurprisingly, $PDMAPAm_{10}$ interacted the most with dsRNA through interHBs and/or electrostatic interactions. Even though the oligomers were all initially placed 10 Å away from the dsRNA chain, $PDMAPAm_{10}$ is shown to quickly associate with the negatively charged dsRNA chain and settle into the major grooves of the dsRNA due to strong electrostatic interactions (not shown). Like hydrogen bonds, electrostatic interactions between polycations and nucleic acids have experimentally been shown to be transient such that the nucleic acids can undergo exchange with different polycation chains,[29] yet $PDMAPAm_{10}$ generally remains bound to the dsRNA after initial attachment. This is also observed for the two statistical cationic oligomers, where the electrostatic interactions between the cationic amines and the negatively charged phosphate backbone of the dsRNA began to appear soon after the simulations begin. This highlights the importance of cationic charges in the copolymer chains for complexation with nucleic acids. No significant difference was observed in the interactions of the two statistical oligomers P(Glc_7-s-$DMAPAm_3$) and P(Glc_7-s-$DMAPAm_3$) with dsRNA (summarized in Table B.8).

3.4 Conclusions

Molecular dynamics simulations were conducted with glycomonomers functionalized with either β,D-Glc or β,D-Gal pendant groups to understand the effect of saccharide stereochemistry on the related hydrogen bonding patterns in aqueous solution.

Although these two glycomonomers differ only in the saccharide stereochemistry at OH4, the subtle change in monomer structure was shown to impact the resulting monomer conformations, saccharide electrostatic potentials, the strength of intermolecular hydrogen bonds with surrounding water molecules, and the frequency at which hydrogen bonding events occur with surrounding water molecules. Here, because GalEAm exhibits an axial OH at C4, it results in stronger hydrogen bonds with surrounding molecules through both OH4 and OH6 in comparison to GlcEAm. This demonstrates that intermolecular hydrogen bonding interactions involving saccharide-functionalized monomers can be tuned by simply controlling monomer stereochemistry.

Neutral and cationic oligomers based on these acrylamide monomers with β,D-Gal and β,D-Glc pendant groups were then simulated in aqueous solution to model the intermolecular interactions of the cationic glycopolyelectrolytes synthesized in Chapter II for binding and transfection of dsRNA. In these MD simulations, it is shown that the glucose-functionalized oligomers are able to undergo more intramolecular hydrogen bonding events than the galactose-functionalized oligomers, while the galactose-functionalized oligomers are more likely to be involved in intermolecular hydrogen bonding with surrounding molecules. This suggests that intermolecular interactions involving glycopolymers can be tuned by changing pendant group saccharide structure. Interchain associations between neutral and cationic oligomer chains are observed in simulations conducted with multiple saccharide-functionalized oligomers which results from extensive hydrogen bonding between the hydrophilic pendant groups. This is consistent with experimentally observed cationic glycopolymer aggregation resulting from interchain interactions reported in Chapter II. Saccharide-functionalized monomers

and oligomers simulated in the presence of a model dsRNA are shown to undergo multiple types of transient hydrogen bonding interactions with not only the sugar-phosphate backbone of dsRNA, but also with the nucleic acid base pairs. Each of the cationic oligomers are shown to quickly bind to RNA through a combination of electrostatic and hydrogen bonding interactions, demonstrating the importance of cationic charge on the glycopolymers for copolymer/dsRNA binding. Although differences in intermolecular hydrogen bonding behavior are observed in simulations with the monomers with water, it was not possible to distinguish differences in RNA binding for the cationic glyco-oligomers under these simulation conditions. The simulations show the importance of saccharide structure and copolymer composition in intermolecular and intramolecular hydrogen bonding interactions in aqueous solution and provide greater understanding of design requirements for creating glycopolymer-based non-viral gene delivery vehicles.

3.5 References

1. Dashnau, J. L.; Sharp, K. A.; Vanderkooi, J. M., Carbohydrate Intramolecular Hydrogen Bonding Cooperativity and Its Effect on Water Structure. *The Journal of Physical Chemistry B* **2005,** *109* (50), 24152-24159.

2. Deshmukh, M. M.; Bartolotti, L. J.; Gadre, S. R., Intramolecular Hydrogen Bonding and Cooperative Interactions in Carbohydrates via the Molecular Tailoring Approach. *Journal of Physical Chemistry A* **2008,** *112* (2), 312-321.

3. Suzuki, T., The hydration of glucose: the local configurations in sugar-water hydrogen bonds. *Physical Chemistry Chemical Physics* **2008,** *10* (1), 96-105.

4. Madeira do O, J.; Foralosso, R.; Yilmaz, G.; Mastrotto, F.; King, P. J. S.; Xerri, R. M.; He, Y.; van der Walle, C. F.; Fernandez-Trillo, F.; Laughton, C. A.; Styliari, I.; Stolnik, S.; Mantovani, G., Poly(triazolyl methacrylate) glycopolymers as potential targeted unimolecular nanocarriers. *Nanoscale* **2019,** *11* (44), 21155-21166.

5. Vuković, L.; Koh, H. R.; Myong, S.; Schulten, K., Substrate recognition and specificity of double-stranded RNA binding proteins. *Biochemistry* **2014,** *53*, 3457-3466.

6. Ryter, J. M.; Schultz, S. C., Molecular basis of double-stranded RNA-protein interactions: structure of a dsRNA-binding domain complexed with dsRNA. *EMBO J* **1998,** *17* (24), 7505-7513.

7. Berendsen, H. J. C.; Grigera, J. R.; Straatsma, T. P., The missing term in effective pair potentials. *Journal of Physical Chemistry* **1987,** *91* (24), 6269-71.

8. Jorgensen, W. L.; Chandrasekhar, J.; Madura, J. D.; Impey, R. W.; Klein, M. L., Comparison of simple potential functions for simulating liquid water. *Journal of Chemical Physics* **1983,** *79* (2), 926-35.

9. Agirre, J., Strategies for carbohydrate model building, refinement and validation. *Acta Crystallographica Section D, Structural Biology* **2017,** *73* (2), 171-186.

10. Weis, W. I.; Drickamer, K., Structural basis of lectin-carbohydrate recognition. *Annual Review of Biochemistry* **1996,** *65*, 441-473.

11. Gabius, H.-J.; Andre, S.; Jimenez-Barbero, J.; Romero, A.; Solis, D., From lectin structure to functional glycomics: principles of the sugar code. *Trends in Biochemical Sciences* **2011,** *36* (6), 298-313.

12. Lemieux, R. U., How Water Provides the Impetus for Molecular Recognition in Aqueous Solution. *Accounts of Chemical Research* **1996,** *29* (8), 373-380.

13. Horowitz, S.; Trievel, R. C., Carbon-Oxygen Hydrogen Bonding in Biological Structure and Function. *Journal of Biological Chemistry* **2012,** *287* (50), 41576-41582.

14. Hudson, K. L.; Bartlett, G. J.; Diehl, R. C.; Agirre, J.; Gallagher, T.; Kiessling, L. L.; Woolfson, D. N., Carbohydrate–Aromatic Interactions in Proteins. *Journal of the American Chemical Society* **2015,** *137* (48), 15152-15160.

15. Dougherty, D. A., The Cation-π Interaction. *Accounts of Chemical Research* **2013,** *46* (4), 885-893.

16. Shibata, M.; Zielinski, T. J., Computer graphics presentations and analysis of hydrogen bonds from molecular dynamics simulation. *Journal of Molecular Graphics* **1992,** *10* (2), 88-95.

17. Leroux, B.; Bizot, H.; Brady, J. W.; Tran, V., Water structuring around complex solutes: theoretical modeling of α-D-glucopyranose. *Chemical Physics* **1997,** *216* (3), 349-363.

18. Molteni, C.; Parrinello, M., Glucose in Aqueous Solution by First Principles Molecular Dynamics. *Journal of the American Chemical Society* **1998,** *120* (9), 2168-2171.

19. Pagnotta, S. E.; McLain, S. E.; Soper, A. K.; Bruni, F.; Ricci, M. A., Water and Trehalose: How Much Do They Interact with Each Other? *Journal of Physical Chemistry B* **2010,** *114* (14), 4904-4908.

20. Imberti, S.; McLain, S. E.; Rhys, N. H.; Bruni, F.; Ricci, M. A., Role of Water in Sucrose, Lactose, and Sucralose Taste: The Sweeter, The Wetter? *ACS Omega* **2019,** *4* (27), 22392-22398.

21. Lonardi, A.; Oborský, P.; Hünenberger, P. H., Solvent-Modulated Influence of Intramolecular Hydrogen-Bonding on the Conformational Properties of the Hydroxymethyl Group in Glucose and Galactose: A Molecular Dynamics Simulation Study. *Helvetica Chimica Acta* **2017,** *100* (1), e1600158.

22. Lomas, J. S., Intramolecular O-H···O and C-H···O hydrogen bond cooperativity in D-glucopyranose and D-galactopyranose-A DFT/GIAO, QTAIM/IQA, and NCI approach. *Magnetic Resonance in Chemistry* **2018,** *56* (8), 748-766.

23. Knapp, B.; Frantal, S.; Cibena, M.; Schreiner, W.; Bauer, P., Is an intuitive convergence definition of molecular dynamics simulations solely based on the root mean square deviation possible? *Journal of Computational Biology* **2011,** *18* (8), 997-1005.

24. Mura, C.; McAnany, C. E., An introduction to biomolecular simulations and docking. *Molecular Simulation* **2014,** *40* (10-11), 732-764.

25. Bristol, A. N.; Saha, J.; George, H. E.; Das, P. K.; Kemp, L. K.; Jarrett, W. L.; Rangachari, V.; Morgan, S. E., Effects of Stereochemistry and Hydrogen Bonding on Glycopolymer – Amyloid-β Interactions. *Biomacromolecules* **2020**.

26. Zidar, J.; Lim, G. S.; Cheong, D. W.; Klähn, M., Protein-Like Dynamics of Polycarbonate Polymers in Water. *The Journal of Physical Chemistry B* **2015,** *119* (1), 316-329.

27. Mintis, D. G.; Dompé, M.; Kamperman, M.; Mavrantzas, V. G., Effect of Polymer Concentration on the Structure and Dynamics of Short Poly(N,N-dimethylaminoethyl methacrylate) in Aqueous Solution: A Combined Experimental and Molecular Dynamics Study. *The Journal of Physical Chemistry B* **2020,** *124* (1), 240-252.

28. Zgarbová, M.; Otyepka, M.; Šponer, J.; Lankaš, F.; Jurečka, P., Base Pair Fraying in Molecular Dynamics Simulations of DNA and RNA. *Journal of Chemical Theory and Computation* **2014,** *10* (8), 3177-3189.

29. Pigeon, L.; Gonçalves, C.; Pichon, C.; Midoux, P., Evidence for plasmid DNA exchange after polyplex mixing. *Soft Matter* **2016,** *12* (33), 7012-7019.

CHAPTER IV - NANOECHANICS OF STIMULI-RESPONSIVE POLY(METHACRYLIC ACID) MULTILAYER HYDROGELS PROBED BY AFM

4.1 Introduction

Hydrogels provide an effective platform for non-viral gene delivery due to their tunable biocompatibility and tissue-like viscoelastic characteristics.[1] A variety of crosslinked hydrogel systems prepared by free radical polymerization have been used to load and deliver siRNA and pDNA,[2-7] but a major drawback to using bulk hydrogels is uncontrolled swelling and rapid polynucleotide release. In contrast, incorporation of polynucleotides into multilayered polyelectrolyte systems prepared by layer-by-layer (LbL) assembly has been shown to facilitate controlled release of siRNA with high silencing efficiency in a range of mammalian cell lines.[8-10] Nanostructured films and microcapsules have also enabled enhanced delivery of proteins[11-13] and a variety of medicinal drugs.[14-18]

Due to their tunable responses to environmental stimuli including pH and temperature, multilayered materials have shown great promise for other biomedical applications, including tissue engineering, sensing, and antibacterial surfaces.[19-26] Post-assembly crosslinking of multilayer films allows for formation of covalently crosslinked hydrogel networks, enabling further control over material properties such as crosslink density, network architecture, film thickness, and swelling, thus providing more tunable drug delivery platforms.[27] Covalent multilayers based on weak polyacids are ideal for a variety of biomedical applications, where controlled pH-triggered swelling is achievable

through reversible protonation/deprotonation processes at physiologically relevant pH values (Figure 4.1).

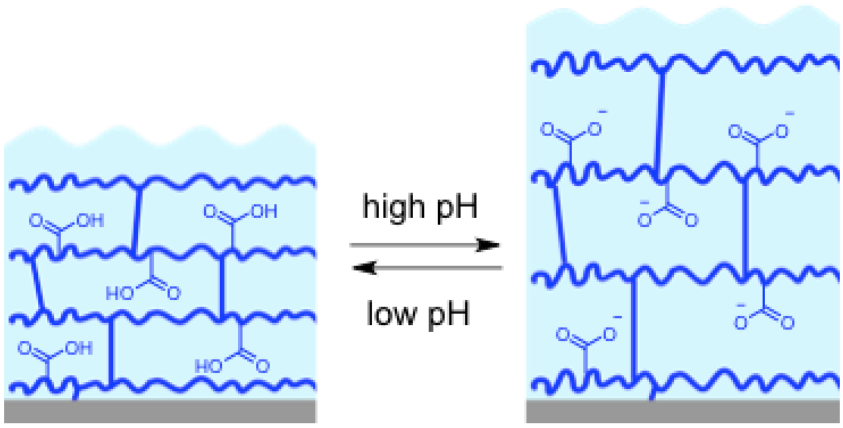

Figure 4.1 *pH-responsive swelling in crosslinked LbL-derived hydrogel films.*

Kharlampieva and coworkers have shown that the swelling response of LbL-derived hydrogels is also highly dependent on the materials' internal organization. This can be precisely controlled through LbL assembly conditions, where the simplest parameters to change include the assembly method (spin-assisted LbL or dipped LbL) and the molecular weight of the polymers used pH-responsive LbL-derived multilayer hydrogels have been prepared by first alternating the deposition of polymethacrylic acid (PMAA) and poly(N-vinyl pyrrolidone) (PVPON), followed by post-assembly crosslinking of the PMAA layers and removal of the PVPON sacrificial template layers, where neutron reflectometry experiments showed that the hydrogels assembled using a spin-assisted (SA) approach exhibited a highly stratified internal organization in contrast to the hydrogels formed via dipped LbL assembly.[28-29] As a result, the SA hydrogels underwent a 10-fold increase in swelling when changing from pH 5.0 to 7.5, whereas less-organized dipped PMAA hydrogels displayed only a 2-fold increase in swelling. In

traditionally (randomly) crosslinked hydrogel networks, increased swelling is typically accomplished by decreasing crosslink density, and is accompanied by a decrease in network modulus. However, there has been little investigation into how LbL-derived hydrogel modulus is affected by changes in assembly conditions, as well as how hydrogel surface/morphology and modulus vary in response to changes in pH. Kolewe and coworkers demonstrated that hydrogel surface modulus can play a significant role in biological processes, including how cells interact with the hydrogel surfaces.[30-31] Mechanical properties of thin films and microparticles are commonly investigated using buckling[32-34] and osmotic swelling[35-36] techniques, yet nanoindentation testing via atomic force microscopy (AFM) is an especially useful non-destructive technique which provides insight into both surface morphology and modulus under a variety of environmental (ambient or hydrated) conditions.[20, 26, 30, 37-40]

In this study, the roles of LbL assembly conditions and PVPON sacrificial layer molecular weight on the pH-responsive modulus changes of LbL-derived PMAA hydrogel films were investigated through AFM nanoindentation experiments under both ambient and hydrated conditions. Understanding the interrelationships between network architecture and surface modulus of pH-responsive multilayer hydrogels is critical to enable the design of better stimuli-responsive polyelectrolyte-based multilayer drug delivery platforms. Parts of this chapter have been published in collaboration with the Kharlampieva Research Group at the University of Alabama at Birmingham in the journal *ACS Applied Polymer Materials*.[41]

4.2 Experimental

4.2.1 Materials

Poly(methacrylic acid) (PMAA, average M_w 100 kDa) and poly(N-vinyl pyrrolidone) (PVPON, average M_w 58 kDa and average M_w 360 kDa) were obtained from Sigma-Aldrich. 3-(3-Dimethylaminopropyl)-1-ethylcarbodiimide hydrochloride (99%+, EDC) was received from Chem-Impex International. Poly(glycidyl methacrylate) (PGMA) was synthesized from glycidyl methacrylate by radical polymerization using AIBN in 2-butanone as described previously.[42] Silicon wafers (two-inches in diameter with one polished side) were purchased from the Institute of Electronic Materials Technology (EL-Cat Inc.). All other materials were purchased from Fisher Scientific and used without further purification.

4.2.2 Preparation of hydrogels

Multilayer films were prepared by the Kharlampieva Research Group at the University of Alabama at Birmingham. Silicon wafer substrates were cut into 2 cm x 5 cm dimensions and cleaned by immersing in piranha solution (1:3 v:v H_2SO_4:H_2O_2) for 1 hour. The substrates were then rinsed with DI H_2O and dried under a stream of N_2. A solution of poly(glycidyl methacrylate) (PGMA) (0.1 mg mL^{-1} in chloroform) was spin-cast onto the substrates and the wafers were heated at 110 °C for 1 hour to prime the substrates with a PGMA monolayer with 2 nm dry thickness.[23] Unattached PGMA was removed by rinsing with chloroform. A PMAA layer was then adsorbed onto the PGMA-primed wafers from a 1 mg mL^{-1} solution in methanol and crosslinked at 100°C for 40 minutes followed by rinsing with DI H_2O.

Aqueous polymer solutions (1 mg mL^{-1}) were deposited by either a SA LbL technique using a Laurell Technologies spin-coater (3000 rpm) or by dipping LbL. For SA hydrogen-bonded films, $(PMAA/PVPON)_n$ LbL multilayers were deposited on the precursor-coated wafers as described in previous publications.[28, 43] Briefly, 3 mL aliquots of PMAA or PVPON solutions in 0.01 M phosphate buffer at pH 2.5 were sequentially dropped onto clean silicon substrates, rotated on a spin-coater (30 seconds; 3000 rpm), and rinsed twice with the buffer solution before the deposition of the next layer. For dipped hydrogen bonded films, $(PMAA/PVPON)_n$ multilayers were constructed as described earlier.[29, 44] Briefly, the PGMA-primed wafers were exposed to alternating polymer solutions (0.5 mg mL^{-1} in 0.01 M phosphate buffer, pH 2.5) with two rinsing steps between polymer layering. Adsorption was allowed to occur for 5 minutes per layer.

To produce the crosslinked hydrogels, PMAA layers within the hydrogen bonded multilayers were chemically crosslinked as described previously.[29] Films were exposed to an EDC solution (5 mg mL^{-1}, 0.01 M phosphate buffer, pH 5.0) for 40 minutes, followed by crosslinking with ethylenediamine (EDA) (5 mg mL^{-1}, 0.01 M phosphate buffer, pH 5.8) for 12 and 24 hours for dipped and SA films, respectively. The crosslinked PMAA hydrogel films were submerged in buffer solutions (0.01 M phosphate buffer, pH 8.0) for 24 hours, followed by de-swelling for 15 min in 0.01 M phosphate buffer at pH 5, and drying at ambient conditions. Samples were stored in a desiccator until AFM imaging.

4.2.3 Atomic force microscopy

AFM analysis was conducted using a Dimension Icon atomic force microscope (Bruker) in PeakForce^{TM} Quantitative NanoMechanics mode (QNM) to observe structural

and mechanical properties of the surface-attached multilayer films. AFM scanning was performed using NanoScope v8.15 software and image analysis was completed in NanoScope Analysis v1.50 software. Images sizes of 10 μm x 10 μm (1.0 Hz scan rate), 5 μm x 5 μm (1.0 Hz scan rate), and 1 μm x 1 μm (0.5 Hz scan rate) were acquired for each sample to ensure measurements were representative of the entire sample. All images were acquired with 512 x 512 data point resolution. Three images were acquired for each multilayer sample near the middle of the silicon wafer. In the height image z-scales, the lowest number on the z-scale bar is zero (represented in black), whereas the white color represents the highest areas on the surface.

QNM of the dried samples was performed using an RTESP probe (nom. resonance frequency of 300 kHz; nom. spring constant of 40 N/m, nom. tip radius of 20 nm) in a standard probe holder under ambient conditions. The deflection sensitivity of the probe was determined by averaging three measurements against a sapphire standard (Veeco). The drive 3 amplitude sensitivity (DDS3) was adjusted such that the linear regression of the deflection sensitivity had a slope of approximately 1.00. The sync distance was determined using the same sapphire standard and the sync distance of each subsequent sample was set to that of the sapphire standard. The tip radius was calibrated using a polystyrene (PS) standard (2.70 GPa, Veeco). The peak force setpoint (75-150 nN) was adjusted such that the indentation depth of the tip into the PS surface was 5-10 nm as indicated by force-deflection curves. Peak force amplitude and peak force frequency was kept constant at 150 nm and 2 Hz, respectively.

QNM of hydrated samples was performed in freshly prepared aqueous buffers (0.1 M acetate buffer, pH 5.0 or 0.1 M phosphate buffer, pH 6.5) using an SNL-C probe (nom.

frequency of 23 kHz; nom. spring constant of 0.12 N/m; nom. tip radius 2 nm) in a fluid probe holder (DTFML-DD-HE-V2, Bruker). The cantilever was calibrated using both sapphire and polydimethylsiloxane (PDMS) standards (PDMS-SOFT-2-12M, 3.50 MPa, Bruker) prior to image acquisition. The Poisson's ratio (v) for both standards and multilayer samples was assumed to be 0.3.[33, 45] Peak force setpoint (500-750 pN) was adjusted such that the indentation depth of the tip into the PDMS surface was 5-10 nm. Peak force amplitude and peak force frequency was kept constant at 40 nm and 1 Hz, respectively. Buffer pH was measured before each experiment with a calibrated pH meter and pH was adjusted if needed. All buffers were filtered through a 0.45 μm syringe filter before imaging.

4.2.4 AFM image analysis

For AFM height image analysis, surface nanoarchitecture is described by the root mean square surface roughness parameter (R_q). Roughness was determined for individual 1 μm x 1 μm images according to Equation 4.1, where z_i is height and N is the number of data points (512 x 512 data point resolution).

$$R_q = \sqrt{\frac{\sum z_i^2}{N}} \qquad \text{Equation 4.1}$$

The average roughness ($R_{q,avg}$) for a given sample was determined by taking the statistical mean ± standard deviation of three R_q values from three different images of the same size.

Each individual DMT modulus image is the composite of 512 x 512 force displacement curves from indentation on the sample surface. Force-displacement curves were analyzed using the Derjaguin-Müller-Toporov (DMT) model for determining

reduced Young's modulus (referred to as DMT modulus) using Equation 4.2, where F_L is the load force, E^* is the reduced Young's modulus ($E^* = E/(1-\nu^2)$), ν is the Poisson's ratio, R^* is the reduced radius ($1/R = 1/R_{indentor} + 1/R_{surface}$), i is the indentation depth, and $F_{pull\text{-}off}$ is the pull-off force.[46]

$$F_L(i) = \frac{4}{3}E^*\sqrt{R^*}i^{3/2} + F_{pull-off} \qquad \text{Equation 4.2}$$

Average modulus values reported below are represented as the statistical mean ± standard deviation from three separate DMT modulus images of the same size and data point resolution. Supplemental data for 5 μm x 5 μm and 10 μm x 10 μm height and modulus images is provided in APPENDIX C.

A two-sample t-test was used to analyze significant differences for sets of data with a 95% confidence interval, where ($p < 0.05$) was statistically significant. All statistics (p values) were calculated using Minitab 17 software.

4.3 Results and discussion

Multilayer PMAA/PVPON hydrogel networks were prepared through either SA or dipped LbL assembly (Figure 4.2). First, PMAA and PVPON polymers were deposited onto the substrate to form hydrogen-bonded (HB) multilayer films, where alternating layers were held together through hydrogen-bonding interactions primarily between the PMAA carboxylic acid and PVPON amide functionalities. Then, PMAA chains were covalently crosslinked by reacting pendant carboxylic acids with EDA using aqueous carbodiimide crosslinker chemistry (EDC coupling). Finally, the sacrificial PVPON template was removed by swelling the crosslinked films in buffer to yield covalently crosslinked multilayer hydrogel networks.

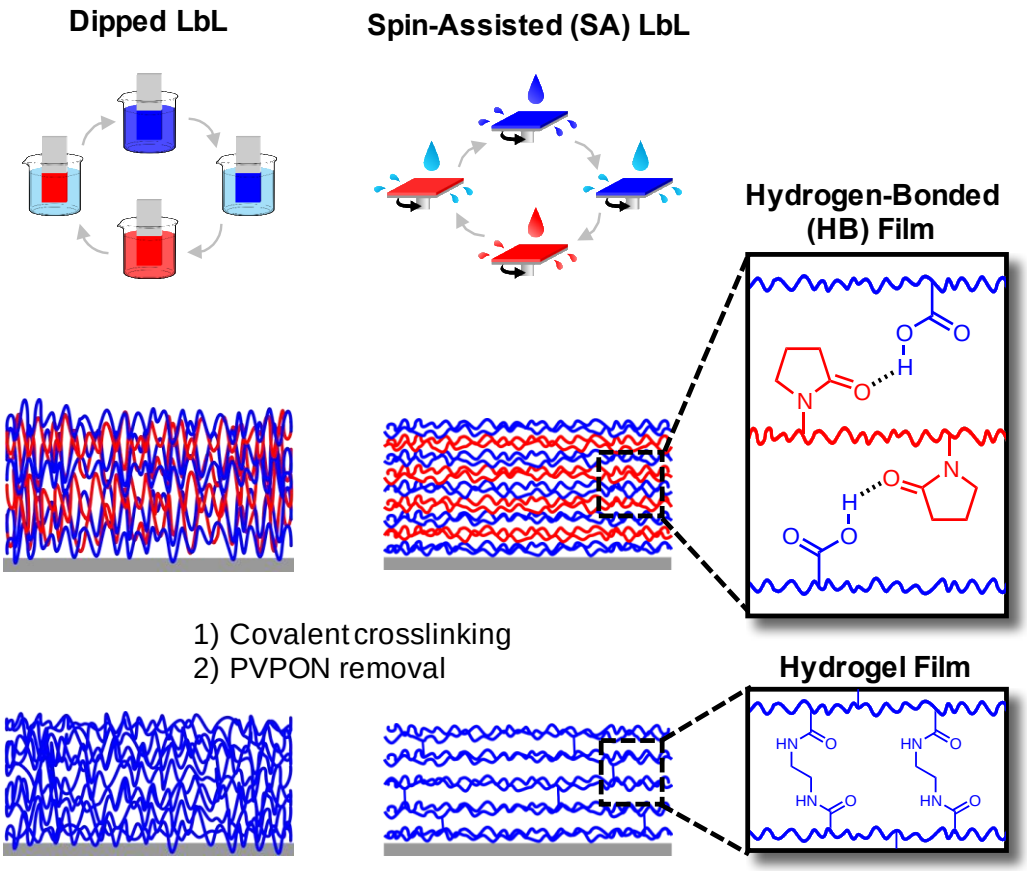

Figure 4.2 *Preparation of spin-assisted (SA) and dipped PMAA hydrogels from hydrogen-bonded (HB) template films and EDC coupling.*

4.3.2 Effect of PVPON molecular weight on hydrogen-bonded film properties

Kozlovskaya and coworkers previously demonstrated that multilayer film thickness, morphology, and architecture of HB films constructed by LbL can be tailored by modulating the PVPON M_w during the film assembly process.[28] Lisunova and coworkers showed that PVPON M_w influenced both the thickness and elasticity of HB tannic acid/PVPON multilayer shells, where higher PVPON M_w resulted in increased shell modulus.[39] Therefore, it was of interest to determine whether the PVPON M_w influenced the modulus of HB PMAA/PVPON multilayer film templates prior to crosslinked network formation. Two SA multilayer films were prepared by alternating

deposition of PMAA (100 kDa) and PVPON (either 58 kDa or 360 kDa) on Si wafers for a total of 35 bilayers. The thickness of the two resulting hydrogen-bonded films (denoted SA HB PVPON58 and SA HB PVPON360) was determined by ellipsometry to be 76.6 nm and 90.8 nm.

In AFM height images, features that are higher or lower on the surface are represented by the lighter and darker colors, respectively. Similarly, for DMT modulus images, features that have higher or lower modulus are represented by lighter and dark colors, respectively. AFM characterization of the SA HB films shows that the two HB films exhibit similar morphologies and moduli (Figure 4.3).

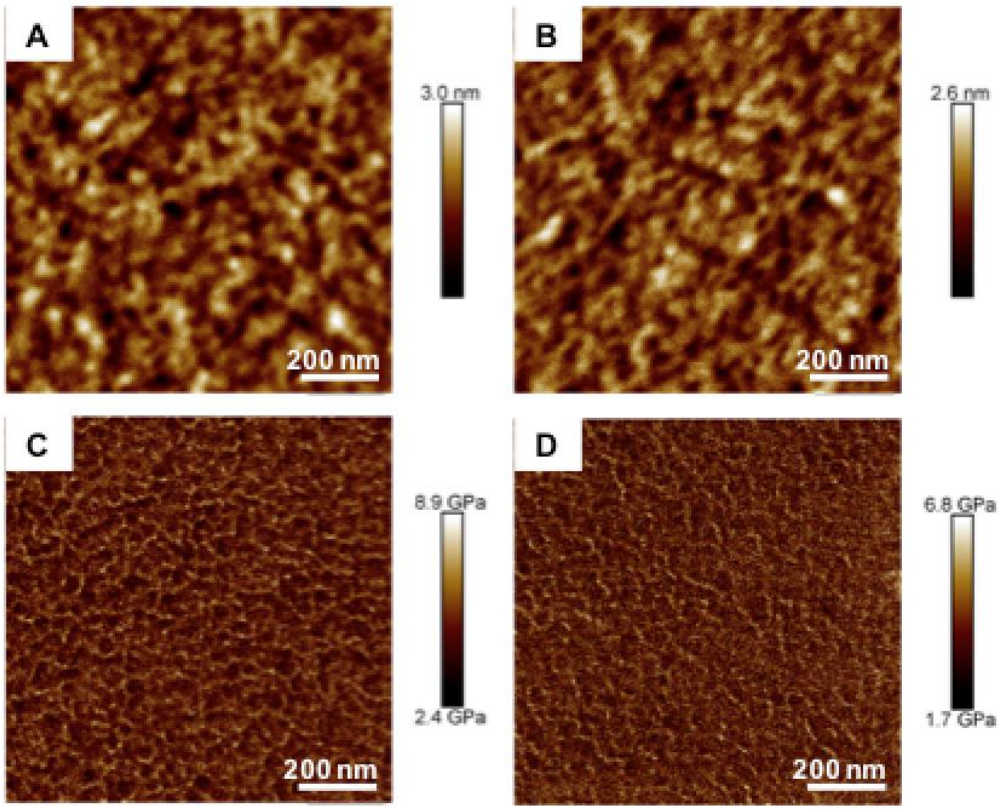

Figure 4.3 *(A) HB PVPON58 height image, (B) HB PVPON360 height image, (C) HB PVPON58 DMT modulus image, and (D) HB PVPON360 DMT modulus image. All images are 1 µm x 1 µm.*

AFM height images show that the surfaces of HB PVPON58 and HB PVPON360 both have low surface roughness ($R_{q,avg}$ = 0.43 ± 0.06 nm and 0.40 ± 0.02 nm, respectively) and lack distinguishing features, which is typical of spin-coated films. DMT modulus images (Figure 4.3C,D) for both multilayer films are also similar. SA HB PVPON58 has an average modulus of 4.58 ± 0.41 GPa and SA HB PVPON360 has an average modulus of 4.16 ± 0.39 GPa. The difference in modulus between the two samples is not statistically significant, and the modulus range is similar to that obtained for other polyelectrolyte-based multilayer films by Nolte and coworkers (ranging between 2-10 GPa).[33] These results indicate that there is no discernable effect of PVPON molecular weight on the modulus of HB multilayer films under ambient conditions.

4.3.3 Effect of crosslinking on SA film properties

The height and DMT modulus images of crosslinked films show several key differences in comparison to the non-crosslinked HB films (Figure 4.4).

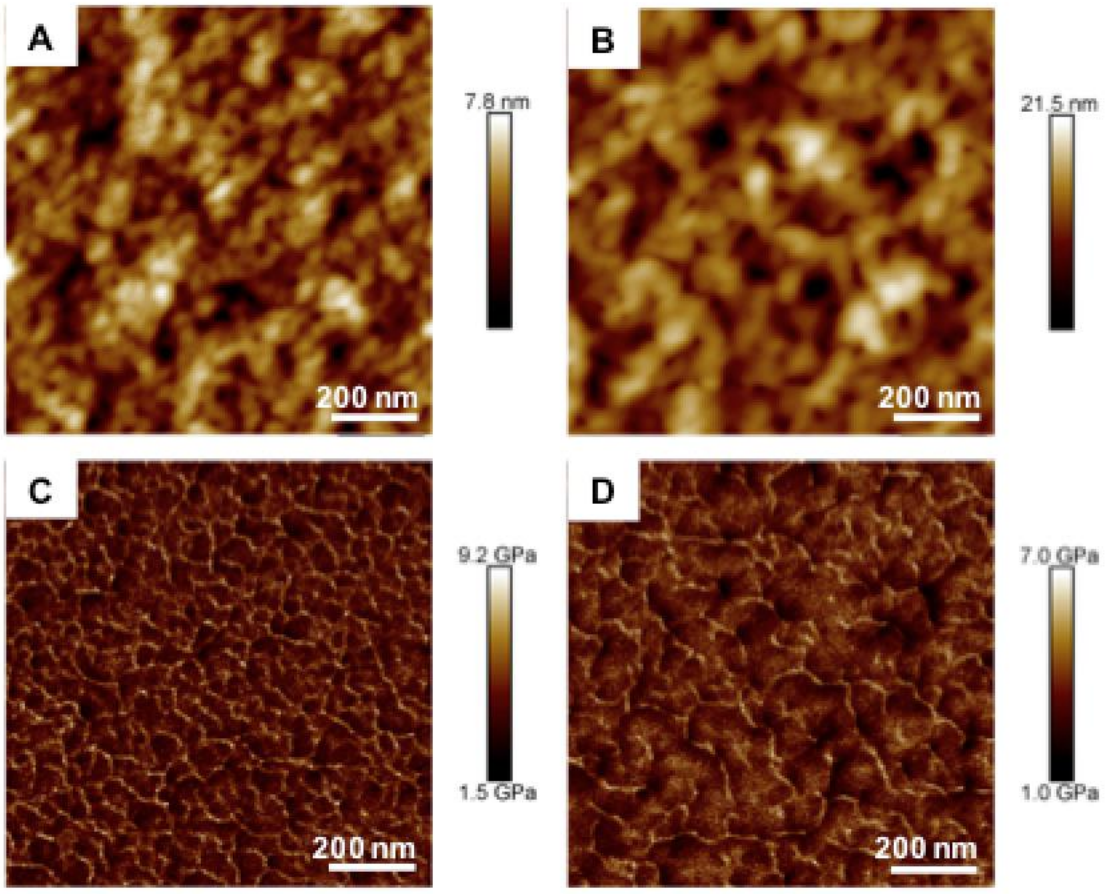

Figure 4.4 *(A) SA Hydrogel PVPON58 height image, (B) SA Hydrogel PVPON360 height image, (C) SA Hydrogel PVPON58 DMT modulus image, and (D) SA Hydrogel PVPON360 DMT modulus image. All images are 1 µm x 1 µm.*

Crosslinked films show increases in roughness, with $R_{q,avg}$ values of SA Hydrogel PVPON58 and SA Hydrogel PVPON360 of 1.25 ± 0.14 nm and 3.32 ± 0.19 nm, respectively, and a small-grain morphology that is consistent with crosslinked multilayer films (Figure 4.4A,B).[21, 28, 47] Greater grain size and $R_{q,avg}$ are observed in the SA Hydrogel PVPON360 film, attributed to higher mesh size resulting from the higher molecular weight of the PVPON sacrificial layer. In general, the crosslinked films have higher $R_{q,avg}$ values than their parent non-crosslinked HB multilayer analogues.

Although there are limited studies relating the modulus of pre- vs. post-crosslinked HB multilayer films, it was expected that crosslinking multilayers might increase the modulus of the films; increased modulus post-crosslinking has been observed in a number of similar multilayer systems where the layers were held together through electrostatic interactions rather than hydrogen bonding.[48-50] DMT modulus images of the crosslinked SA hydrogel films display interconnected regions of higher modulus attributed to crosslink-induced localized stresses (Figure 4.4C,D). The regions of higher modulus are more widely separated in the SA Hydrogel PVPON360 than in the SA Hydrogel PVPON58, attributed to the larger mesh size resulting from the higher molecular weight PVPON. Interestingly, although the moduli of the SA HB films are similar, differences are observed in the moduli of the two crosslinked SA hydrogels (Figure 4.5).

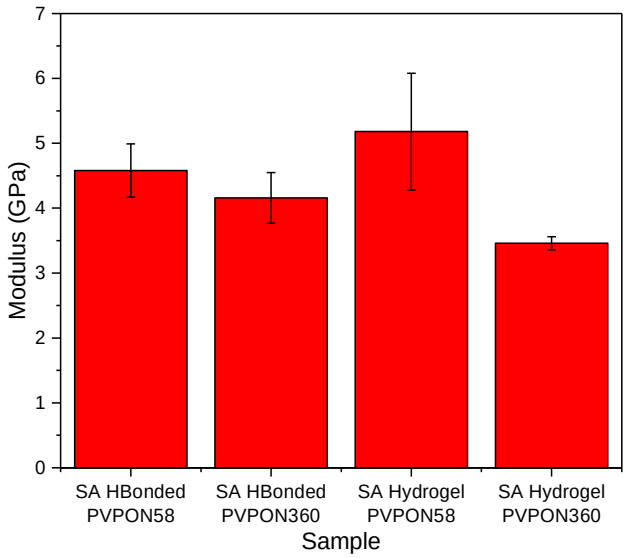

Figure 4.5 *Modulus of SA HB films and SA hydrogel films under ambient conditions.*

Crosslinked SA Hydrogel PVPON58 (5.18 ± 0.90 GPa) shows no change in modulus compared to the parent non-crosslinked HB film, but SA Hydrogel PVPON360 (3.46 ± 0.10 GPa) displays a 17% decrease in comparison to its non-crosslinked analogue ($p = 0.042$). These results show that both the crosslinking process and the PVPON molecular weight influence the modulus of crosslinked SA hydrogel films.

4.3.4 Effect of assembly conditions on hydrogel properties

To understand the impact of assembly conditions (SA vs. dipped LbL) on morphology and modulus of crosslinked films, crosslinked hydrogels prepared using dipped LbL were characterized by AFM under ambient conditions (Figure 4.6).

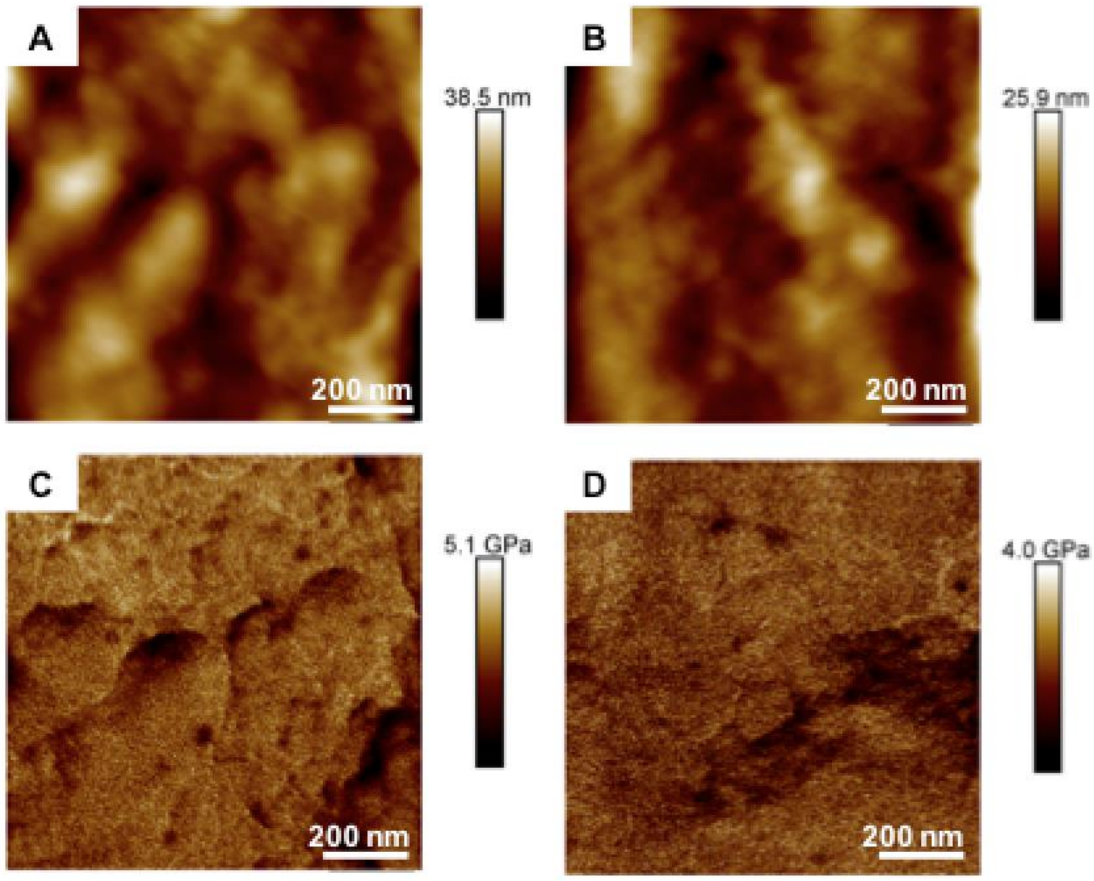

Figure 4.6 *(A) Dipped Hydrogel PVPON58 height image, (B) Dipped Hydrogel PVPON360 height image, (C) Dipped Hydrogel PVPON58 DMT modulus image, and (D) Dipped Hydrogel PVPON360 DMT modulus image. All images are 1 µm x 1 µm.*

The surface morphologies of Dipped Hydrogel PVPON58 and Dipped Hydrogel PVPON360 appear similar, although the $R_{q,avg}$ of Dipped Hydrogel PVPON58 is higher (7.23 ± 1.82 nm) than that of Dipped Hydrogel PVPON360 (3.86 ± 0.85 nm). In comparison to the SA hydrogel films, the height images display relatively rough surfaces with no apparent periodicity in terms of grain size. Similarly, relatively homogeneous modulus is displayed in DMT modulus images of the dipped hydrogel series (Figure 4.6C,D), in contrast to the SA hydrogel films (Figure 4.4C,D), where interconnected

regions of higher modulus are prevalent. Additionally, no significant difference is observed in the modulus of the crosslinked LbL films of different PVPON molecular weight (Table 4.1), unlike that observed for the SA films. The modulus of non-crosslinked HB films prepared via dipped LbL assembly were not tested.

The reason that dipped hydrogel films do not exhibit differences in moduli is likely due to their similarities in internal organization; during dipped LbL assembly of the parent HB films, neutron reflectometry has shown that the PMAA/PVPON films become more disorganized as more layers are added.[29] This disorganization in the multilayers is retained post-crosslinking, which results in similar morphologies and moduli for networks derived from dipped LbL assembly. A summary of the multilayer film moduli measured under ambient conditions is summarized in Table 4.1.

Table 4.1 *Summary of AFM characterization of dry SA and dipped films.*

Sample	$R_{q,avg}$ (nm)	DMT modulus (GPa)
SA HB PVPON58	0.43 ± 0.06	4.58 ± 0.41
SA HB PVPON360	0.40 ± 0.02	4.16 ± 0.39
SA Hydrogel PVPON58	1.25 ± 0.14	5.18 ± 0.90
SA Hydrogel PVPON360	3.32 ± 0.19	3.46 ± 0.10
Dipped Hydrogel PVPON58	7.23 ± 1.82	4.86 ± 0.12
Dipped Hydrogel PVPON360	3.86 ± 0.85	4.72 ± 0.20

4.3.5 Effect of assembly conditions on pH-responsive swelling

Characterization of hydrated films is generally recognized as a challenge because information about both morphology and modulus often cannot be obtained using the same experimental technique.[51] Immersion of hydrogel networks in water results in an ingress of water due to swelling and a drastic reduction in modulus, often by an order of

magnitude or more. For example, Nolte and coworkers showed that hydration of poly(allylamine hydrochloride) and polystyrene sulfonate multilayer films (75 layers) in DI water resulted in a modulus reduction from 5.8 GPa to 590 MPa using buckling measurement techniques.[33] Hydrated polymer network modulus is frequently measured using colloidal or spherical AFM probes as they are more accurate in terms of determining the modulus of soft materials.[52] However, information is lost about the morphology of the materials, thus there is little known about the surface morphology of LbL-derived crosslinked networks.

To understand how LbL assembly conditions affect the morphology and modulus of the crosslinked hydrogel films in liquid environments, hydrated PMAA networks were immersed in either pH 5 or pH 6.5 buffers and characterized utilizing an AFM probe in a fluid probe holder. Here, the hydrogels were expected to be protonated at low pH (pH 5) and deprotonated at higher pH (pH 6.5) based on previous literature reports. Upon immersion of SA Hydrogel PVPON58 (Figure 4.7) in a pH 5 buffer, the granular morphology of the surfaces was largely retained and expanded Z direction scales are indicative of swelling. The modulus decreased by three orders of magnitude into the low MPa range (1.17 ± 0.30 MPa). When the pH of was increased to pH 6.5, height images of the surfaces show swollen surface morphologies and greater height variations in the Z direction. Interestingly, although there are qualitative changes in the surface morphology, differences in the moduli between SA Hydrogel PVPON58 at pH 5 (1.17 ± 0.30 MPa) and pH 6.5 (1.00 ± 0.50 MPa) are not statistically significant.

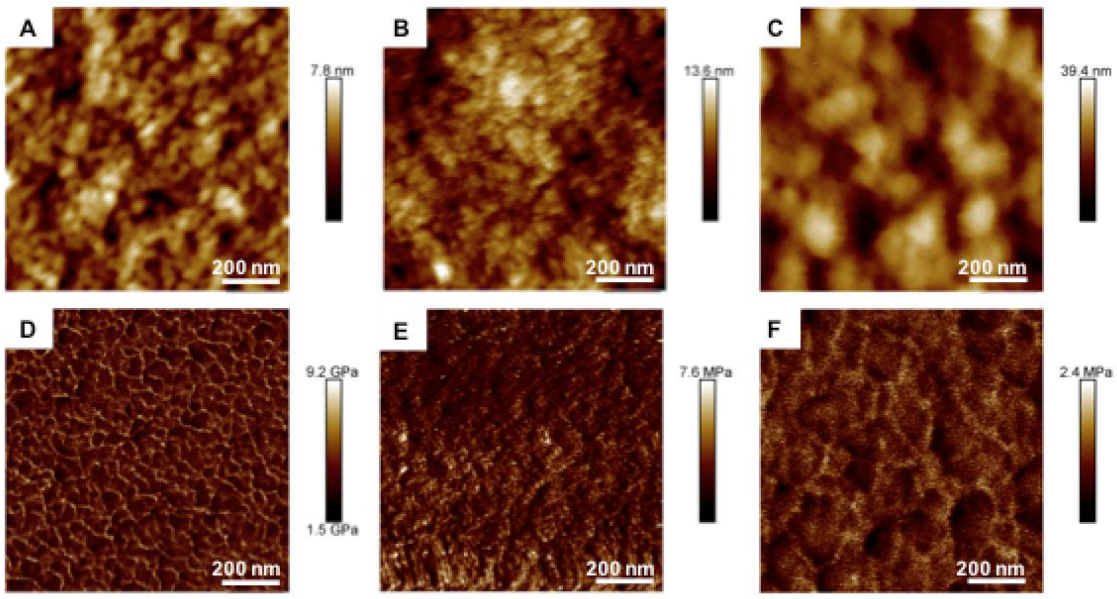

Figure 4.7 *(A) Dry film height image, (B) pH 5 height image, (C) pH 6.5 height image, (D) Dry film DMT modulus image, (E) pH 5 DMT modulus image, and (F) pH 6.5 DMT modulus image for SA Hydrogel PVPON58. All images are 1 x 1 µm.*

Similarly, upon hydration of SA Hydrogel PVPON360 at pH 5, the granular morphology was retained and a greater height variation in the Z direction is observed (Figure 4.8), indicative of network swelling. At pH 5, the modulus is 1.73 ± 0.34 MPa, and further increase of the pH to 6.5 is accompanied by a dramatic 84% reduction in modulus to 0.28 ± 0.11 MPa (p=0.002).

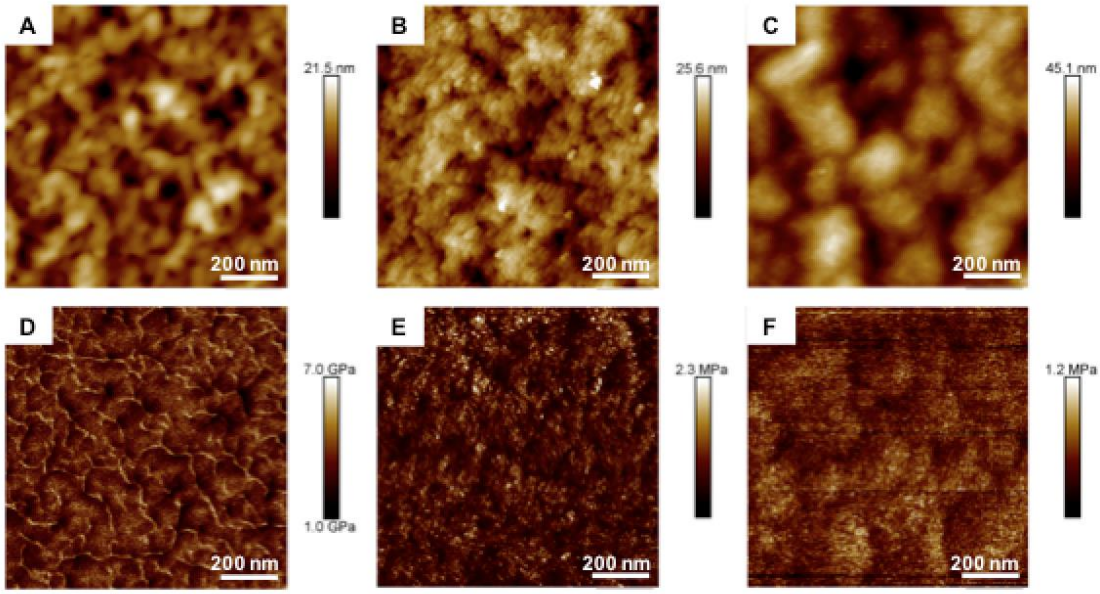

Figure 4.8 *(A) Dry film height image, (B) pH 5 height image, (C) pH 6.5 height image, (D) Dry film DMT modulus image, (E) pH 5 DMT modulus image, and (F) pH 6.5 DMT modulus image for SA Hydrogel PVPON360. All images are 1 µm x 1 µm.*

Interestingly, although there is a difference in the dry moduli of SA Hydrogel PVPON58 and SA Hydrogel PVPON360, there is no statistically significant difference in hydrated moduli at pH 5. At this pH, all the carboxylic acids are protonated and there is little driving force for the network to swell. Increasing the pH to 6.5 causes a significant amount of swelling to occur, and the differences in moduli of SA Hydrogel PVPON58 and SA Hydrogel PVPON360 are close to being statistically significant ($p=0.072$). Based on these findings, sacrificial layer molecular weight influences pH-responsive modulus changes, where the use of higher molecular weight sacrificial layers in the SA LbL assembly process results in multilayer hydrogels with tunable swelling in response to pH changes. However, as expected, swelling is highly dependent on pH, and differentiating

the hydrated modulus may only be possible at higher pH values when the networks are expanded.

The dipped hydrogels also experience swelling in the Z direction and an increase in surface roughness while largely retaining their surface morphology upon hydration at pH 5 (Figure 4.9 and Figure 4.10). The surface roughness of Dipped Hydrogel PVPON58 increases upon immersion in pH 5 buffer ($R_{q,avg}$ of 15.15 ± 7.99 nm) and the modulus of Dipped Hydrogel PVPON58 decreases by three orders of magnitude to 5.65 ± 2.67 MPa. When the pH was increased to pH 6.5, Dipped Hydrogel PVPON58 experienced further increase in surface roughness ($R_{q,avg}$ of 26.13 ± 5.50 nm) and another order of magnitude decrease in modulus to 0.50 ± 0.10 MPa. The difference in Dipped Hydrogel PVPON58 modulus between pH 5 and 6.5 are significant (p=0.029).

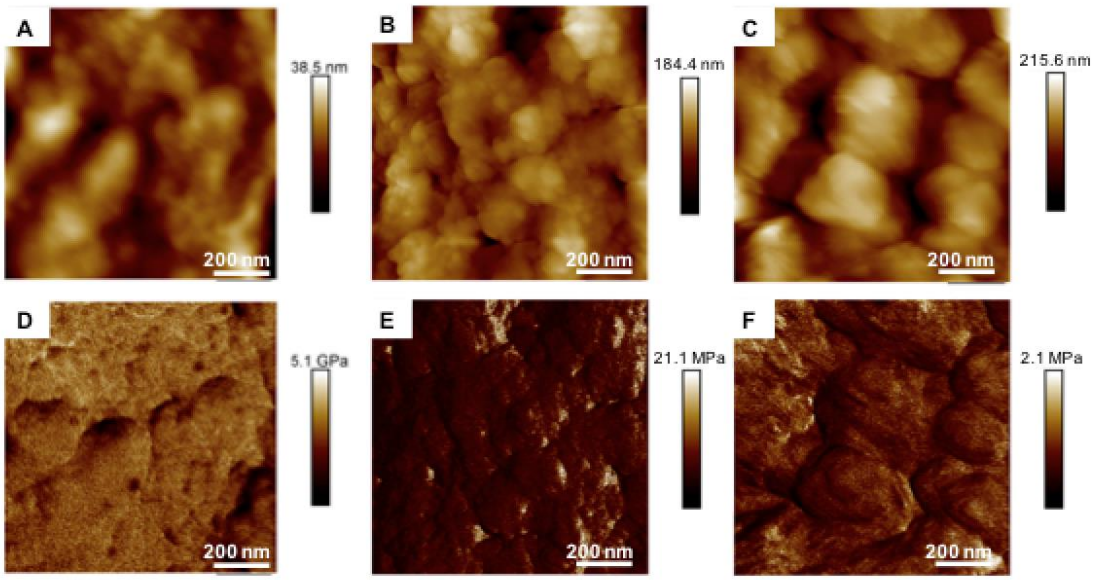

Figure 4.9 *(A) Dry film height image, (B) pH 5 height image, (C) pH 6.5 height image, (D) Dry film DMT modulus image, (E) pH 5 DMT modulus image, and (F) pH 6.5 DMT modulus image for Dipped Hydrogel PVPON58. All images are 1 µm x 1 µm.*

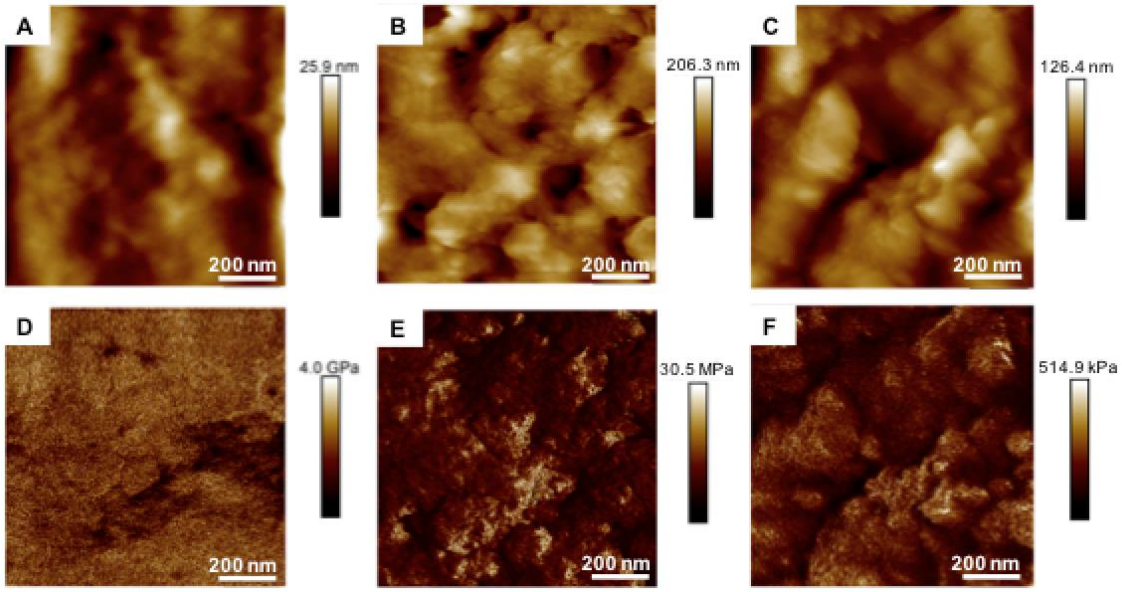

Figure 4.10 *(A) Dry film height image, (B) pH 5 height image, (C) pH 6.5 height image, (D) Dry film DMT modulus image, (E) pH 5 DMT modulus image, and (F) pH 6.5 DMT modulus image for Dipped Hydrogel PVPON360. All images are 1 µm x 1 µm.*

Similar to Dipped Hydrogel PVPON58, immersion of Dipped Hydrogel PVPON360 in pH 5 buffer results in an increase of $R_{q,avg}$ to 29.70 ± 4.09 nm. Likewise, the modulus of Dipped Hydrogel PVPON360 decreases by three orders of magnitude (4.27 ± 1.38 MPa) at pH 5 in comparison to the dry films. Further increasing to pH 6.5 results in another reduction in modulus to 0.26 ± 0.06 MPa. Similar to Dipped Hydrogel PVPON58, the difference in Dipped Hydrogel PVPON360 modulus between pH 5 and 6.5 is significant ($p=0.007$). Comparing the modulus between Dipped Hydrogel PVPON58 and Dipped Hydrogel PVPON360 also shows statistically significant differences in modulus ($p=0.026$). This further demonstrates that, like the SA films, both pH and PVPON M_w influence the hydrated modulus of the deprotonated dipped hydrogels (Figure 4.11).

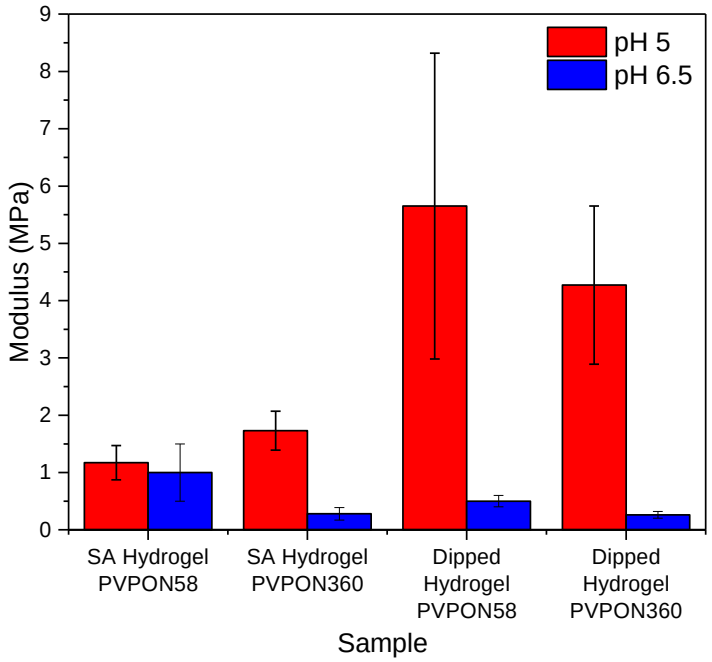

Figure 4.11 *Modulus of SA hydrogels and dipped hydrogels at pH 5 and 6.5.*

Both SA and dipped hydrogels exhibit increased surface roughness upon hydration due to extension of chain loops to the surface. The increase in surface roughness in hydrated PMAA networks is consistent with the increase in swollen film thickness at elevated pH as measured by neutron reflectometry.[41] The topography of dry and hydrated dipped hydrogels is considerably rougher than the corresponding values for their SA counterparts, indicating that extension of chain loops upon swelling is more pronounced in less organized dipped networks whose intrinsic disorder is attributed to the presence of multiple loops and tails adopted during dipped assembly.

At pH 5, the difference in modulus between Dipped Hydrogel PVPON58 and Dipped Hydrogel PVPON360 are statistically insignificant, but the networks do exhibit different moduli when they were immersed in higher pH environments. The dipped hydrogels have a 5-fold greater range in hydrated moduli compared to their SA

counterparts (Table 4.2); this is an important consideration when designing materials for biological applications where control over modulus in liquid environments is critical.

Table 4.2 *Characterization of 1 µm x 1 µm AFM images of SA and dipped hydrogel films at pH 5 and pH 6.5.*

Sample	pH	$R_{q,avg}$ (nm)	DMT Modulus (MPa)
SA Hydrogel PVPON58	5	3.02 ± 0.36	1.17 ± 0.30
SA Hydrogel PVPON58	6.5	6.27 ± 1.13	1.00 ± 0.50
SA Hydrogel PVPON360	5	3.70 ± 0.38	1.73 ± 0.34
SA Hydrogel PVPON360	6.5	6.75 ± 0.62	0.28 ± 0.11
Dipped Hydrogel PVPON58	5	15.15 ± 7.99	5.65 ± 2.67
Dipped Hydrogel PVPON58	6.5	26.13 ± 5.50	0.50 ± 0.10
Dipped Hydrogel PVPON360	5	29.70 ± 4.09	4.27 ± 1.38
Dipped Hydrogel PVPON360	6.5	12.16 ± 4.99	0.26 ± 0.06

4.4 Conclusions

The morphology and elastic behavior of dry and hydrated SA and dipped hydrogels under different pH conditions was determined using AFM nanoindentation testing. Both SA and dipped films exhibited elevated roughness upon hydration that was indicative of loop extensions to the surface caused by the osmotic pressure of ions and electrostatic repulsion in the ionized state. It was shown that pH-responsive modulus changes in the hydrogels can be tuned through modifications in the LbL assembly process by either using a SA or dipped LbL approach, or by changing the molecular weight of the sacrificial polymer layer (in this case, PVPON) during assembly.

These findings open opportunities for the development of thin hydrogels for tunable drug delivery platforms. The differences in internal architecture, morphology, swelling, and elastic properties of these multilayer hydrogels affords a means of fine

tuning their response to pH, light, temperature, or other stimuli, which can rarely be accomplished in randomly crosslinked hydrogel networks. Applications including tissue regeneration, medical devices, sensors, and activators can also benefit from these findings. The presence of carboxylic acids and amine functional groups in the network structure allows for incorporation of a wide range of biological molecules, including polynucleotides and/or interpolyelectrolyte complexes (polyplexes) for gene therapeutics.

4.5 References

1. Youngblood, R. L.; Truong, N. F.; Segura, T.; Shea, L. D., It's All in the Delivery: Designing Hydrogels for Cell and Non-viral Gene Therapies. *Molecular Therapy* **2018,** *26* (9), 2087-2106.

2. Song, W.; Song, X.; Yang, C.; Gao, S.; Klausen, L. H.; Zhang, Y.; Dong, M.; Kjems, J., Chitosan/siRNA functionalized titanium surface via a layer-by-layer approach for in vitro sustained gene silencing and osteogenic promotion. *International Journal of Nanomedicine* **2015,** *10*, 2335-2346.

3. Schuler, C.; Caruso, F., Decomposable hollow biopolymer-based capsules. *Biomacromolecules* **2001,** *2* (3), 921-6.

4. Husteden, C.; Doberenz, F.; Goergen, N.; Pinnapireddy, S. R.; Janich, C.; Langner, A.; Syrowatka, F.; Repanas, A.; Erdmann, F.; Jedelska, J.; Bakowsky, U.; Groth, T.; Woelk, C., Contact-Triggered Lipofection from Multilayer Films Designed as Surfaces for in Situ Transfection Strategies in Tissue Engineering. *ACS Applied Materials & Interfaces* **2020,** *12* (8), 8963-8977.

5. Xie, L.; Ding, X.; Budry, R.; Mao, G., Layer-by-layer DNA films incorporating highly transfecting bioreducible poly(amido amine) and polyethylenimine for sequential gene delivery. *International Journal of Nanomedicine* **2018,** *13*, 4943-4960.

6. Chun, K. W.; Lee, J. B.; Kim, S. H.; Park, T. G., Controlled release of plasmid DNA from photo-cross-linked pluronic hydrogels. *Biomaterials* **2005,** *26* (16), 3319-3326.

7. Lei, Y.; Huang, S.; Sharif-Kashani, P.; Chen, Y.; Kavehpour, P.; Segura, T., Incorporation of active DNA/cationic polymer polyplexes into hydrogel scaffolds. *Biomaterials* **2010,** *31* (34), 9106-9116.

8. Fujimoto, H.; Kato, K.; Iwata, H., Layer-by-layer assembly of small interfering RNA and poly(ethyleneimine) for substrate-mediated electroporation with high efficiency. *Analytical and Bioanalytical Chemistry* **2010,** *397* (2), 571-578.

9. Tan, Y. F.; Mundargi, R. C.; Chen, M. H.; Lessig, J.; Neu, B.; Venkatraman, S. S.; Wong, T. T., Layer-by-layer nanoparticles as an efficient siRNA delivery vehicle for SPARC silencing. *Small* **2014,** (1613-6829 (Electronic)).

10. Tan, Y. F.; Lee, Y. S.; Seet, L.-F.; Ng, K. W.; Wong, T. T.; Venkatraman, S., Design and in vitro release study of siRNA loaded Layer by Layer nanoparticles with sustained gene silencing effect. *Expert Opinion on Drug Delivery* **2018,** *15* (10), 937-949.

11. Shchukin, D. G.; Shutava, T.; Shchukina, E.; Sukhorukov, G. B.; Lvov, Y. M., Modified Polyelectrolyte Microcapsules as Smart Defense Systems. *Chemistry of Materials* **2004,** *16* (18), 3446-3451.

12. Kozlovskaya, V.; Ankner, J. F.; O'Neill, H.; Zhang, Q.; Kharlampieva, E., Localized entrapment of green fluorescent protein within nanostructured polymer films. *Soft Matter* **2011,** *7* (24), 11453-11463.

13. Zhang, P.; Hu, Y.; Ma, R.; Li, L.; Lu, J., Enhanced green fluorescence protein/layered double hydroxide composite ultrathin films: bio-hybrid assembly and potential application as a fluorescent biosensor. *Journal of Materials Chemistry B* **2017,** *5* (1), 160-166.

14. Chen, J.; Ratnayaka, S.; Alford, A.; Kozlovskaya, V.; Liu, F.; Xue, B.; Hoyt, K.; Kharlampieva, E., Theranostic Multilayer Capsules for Ultrasound Imaging and Guided Drug Delivery. *ACS Nano* **2017,** *11* (3), 3135-3146.

15. Kozlovskaya, V.; Alexander, J. F.; Wang, Y.; Kuncewicz, T.; Liu, X.; Godin, B.; Kharlampieva, E., Internalization of Red Blood Cell-Mimicking Hydrogel Capsules with pH-Triggered Shape Responses. *ACS Nano* **2014,** *8* (6), 5725-5737.

16. Kozlovskaya, V.; Chen, J.; Tedjo, C.; Liang, X.; Campos-Gomez, J.; Oh, J.; Saeed, M.; Lungu, C. T.; Kharlampieva, E., pH-responsive hydrogel cubes for release of doxorubicin in cancer cells. *Journal of Materials Chemistry B* **2014,** *2* (17), 2494-2507.

17. Xue, B.; Kozlovskaya, V.; Sherwani, M. A.; Ratnayaka, S.; Habib, S.; Anderson, T.; Manuvakhova, M.; Klampfer, L.; Yusuf, N.; Kharlampieva, E., Peptide-Functionalized Hydrogel Cubes for Active Tumor Cell Targeting. *Biomacromolecules* **2018,** *19* (10), 4084-4097.

18. Kozlovskaya, V.; Chen, J.; Zavgorodnya, O.; Hasan, M. B.; Kharlampieva, E., Multilayer Hydrogel Capsules of Interpenetrated Network for Encapsulation of Small Molecules. *Langmuir* **2018,** *34* (39), 11832-11842.

19. Kharlampieva, E.; Sukhishvili, S. A., Hydrogen-bonded layer-by-layer polymer films. *Polymer Reviews* **2006,** *46* (4), 377-395.

20. Lavalle, P.; Voegel, J.-C.; Vautier, D.; Senger, B.; Schaaf, P.; Ball, V., Dynamic Aspects of Films Prepared by a Sequential Deposition of Species: Perspectives for Smart and Responsive Materials. *Advanced Materials* **2011,** *23* (10), 1191-1221.

21. Kozlovskaya, V.; Kharlampieva, E.; Khanal, B. P.; Manna, P.; Zubarev, E. R.; Tsukruk, V. V., Ultrathin Layer-by-Layer Hydrogels with Incorporated Gold Nanorods as pH-Sensitive Optical Materials. *Chemistry of Materials* **2008,** *20* (24), 7474-7485.

22. Kozlovskaya, V.; Kharlampieva, E.; Drachuk, I.; Cheng, D.; Tsukruk, V. V., Responsive microcapsule reactors based on hydrogen-bonded tannic acid layer-by-layer assemblies. *Soft Matter* **2010,** *6* (15), 3596-3608.

23. Liang, X.; Kozlovskaya, V.; Chen, Y.; Zavgorodnya, O.; Kharlampieva, E., Thermosensitive Multilayer Hydrogels of Poly(N-vinylcaprolactam) as Nanothin Films and Shaped Capsules. *Chemistry of Materials* **2012,** *24* (19), 3707-3719.

24. Higgins, W.; Kozlovskaya, V.; Alford, A.; Ankner, J.; Kharlampieva, E., Stratified Temperature-Responsive Multilayer Hydrogels of Poly(N-vinylpyrrolidone) and Poly(N-vinylcaprolactam): Effect of Hydrogel Architecture on Properties. *Macromolecules* **2016,** *49* (18), 6953-6964.

25. Albright, V.; Zhuk, I.; Wang, Y.; Selin, V.; van de Belt-Gritter, B.; Busscher, H. J.; van der Mei, H. C.; Sukhishvili, S. A., Self-defensive antibiotic-loaded layer-by-layer coatings: Imaging of localized bacterial acidification and pH-triggering of antibiotic release. *Acta Biomateriala* **2017,** *61*, 66-74.

26. Lu, Y.; Wu, Y.; Liang, J.; Libera, M. R.; Sukhishvili, S. A., Self-defensive antibacterial layer-by-layer hydrogel coatings with pH-triggered hydrophobicity. *Biomaterials* **2015,** *45*, 64-71.

27. Kozlovskaya, V.; Kharlampieva, E.; Erel, I.; Sukhishvili, S. A., Multilayer-derived, ultrathin, stimuli-responsive hydrogels. *Soft Matter* **2009,** *5* (21), 4077-4087.

28. Kozlovskaya, V.; Zavgorodnya, O.; Ankner, J. F.; Kharlampieva, E., Controlling Internal Organization of Multilayer Poly(methacrylic acid) Hydrogels with Polymer Molecular Weight. *Macromolecules* **2015,** *48* (23), 8585-8593.

29. Kozlovskaya, V.; Zavgorodnya, O.; Wang, Y.; Ankner, J. F.; Kharlampieva, E., Tailoring Architecture of Nanothin Hydrogels: Effect of Layering on pH-Triggered Swelling. *ACS Macro Letters* **2013,** *2* (3), 226-229.

30. Kolewe, K. W.; Zhu, J.; Mako, N. R.; Nonnenmann, S. S.; Schiffman, J. D., Bacterial Adhesion Is Affected by the Thickness and Stiffness of Poly(ethylene glycol) Hydrogels. *ACS Applied Materials & Interfaces* **2018,** *10* (3), 2275-2281.

31. Kolewe, K. W.; Kalasin, S.; Shave, M.; Schiffman, J. D.; Santore, M. M., Mechanical Properties and Concentrations of Poly(ethylene glycol) in Hydrogels and Brushes Direct the Surface Transport of Staphylococcus aureus. *ACS Applied Materials & Interfaces* **2019,** *11* (1), 320-330.

32. Nolte, A. J.; Cohen, R. E.; Rubner, M. F., A Two-Plate Buckling Technique for Thin Film Modulus Measurements: Applications to Polyelectrolyte Multilayers. *Macromolecules* **2006,** *39* (14), 4841-4847.

33. Nolte, A. J.; Rubner, M. F.; Cohen, R. E., Determining the Young's modulus of polyelectrolyte multilayer films via stress-induced mechanical buckling instabilities. *Macromolecules* **2005,** *38* (13), 5367-5370.

34. Stafford, C. M.; Harrison, C.; Beers, K. L.; Karim, A.; Amis, E. J.; VanLandingham, M. R.; Kim, H.-C.; Volksen, W.; Miller, R. D.; Simonyi, E. E., A buckling-based metrology for measuring the elastic moduli of polymeric thin films. *Nature Materials* **2004,** *3* (8), 545-550.

35. Vinogradova, O. I.; Andrienko, D.; Lulevich, V. V.; Nordschild, S.; Sukhorukov, G. B., Young's Modulus of Polyelectrolyte Multilayers from Microcapsule Swelling. *Macromolecules* **2004,** *37* (3), 1113-1117.

36. Gao, C.; Donath, E.; Moya, S.; Dudnik, V.; Mohwald, H., Elasticity of hollow polyelectrolyte capsules prepared by the layer-by-layer technique. *European Physical Journal E* **2001,** *5* (1), 21-27.

37. Kovalev, A.; Shulha, H.; Lemieux, M.; Myshkin, N.; Tsukruk, V. V., Nanomechanical probing of layered nanoscale polymer films with atomic force microscopy. *Journal of Materials Research* **2004,** *19* (3), 716-728.

38. Shulha, H.; Kovalev, A.; Myshkin, N.; Tsukruk, V. V., Some aspects of AFM nanomechanical probing of surface polymer films. *European Polymer Journal* **2004,** *40* (5), 949-956.

39. Lisunova, M. O.; Drachuk, I.; Shchepelina, O. A.; Anderson, K. D.; Tsukruk, V. V., Direct Probing of Micromechanical Properties of Hydrogen-Bonded Layer-by-Layer Microcapsule Shells with Different Chemical Compositions. *Langmuir* **2011,** *27* (17), 11157-11165.

40. Lehaf, A. M.; Hariri, H. H.; Schlenoff, J. B., Homogeneity, Modulus, and Viscoelasticity of Polyelectrolyte Multilayers by Nanoindentation: Refining the Buildup Mechanism. *Langmuir* **2012,** *28* (15), 6348-6355.

41. Kozlovskaya, V.; Stockmal, K. A.; Higgins, W.; Ankner, J. F.; Morgan, S. E.; Kharlampieva, E., Architecture of Hydrated Multilayer Poly(methacrylic acid) Hydrogels: The Effect of Solution pH. *ACS Applied Polymer Materials* **2020,** *2* (6), 2260-2273.

42. Sidorenko, A.; Krupenkin, T.; Aizenberg, J., Controlled switching of the wetting behavior of biomimetic surfaces with hydrogel-supported nanostructures. *Journal of Materials Chemistry* **2008,** *18* (32), 3841-3846.

43. Kozlovskaya, V.; Higgins, W.; Chen, J.; Kharlampieva, E., Shape switching of hollow layer-by-layer hydrogel microcontainers. *Chemical Communications* **2011,** *47* (29), 8352-8354.

44. Kharlampieva, E.; Kozlovskaya, V.; Ankner, J. F.; Sukhishvili, S. A., Hydrogen-Bonded Polymer Multilayers Probed by Neutron Reflectivity. *Langmuir* **2008,** *24* (20), 11346-11349.

45. Mueller, R.; Köhler, K.; Weinkamer, R.; Sukhorukov, G.; Fery, A., Melting of PDADMAC/PSS Capsules Investigated with AFM Force Spectroscopy. *Macromolecules* **2005,** *38* (23), 9766-9771.

46. Derjaguin, B. V.; Muller, V. M.; Toporov, Y. P., Effect of contact deformations on the adhesion of particles. *Journal of Colloid and Interface Science* **1975,** *53* (2), 314-326.

47. Zavgorodnya, O.; Kozlovskaya, V.; Kharlampieva, E., Nanostructured highly-swollen hydrogels: Complexation with amino acids through copper (II) ions. *Polymer* **2015,** *74*, 94-107.

48. Blacklock, J.; Sievers, T. K.; Handa, H.; You, Y.-Z.; Oupický, D.; Mao, G.; Möhwald, H., Cross-Linked Bioreducible Layer-by-Layer Films for Increased Cell Adhesion and Transgene Expression. *The Journal of Physical Chemistry B* **2010,** *114* (16), 5283-5291.

49. Moussallem, M. D.; Olenych, S. G.; Scott, S. L.; Keller, T. C. S., III; Schlenoff, J. B., Smooth Muscle Cell Phenotype Modulation and Contraction on Native and Cross-Linked Polyelectrolyte Multilayers. *Biomacromolecules* **2009,** *10* (11), 3062-3068.

50. Han, B.; Ma, T.; Vergara, J. H.; Palmese, G. R.; Yin, J.; Lee, D.; Han, L., Non-additive impacts of covalent cross-linking on the viscoelastic nanomechanics of ionic polyelectrolyte complexes. *RSC Advances* **2017,** *7* (84), 53334-53345.

51. An, Q.; Huang, T.; Shi, F., Covalent layer-by-layer films: chemistry, design, and multidisciplinary applications. *Chemical Society Reviews* **2018,** *47* (13), 5061-5098.

52. Dokukin, M. E.; Sokolov, I., Quantitative Mapping of the Elastic Modulus of Soft Materials with HarmoniX and PeakForce QNM AFM Modes. *Langmuir* **2012,** *28* (46), 16060-16071.

CHAPTER V – CONCLUSIONS AND FUTURE WORK

In summary, bioinspired polyelectrolytes with controlled architectures were synthesized and characterized to understand the structure-property relationships relevant for drug and gene delivery applications. Understanding the role of saccharide stereochemistry, as well as charge, on polymer behavior in aqueous solution and the interactions with nucleic acids can provide insight into how synthetic polyelectrolytes can be used for non-viral gene delivery and other biological applications.

5.1 Chapter II: Cationic glycopolyelectrolytes for RNA interference in tick cells

In Chapter II, cationic glycopolymers functionalized with either β,D-glucose or β,D-galactose pendant groups were used to study the effect of saccharide stereochemistry on dsRNA binding and transfection in tick cells in collaboration with the Karim Research Group at the University of Southern Mississippi. The cationic glycopolymers were synthesized by RAFT polymerization and characterized by ^{1}H NMR, ASEC-MALLS, and DLS. Despite the presence of cationic charges on the polymer chains, each cationic glycopolymer was shown to aggregate in both PBS and OptiMEM solutions into particles with two to three size distributions. Incorporation of saccharides onto the polymer chains was shown to significantly decrease the cytotoxicity of the polymer chains in ISE6 cells in comparison to fully cationic polymer chains and a commercially available transfection agent (Lipofectamine). However, there was little difference in cytotoxicity between saccharide structures. Copolymer/dsRNA binding was assessed using gel electrophoresis, where the polymers with higher loadings of cationic charges (up to 35 mol%) were shown to bind better to dsSelK in comparison to those with lower cationic monomer loadings (up to 13 mol%). These interactions were further characterized by zeta potential

experiments, where it was demonstrated that the cationic polymers with pendant saccharides were better able to shield the negative charges of the dsRNA. Similarly, copolymer/dsRNA polyplex transfection experiments showed that the highest SelK transcript knockdown occurred with the galactose-functionalized polymers at N:P ratios of 10, but addition of higher amounts of copolymer hindered transfection. This comparative study demonstrates that saccharide structure will influence not only the in vitro intermolecular interactions between cationic glycopolymers and dsRNA, but also can affect the delivery of dsRNA and gene knockdown. Evaluation of polyplex/dsRNA uptake in isolated salivary glands and tick organisms will also be assessed by evaluating cross-sections via fluorescence microscopy to understand how the copolymers affect dsRNA delivery on an organismal level.

5.1.1 Recommendations for future work

Polymer structure will affect gene delivery and gene knockdown. Future work should include further characterization of polyplex morphology through transmission electron microscopy. The polyplexes may also be separated on basis of size by either centrifugal or asymmetric field-flow fractionation with light scattering. Cationic glycopolymers with higher cationic monomer loadings may also be synthesized to facilitate better dsRNA complexation, as well as mannose-functionalized polyacrylamides and cationic/glyco-block copolymers to further understand the role of polymer architecture on cytotoxicity and polyplex morphology. RNA degradation studies should be conducted to understand how variations in cationic glycopolymer architectures protect the dsRNA against enzymatic degradation.

Cytotoxicity of cationic polymers can be mitigated through incorporation of saccharide pendent moieties, and the cytotoxicity of the copolymers can vary depending on cell line. The microbiome of *I. scapularis* hosts a plethora of pathogenic viruses and bacteria, including the Lyme disease spirochete *B. burgdorferi*. Future studies should include investigations into the antibacterial properties of cationic glycopolymers, particularly for those commonly found in tick vectors.

Another critical process involved in pathogen transmission through ticks is attachment of the ticks to the host. Here, expression of glycine-rich proteins (GRPs) in the salivary glands is important to enable prolonged attachment through a protein curing mechanism that helps to anchor the tick to the host. Thus, future work may include complexation and transfection of other RNAs for knockdown of transcripts coding for the production of select GRPs.

5.2 Chapter III: Characterization of Noncovalent Interactions Between Glycopolymers and dsRNA by All-Atomistic Molecular Dynamics Simulations

In Chapter III, molecular dynamics simulations were conducted to further understand the role of saccharide stereochemistry on polymer behavior and intermolecular interactions with RNA in aqueous solution. Saccharide stereochemistry was shown to play a role in not only intermolecular hydrogen bonding between the pendant saccharides and water, but also the intramolecular hydrogen bonding behavior in the oligomeric systems. Saccharide-functionalized oligomers were shown to interact with one another, which supports evidence of glycopolymer aggregation from Chapter II and previous studies resulting from extensive hydrogen bonding between pendant groups. In the presence of a model dsRNA, monomers and oligomers functionalized with galactose

exhibited more hydrogen bonding with the duplex in comparison to those functionalized with glucose. However, the cationic functionalities on the oligomers were crucial for dsRNA binding.

5.2.1 Recommendations for future work

While molecular dynamics are useful for gaining insight into molecular level interactions between the saccharides and/or cationic charges with dsRNA, they are no substitute for experimental data. Therefore, the molecular dynamics data should be compared to experimental data for validation the simulation parameters. There are computational limitations for the simulation box sizes as well as simulation time scale when using an all-atomistic approach, and future directions may include the investigation of full-scale polymers and longer simulation times using coarse-grained approaches. This would also allow for more in-depth studies into glycopolymer chain entanglements and how this affects neutral and/or cationic glycopolymer aggregation. For the simulations with dsRNA, other force fields may be investigated, including CHARMM or AMBER, both of which are particularly useful for MD simulations of nucleic acids. The methods used in this work to understand the intermolecular interactions between the neutral and/or cationic glycopolymers with dsRNA may also be extended to peptide-based systems to understand the role of saccharide stereochemistry and how this pertains to copolymer/protein binding and glycopolymer-mediated protein aggregation pathways.

5.3 Chapter IV: Nanomechanics of Stimuli-Responsive Poly(methacrylic acid) Multilayer Hydrogels Probed by AFM

In Chapter IV, anionic multilayer hydrogels were characterized using an atomic force microscopy nanoindentation technique in collaboration with the Kharlampieva

Research Group at the University of Alabama at Birmingham. Here, it was shown that both layer-by-layer deposition technique (spin-assisted LbL or dipped LbL) and the molecular weight of the sacrificial PVPON layer affected the surface topology and surface modulus of the resulting multilayer PMAA hydrogels. At ambient conditions, the modulus of the spin-assisted hydrogels could be modulated depending on the PVPON molecular weight, but no change in modulus of the analogous dipped films was observed. Fluid nanoindentation experiments of the multilayer hydrogels at pH 5 and 6.5 indicate that swelling in response to pH changes can be modulated by both PVPON molecular weight and LbL deposition method, which ultimately reflects the internal architecture of the multilayer hydrogels. These experiments open opportunities for the facile development of stimuli-responsive hydrogels with complex internal organization for a range of biomedical applications where precise control over swelling is critical.

5.3.1 Recommendations for future work

Future studies should include the characterization of the multilayer hydrogels using colloidal AFM probes (with 5 μm tip radii) to provide more accurate modulus values of multilayer hydrogels under fluid conditions. Stimuli-responsive saccharide-functionalized multilayer hydrogels may also be investigated to understand how hydrogel structure can influence the interactions with biological materials, such as peptides, nucleic acids, or even cell surfaces. Multilayer hydrogels could also be loaded with nucleic acid/copolymer polyplexes for controlled release of RNA for gene delivery.

APPENDIX A – SUPPLEMENTAL INFORMATION FOR CHAPTER II

A.1 Synthesis of chain transfer agent CEP

A.1.1 Materials

Ethanethiol (97%), sodium hydride (60% dispersion in mineral oil), iodine (≥99.8%), iodine (99.8%) 4,4'-azobis(4-cyanovaleric acid) (≥98%), anhydrous sodium sulfate (≥99%) were purchased from Sigma-Aldrich. Carbon disulfide (99+%) was purchased from Acros Organics. Concentrated hydrochloric acid, glacial acetic acid, and solvents were purchased from Fisher Scientific. All materials were used as received unless otherwise specified.

A.1.2 Synthesis of CEP

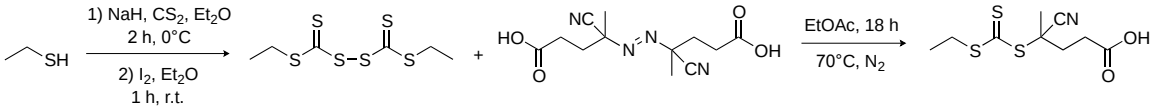

Synthesis of sodium ethyl trithiocarbonate.

Sodium hydride (3.52 g, 88 mmol) was suspended in 150 mL anhydrous Et_2O and cooled to 0°C in an ice bath. Ethanethiol (6.83 mL, 92.2 mmol) was added dropwise to the suspension over 15 minutes with vigorous evolution of H_2 gas and the reaction was stirred for an additional 45 minutes at 0°C. Carbon disulfide (5.57 mL, 92.3 mmol) was added dropwise over 5 minutes at room temperature. After stirring for an hour, the solution was poured into 200 mL cold hexane and the yellow precipitate was isolated via vacuum filtration and dried under vacuum.

Synthesis of bisethyl trithiocarbonate

Dry sodium ethyl trithiocarbonate (11.5 g, 71.78 mmol) was suspended in 200 mL Et_2O at room temperature. Solid iodine (10.028 g, 39.51 mmol) was added to the suspension over 5 minutes and the reaction was stirred for 60 minutes at room temperature. The precipitate was removed via vacuum filtration and the filtrate was washed with 5 wt% sodium thiosulfate (3 x 150 mL), brine (3 x 150 mL), and the organic phase was dried with Na_2SO_4. After filtering out the solids, solvent was removed via rotary evaporation and bisethyl trithiocarbonate was isolated as a yellow solid.

Synthesis of 4-cyano-4-(ethylsulfanylthiocarbonylsulfanyl) pentanoic acid

Bisethyl trithiocarbonate was added to a 3-necked 500 mL and equipped with 250 mL EtOAc, stir bar, condenser, and V-501 initiator (1.5 eq). The solution was sparged for 30 min with N_2 then heated to reflux at 80°C. After 18 hours, the reaction was quenched by exposure to air and the reaction was cooled to room temperature. The crude reaction solution was concentrated via rotary evaporation and the product was purified via column chromatography (SiO_2, 60:35:5 Hexane:EtOAc:AcOH). Fractions containing pure product were combined and washed with 0.05 M HCl (3 x 150 mL), and brine (3 x 150 mL), and dried with Na_2SO_4. Solvent was removed under rotary evaporation and the CEP was crystallized as -40°C.

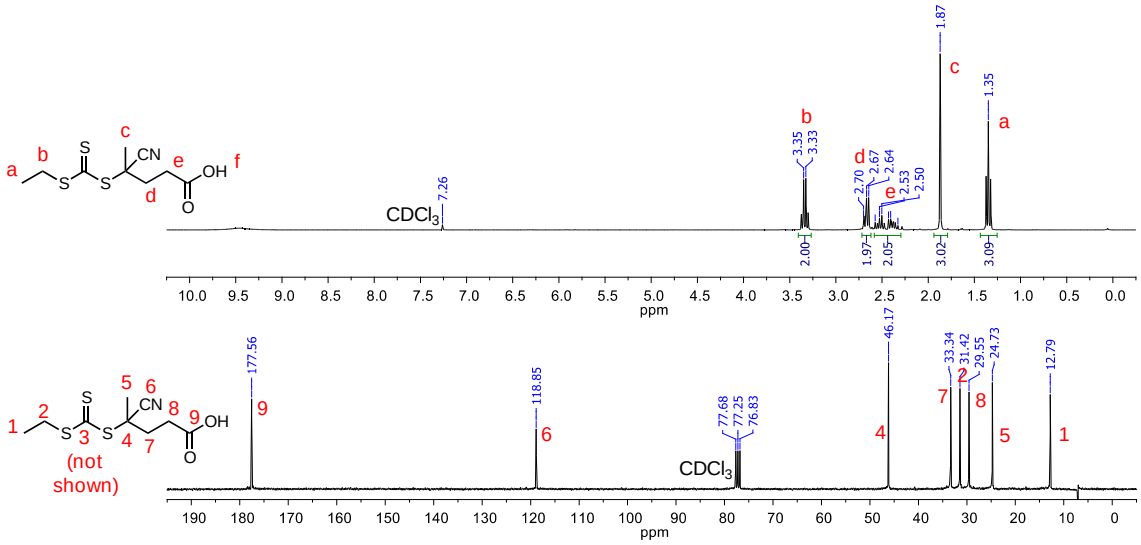

Figure A.1 *^{1}H and ^{13}C NMR of chain transfer agent CEP in $CDCl_3$.*

A.2 Synthesis and characterization of glycopolymers

A.2.1 Synthesis of acetylated glycomonomers

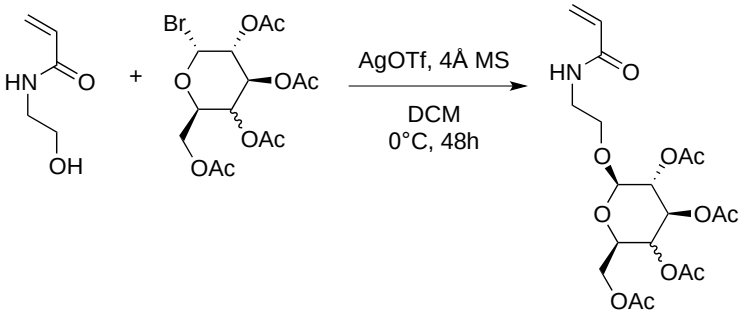

Figure A.2 *Synthesis of acetylated glycomonomers AcGlcEAm and AcGalEAm.*

The acetylated glycomonomers were synthesized similar to a previous literature procedure.[1] Briefly, *N*-hydroxyethyl acrylamide (21.00 g, 182.4 mmol), 4 Å molecular sieves (20 g), and either AcBrGal or AcBrGlc (15.00 g, 34.8 mmol) were dissolved in 400 mL distilled DCM in a 3-neck round-bottomed flask equipped with mechanical stirrer. The mixture was degassed with ultrapure N_2 and submerged in an ice water bath prior to adding AgOTf (14 g, 52.2 mmol), and the reaction was allowed to proceed in the

dark. After 48 hours, the mixture warmed to room temperature, the solids were filtered, and the crude solution was washed with 0.5 M HCl (3 x 50 mL), sat. $NaHCO_3$ (3 x 50 mL), and brine (1 x 50 mL). The mixture was then concentrated and purified via column chromatography (SiO_2, 10:1 EtOAc : Hexanes) to afford a white crystalline solid (3.90 g, 24%).

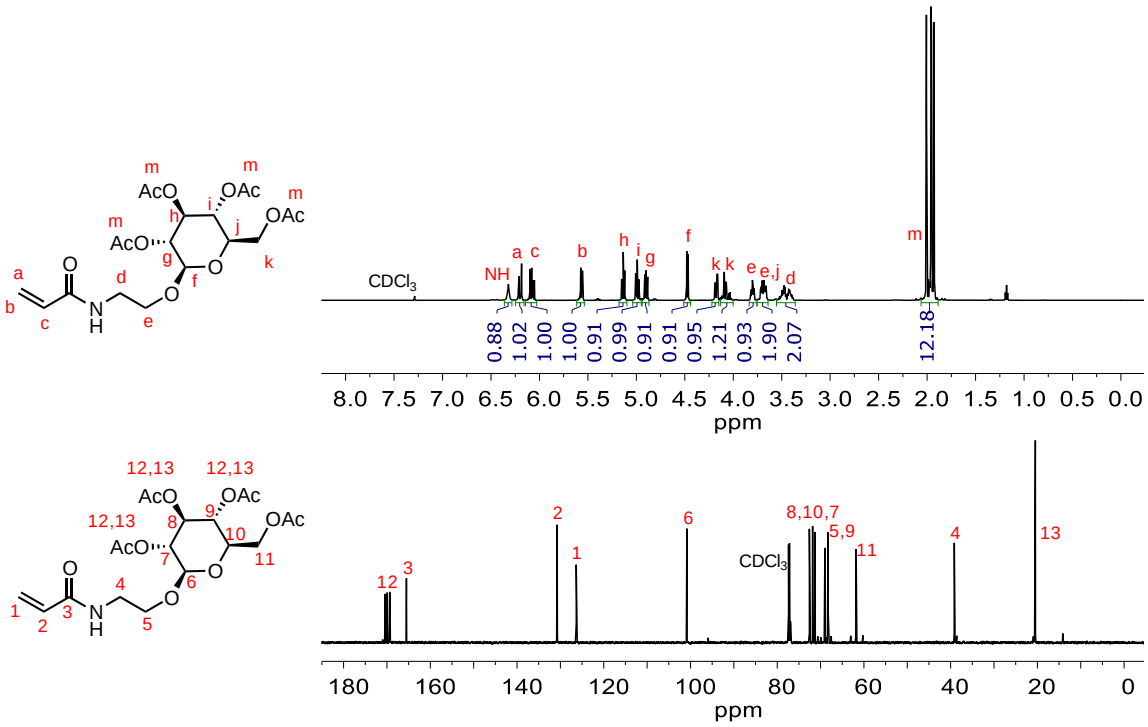

Figure A.3 *^{1}H and ^{13}C NMR of AcGlcEAm in $CDCl_3$.*

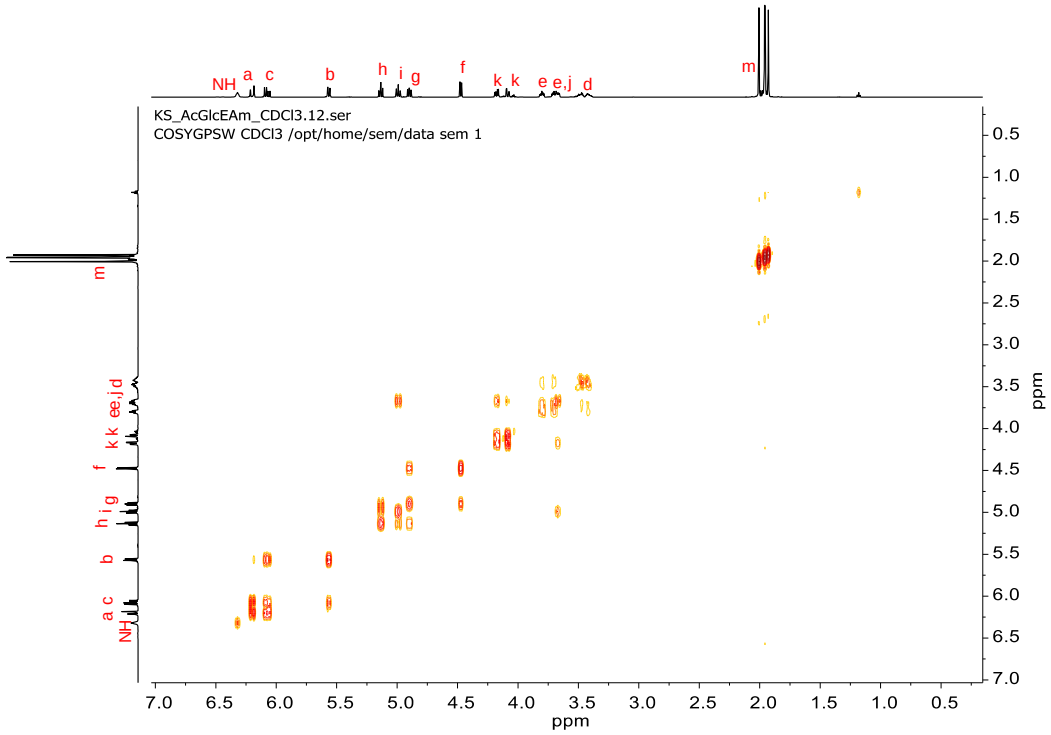

Figure A.4 *COSY NMR of AcGlcEAm in $CDCl_3$.*

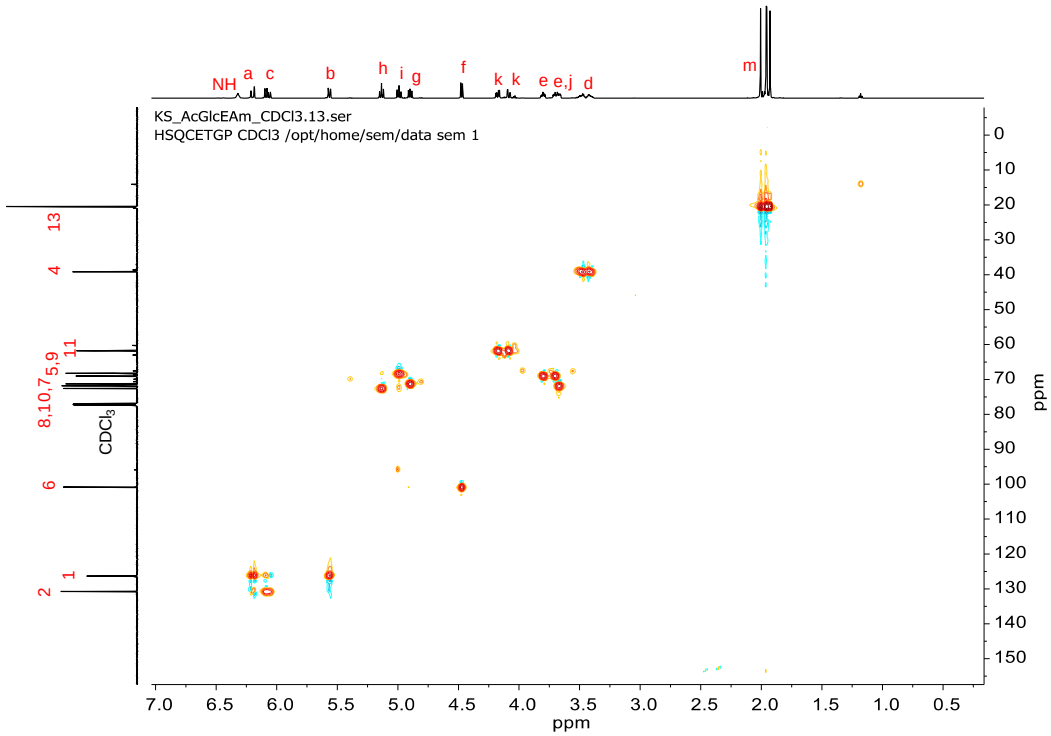

Figure A.5 *HSQC NMR of AcGlcEAm in $CDCl_3$.*

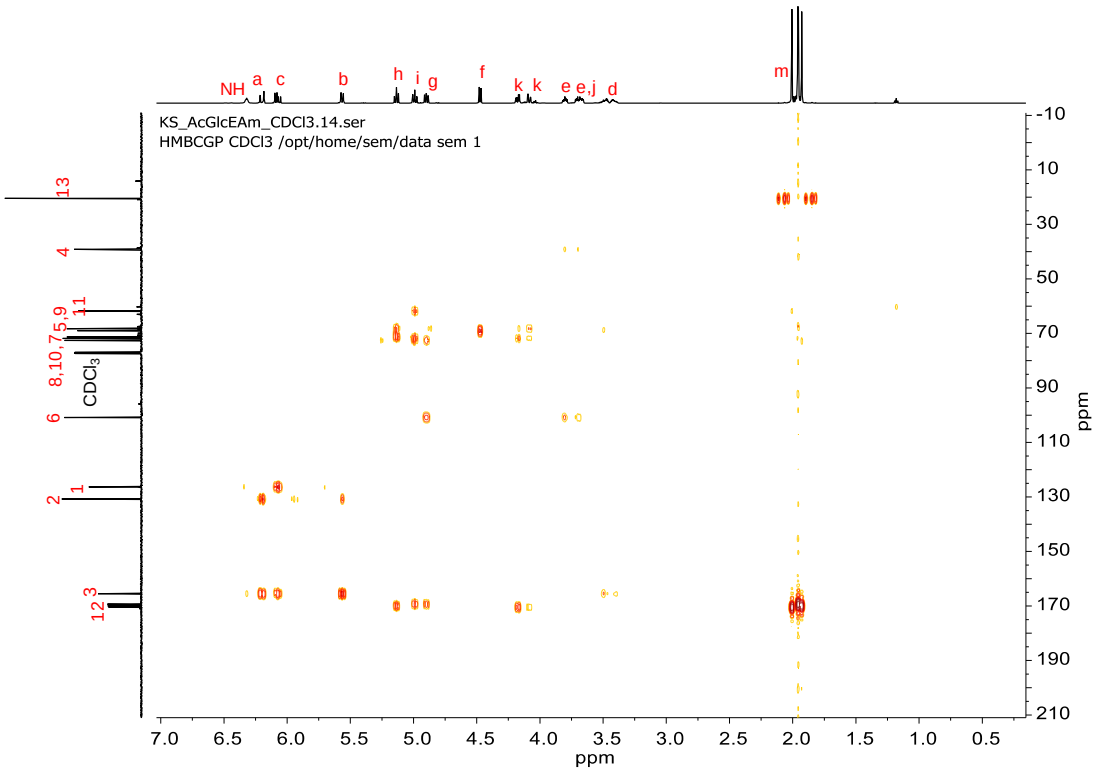

Figure A.6 *HMBC NMR of AcGlcEAm in $CDCl_3$.*

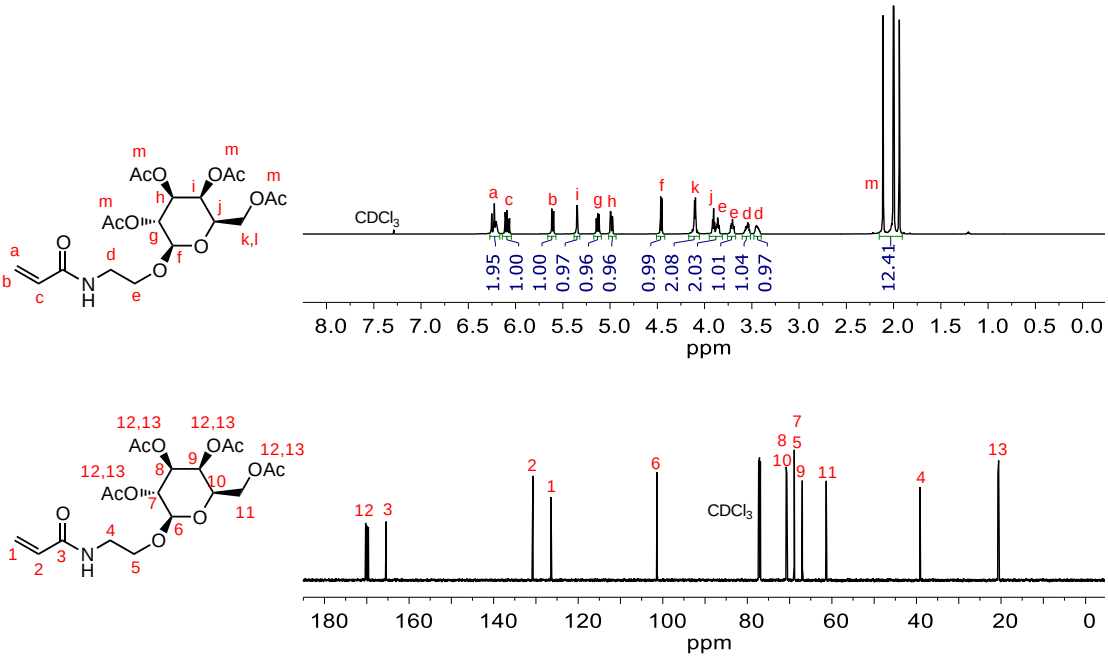

Figure A.7 *^{1}H and ^{13}C NMR of AcGalEAm in $CDCl_3$.*

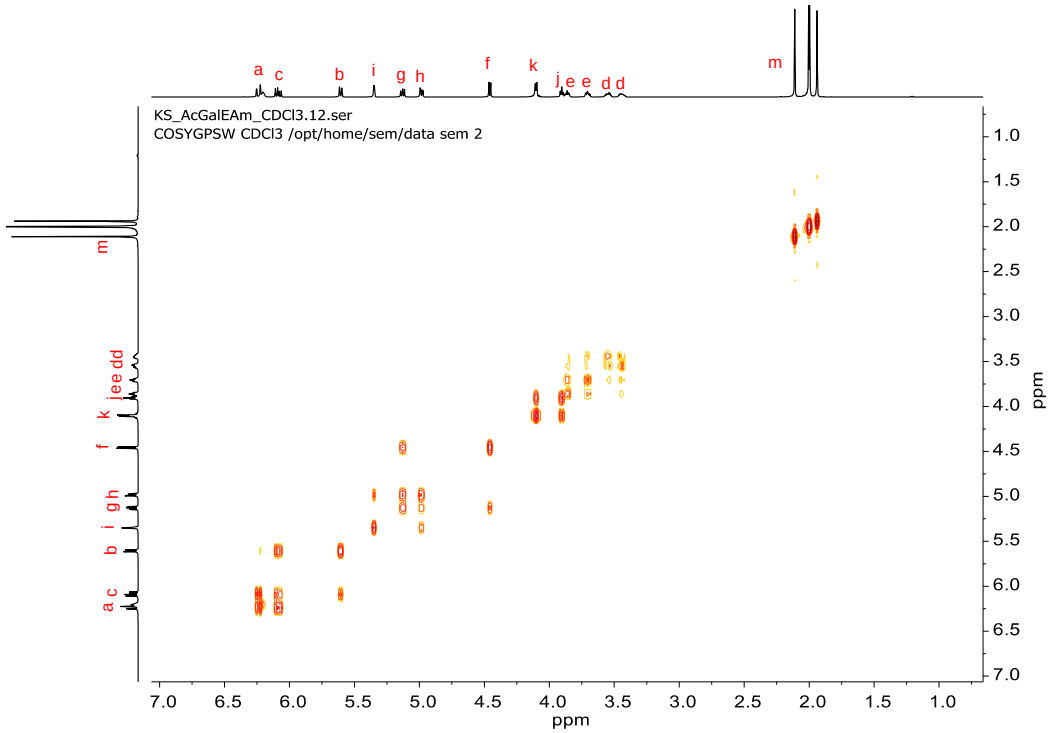

Figure A.8 *COSY NMR of AcGalEAm in $CDCl_3$.*

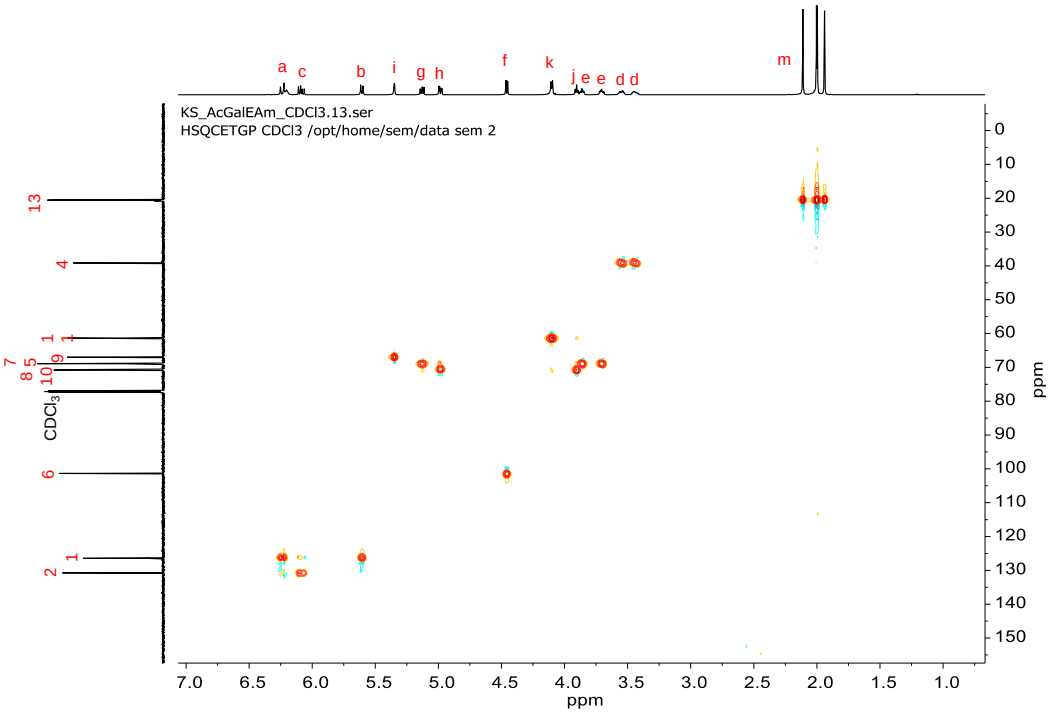

Figure A.9 *HSQC NMR of AcGalEAm in $CDCl_3$.*

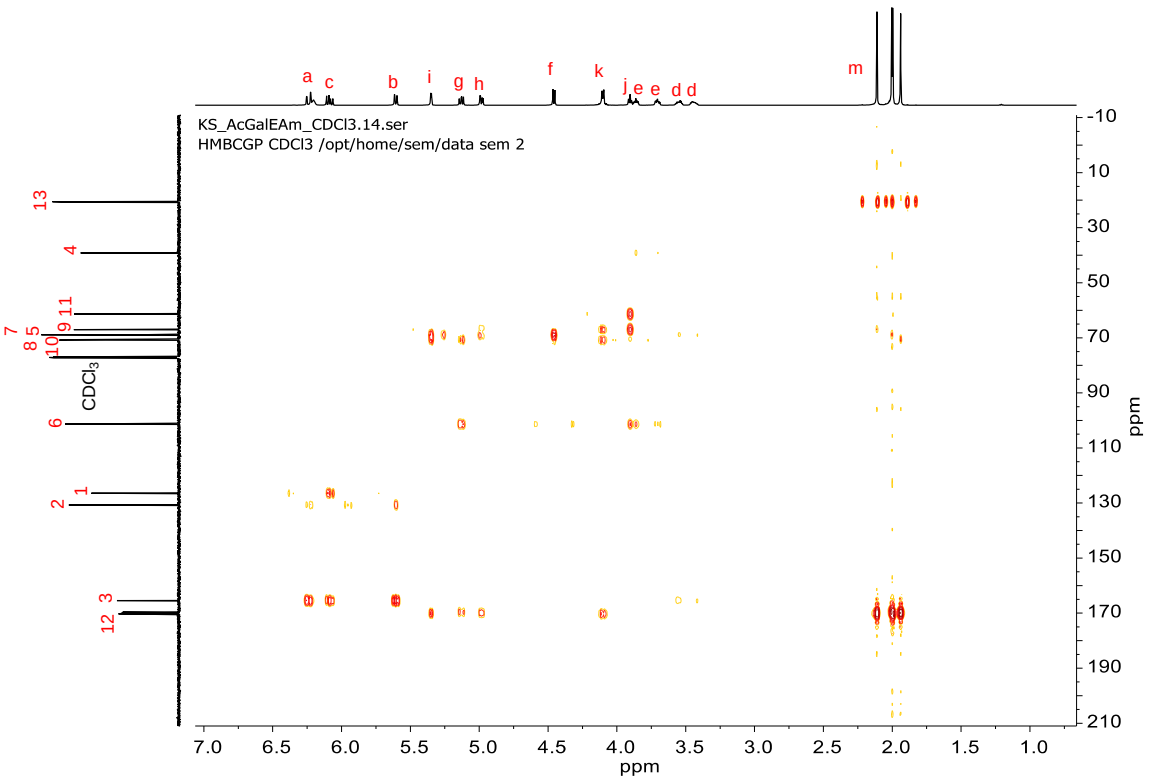

Figure A.10 *HMBC NMR of AcGalEAm in $CDCl_3$.*

A.2.2 PGlc and PGal homopolymers via RAFT in DMSO

The acetyl-protected glycomonomer AcGlcEAm (1.67 g, 3.75 mmol), CEP (13.83 mg, 0.0525 mmol), V-501 (2.94 mg, 0.0105 mmol), and trimesic acid (39.39 mg, 0.187 mmol) were dissolved in anhydrous DMSO and diluted to a total volume of 7.5 mL in a graduated cylinder. The polymerization mixture was transferred to a 25 mL round-bottomed flask, and the solution was degassed with ultrapure N_2 for 45 minutes with stirring. The initial monomer concentration was $[M]_0 = 0.5$ M, and the $[M]_0$:$[CTA]_0$ and $[CTA]_0$:$[I]_0$ were maintained at 71:1 and 5:1, respectively, such that a polymer with a target degree of polymerization of 50 would be achieved at $p = 0.7$. Trimesic acid (0.025 M) was used as an internal standard to monitor the reaction kinetics, where aliquots were

removed from the reaction mixture at 30-minute intervals and quenched with liquid nitrogen before NMR analysis. After 160 minutes, the polymerization flask was quenched in liquid N_2 and purified by precipitating first into DI H_2O. The polymer PAcGlcEAm was further purified by dissolving in EtOAc and precipitating into hexanes. The protected glycopolymer was then isolated and dried under vacuum to yield a yellow solid (1.25 g, 99% yield). To remove the acetyl protecting groups, the polymer was dissolved in anhydrous methanol (25 mL) and a catalytic amount of sodium methoxide was added (0.5 eq. per repeat unit) while stirring, and the deprotected polymer precipitated from solution. After two hours of stirring the deprotection mixture, the glycopolymer precipitate was centrifuged, isolated, and washed again with MeOH. The solid polymer was redissolved in water, dialyzed for 2 days in DI H_2O, and lyophilized to isolate the polymer PGlc as a white solid (0.50 g, 78% yield). The same procedure was used for the synthesis of PGal.

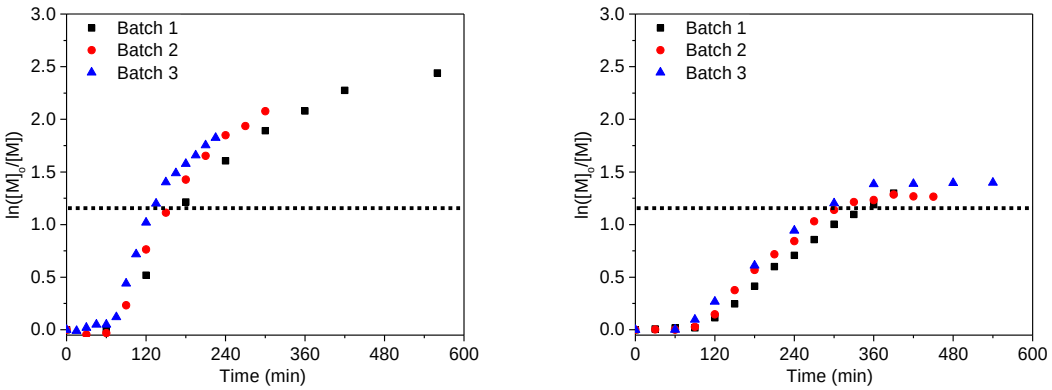

Figure A.11 *Plots of ln([M]$_o$/[M]) vs. time for RAFT polymerization of (left) PAcGlcEAm and (right) PAcGalEAm with CEP and V-501 at 70 °C in DMSO. The dotted line represents a monomer conversion (ρ) of 70%.*

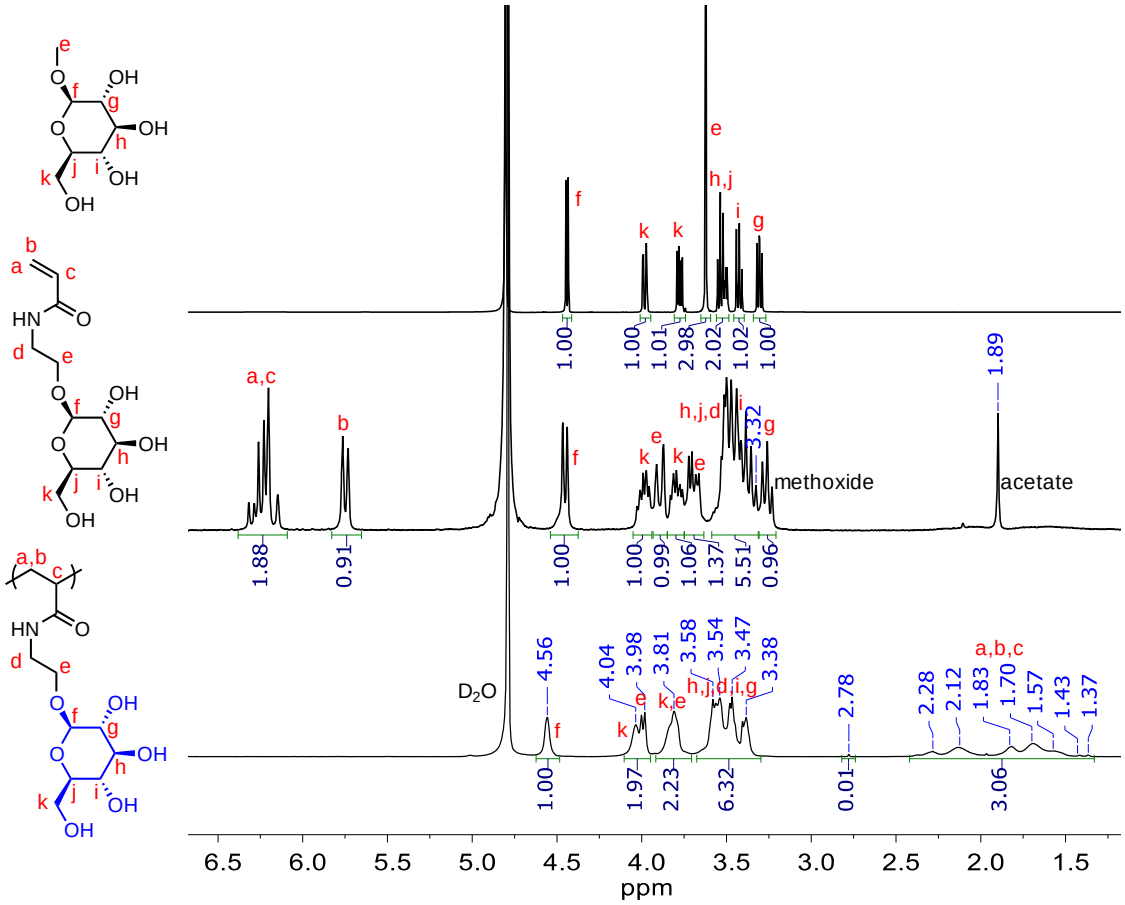

Figure A.12 *^{1}H NMR spectra comparison of PGlc homopolymer with deprotected GlcEAm and Me-β-D-Glc in D_2O.*

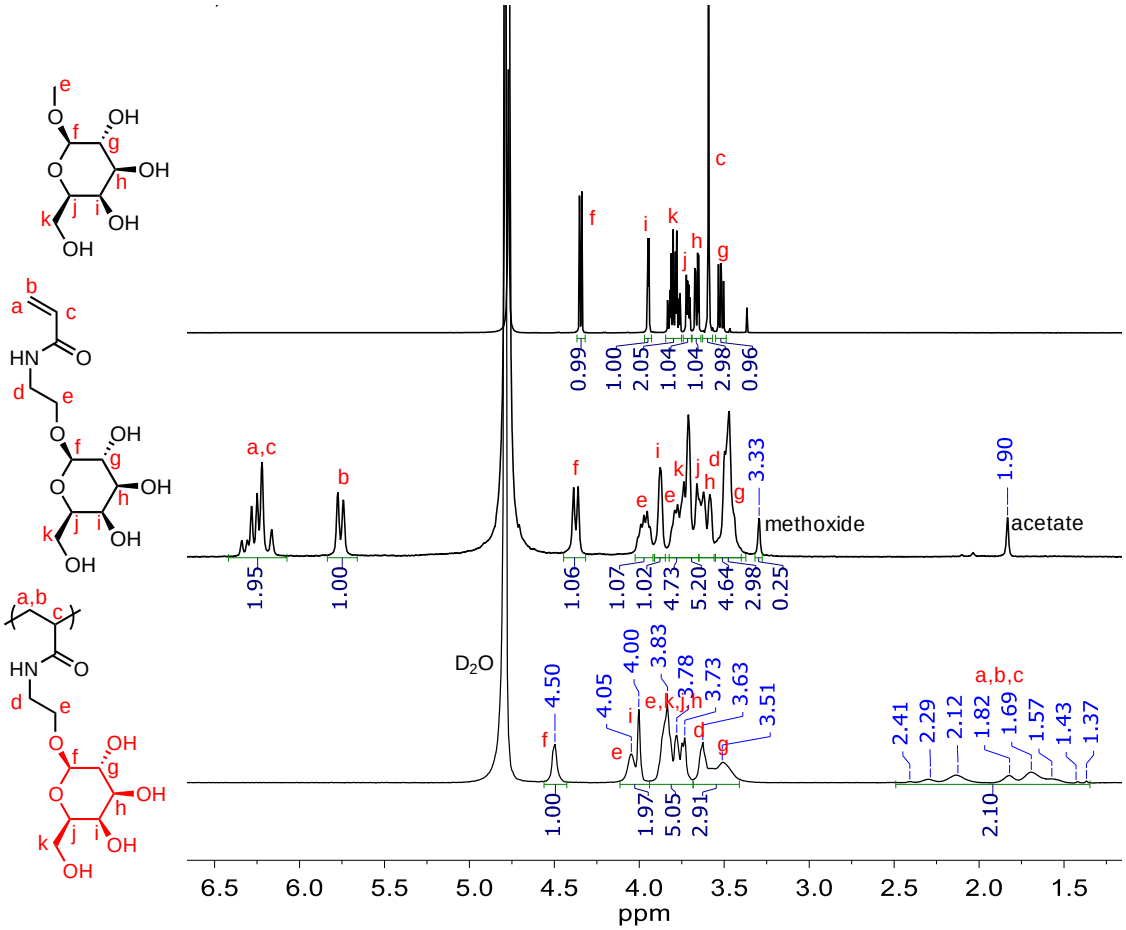

Figure A.13 *[1]H NMR spectra comparison of PGal homopolymer with deprotected GalEAm and Me-β-D-Gal in D_2O.*

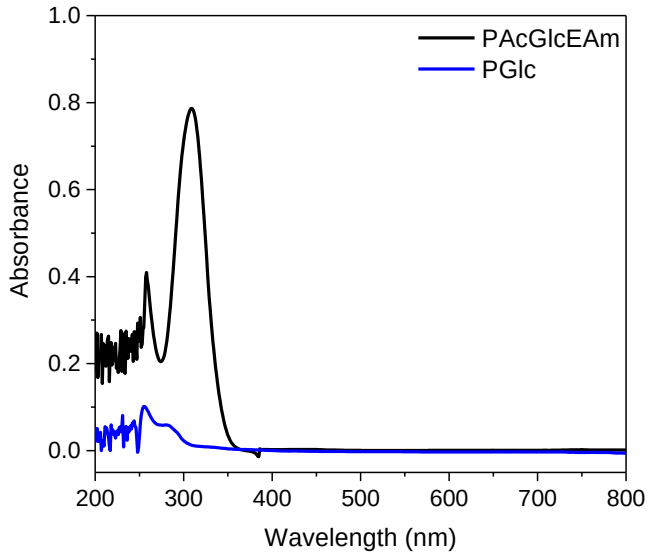

Figure A.14 *UV-Vis absorption spectra of (a) PAcGlcEAm$_{75}$ and (a) PGlc$_{75}$ in DMSO (polymer concentration = 0.05 mM). The decrease in the absorption peak at 308 nm indicates cleavage of the trithiocarbonate chain ends after exposure to NaOMe/MeOH.*

A.3 Synthesis of PDMAPAm

Prior to polymerization, the hydrochloride salt of DMAPAm was prepared by dissolving the DMAPAm (1.172 g, 7.50 mmol) in 5.0 mL of anhydrous DMSO and adding equimolar amounts of concentrated HCl (0.619 mL, 7.50 mmol). The monomer was then polymerized via RAFT polymerization, using the chain transfer agent CEP and the free radical initiator 4,4'-azobis(4-cyanopentanoic acid) (V-501). The initial monomer concentration was $[M]_0$ = 0.5 M, and the $[M]_0$:$[CTA]_0$ and $[CTA]_0$:$[I]_0$ were maintained at 71:1 and 5:1, respectively, such that a polymer with a target degree of polymerization of 50 would be achieved at p = 0.7. Trioxane (0.025 M) was used as an internal standard to monitor the reaction progress, and aliquots were removed from the reaction mixture at regular intervals and quenched with liquid nitrogen before NMR

analysis. Following polymerization, the polymers were dialyzed for 2 days at pH = 3-4 using 1 kDa MWC RC tubing, and then lyophilized to isolate the polymer as a yellow solid.

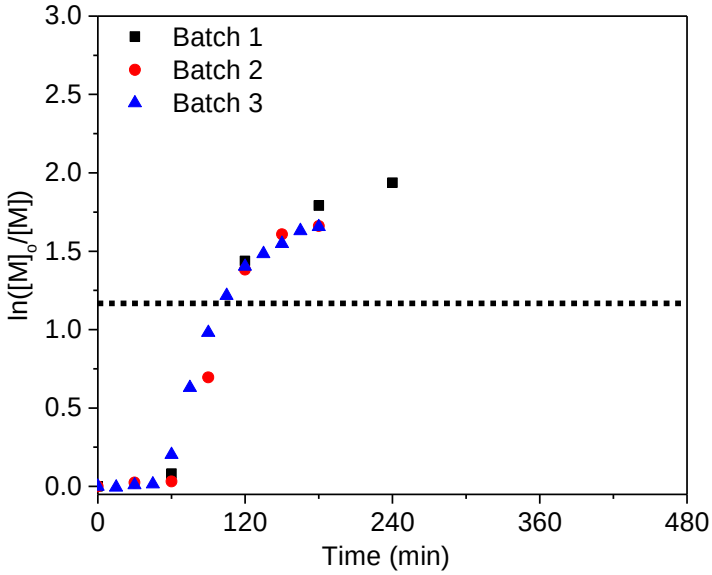

Figure A.15 *Plots of ln([M]$_o$ /[M]) vs. time for RAFT polymerization of PDMAPAm with CEP and V-501 at 70 °C in DMSO. The dotted line represents a monomer conversion (ρ) of 70%.*

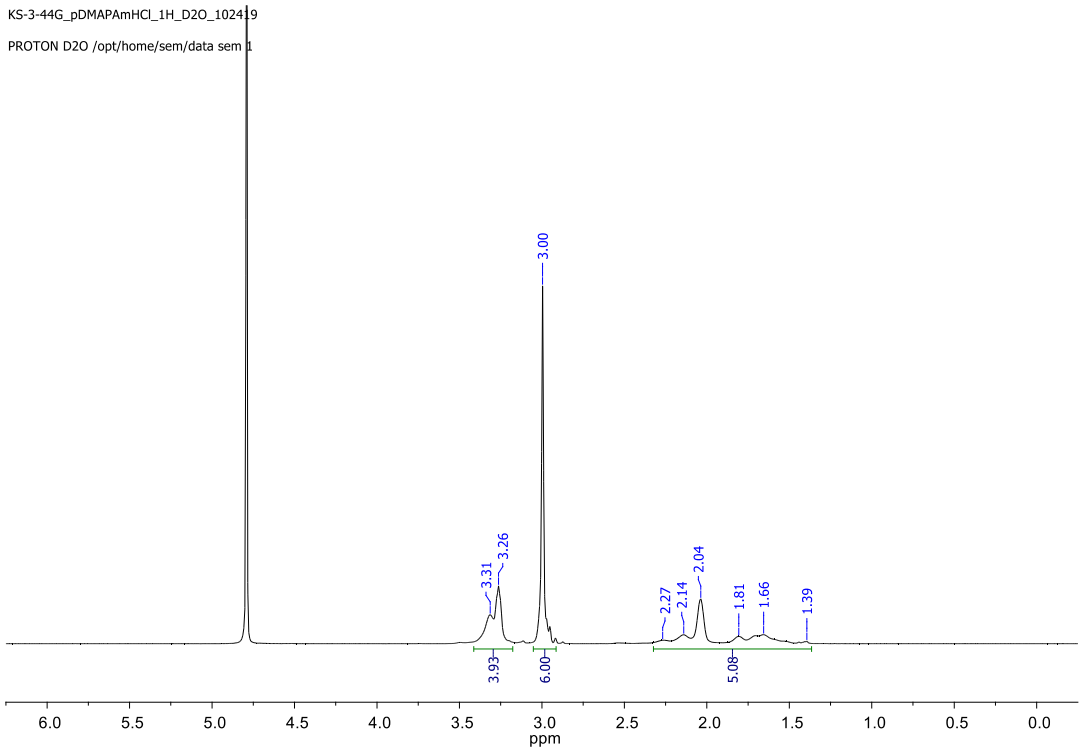

Figure A.16 *^{1}H NMR of $PDMAPAm_{67}$ homopolymer in D_2O.*

A.3.2 Potentiometric titration of DMAPAm and PDMAPAm

A Metrohm 848 Titrino Plus autotitrator was calibrated with pH reference buffers and then used to determine the pK_a of DMAPAm and PDMAPAm. Monomer and polymer solutions were prepared in 18.2 MΩ DI water such that the overall concentration of cationic charges in the solution were 0.05 M. The solutions were adjusted to pH < 2 using 1 M HCl and titrated to pH = 12 using 0.05 M NaOH at 25 °C.

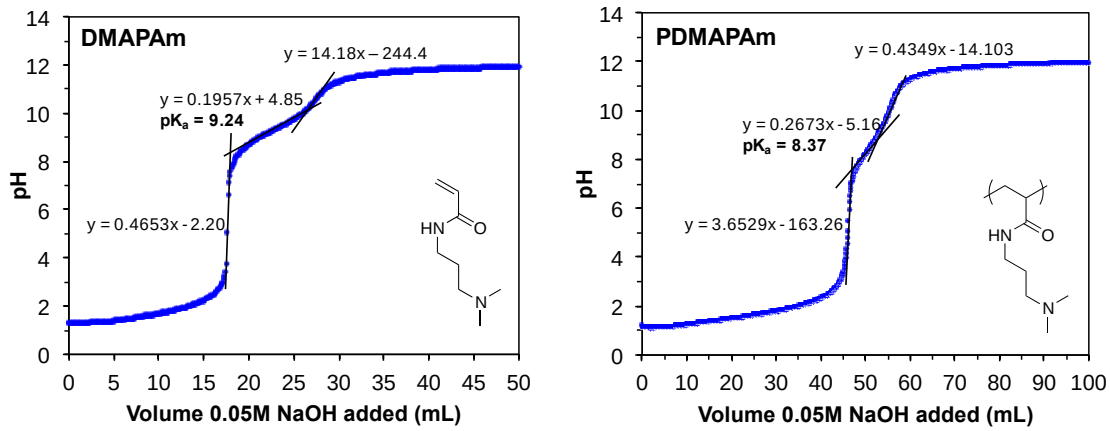

Figure A.17 *Potentiometric titration of (left) DMAPAm·HCl monomer and (right) PDMAPAm$_{67}$ homopolymer.*

A.4 Cytotoxicity

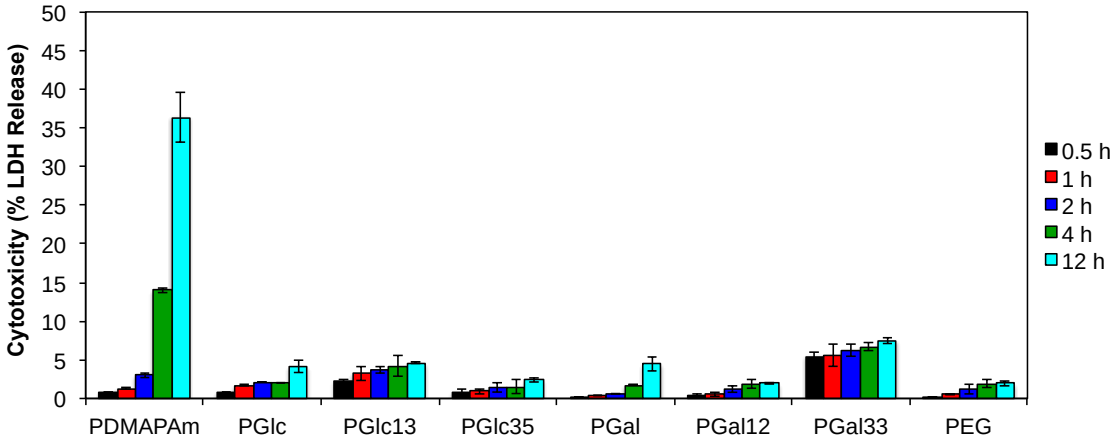

Figure A.18 *Time-dependent polymer cytotoxicity in ISE6 cells (polymer concentration of 20 ng/µL) determined via LDH assay.*

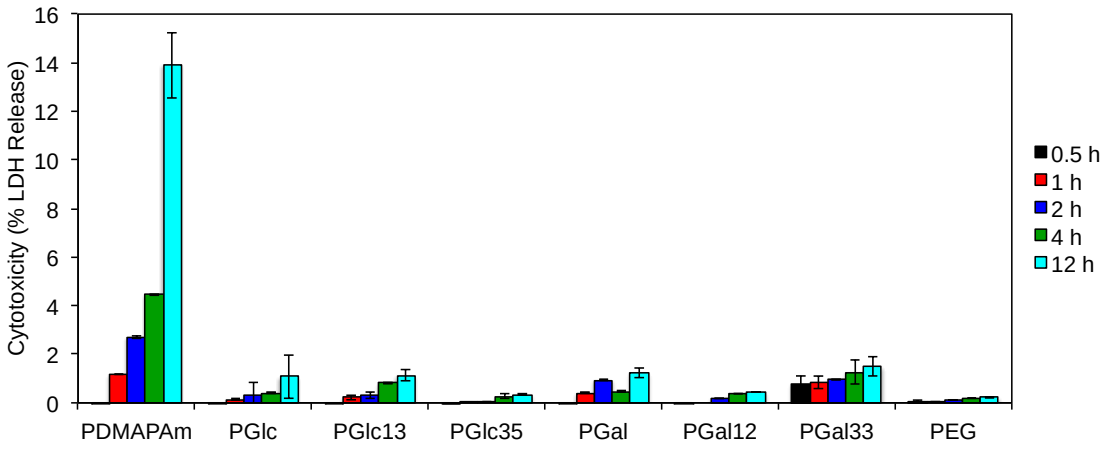

Figure A.19 *Time-dependent polymer cytotoxicity in ISE6 cells (polymer concentration of 5 ng/µL) determined via LDH assay.*

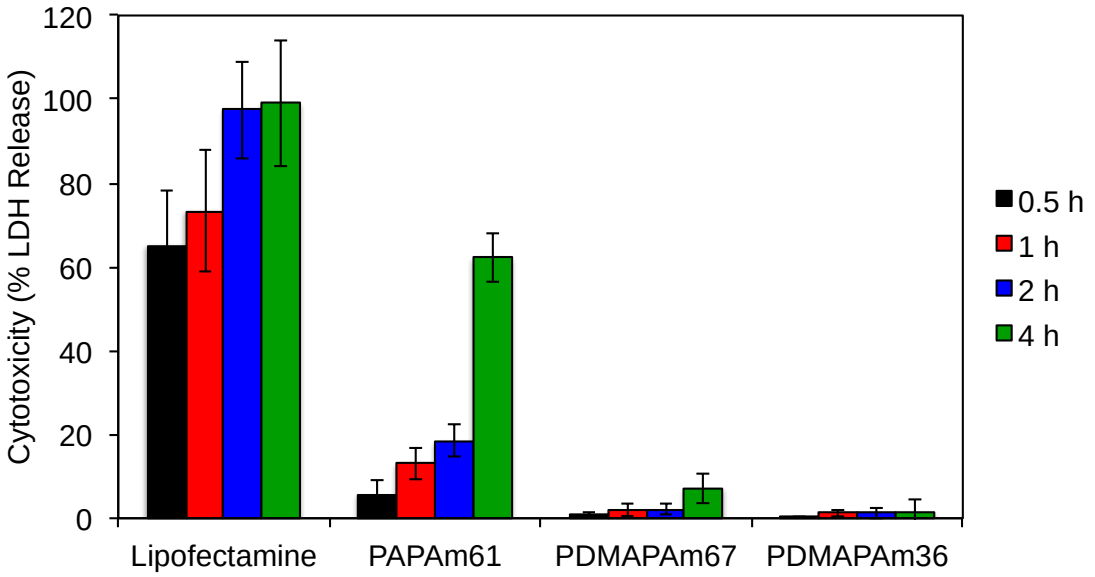

Figure A.20 *Time-dependent polymer cytotoxicity of cationic polymers in ISE6 cells (polymer concentration of 10 ng/µL) determined via LDH assay.*

A.5 Synthesis of PAPAm

A.5.1 Materials

1,3-diaminopropane (≥99%), acryloyl chloride (≥97%), sodium bicarbonate (≥99.5%), anhydrous sodium sulfate (≥99%), and triethylamine (Et_3N, ≥99%) were purchased from Sigma Aldrich. Di-*tert*-butyl dicarbonate (>95%) was purchased from TCI Chemicals. Basic aluminum oxide (Al_2O_3) was purchased from Acros Organics. HCl (4.0 M) in dioxane was purchased from Oakwood Chemicals. All solvents were purchased from Fisher Scientific unless otherwise stated.

A.5.2 Synthesis of bocAPAm monomer

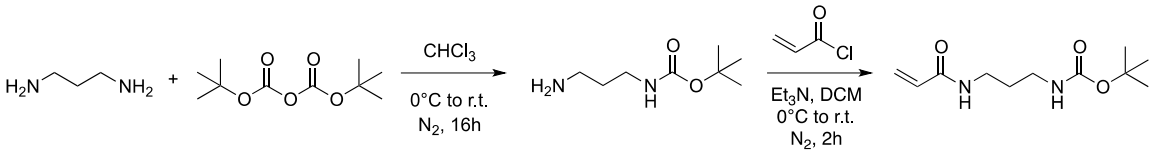

The protected monomer *tert*-butyl (3-acrylamidopropyl)carbamate (bocAPAm) was synthesized by adapting previous literature procedures.[2-3] Briefly, 1,3-diaminopropane (33.96 g, 458 mmol) was dissolved in 80 mL $CHCl_3$ and degassed with ultrapure N_2 for 30 minutes. Di-*tert*-butyl dicarbonate (10.00 g, 45.8 mol) was then dissolved in 10 mL $CHCl_3$ and added dropwise to the stirring solution over 2 hours at 0 °C. After stirring for an additional 14 hours at room temperature, the reaction mixture was washed with brine (3 x 100 mL), DI H_2O (1 x 100 mL), and dried with Na_2SO_4. The solution was filtered and concentrated in vacuo to afford the boc-protected propylenediamine (boc-PD, 6.41 g) as a colorless oil, which was used without further purification. The oil was dissolved in 300 mL distilled DCM with Et_3N (5.64 mL, 40.5

mmol) and degassed with N_2 for 30 minutes. Acryloyl chloride (3.14 mL, 38.6 mmol) was then added dropwise to the solution over 1 hour at 0 °C. After stirring for an additional hour, the reaction mixture was washed with 0.1 M HCl (1 x 100 mL), saturated $NaHCO_3$ (1 x 100 mL), brine (1 x 100 mL), and DI H_2O (1 x 100 mL). The crude reaction mixture was dried using Na_2SO_4 and basic Al_2O_3, filtered, and concentrated in vacuo. The product bocAPAm then purified by column chromatography (10:5:1 EtOAc : DCM : hexanes) and recrystallized from hexanes (4.45 g, 53%).

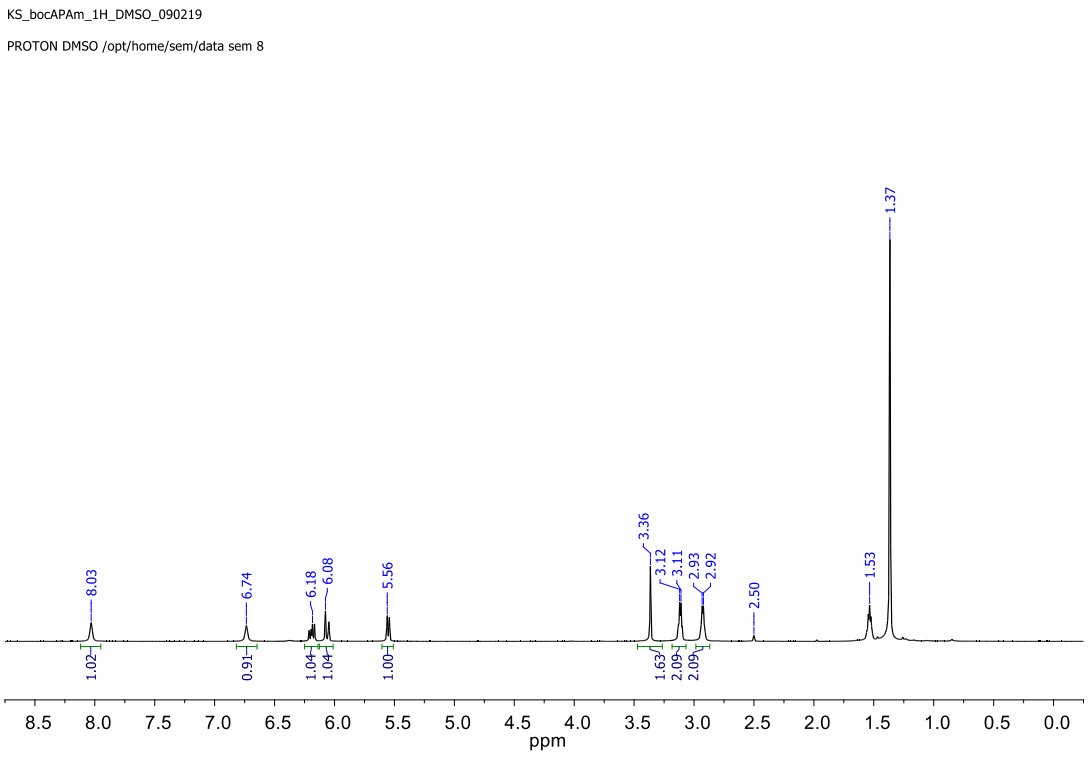

Figure A.21 *^{1}H NMR of bocAPAm in DMSO-d_6.*

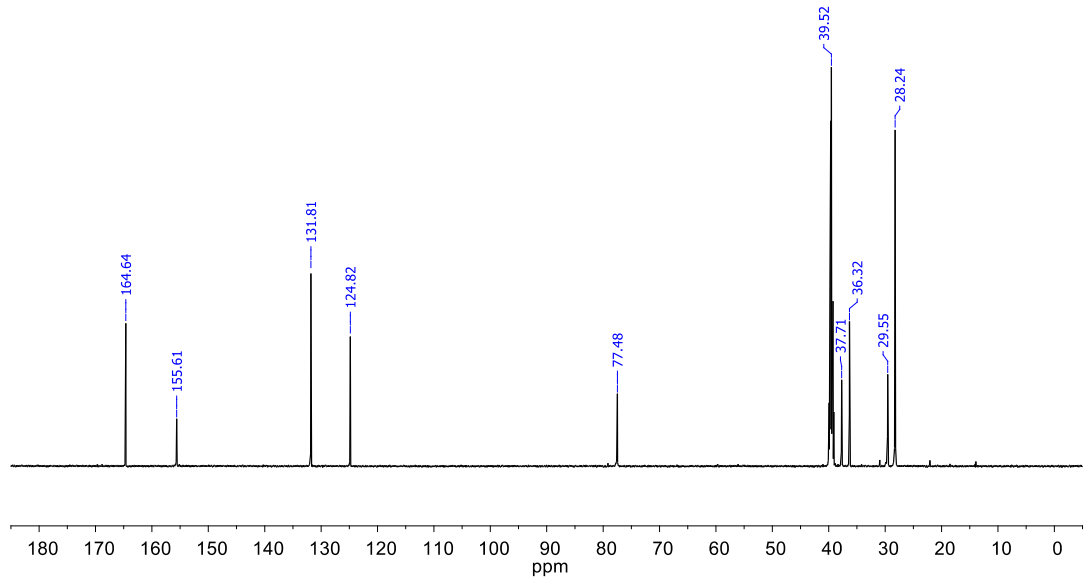

Figure A.22 *^{13}C NMR of bocAPAm in DMSO-d_6.*

A.5.3 Synthesis of PAPAm

The synthesized monomer bocAPAm (1.712 g, 7.50 mmol), CEP (27.65 mg, 0.105 mmol), V-501 (5.89 mg, 0.021 mmol), and trioxane (33.78 mg, 0.375 mmol) were dissolved in DMSO, diluted to a total volume of 15.00 mL, and then degassed with ultrapure N_2 for 45 minutes. The polymerization solution was allowed to react at 70 °C for 140 minutes and the reaction was stopped by opening the reaction to air and quenching in liquid N_2. The polymer pbocAPAm was purified by first precipitating into DI H_2O, redissolving in EtOAc, and precipitating twice into hexanes. After drying under vacuum, pbocAPAm was isolated as a yellow solid (1.12 g). The boc protecting groups were then removed by stirring the pbocAPAm in an excess of 4 M HCl/dioxane (25 mL, 20 eq. per protecting group) for 4 hours under ambient conditions, where the deprotected

polymer precipitated from solution. The mixture was centrifuged and the pAPAm was purified by dialyzing for 2 days (1 kDa MWC) under acidic conditions (pH=3-4) with frequent water exchanges. The polymer was lyophilized and isolated as a yellow solid (0.45 g).

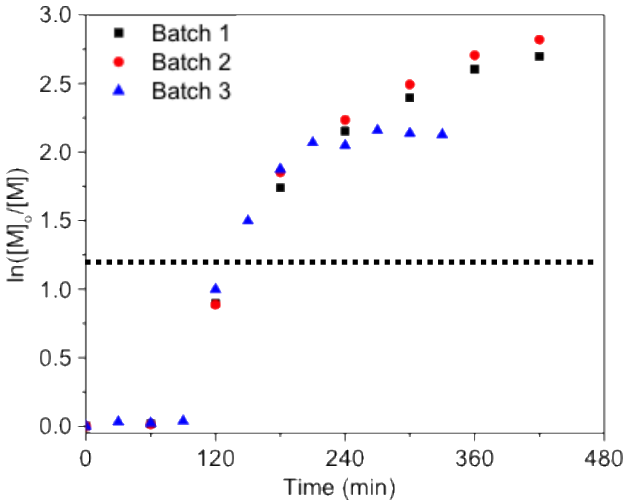

Figure A.23 *Plots of ln([M]$_o$/[M]) vs. time for RAFT polymerization of PbocAPAm with CEP and V-501 at 70 °C in DMSO. The dotted line represents a monomer conversion (ρ) of 70%.*

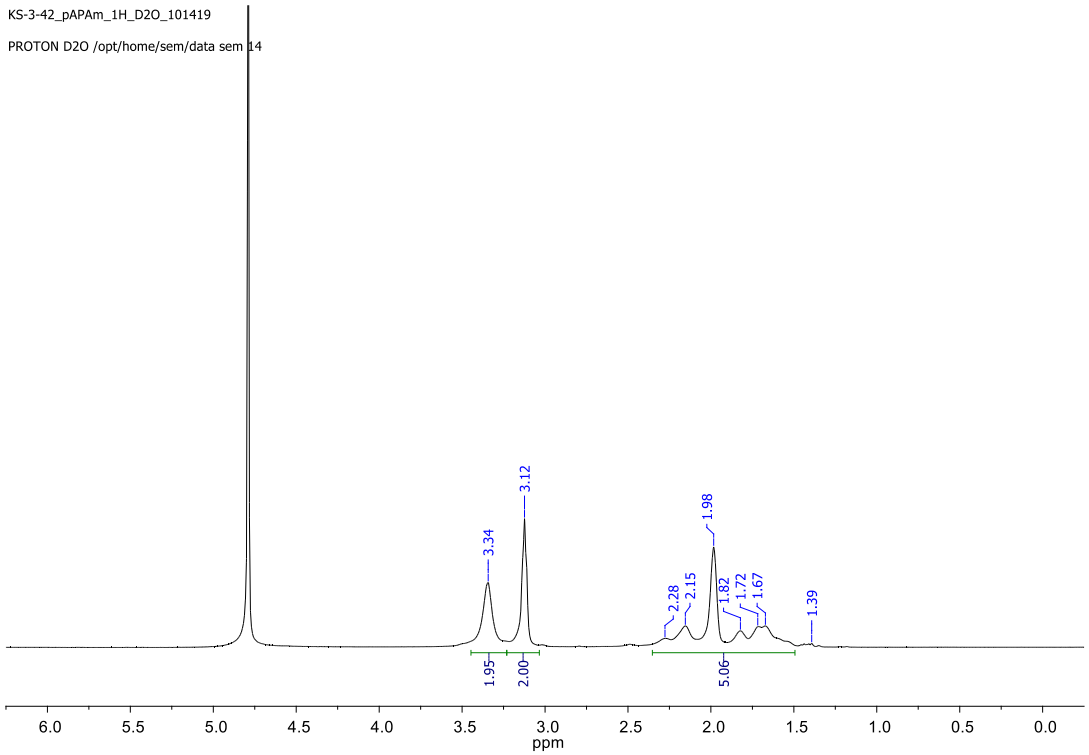

Figure A.24 *^{1}H NMR of $PAPAm_{61}$ homopolymer in D_2O.*

A.6 Polymer/dsRNA interactions

A.6.1 Synthesis of dsRNA

Table A.1 *Primer sequences for synthesis of dsSelK*

Gene	**Gen. Bank Accession #**	**5' Primer Sequence 3'**	**Amplicon Length (bp)**
SelenoK	XM_002403043.1	**F:**CGACGGACAATCGGACAAATA **R:**TGCTTCAACGGGAAGTAAGG	82
T7- *SelenoK* (For dsRNA synthesis)	XM_002403043.1	**F:**GAATTAATACGACTCACTATAGGGAGATGCTTCAACGGGAAGTAAGG **R:**GAATTAATACGACTCACTATAGGGAGTGGAGCCAGAAGACCTAGAA	367

A.6.2 Gel electrophoresis

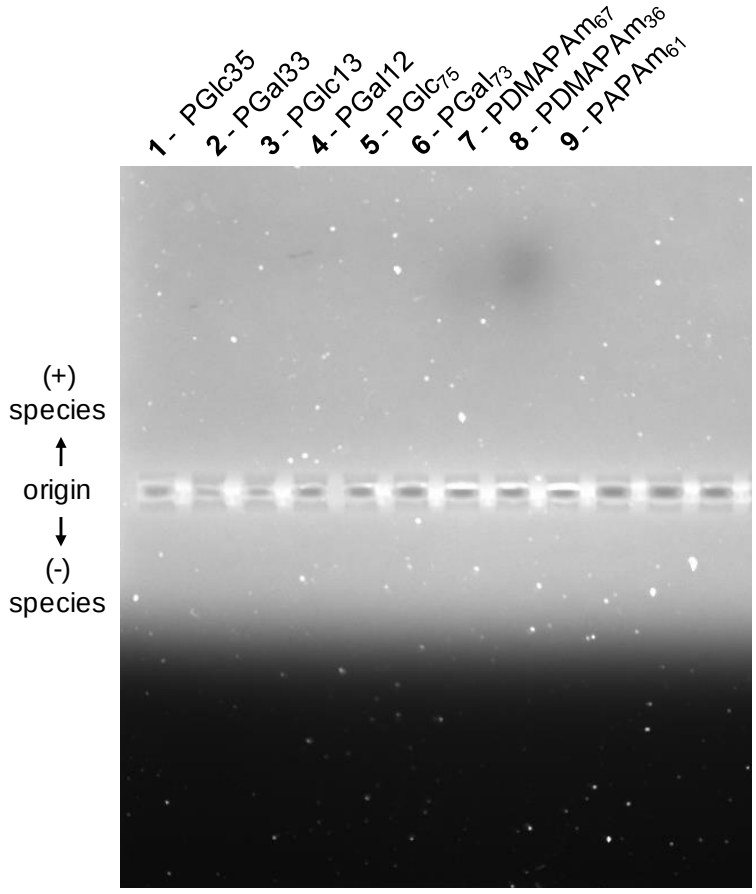

Figure A.25 *Gel electrophoresis of cationic glycopolymers in TAE buffer (pH = 8.0). The PDMAPAm homopolymers are slightly fluorescent due to the RAFT CTA (CEP) chain ends. No other polymers have any fluorescent response.*

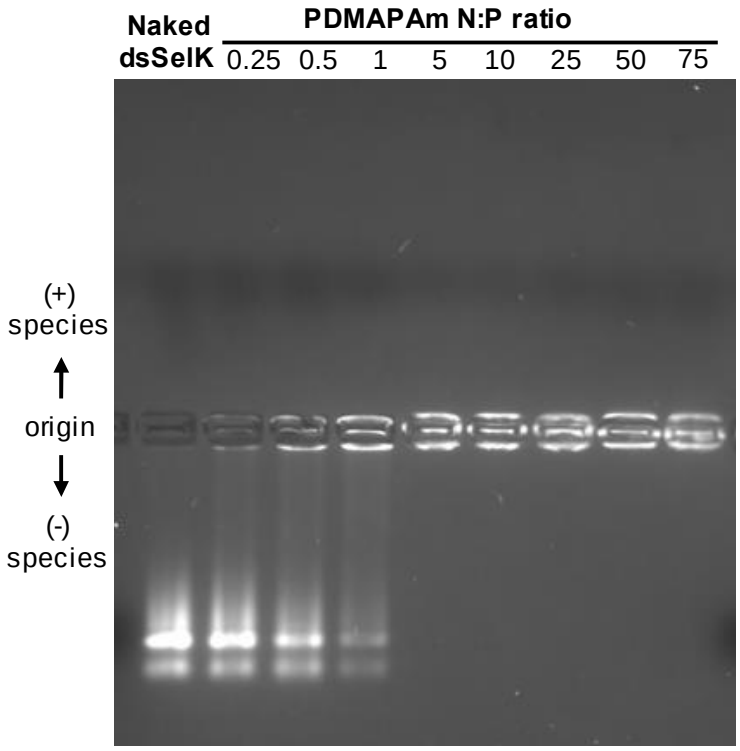

Figure A.26 *Gel electrophoresis of cationic homopolymer PDMAPAm/dsSelK polyplexes in TAE buffer (pH = 8.0). Numbers represent polyplex N:P ratios. Visualization of dsRNA and copolymer/dsRNA polyplexes was achieved with fluorescent EtBr staining.*

A.7 Zeta potential

Table A.2 *Zeta potential of homopolymers and copolymers in PBS and OptiMEM*

Sample[a]	ζ-potential (mV) PBS[b]	ζ-potential (mV) OptiMEM[b]
$PGlc_{75}$	-3.04 ± 0.99	-2.97 ± 0.29
$PGal_{73}$	-6.35 ± 0.75	-6.73 ± 0.36
$PDMAPAm_{67}$	14.50 ± 0.87	3.91 ± 0.19
$PAPAm_{61}$	16.90 ± 1.15	10.30 ± 0.72
PGlc13	0.76 ± 0.33	2.18 ± 0.42
PGal12	1.32 ± 0.37	2.02 ± 0.01
PGlc35	0.42 ± 0.57	5.48 ± 0.77
PGal33	0.94 ± 0.04	5.95 ± 0.57
siRNA (21 nt)[c]	-10.40 ± 2.16	--
PEG	-3.88 ± 0.13	-7.26 ± 1.11

[a]1 mg/mL polymer in PBS buffer (ζ-potential = -0.52 ± 0.81 mV) or OptiMEM transfection medium (ζ-potential = -5.03 ± 0.32 mV).

[b]Zeta potential determined from electrophoretic mobility using the Smoluchowski approximation.

[c]siRNA control measured at a concentration of 0.2 mg/mL.

Table A.3 *Zeta potential of cationic glycopolymer/dsRNA polyplexes in PBS and OptiMEM transfection media.*

	N:P = 10		N:P=50	
Polyplex	ζ-potential (mV), PBS	ζ-potential (mV), OptiMEM	ζ-potential (mV), PBS	ζ-potential (mV), OptiMEM
PGlc13 / dsRNA	-12.3 ± 1.36	-8.12 ± 0.85	-5.21 ± 0.67	-5.14 ± 0.40
PGal12 / dsRNA	-12.0 ± 1.54	-8.27 ± 0.58	-4.37 ± 0.82	-6.13 ± 0.66
PGlc35 / dsRNA	2.42 ± 0.41	3.26 ± 0.29	3.90 ± 0.79	8.23 ± 0.57
PGal33 / dsRNA	5.54 ± 0.36	7.03 ± 0.47	7.15 ± 0.78	7.12 ± 0.44
PDMAPAm/dsRNA	13.6 ± 0.45	--	13.2 ± 0.86	--

Table A.4 *Zeta potential of cationic glycopolymer/siRNA polyplexes (N:P=50) in PBS.*

Polyplex	ζ-potential (mV), PBS
PGlc13 / siRNA	1.82 ± 0.49
PGal12 / siRNA	1.75 ± 0.23
PGlc35 / siRNA	5.79 ± 0.71
PGal33 / siRNA	7.32 ± 1.10

A.8 Light scattering

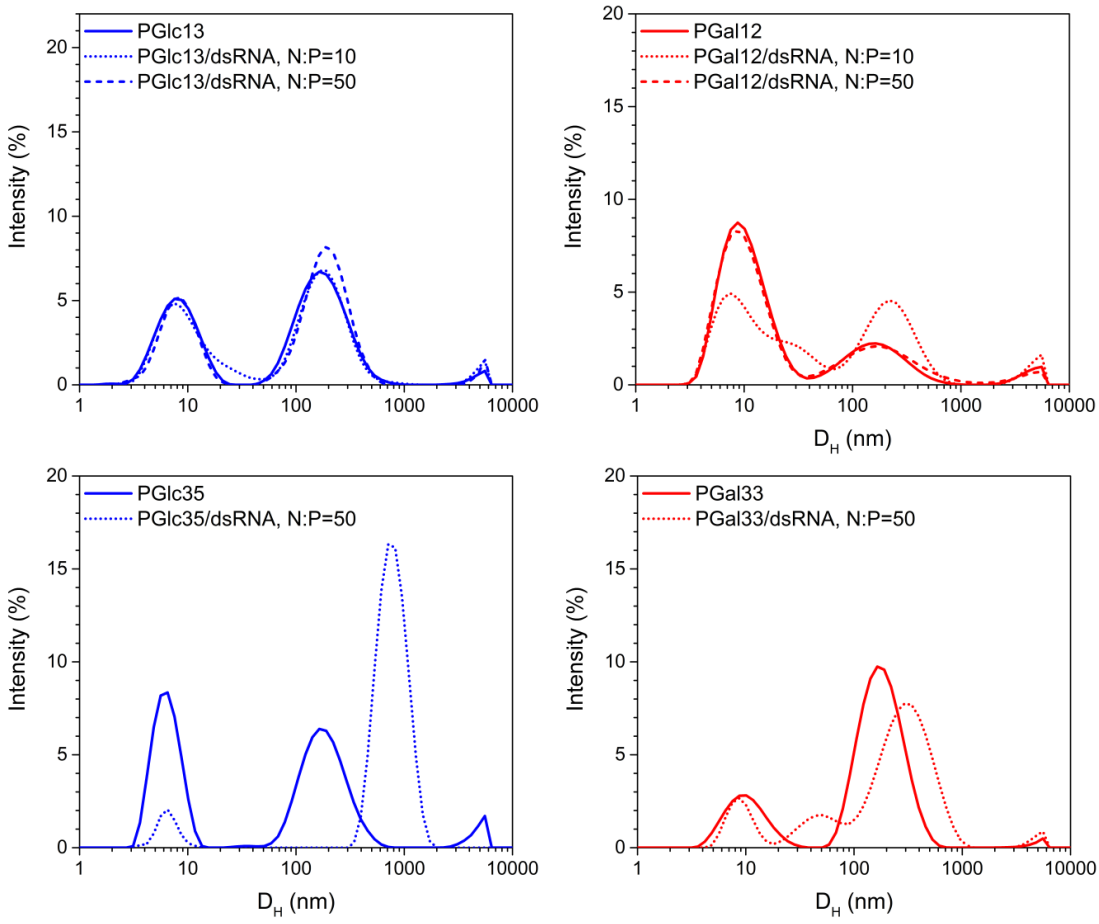

Figure A.27 *Hydrodynamic diameter (D_H) of filtered cationic glycopolymer and dsRNA/copolymer polyplex solutions in OptiMEM (1 mg/mL). Multiple particle size distributions are observed in all solutions.*

A.9 References

1. Das, P. K.; Dean, D. N.; Fogel, A. L.; Liu, F.; Abel, B. A.; McCormick, C. L.; Kharlampieva, E.; Rangachari, V.; Morgan, S. E., Aqueous RAFT Synthesis of Glycopolymers for Determination of Saccharide Structure and Concentration Effects on Amyloid β Aggregation. *Biomacromolecules* **2017,** *18* (10), 3359-3366.

2. Bradberry, S. J.; Dee, G.; Kotova, O.; McCoy, C. P.; Gunnlaugsson, T., Luminescent lanthanide (Eu(iii)) cross-linked supramolecular metallo co-polymeric hydrogels: the effect of ligand symmetry. *Chemical Communications* **2019,** *55* (12), 1754-1757.

3. Judzewitsch, P. R.; Zhao, L.; Wong, E. H. H.; Boyer, C., High-Throughput Synthesis of Antimicrobial Copolymers and Rapid Evaluation of Their Bioactivity. *Macromolecules* **2019,** *52* (11), 3975-3986.

APPENDIX B – SUPPLEMENTAL INFORMATION FOR CHAPTER III

B.1 Simulation box parameters

Table B.1 *Simulation box parameters for glycomonomers in water.*

Monomer	Water Model	Total Molecules	Total Atoms	Box Dimensions (Å)
GlcEAm	SPC/E	816	2486	29.20 x 29.20 x 29.20
GalEAm	SPC/E	782	2381	28.92 x 28.92 x 28.92
GlcEAm	TIP3P	801	2438	29.04 x 29.04 x 29.04
GalEAm	TIP3P	783	2384	28.97 x 28.97 x 28.97

Table B.2 *Simulation box parameters for oligomers in water.*

Monomer	Water Model	Total Molecules	Total Atoms	Box Dimensions (Å)
$PGlc_{10}$	SPC/E	3424	10635	47.54 x 47.54 x 47.54
$PGal_{10}$	SPC/E	2427	7644	39.95 x 42.88 x 45.08
$PDMAPAm_{10}$	SPC/E	2733	8442	44.14 x 44.14 x 44.14
$PGlc_{10}$	TIP3P	2441	7686	38.12 x 40.28 x 49.97
$PGal_{10}$	TIP3P	2482	7809	40.12 x 43.06 x 45.27
$PDMAPAm_{10}$	TIP3P	2595	8028	41.22 x 44.07 x 44.49
$PGlc_7$-*s*-$DMAPAm_3$	TIP3P	2705	8442	39.15 x 40.85 x 53.28
$PGal_7$-*s*-$DMAPAm_3$	TIP3P	2459	7704	37.47 x 42.14 x 49.11
3 $PGlc_{10}$	TIP3P	8513	26628	50.66 x 69.09 x 76.33
3 $PGal_{10}$	TIP3P	9992	31065	67.87 x 67.87 x 67.87
3 $PDMAPAm_{10}$	TIP3P	6588	20493	46.87 x 63.36 x 69.52

Table B.3 *Simulation box parameters for dsRNA/monomer simulations in water.*

Monomer	Water Model	Total Molecules	Total Atoms	Box Dimensions (Å)
dsRNA only	SPC/E	7364	22954	62.58 x 62.58 x 62.58
dsRNA / GlcEAm	SPC/E	10139	31384	69.08 x 69.08 x 69.08
dsRNA / GalEAm	SPC/E	9986	30925	68.02 x 68.02 x 68.02
dsRNA / DMAPAm	SPC/E	9136	28351	66.93 x 66.93 x 66.93
dsRNA only	TIP3P	6250	19612	59.53 x 59.53 x 59.53
dsRNA / 3 GlcEAm	TIP3P	8172	25483	57.83 x 67.95 x 68.89
dsRNA / 3 GalEAm	TIP3P	7223	22666	54.00 x 62.65 x 66.80
dsRNA / 3 DMAPAm	TIP3P	7179	22480	53.74 x 64.75 x 69.50

Table B.4 *Simulation box parameters for dsRNA/oligomer simulations in TIP3P water.*

Monomer	Total Molecules	Total Atoms	Box Dimensions (Å)
dsRNA / $PGlc_{10}$	10399	32422	68.90 x 68.90 x 68.90
dsRNA / $PGal_{10}$	11405	35440	70.89 x 70.89 x 70.89
dsRNA / $PDMAPAm_{10}$	9274	28967	66.33 x 66.33 x 66.33
dsRNA / 3 $PGlc_{10}$	14623	45820	64.11 x 80.70 x 94.05
dsRNA / 3 $PGal_{10}$	21262	65737	87.20 x 87.20 x 87.20
dsRNA / 3 $PDMAPAm_{10}$	15218	47365	60.65 x 74.93 x 108.15
dsRNA / $PGlc_7$-*s*-$DMAPAm_3$	11715	36346	71.57 x 71.57 x 71.57
dsRNA / $PGal_7$-*s*-$DMAPAm_3$	10837	33712	69.77 x 69.77 x 69.77

B.2 Oligomer simulations

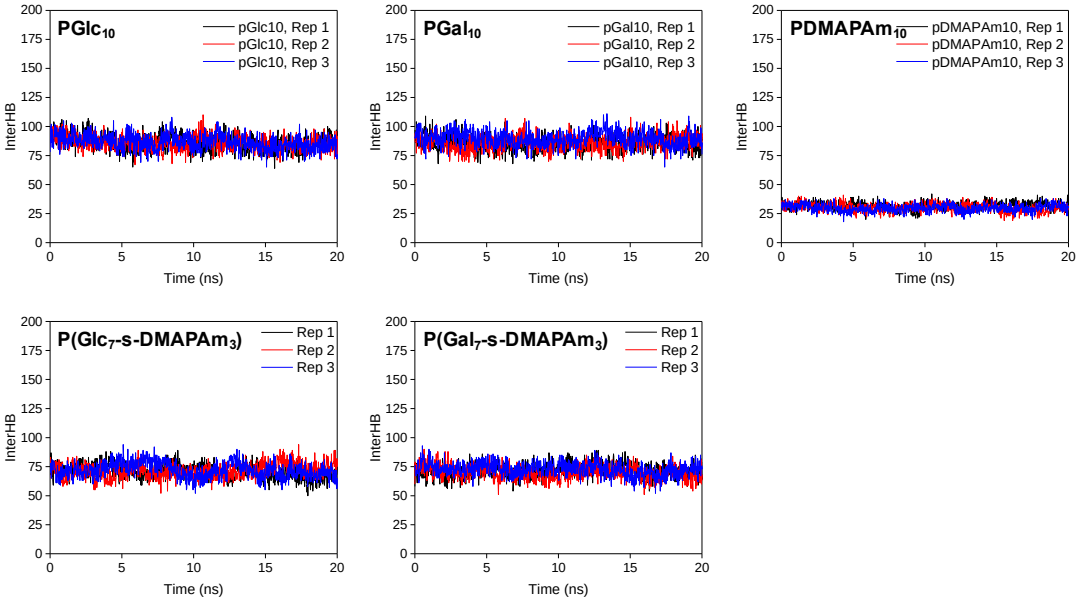

Figure B.1 *InterHBs of neutral and cationic oligomers in TIP3P water.*

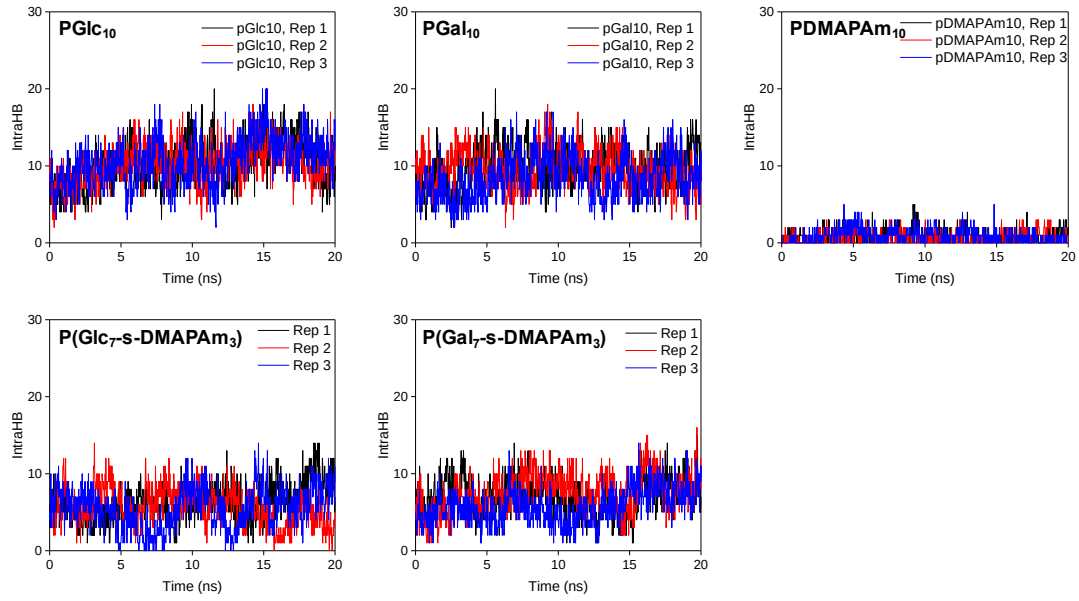

Figure B.2 *IntraHBs of neutral and cationic oligomers in TIP3P water.*

Table B.5 *Neutral and cationic oligomer intermolecular and intramolecular hydrogen bonds in TIP3P water.*

Oligomer	InterHB Range	InterHB Mean ± St. Dev.	IntraHB Range	IntraHB Mean ± St. Dev.
$PGlc_{10}$	69-102	84.5 ± 5.9	4-18	11.4 ± 2.5
$PGal_{10}$	65-109	87.4 ± 6.4	3-16	9.0 ± 2.5
$PDMAPAm_{10}$	19-41	30.4 ± 3.6	0-4	0.8 ± 0.8
$PGlc_7$-*s*-$DMAPAm_3$	50-94	70.6 ± 6.9	0-14	6.4 ± 2.9
$PGal_7$-*s*-$DMAPAm_3$	52-87	69.2 ± 5.7	3-16	3.3 ± 2.1

Table B.6 *Intermolecular and intramolecular hydrogen bonds for 3 oligomers in TIP3P water.*

Oligomer	InterHB Range	InterHB Mean ± St. Dev.	IntraHB Range	IntraHB Mean ± St. Dev.
3 $PGlc_{10}$	212-293	248.3 ± 14.0	22-49	35.5 ± 5.9
3 $PGal_{10}$	200-269	230.9 ± 13.7	27-59	42.4 ± 5.7
3 $PDMAPAm_{10}$	76-111	93.3 ± 5.8	0-8	2.2 ± 1.4
3 $PGlc_7$-*s*-$DMAPAm_3$	185-239	210.4 ± 10.2	10-32	21.0 ± 3.8
3 $PGal_7$-*s*-$DMAPAm_3$	181-252	213.7 ± 10.9	6-35	21.2 ± 4.3

B.3 dsRNA simulations

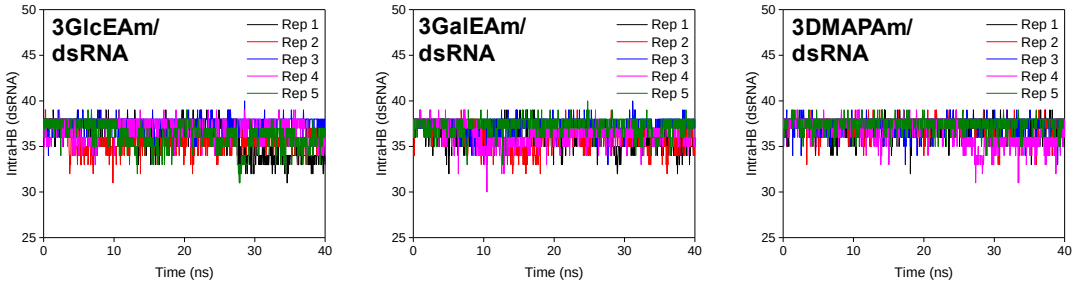

Figure B.3 *The number of interHBs between dsRNA strands from five replicate experiments of monomers with dsRNA in TIP3P water.*

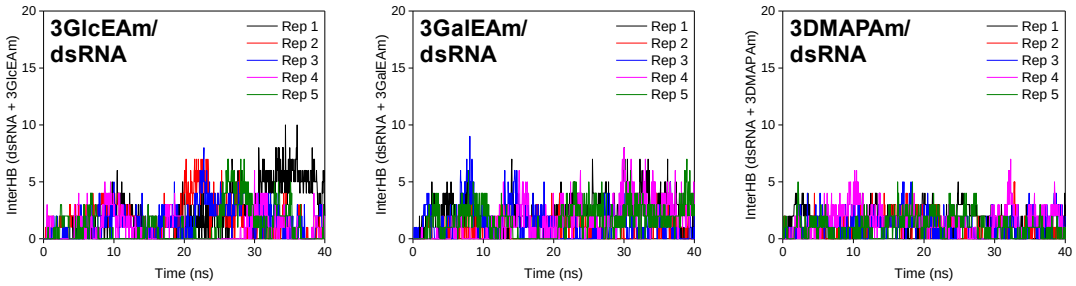

Figure B.4 *Intermolecular hydrogen bonds between dsRNA and (a) GlcEAm, (b) GalEAm, and (c) DMAPAm monomers over the course of 40.0 ns in TIP3P water.*

Table B.7 *Intermolecular interactions in dsRNA/monomer simulations*

Monomer	dsRNA interHBs with water Range	dsRNA interHBs with water Avg ± St. Dev.	dsRNA interHBs with 3 monomers Range	dsRNA interHBs with 3 monomers Avg ± St. Dev.
dsRNA only	294-352	325.4 ± 8.3	--	--
3 GlcEAm	300-355	322.8 ± 8.5	0-10	1.8 ± 2.1
3 GalEAm	289-346	320.2 ± 9.1	0-7	1.9 ± 1.5
3 DMAPAm	287-349	319.5 ± 8.5	0-7	1.1 ± 1.1

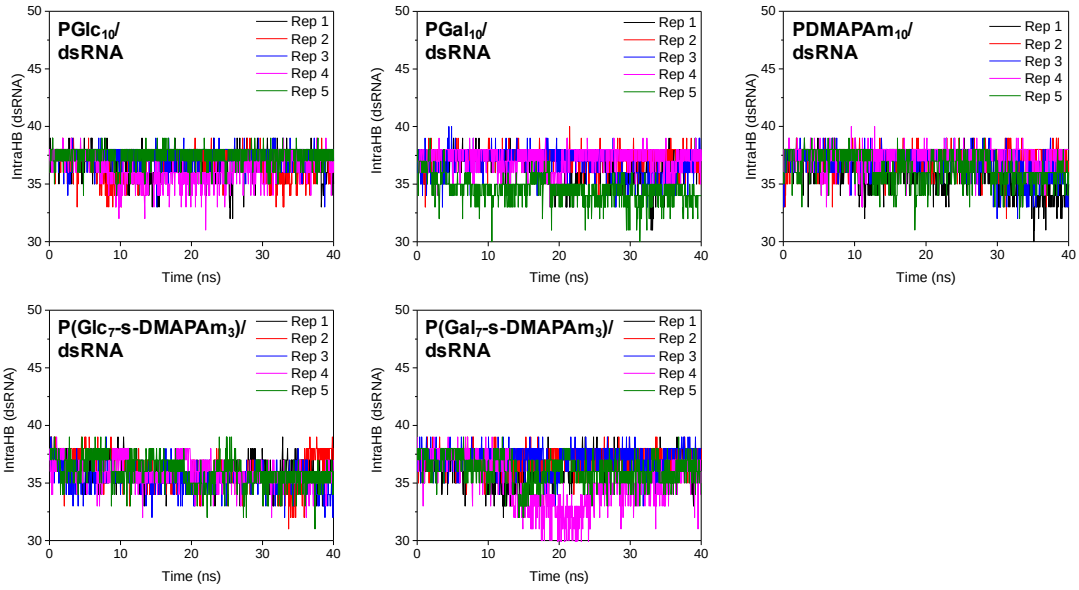

Figure B.5 *The number of interHBs between dsRNA strands from five replicate experiments of oligomers with dsRNA.*

Table B.8 *Intermolecular interactions in dsRNA/oligomer simulations*

Oligomer	dsRNA /water interHB Range	dsRNA /water interHB Avg ± St. Dev.	dsRNA interHBs with oligomer Range	dsRNA interHBs with oligomer Avg ± St. Dev.	Oligomer intraHBs Range	Oligomer intraHBs Avg ± St. Dev	Oligomer interHBs with water Range	Oligomer interHBs with water Avg ± St. Dev
dsRNA only	294-352	325.4 ± 8.3	--	--	--	--	--	--
$PGlc_{10}$	295-346	320.8 ± 8.1	0-9	2.0 ± 2.2	4-23	12.3 ± 3.5	57-103	81.5 ± 7.2
$PGal_{10}$	300-349	322.1 ± 8.7	0-8	1.8 ± 1.8	3-19	10.3 ± 2.6	60-105	83.4 ± 6.4
$PDMAPAm_{10}$	278-333	306.8 ± 8.6	1-11	5.1 ± 1.6	0-5	0.9 ± 1.0	17-38	27.3 ± 3.3
$PGlc_7$-*s*-$DMAPAm_3$	285-343	313.3 ± 9.5	0-13	5.5 ± 2.4	1-17	5.8 ± 2.1	48-81	65.7 ± 5.5
$PGal_7$-*s*-$DMAPAm_3$	277-342	313.9 ± 9.6	0-12	4.4 ± 2.4	1-15	8.1 ± 2.4	46-84	65.2 ± 6.8

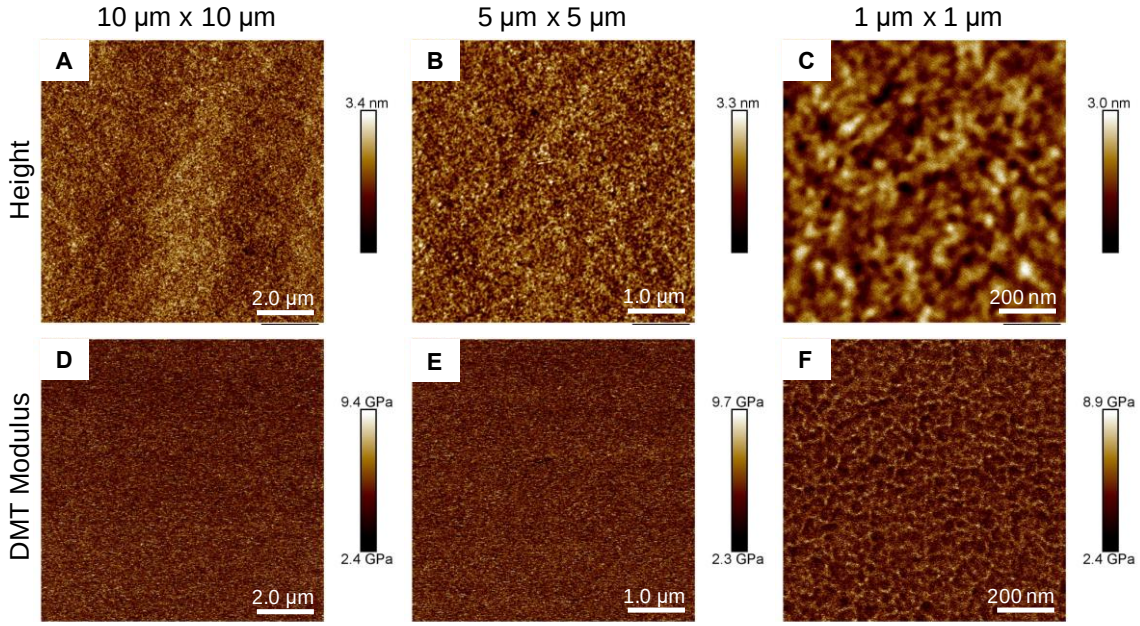

Figure C.1 *(a-c) Height and (d-f) DMT modulus AFM images of SA HB PVPON58 films under ambient conditions.*

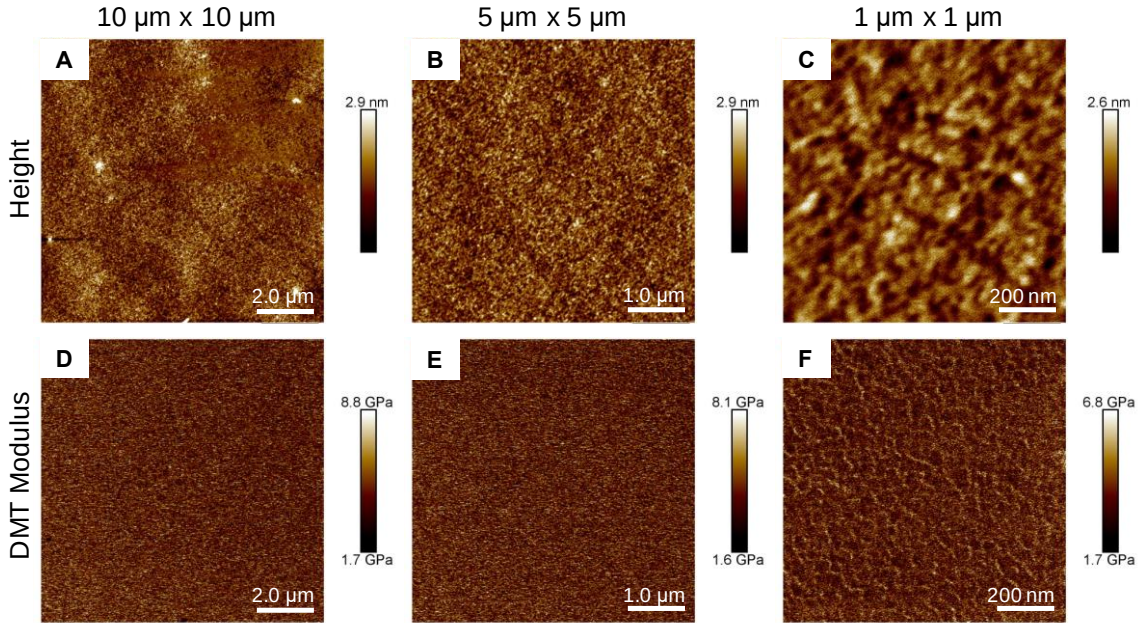

Figure C.2 *(a-c) Height and (d-f) DMT modulus AFM images of SA HB PVPON360 films under ambient conditions.*

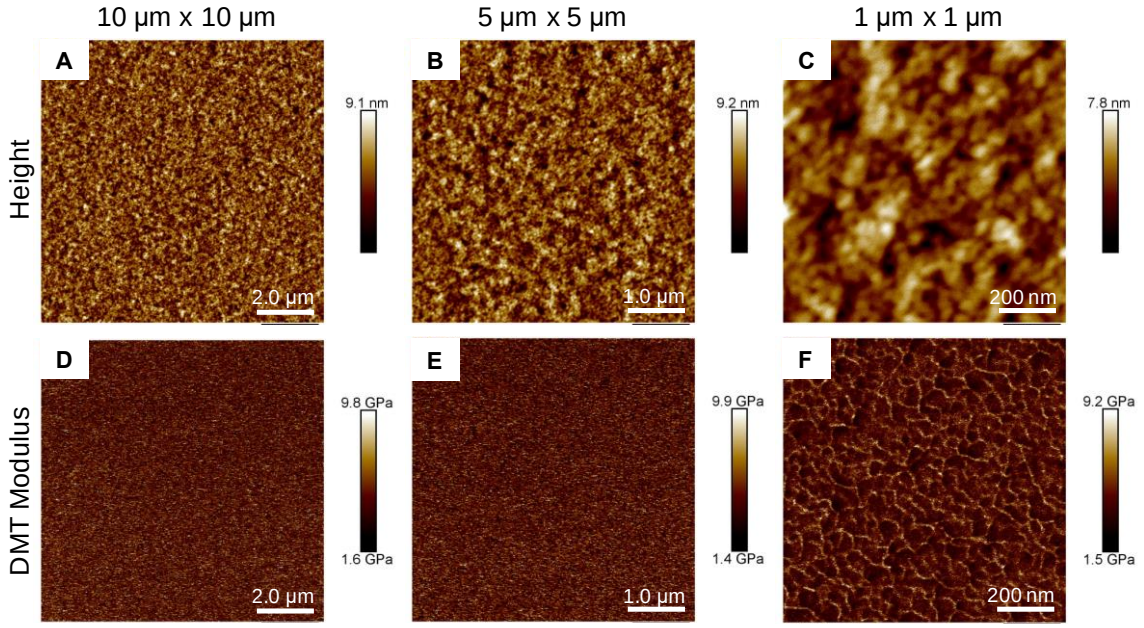

Figure C.3 *(a-c) Height and (d-f) DMT modulus AFM images of SA Hydrogel PVPON58 films under ambient conditions.*

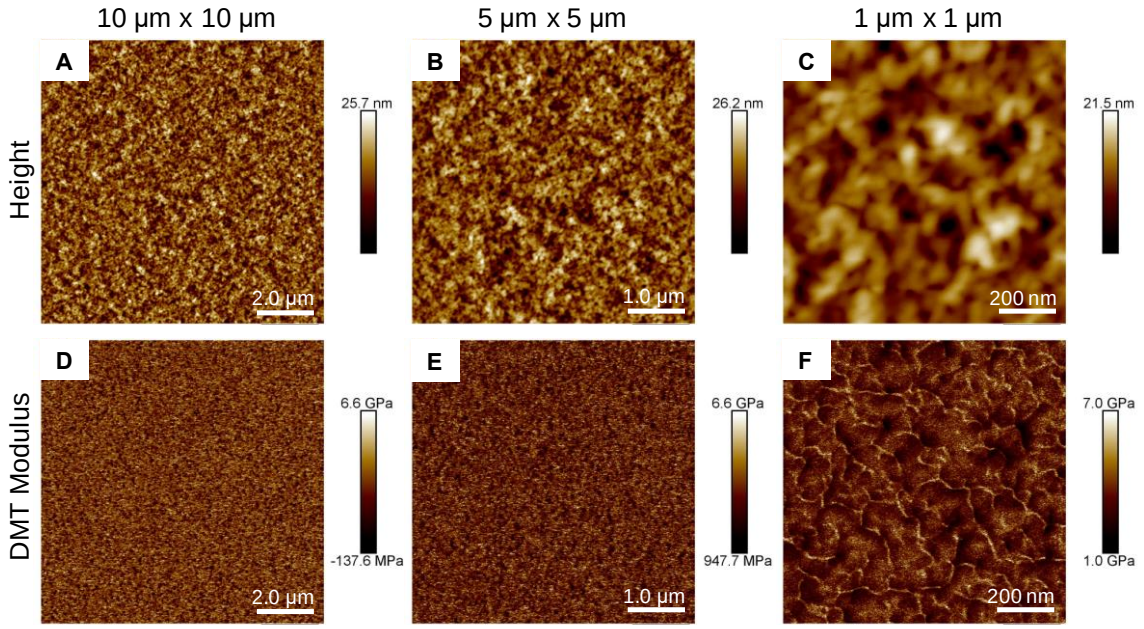

Figure C.4 *(a-c) Height and (d-f) DMT modulus AFM images of SA Hydrogel PVPON360 films under ambient conditions.*

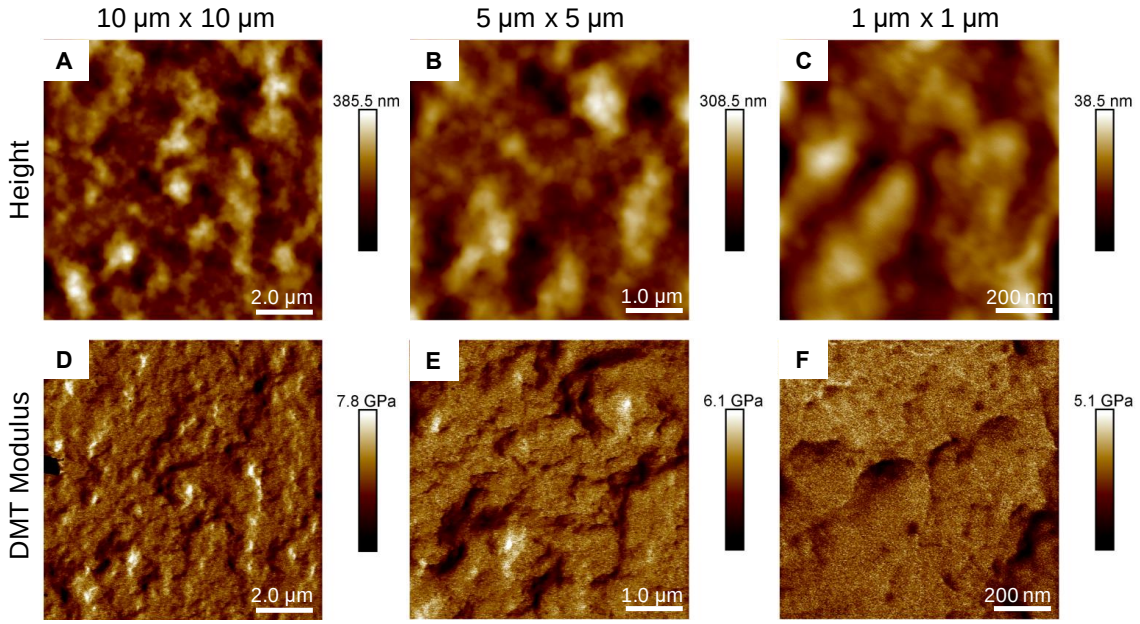

Figure C.5 *(a-c) Height and (d-f) DMT modulus AFM images of Dipped Hydrogel PVPON58 films under ambient conditions.*

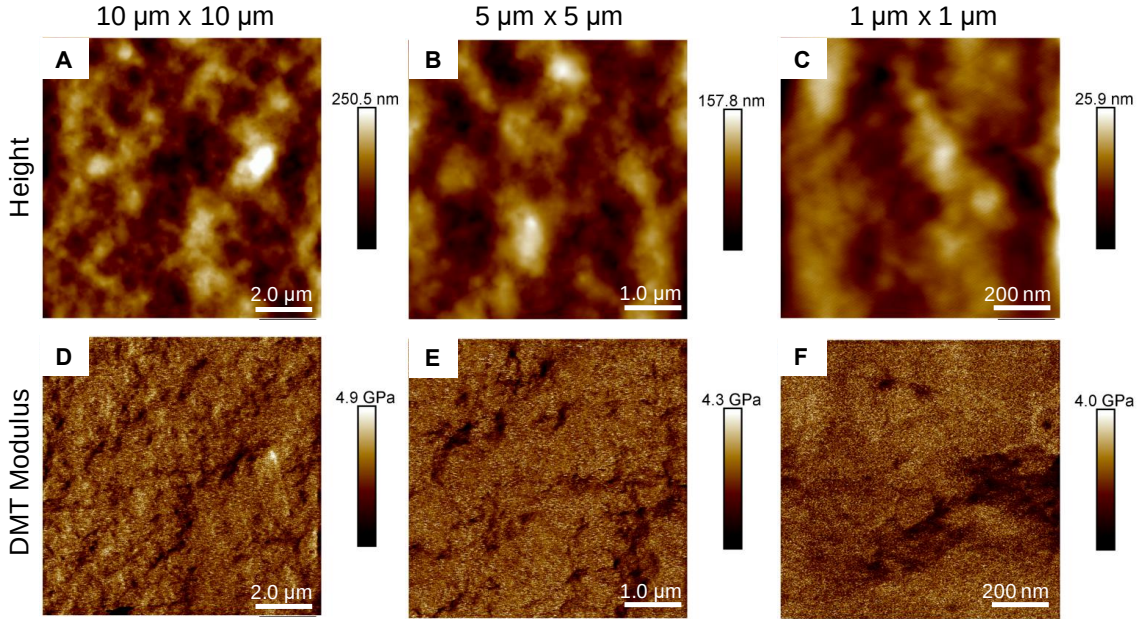

Figure C.6 *(a-c) Height and (d-f) DMT modulus AFM images of Dipped Hydrogel PVPON360 films under ambient conditions.*

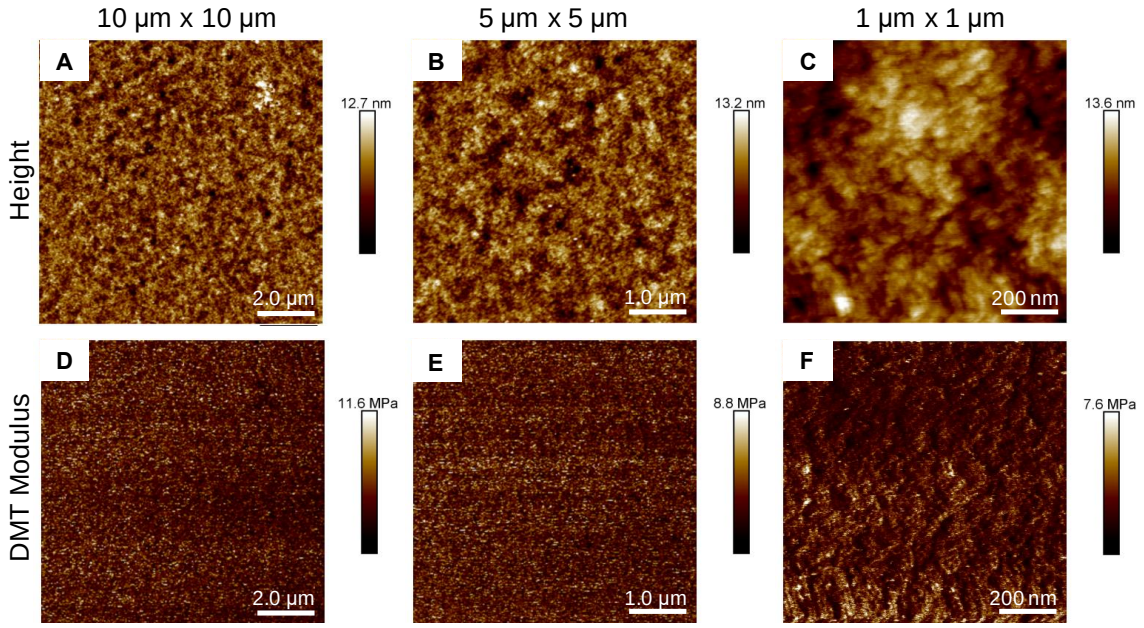

Figure C.7 *(a-c) Height and (d-f) DMT modulus AFM images of SA Hydrogen PVPON58 films measured at pH 5.*

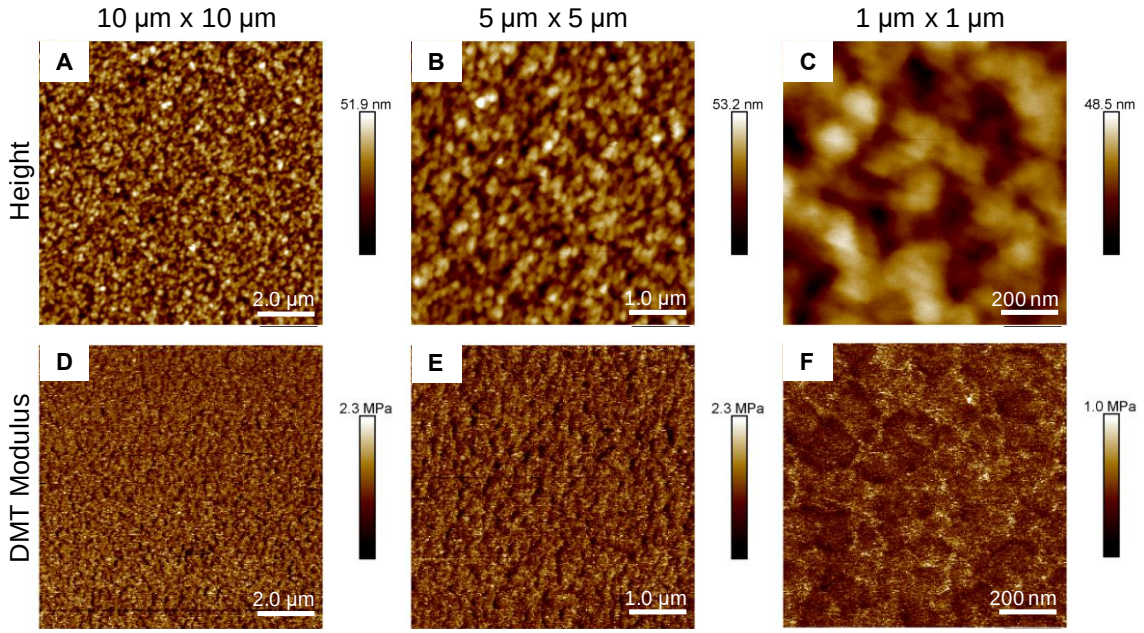

Figure C.8 *(a-c) Height and (d-f) DMT modulus AFM images of SA Hydrogel PVPON58 films measured at pH 6.5.*

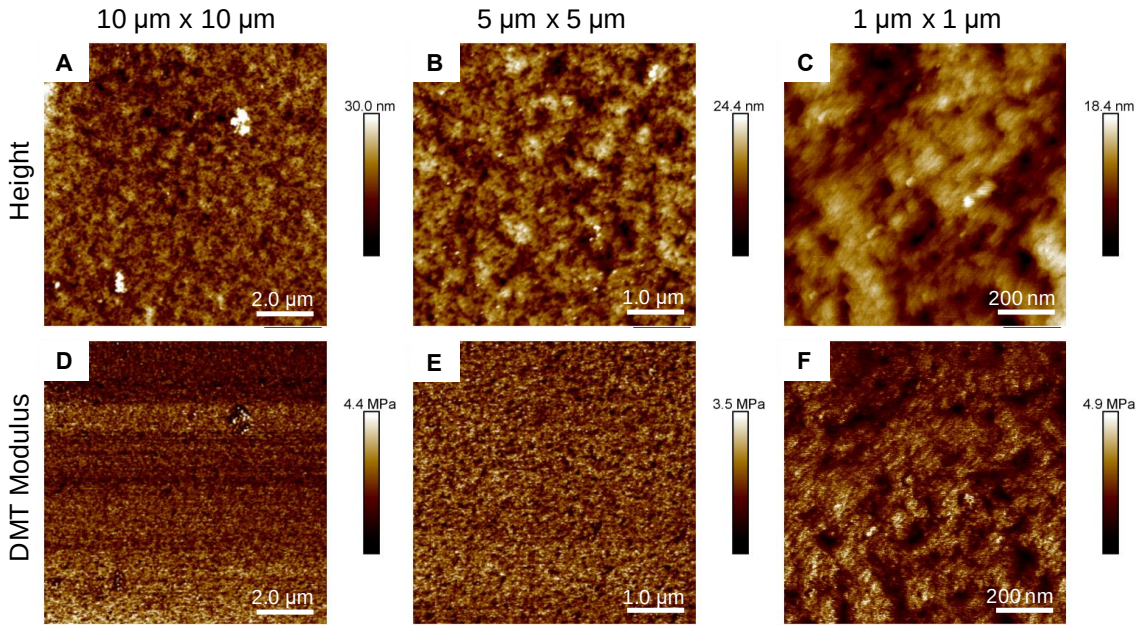

Figure C.9 *(a-c) Height and (d-f) DMT modulus AFM images of SA Hydrogel PVPON360 films measured at pH 5.*

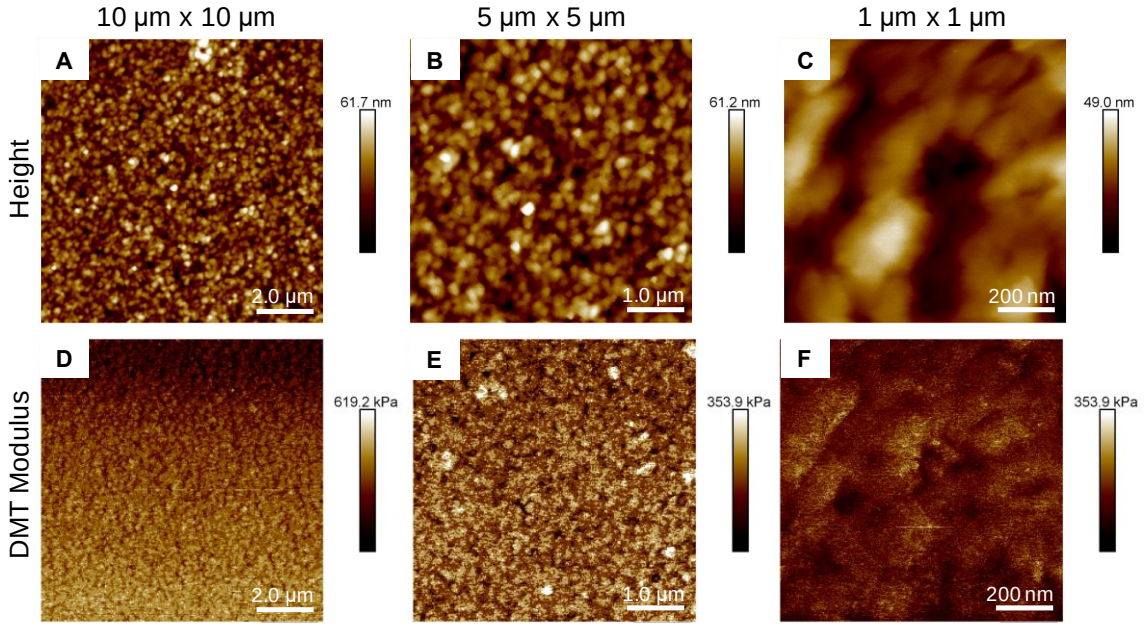

Figure C.10 *(a-c) Height and (d-f) DMT modulus AFM images of SA Hydrogel PVPON360 films measured at pH 6.5.*

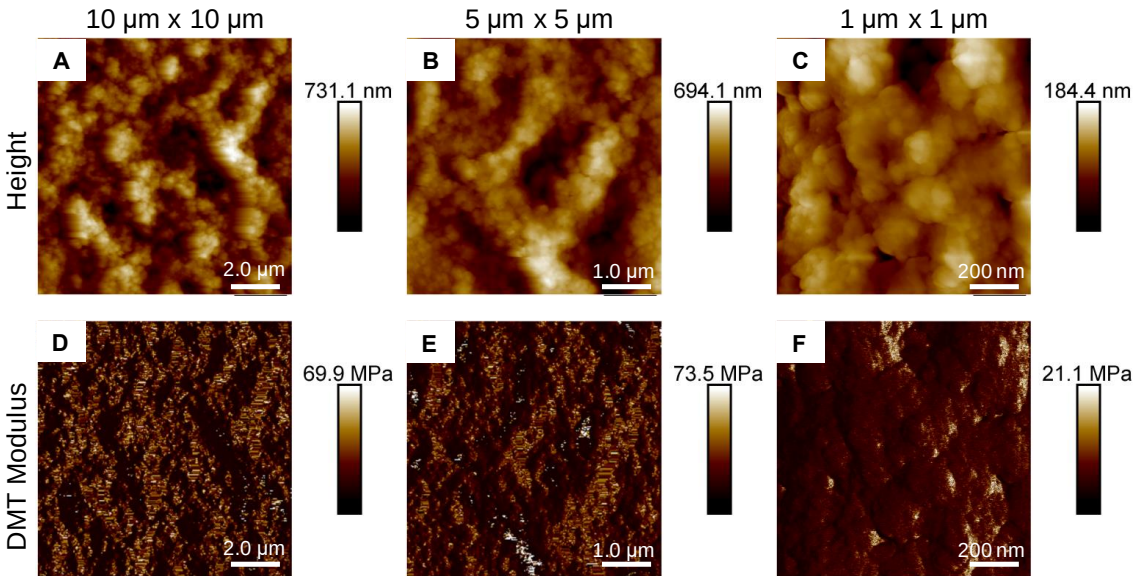

Figure C.11 *(a-c) Height and (d-f) DMT modulus AFM images of Dipped Hydrogel PVPON58 films measured at pH 5.*

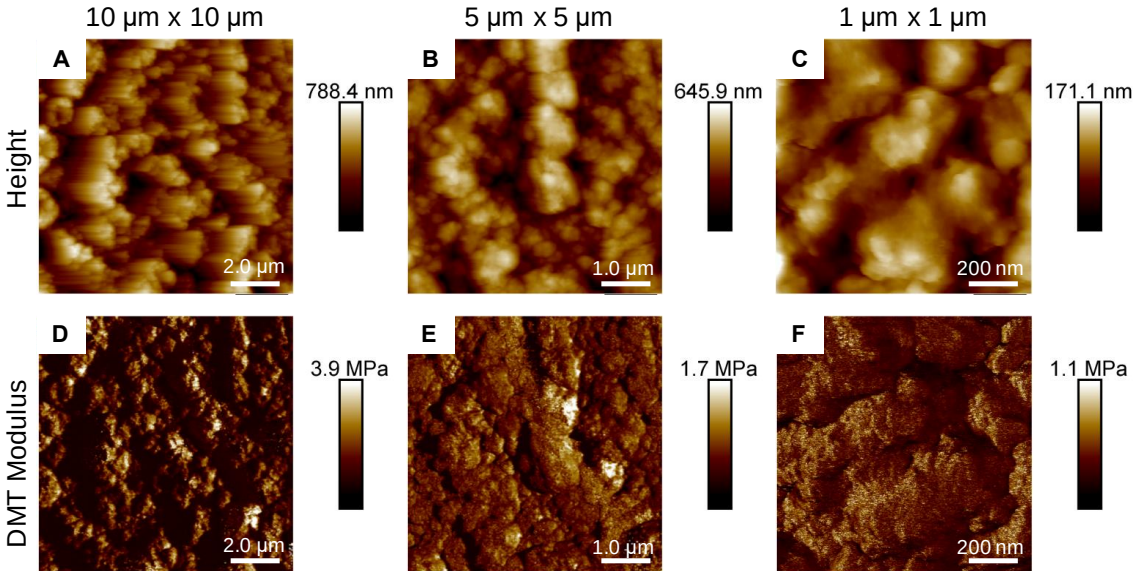

Figure C.12 *(a-c) Height and (d-f) DMT modulus AFM images of Dipped Hydrogel PVPON58 films measured at pH 6.5.*

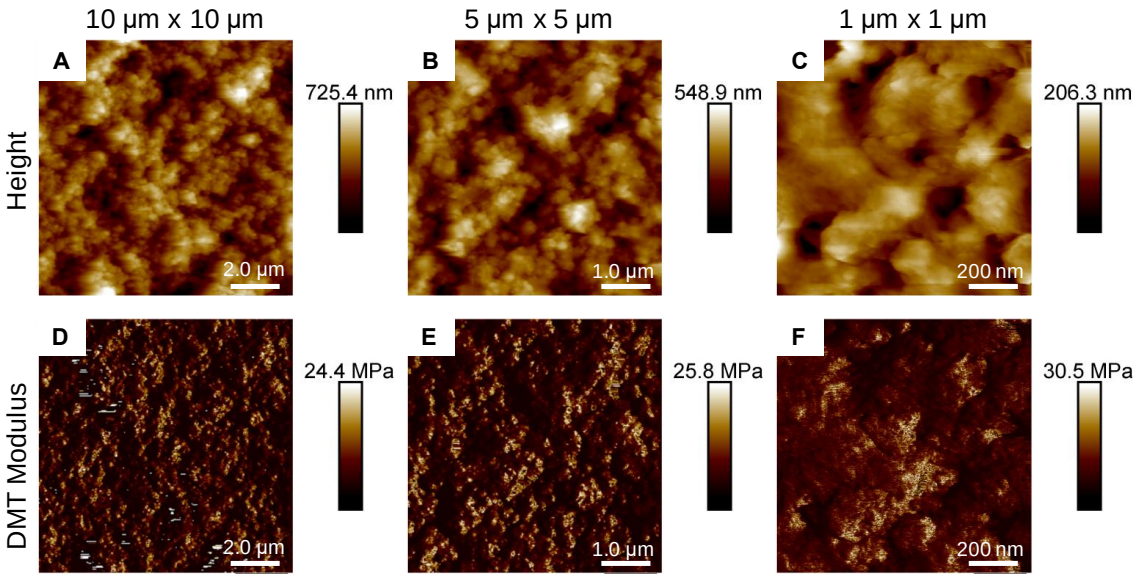

Figure C.13 *(a-c) Height and (d-f) DMT modulus AFM images of Dipped Hydrogel PVPON360 films measured at pH 5.*

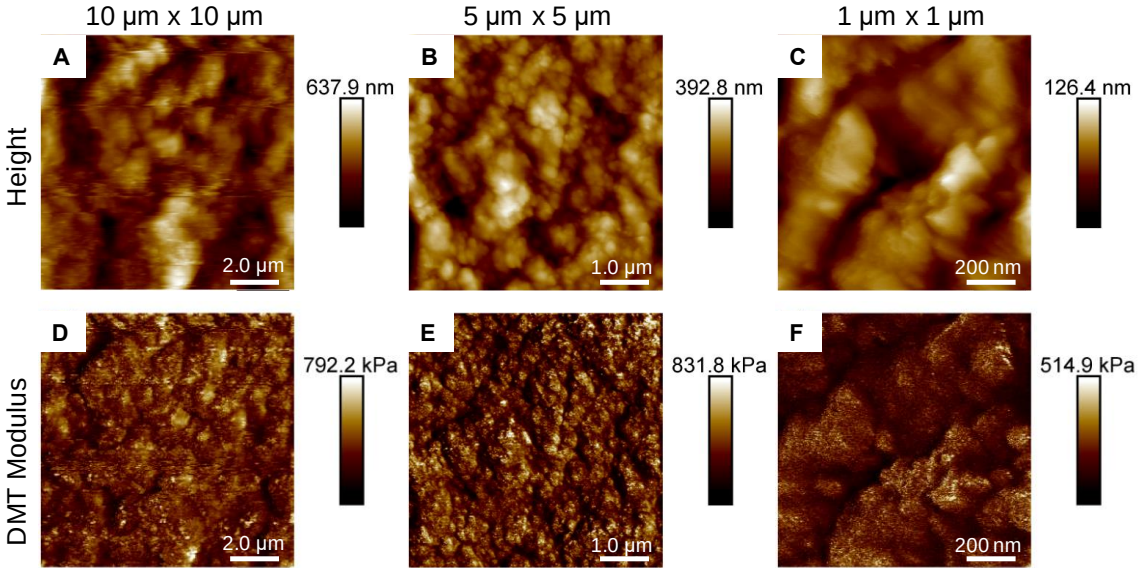

Figure C.14 *(a-c) Height and (d-f) DMT modulus AFM images of Dipped Hydrogel PVPON360 films measured at pH 6.5.*

Table C.2 *Characterization of 10 µm x 10 µm AFM images of dry H-bonded and hydrogel films*

Sample	$R_{q,avg}$ (nm)	DMT Modulus (GPa)
SA H-bonded PVPON58	0.60 ± 0.18	4.98 ± 0.39
SA H-bonded PVPON360	0.53 ± 0.02	4.62 ± 0.18
SA Hydrogel PVPON58	1.52 ± 0.20	5.24 ± 0.75
SA Hydrogel PVPON360	3.71 ± 0.01	3.07 ± 0.04
Dipped Hydrogel PVPON58	64.53 ± 9.76	4.59 ± 0.43
Dipped Hydrogel PVPON360	35.87 ± 2.87	4.71 ± 0.23

Table C.3 *Characterization of 5 µm x 5 µm AFM images of dry H-bonded and hydrogel films.*

Sample	$R_{q,avg}$ (nm)	DMT Modulus (GPa)
SA H-bonded PVPON58	0.47 ± 0.09	4.76 ± 0.52
SA H-bonded PVPON360	0.44 ± 0.01	4.12 ± 0.11
SA Hydrogel PVPON58	1.47 ± 0.15	4.87 ± 0.32
SA Hydrogel PVPON360	3.76 ± 0.05	3.32 ± 0.10
Dipped Hydrogel PVPON58	41.83 ± 1.85	4.24 ± 0.26
Dipped Hydrogel PVPON360	21.33 ± 1.19	4.49 ± 0.17

Table C.4 *Characterization of 10 µm x 10 µm AFM images of hydrated hydrogel films.*

Sample	pH	$R_{q,avg}$ (nm)	DMT Modulus (MPa)
SA Hydrogel PVPON58	5	4.34 ± 2.01	1.29 ± 0.48
SA Hydrogel PVPON58	6.5	7.61 ± 0.69	0.67 ± 0.14
SA Hydrogel PVPON360	5	6.20 ± 2.77	6.00 ± 2.28
SA Hydrogel PVPON360	6.5	8.73 ± 0.11	0.29 ± 0.15
Dipped Hydrogel PVPON58	5	120.33 ± 17.04	8.64 ± 1.68
Dipped Hydrogel PVPON58	6.5	128.33 ± 11.55	0.66 ± 0.22
Dipped Hydrogel PVPON360	5	98.43 ± 13.14	3.53 ± 0.51
Dipped Hydrogel PVPON360	6.5	106.23 ± 20.67	1.06 ± 0.79

Table C.5 *Characterization of 5 µm x 5 µm AFM images of hydrated hydrogel films.*

Sample	pH	$R_{q,avg}$ (nm)	DMT Modulus (MPa)
SA Hydrogel PVPON58	5	3.10 ± 0.29	1.75 ± 0.73
SA Hydrogel PVPON58	6.5	7.15 ± 0.45	0.84 ± 0.25
SA Hydrogel PVPON360	5	4.25 ± 0.26	2.37 ± 0.79
SA Hydrogel PVPON360	6.5	8.59 ± 0.13	0.52 ± 0.24
Dipped Hydrogel PVPON58	5	88.37 ± 9.91	8.78 ± 1.37
Dipped Hydrogel PVPON58	6.5	103.10 ± 5.99	0.93 ± 0.77
Dipped Hydrogel PVPON360	5	78.70 ± 0.87	4.72 ± 2.18
Dipped Hydrogel PVPON360	6.5	53.17 ± 7.18	0.28 ± 0.07